Modelling Nearshore Waves, Runup and Overtopping

A thesis submitted to the University of Manchester for the degree of Doctor of Philosophy in the Faculty of Engineering and Physical Sciences

2011

Maurice McCabe

School of Mechanical, Aerospace and Civil Engineering

Contents

List of Figures

List of Tables

List of Symbols

The following are the main symbols used in the thesis. Where other symbols have been used, they will be defined in the text. In some cases, symbols have more than one meaning; additional meanings will be given in the text. If no explanation is given in the text the symobol will have the definition shown below. Where applicable, units are shown in brackets.

a	Wave amplitude (m)
B	Constant to control the linear dispersion characteristics in the Boussinesq equations
c	Wave celerity ($= {}^{L}/_{T}$) ($\mathrm{m\,s^{-1}}$)
c_g	Wave group velocity ($\mathrm{m\,s^{-1}}$)
C_b	Breaking coefficient
C_{bt}, C_{bh}	Breaking coefficient, respectively using ${}^{\partial\eta}/_{\partial t}$ or ${}^{H}/_{h}$ as a breaking parameter
C_f	Friction factor
$d(x)$	Still water depth (m)
d_{in}	Still water depth at wave input location (m)
dt, dx	Model timestep (s), model spatial step (m)
E	Wave energy ($\mathrm{J\,m^{-2}}$)
f	Frequency (Hz)
f_p	Spectral peak frequency (Hz)
F	Force (N)
F_{wall}	Force imposed by seawall (N)
g	Gravitational acceleration ($= 9.81\,\mathrm{m\,s^{-2}}$)
$h(x,t)$	Water depth (m)
H	Wave height (m)
H_0	Deepwater wave height (m)
$H_{1/3}$	Mean height of highest third of waves (m)
H_b	Breaking wave height (m)
H_{m0}	Spectral significant wave height (m)

H_{rms}	Root mean square wave height (m)
H_s	Significant wave height (either $H_{1/3}$ or H_{m0}) (m)
k	Wave number ($= {}^{2\pi}/_{L}$) (m^{-1})
k_p	Wave number corresponding to peak frequency ($= {}^{2\pi}/_{L_p}$) (m^{-1})
L	Wavelength (m)
L_0	Deepwater wavelength (m)
L_p	Wavelength corresponding to peak frequency f_p (m)
m_n	n-th spectral moment, i.e. $\int^f f^n S(f) df$
p	Pressure ($\mathrm{N\,m}^{-2}$)
q	Overtopping discharge ($\mathrm{m}^3\,\mathrm{m}^{-1}\,\mathrm{s}^{-1}$)
q_m	Mean overtopping discharge ($\mathrm{m}^3\,\mathrm{m}^{-1}\,\mathrm{s}^{-1}$)
Q_b	Proportion of breaking wvaes
R	Runup level, above still water level (m)
$R_{1/3}$	Mean level of highest third of runups (m)
$R_{1/10}$	Mean level of highest tenth of runups (m)
$R_{2\%}$	98th percentile runup level (m)
R_c	Crest freeboard (m)
S	Spectral energy density ($\mathrm{m}^2\,\mathrm{s}$)
t	Time (s)
T	Wave period (s)
$T_{1/3}$	Significant wave period - mean period of highest third of waves (s)
T_{m02}	Spectral mean wave period ($= \sqrt{{}^{m_0}/_{m_2}}$) (s)
T_p	Peak wave period ($= {}^{1}/_{f_p}$) (s)
T	Wave period (s)
u, v	Horizontal velocities (in x and y direction respectively, usually depth-averaged) ($\mathrm{m\,s}^{-1}$)
Ur	Ursell number ($= {}^{HL^2}/_{d^3}$)
V	Volume (m^3)
w	Vertical velocity (in z direction) ($\mathrm{m\,s}^{-1}$)
x, y	Horizontal axes, horizontal distance (m)
z	Vertical axis, vertical distance (m)
$z_b(x)$	Bed level above datum level (m)
β	Angle of bed slope from horizontal (rad)
ε	Nonlinearity ($= {}^{a}/_{d}$)
$\zeta(x,t)$	Excursion of free surface level relative to still water level (m)

$\eta(x,t)$	Free surface level above datum level ($\eta = \zeta$ when datum is still water level) (m)
θ	Wave direction ($^\circ$)
μ	Relative depth ($= {}^{d}/_{L}$)
ν, ν_e	Kinematic viscosity (of water), eddy viscosity ($\mathrm{m^2\,s^{-1}}$)
ξ_0	Surf similarity parameter ($= \tan\beta/\sqrt{{}^{H_0}/_{L_0}}$)
ρ	Density (of water) ($\mathrm{kg\,m^{-3}}$)
τ	Shear stress ($\mathrm{N\,m^{-2}}$)
ϕ	Phase angle (rad)
ω	Angular frequency ($= {}^{2\pi}/_{T}$) ($\mathrm{rad\,s^{-1}}$)

Abstract

University of Manchester

Maurice McCabe

Doctor of Philosophy (PhD)

Modelling Nearshore Waves, Runup and Overtopping

27th September 2011

Coastal flooding from wave overtopping causes considerable damage. Presently, to model wave overtopping one can either make use of physical model tests or empirical tools such as those described in the EurOtop manual. Both these methods have limitations; therefore, a quick and reliable numerical model for wave overtopping would be a very useful tool for a coastal engineer.

This research aims to test and develop a numerical model (in one horizontal dimension) for nearshore waves, runup and overtopping. The Shallow Water And Boussinesq (SWAB) model solves the Boussinesq-type equations of Madsen and Sorensen (1992) for non breaking waves and the nonlinear shallow water equations for breaking waves. Through testing against a range of physical model data using regular and random waves, the SWAB model's transfer from non-breaking to breaking waves was optimised. It was found that a wave height to water depth ratio worked consistently well as a breaking criterion.

A set of physical model tests were carried out, based on previous field testing of wave overtopping that had previously taken place at Anchorsholme, Blackpool. The SWAB model was used to simulate some of these physical model tests, giving good results for mean overtopping rates. SWAB models the force imposed by steep walls and recurve walls on the incident flow; this force was found to have a significant effect on overtopping rates. A comparison was made between mean overtopping rates from the SWAB model, the physical model tests, empirically-based software (PC-Overtopping) and the field data. The physical model and SWAB results compared well with the field data, though the empirical software gave large overestimates.

The SWAB model was applied to the analysis of overtopping at Walcott, Norfolk. It was found that beach levels affected overtopping rates, but not as much as different randomly phased wave trains. A simulation of a recent storm event was performed, with overtopping rates being slightly lower than those reported by local residents. A joint probability analysis showed that the predicted frequency of such an event was in line with these reports.

An alternative modelling technique was also tested, where a spectral energy model was coupled with a nonlinear shallow water solver. Results for wave runup parameters were very accurate, when the coupling location is at the seaward edge of the surf zone. Extension of this modelling technique into two horizontal dimensions would be more straightforward than with the SWAB model.

Declaration

No portion of the work referred to in the thesis has been submitted in support of an application for another degree or qualification of this or any other university or other institute of learning

Copyright

Acknowledgements

I would first like to thank my supervisors, Prof Peter Stansby and Dr David Apsley, whose help, enthusiasm and constructive advice has been invaluable. I appreciate all the time they have given me.

I would also like to thank the other people involved with the FRMRC Coastal Flooding Group (SWP2). Unusually, I suspect for a PhD student, I have enjoyed being part of a team working on some potentially useful research. In particular, I would like to thank Kuo Yan, who helped out with the wave flume experiments at HR Wallingford, and Nicolas Chini with whom I have worked closely on several aspects of this project. In particular, at Walcott he provided the bathymetry and the incoming waves and water levels (including the conditions for the joint probability analysis) and helped out with using the EurOtop Neural Network. I also would like to thank him for answering my questions on all aspects of this modelling.

I would like to thank Dr Tim Pullen and the technical staff at HR Wallingford for their help with carrying out the wave overtopping experiments, and providing the associated field data (on behalf of the Environment Agency).

I would like to mention my friends and family, including Cathy, Mike, Mum and Dad for their love, support and interest. Thanks to Margaret Booth with helping out with the proof reading. I especially would like to thank Erica Brown for her love, kindness and ability to make me laugh.

I would finally like to make an anti-acknowledgement to the idiot whose surf board recently broke Erica's leg! I really did not want to become a part-time nurse in the final stages of writing this thesis!

Chapter 1

Background

1.1 Coastal Flooding

1.1.1 Coastal flooding costs

Humans have lived near the coast throughout their existence, and the threat of coastal flooding has always been apparent. In more recent human history, we have tried to engineer the coastline, either for ports and harbours, or to provide a barrier against the sea. Over the past few centuries, and especially in the latter half of the 20th century, our experience and scientific understanding of coastal processes has greatly increased. As a result, we can now make more accurate calculations of the likelihood and severity of events, and are able to make designs or plans to mitigate against these events. To generalise, coastal flooding is caused by a combination of large waves and high water levels. Such conditions can cause sea water to overtop coastal defences and flood low lying areas; in severe cases, the overtopping can cause the defences to be breached, causing considerably more flood damage. In addition, such conditions can cause loss of beach sediment or cliff erosion, and further damage to properties and infrastructure as well as loss of life.

Throughout the world, coastal areas tend to be more densely populated than inland areas; therefore large numbers of people are potentially at risk from coastal flooding. It is estimated that a population of about 450 million lived below 20 m elevation and within 20 km of the coastline in 1990 [Small and Nicholls, 2003]. With the global population increasing rapidly, this figure is already likely to much higher. In the UK alone, it is estimated that over one million properties are potentially at risk from coastal flooding and coastal erosion, with an asset value of approximately £140 billion at 2000 prices [Halcrow Group, 2001].

In the future, expected rates of sea level rise could increase the likely costs of coastal flood-

ing and the number of people affected. Although it is impossible to make exact predictions of sea levels over the next century, a range of climate change scenarios can be used to estimate the associated effects. For the UK, the UKCIP02 report by Hulme et al. [2002] used four scenarios for greenhouse gas emissions, giving associated sea level rises from 9 cm to 69 cm by 2080 (relative to the 1960 to 1990 average sea level), mostly due to the thermal expansion of the oceans. Uncertainties arise due to regional differences in oceanic temperature change; Hulme et al. [2002] recommended modifying values by $\pm 50\,\%$ to take account of this. In addition, in south-east England the land is sinking by up to 1.5 mm per year leading to a greater relative sea level rise. Hall et al. [2006] studied the costs associated with coastal flooding; they calculated that the expected annual damage was £0.5 billion in 2002. Using different climate change scenarios, but assuming no upgrades to existing defences, the expected damage could increase to between £1.0 billion and £13.5 billion by 2080 (at 2002 prices). However, by adapting defences to these more severe conditions, Hall et al. [2006] calculated that engineering works with a one-off capital cost of £12 billion to £40 billion could reduce coastal flood risk to a factor of 0.4 to 1.6 times its current level.

The ability to accurately predict, or to accurately calculate the probability of wave overtopping is therefore of great importance. Firstly, the forecasting of overtopping due to an incoming storm enables people and emergency services to plan for the event; secondly, it allows coastal engineers to make good designs, reducing the need to "over-engineer" defences, thus saving money; and thirdly, by being able to make more accurate predictions of potential flood damages, planning decisions can be more effectively optimised.

1.1.2 The Flood Risk Management Research Consortium

The Flood Risk Management Research Consortium (FRMRC) is funded by the UK Engineering and Physical Sciences Research Council, with additional funding from the Environment Agency and the Department for the Environment, Food and Rural Affairs, the Northern Ireland Rivers Agency and the Office of Public Works of the Republic of Ireland. It aims to provide inter-disciplinary research on the prediction and management of flood risk. This research includes the delivery of tools and techniques to support more accurate flood forecasting and warning, improvements to flood management infrastructure and the reduction of flood risk to people, property and the environment [FRMRC Website, 2008].

The second phase of the FRMRC is running from October 2007 to December 2011. It contains five "super work packages", the second of which (SWP2) is entitled, "Inundation Modelling - Coastal Flooding". The aim of SWP2 is to improve our ability to predict coastal flooding and its effects. Therefore, the research includes the development of and improvements to

models on a range of scales: oceanic winds and waves; surge modelling on the continental shelf; the coastal wave climate; nearshore waves and wave overtopping; and coastal flood inundation modelling. Associated morphological changes are also considered: from the offshore modelling of the sea bed to statistical analyses of beach profiles, as well as the development of a model for breaching. Additionally, different scenarios are tested to estimate the effects of climate change on coastal flood risk. SWP2 is a collaborative set of projects, with teams from the Met Office, the National Oceanography Centre (NOC) in Liverpool, the University of Oxford, the University of Plymouth as well as the University of Manchester, including researchers based at the Tyndall Centre for Climate Change.

Figure 1.1 shows the "Road Map" for the Coastal Flooding super work package. This gives an overview of the different scales of modelling required to give accurate predictions of coastal flood inundation, and how these different models fit together. The pale blue boxes show the main pathway to predicting coastal flooding, and the white boxes are additional areas of importance, which either feed into this modelling or are by-products of this approach. We start with global and regional climate modelling (GCM and RCM), which produces the waves and storm surges that affect continental seas (CS3 is the continental shelf model, used by the NOC). This modelling feeds into coastal wave and morphological models, which can provide data on water levels and parameterised wave conditions. These results can feed into a wave-by-wave model, which is only of practical use within a few wavelengths of the shoreline but, if effective, should be able to provide useful time-series of overtopping rates. These results are an essential input for the modelling of flood inundation or for the modelling of the onset of breaching. The research carried out here forms part of the task highlighted in yellow, thereby forming a key part of the main pathway to the prediction of coastal flooding. SWAB is the wave-by-wave model that will be used here, and will be described in detail in Chapter 3. Smoothed Particle Hydrodynamics (or SPH) is another type of model, which requires considerably greater computer power but, being meshless, it offers a greater range of flexibility with respect to model bathymetry, breaking waves or forces on moveable objects. It will not be discussed here, but the interested reader is referred to the SPHysics website (http://wiki.manchester.ac.uk/sphysics/index.php/Main_Page).

This thesis therefore aims to perform part of the research required of SWP2: to improve our understanding of, and the computational modelling of nearshore waves and wave overtopping. A shallow-water and Boussinesq (SWAB) model will be used for the majority of this research. This type of model makes assumptions on the velocity profile across the water depth, enabling a reasonable level of accuracy without the computational demands of some other models. Therefore whole storms can be analysed on a wave-by-wave basis. The follow-

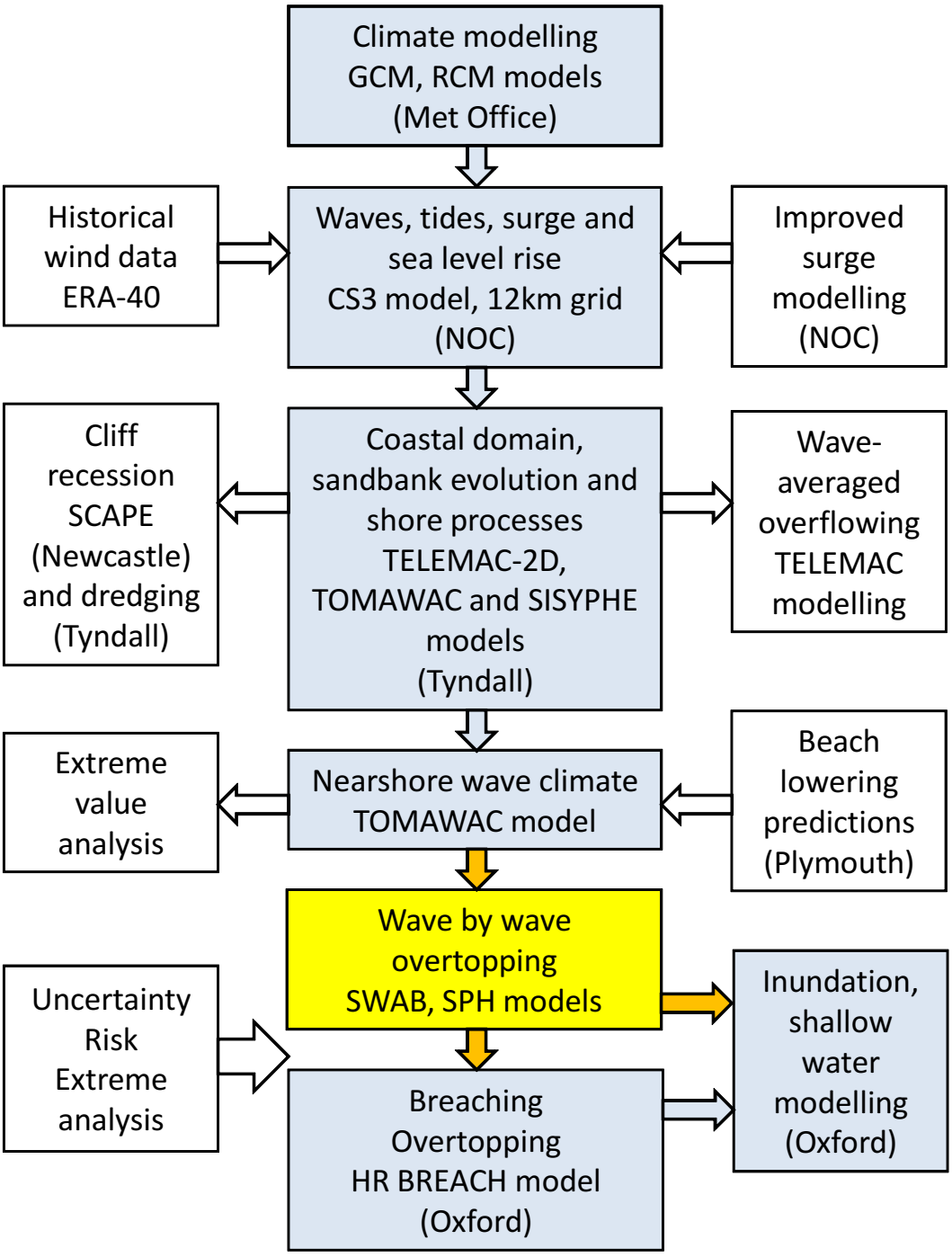

Figure 1.1: FRMRC SWP2 "Road Map"

ing section will discuss the aims of this thesis in more detail.

1.2 Research Objectives

The aim of this research is to develop and use a shallow-water and Boussinesq (SWAB) model to model nearshore waves and wave overtopping. This will be done in the following way:

1. The region of the SWAB model's validity will be assessed with respect to wave conditions and water depths.

2. The SWAB model's performance in the nearshore will be validated against data for regular waves, wave groups and random waves. Modifications to the wave breaking model will be tested, including the use of techniques to terminate the breaking process for waves moving into deeper water.

3. The SWAB model will be used to model wave runup on shorelines, with and without an offshore reef. Its performance in accurately reproducing wave runup distributions will be analysed.

4. Physical model tests and field data of wave overtopping will be used to test the SWAB model's performance in representing storm conditions. The SWAB model's ability to represent vertical walls and recurve walls will be tested.

5. An analysis of nearshore waves and wave runup will be carried out using a coupled spectral energy model and shallow water model. Optimal coupling locations will also be determined.

The outcome of this research should produce a model suitable for the wave-by-wave calculation of nearshore waves and wave overtopping. It should assess the advantages, limitations and possibilities of the modelling methods, and determine whether a Boussinesq-type, or a coupled spectral energy - shallow water model, gives better results.

1.3 The Thesis

The subsequent chapters of this thesis run as follows: Chapter 2 will present a background to waves and wave modelling, with a literature review; Chapter 3 will describe the SWAB model, its equations and solver, as well as practical aspects of its use and tests of its behaviour in certain situations; Chapter 4 will describe the range of physical model tests that have been used to test the SWAB model; Chapter 5 will examine the model's simulation of nearshore waves,

especially looking at the effective modelling of breaking waves; Chapter 6 will continue from Chapter 5, focussing on the modelling of wave runup. Chapter 7 will use results from physical model experiments of Anchorsholme seawall in Blackpool to study the SWAB model's ability to calculate wave overtopping. It will look at the modelling of vertical sections of wall and recurve walls, and also make use of available field data. Chapter 8 will make use of a flooding event at Walcott in Norfolk, describing how the SWAB model can be used to study various aspects of wave overtopping; Chapter 9 will present an alternative to the SWAB model, instead coupling a spectral energy model to a nonlinear shallow water model, showing results for nearshore waves and wave runup; and finally Chapter 10 will discuss and summarise the main findings from this research.

Chapter 2

Theory and Literature Review

This chapter will examine the various theories and models that have been derived and developed to explain how water waves propagate and transform. However, it will first be useful to briefly examine what causes the various phenomena that cause water levels to fluctuate. These water level variations exist at many scales and time scales, and include [Reeve et al., 2004]:

- Astronomical tides, caused by gravitational forces between the oceans and the Sun and Moon. They are also affected by the existence of continents, the oceanic bathymetry, bed friction and coriolis forces (due to the Earth's rotation). Tides have a daily or bi-daily period, as well as a fortnightly spring-neap cycle, and can range in magnitude from zero to over 10 m.

- Storm surges, caused by the winds and low pressure associated with weather systems, lasting over a period of hours. Their magnitude can vary; the notorious storm surge of 1953 in the North Sea caused water levels over 3 m above high tide levels [Rossiter, 1954] and the one due to Hurrican Katrina reached a height of 10 m [Fritz et al., 2007].

- Tsunamis, which are waves with a typical period of 20 to 30 minutes, caused by disturbances such as earthquakes or landslides.

- Wind waves, which have a period in the order of seconds. A wind blowing over a body of water imposes a shear stress on the water surface, which initiates and causes the growth of waves. Most wind wave energy is caused by local winds, with the generated wave heights being dependent on the wind speed as well as the distance over which the wind is acting (fetch length). Swell consists of decaying waves that have propagated away from the local area. These waves have longer periods, generally above 8 s, and

can therefore have an important effect on wave runup and overtopping. Hawkes et al. [1997] have produced an atlas on swell wave conditions around the UK.

Wave overtopping of coastal defences is generally caused by combinations of the water level variations described above. Other research carried out by the FRMRC SWP2 is concerned with the improvement of storm surge modelling and the propagation waves and surges towards the coast. This thesis will concentrate on nearshore wind waves and their interaction with the coastline. This section will describe some of the theoretical background and physics of wave theory, as well as the transformation of waves as they move into shallower water. The following sections will review and discuss the numerical modelling of water waves, as well as existing research into wave runup and overtopping.

2.1 Wave Theory

2.1.1 Linear wave theory

The two fundamental principles used in fluid mechanics are the conservation of mass and the conservation of momentum. The principle of conservation of mass states that mass cannot be created or destroyed; for an incompressible liquid (which we can assume is true for water) this is equivalent to saying that a volume of liquid cannot be created or destroyed. Likewise, the total momentum in a system will remain unchanged unless an external force acts upon it. According to Newton's second law, the force acting upon a body will equal its rate of change of momentum.

For irrotational flow, fluid velocity can be expressed as velocity potentials, such that:

$$u = \frac{\partial \phi}{\partial x}, v = \frac{\partial \phi}{\partial y}, w = \frac{\partial \phi}{\partial z} \tag{2.1}$$

By using velocity potentials, the conservation of mass equation:

$$\frac{\partial u}{\partial x} + \frac{\partial v}{\partial y} + \frac{\partial w}{\partial z} = 0 \tag{2.2}$$

can be expressed neatly as:

$$\nabla^2 \phi = 0 \tag{2.3}$$

known as the Laplace equation [Dean and Dalrymple, 1991].

Linear water wave theory was developed through the 18th and early 19th century by a range of mathematicians and physicists with a comprehensive theory given by Airy in 1841

in his article on "Tides and Waves" [Craik, 2004]. Linear wave theory gives a solution to the Laplace equation (2.3), making the assumption that the wave amplitude is small. This allows the removal of second order displacement and velocity terms. Four boundary conditions are applied:

- The periodic lateral boundary condition, which specifies that the waves must be temporally and laterally periodic;
- The bottom boundary condition, which assumes the bed is impermeable, thus implying that the flow at the bed is tangential to the bed. This implies:

$$w = -u\frac{\partial d}{\partial x} \tag{2.4}$$

  where d is the still-water depth;

- The kinematic free surface boundary condition, which effectively makes the assumption that a particle at the surface remains at the surface. This can be expressed as:

$$w = \frac{\partial \zeta}{\partial t} + u\frac{\partial \zeta}{\partial x}\bigg|_{\text{on } z=\zeta(x,t)} \tag{2.5}$$

  where $\zeta(x,t)$ is the free surface level.

- The dynamic free surface boundary condition, which is an application of Newton's second law to the water surface, assuming that the external pressure acting on the surface is uniform and constant. This gives:

$$-\frac{\partial \phi}{\partial t} + \frac{1}{2}\left(u^2 + w^2\right) + \frac{p_\zeta}{\rho} + g\zeta = C(t) \tag{2.6}$$

  where p_ζ is the atmospheric pressure, which can be assumed to be zero, and $C(t)$ is a function of time.

These boundary conditions give a solution with a sinusoidal free surface of form:

$$\zeta = \frac{H}{2}\cos(kx - \omega t) \tag{2.7}$$

where:

$$k = \frac{2\pi}{L} \tag{2.8}$$

$$\omega = \frac{2\pi}{T} \tag{2.9}$$

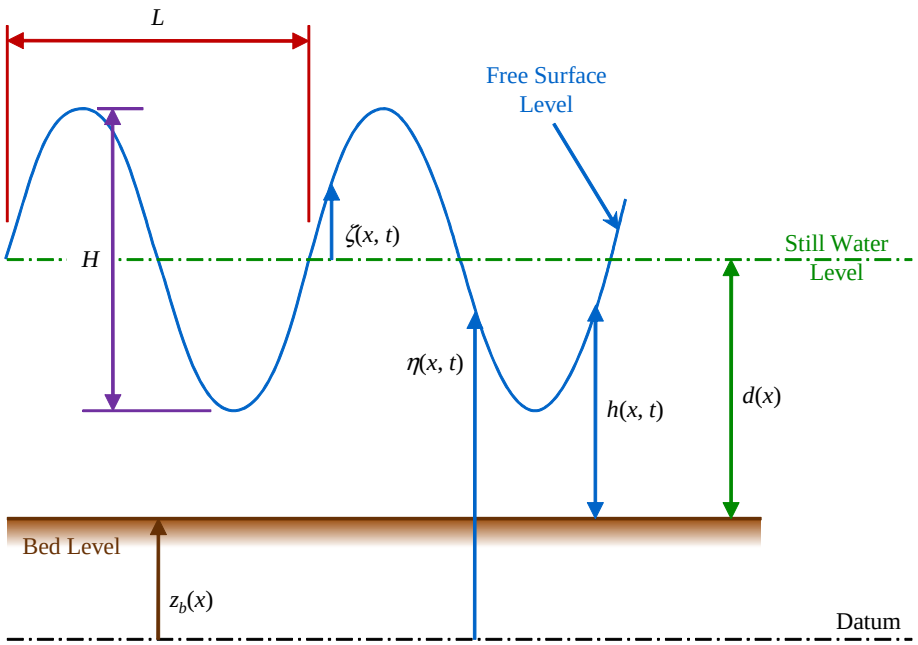

Figure 2.1: Water wave variables

which are respectively described as the wave number and angular frequency. Figure 2.1 shows a water wave, with some of the commonly used variables.

The wavelength and wave period (or k and ω) are related by the dispersion relation:

$$\omega^2 = gk \tanh(kd) \tag{2.10}$$

which is of great importance to coastal engineers. This is because it provides a link between wave period (which would remain unchanged in any depth of water), wavelength (which does not remain unchanged) and water depth; it therefore becomes the basis for the transformation of waves across different depths. Indeed, equation (2.10) results in definitions of deep and shallow water. In deep water, when $d/L > 0.5$, $\tanh(kd)$ becomes approximately 1 and the wave's celerity is:

$$c = \frac{L}{T} = \frac{1}{T}\frac{gT^2}{2\pi}\tanh(kd) \approx \frac{gT}{2\pi} \; (= c_0) \tag{2.11}$$

and is thus proportional to the wave's period. In shallow water, when $d/L < 0.04$, $\tanh(kd)$ becomes approximately kd and the wave celerity becomes:

$$c \approx \sqrt{gd} \tag{2.12}$$

When d/L is between 0.04 and 0.5, in intermediate depths, simple approximations cannot be made, and the dispersion relation becomes rather less easy to use. Here, calculations require

an iterative process, though few iterations are required for an accurate answer.

Despite the small amplitude assumption, Airy wave theory has a remarkably wide range of validity. It can be used to describe many important wave phenomena such as shoaling, refraction, reflection, diffraction and wave setup; these will be described later. However, as shown by Hedges [1995], for steep waves ($H/L > 0.04$) and high Ursell numbers ($HL^2/d^3 > 40$), other wave theories must be used. Additionally, real seas consist of irregular waves of varying height and frequency. The nature and effect of these waves can be considerably different from those of regular waves, and most current research focusses on irregular waves.

2.1.2 Nonlinear wave theories

Linear wave theory relies on small amplitudes; therefore any quantities of order $(ka)^2$, where a is the wave amplitude (i.e. $a = H/2$), are neglected. For Stokes waves, these terms are included in the derivation by expressing quantities as a power series [Dean and Dalrymple, 1991]; this is known as a perturbation approach. For example, the equation for velocity potential becomes:

$$\Phi = \Phi_1 + (ka)\Phi_2 + (ka)^2\Phi_3 + ... \tag{2.13}$$

where Φ is the dimensionless form for velocity potential:

$$\Phi = \frac{k\phi}{a\sqrt{gk}} \tag{2.14}$$

The boundary conditions are applied using the power series for all the relevant quantities (such as free surface elevation and velocity potential), with higher order terms being neglected as required. Stokes calculated second order solutions in 1847, with higher orders having been derived more recently. The second order solution gives the following free surface [Dean and Dalrymple, 1991]:

$$\zeta(x,t) = \frac{H}{2}\cos(kx - \omega t) + \frac{H^2k}{16}\frac{\cosh(kd)}{\sinh^3 kd}(2 + \cosh 2kd)\cos 2(kx - \omega t) \tag{2.15}$$

with the same dispersion relation as for Airy waves (equation (2.10)). This solution produces wave components of twice the frequency and half the wavelength, with a celerity the same as that of the first order wave (i.e. $2\omega/2k = \omega/k$). These are described as *bound waves*. It should be noted that there is a modification to the dispersion relation for higher orders.

Obviously, in order for this method to work the series must converge; for the Stokes perturbation this places a severe restriction on wave heights in shallow water [Dean and Dalrymple, 1991]. However, it is possible to use the perturbation approach with other quantities. We can

define two ratios: amplitude to water depth ($\varepsilon = {}^{a}/_{d}$) and depth to wavelength $\mu = {}^{d}/_{L}$. The first ratio, ε, is a measure of the degree of nonlinearity of the system (note linear wave theory assumes the amplitude is small); the second, μ, is a measure of dispersion (note the dependence on $kd = {}^{2\pi d}/_{L}$ in the dispersion equation (2.10)). For the Stokes perturbation, $\mu^2 \gg \varepsilon$; if they are maintained of a similar order, the dispersion and nonlinear effects cancel and one can obtain the Korteweg-de Vries equation. Korteweg and de Vries [1895] calculated the following cnoidal wave solution to their equation:

$$\zeta = a\,\mathrm{cn}^2\left((x - ct)\sqrt{\frac{3a}{4d^3k^2}}, k^2\right) \tag{2.16}$$

where a in this case is the wave amplitude *from crest to trough*, and k in this case is a modulus (**not** the wave number, ${}^{2\pi}/_{L}$). Unfortunately, the mathematics required to understand and make calculations using cnoidal theory is well above the level of most engineers. Therefore, where cnoidal wave theory is used, calculations are usually made with the aid of design charts, such as those developed by Wiegel [1960].

When k from equation (2.16) approaches zero the waves become similar to sinusoidal waves, but when $k = 1$ the solution is a solitary wave. Solitary waves were first observed by Russell in 1834, and Boussinesq [1872] derived a solitary wave solution to his equation (which is very closely related to the Korteweg-de Vries equation), but their existence as a steady-state wave-form was disputed until the work of Korteweg and de Vries [1895][Bullough and Caudrey, 1995]. These waves have the form:

$$\zeta = a\,\mathrm{sech}^2\left((x - ct)\sqrt{\frac{3a}{4d^3}}\right) \tag{2.17}$$

where the celerity, c, is:

$$c = \sqrt{gd}\left(1 + \frac{a}{2d}\right) \tag{2.18}$$

with an infinite wavelength. Although solitary waves are rarely seen in nature, they have been used as a model for periodic waves in shallow water [Munk, 1949] and for tsunamis (e.g. Synolakis, 1987). However, Madsen et al. [2008] urge caution in their use as a model for tsunami propagation and runup, suggesting significant differences between solitary waves and tsunami. They state that tsunami often steepen as they approach the shore, disintegrating into undular bores with short transient waves.

Another approach is to develop solutions for the stream function, ψ, as a Fourier expansion. Various methods have been developed; these are discussed by Sobey [1989]. The stream function is related to the velocity potential; it is the line integral of the velocity component

perpendicular to the line element in two dimensions. That is:

$$w = \frac{\partial \psi}{\partial x}, u = -\frac{\partial \psi}{\partial z} \tag{2.19}$$

The continuity equation and boundary conditions can all be rewritten in terms of the stream function; one advantage of this approach is that the kinematic free surface boundary condition is automatically met as the free surface itself is a streamline. Dean [1974] developed a method to calculate the Fourier coefficients to satisfy the dynamic free surface boundary condition. Subsequently, Rienecker and Fenton [1981] improved upon this method, allowing the calculation of solutions with waves and currents. From the stream function accurate values for free surface level and fluid velocities can be obtained over a much wider range of conditions than Stokes or cnoidal wave solutions. However, it should be noted that a computer is required to calculate the coefficients and the accuracy of the solution is dependent on the truncation of the Fourier series [Sobey, 1989]. Despite the advantages of these analytical-numerical theories over Airy, Stokes and cnoidal theories, they have all been developed for horizontal beds, and do not consider the spectrum of waves of multiple frequencies and directions that occur in real seas.

A common characteristic of these nonlinear wave theories is that calculations are mathematically difficult, and this reduces their flexibility when dealing with problems involving real seas with a spectrum of waves of different frequencies and directions, propagating over complex bathymetries. For this, we require numerical wave models. The numerical solution of equations of fluid flow will be covered later; firstly, the development of Boussinesq-type equations will be discussed.

2.1.3 Shallow water and Boussinesq-type equations

It has already been mentioned that the two fundamental principles in fluid mechanics are those of the conservation of mass (2.3) and the conservation of momentum. Application of Newton's second law to a fluid gives the Navier-Stokes equations, quoted by Dean and Dalrymple [1991] as:

$$\frac{Du}{Dt} = -\frac{1}{\rho}\frac{\partial p}{\partial x} + \frac{1}{\rho}\left(\frac{\partial \tau_{xx}}{\partial x} + \frac{\partial \tau_{yx}}{\partial y} + \frac{\partial \tau_{zx}}{\partial z}\right) + F_x \tag{2.20}$$

$$\frac{Dv}{Dt} = -\frac{1}{\rho}\frac{\partial p}{\partial y} + \frac{1}{\rho}\left(\frac{\partial \tau_{xy}}{\partial x} + \frac{\partial \tau_{yy}}{\partial y} + \frac{\partial \tau_{zy}}{\partial z}\right) + F_y \tag{2.21}$$

$$\frac{Dw}{Dt} = -\frac{1}{\rho}\frac{\partial p}{\partial z} + \frac{1}{\rho}\left(\frac{\partial \tau_{xz}}{\partial x} + \frac{\partial \tau_{yz}}{\partial y} + \frac{\partial \tau_{zz}}{\partial z}\right) + F_z \tag{2.22}$$

where the total derivative D/Dt is defined as:

$$\frac{D}{Dt} = \frac{\partial}{\partial t} + u\frac{\partial}{\partial x} + v\frac{\partial}{\partial y} + w\frac{\partial}{\partial z} \tag{2.23}$$

and p is pressure, τ are internal stresses, and F_x, F_y and F_z are external forces in the x, y and z directions respectively. If the shear stresses are assumed to be zero, these equations are known as the Euler equations. Numerical solution of these equations for free-surface problems is not easy: firstly, the free surface location is not directly obtainable; and secondly, we need some way of calculating the internal stresses in the fluid. Methods are available to overcome both these difficulties: Hirt and Nichols [1981] developed the volume of fluid method as a means of locating and tracking a free surface and assumptions can be made to account for the stresses associated with turbulent flow. Lin and Liu [1998] used a volume of fluid method with a $k-\epsilon$ turbulence model to model breaking waves. However, these methods still require very large computation times (see Stansby et al. [2008] for an example of comparitive calculation times for a wave overtopping model), and are impractical for many engineering problems. Therefore we must simplify the equations in some way; the Boussinesq-type equations are a popular method for the nearshore and will be discussed below.

If we assume that pressure is hydrostatic, and apply the conservation of momentum to a fluid neglecting all velocity-squared terms, we obtain the linear long wave equation. In one horizontal dimension, this gives:

$$\frac{\partial^2\zeta}{\partial t^2} = gd\frac{\partial^2\zeta}{\partial x^2} \tag{2.24}$$

An equivalent equation to this was derived by Airy in 1841 [Craik, 2004]. This equation has a periodic solution of the same form as equation (2.7), with celerity $c = \sqrt{gd}$. Note that there is no vertical velocity variable in the equation; with the hydrostatic assumption, we have reduced the number of dimensions in the problem, but it is only valid in shallow water, for small-amplitude waves. One can also manipulate the Euler equations in the horizontal direction, making the assumption that the vertical velocity is zero and the pressure is hydrostatic (i.e. $p/\rho g = \eta - z$). This gives the nonlinear shallow water equations, which include the continuity equation and the following momentum equation:

$$\frac{\partial hu}{\partial t} + \frac{\partial hu^2}{\partial x} + gh\frac{\partial \eta}{\partial x} = 0 \tag{2.25}$$

This equation does not have finite-amplitude steady periodic solutions. Any finite amplitude wave will steepen to form a bore, moving at speed $c = \sqrt{gh}$ where h is the water depth at the crest of the bore. Such equations will be discussed later, with respect to breaking waves,

but are not relevant to steady periodic waves, where the non-hydrostatic effect of the vertical water velocity becomes important.

Boussinesq [1872] derived an analytical solution for solitary waves in water of constant depth (whose existence was still at that time disputed [Craik, 2004]). The derivation relied on a double integration of the Laplace equation (2.3) with respect to z, and substituting approximations of the velocity potential (based on the conditions at the bed) into equations for the kinematic and dynamic free-surface boundary conditions [Dingemans, 1997]. This gives:

$$\frac{\partial^2 \zeta}{\partial t^2} - gd\frac{\partial^2 \zeta}{\partial x^2} = gd\frac{\partial^2}{\partial x^2}\left(\frac{3}{2}\frac{\zeta^2}{d}\right) + gd\frac{\partial^2}{\partial x^2}\left(\frac{d^2}{3}\frac{\partial^2 \zeta}{\partial x^2}\right) \tag{2.26}$$

which is similar to equation (2.24) but with extra terms on the right hand side. Ursell [1953] derived these equations in a Lagrangian form, showing that the first term on the right hand side reduces to zero when the nonlinearity is much less than the frequency dispersion ($\varepsilon \ll \mu^2$) and the second term to zero when it is much greater ($\varepsilon \gg \mu^2$). When they are of the same order, both terms are included and a solitary wave solution exists; in effect the nonlinear wave steepening is balanced by the vertical water acceleration that causes dispersion. The ratio of nonlinearity to dispersion (ε/μ^2) is known as the Ursell number.

Peregrine [1967] derived a set of equations in a different way, again to represent solitary waves, but this time allowing for a variable slope. Peregrine's [1967] derivation used a perturbation expansion for dimensionless forms of ζ, p, and the depth-averaged horizontal velocity, all in terms of ε^n. The vertical velocity was expanded in terms of $\mu\varepsilon^n$, once again with the assumption that μ^2 and ε are of the same order. Integrations of the Euler equations (equations (2.20), (2.21) and (2.22), without the internal stresses) were used to calculate the pressure, and the continuity equation (2.2) was used to calculate the vertical velocity terms. The expansion was taken to the second order, giving the following equations in one horizontal dimension:

$$\frac{\partial \zeta}{\partial t} + \frac{\partial (d+\zeta)\bar{u}}{\partial x} = 0 \tag{2.27}$$

$$\frac{\partial \bar{u}}{\partial t} + \bar{u}\frac{\partial \bar{u}}{\partial x} + g\frac{\partial \zeta}{\partial x} = \frac{d}{2}\frac{\partial^3 (d\bar{u})}{\partial t \partial x^2} - \frac{d^2}{6}\frac{\partial^3 \bar{u}}{\partial t \partial x^2} \tag{2.28}$$

where $\bar{u}$ is the depth-averaged (dimensional) horizontal velocity. According to Liu and Losada [2002], these equations break down when $d/L_0 > 1/5$. Nevertheless, they were used by Abbott et al. [1978] to model periodic waves in shallow water in two horizontal dimensions, including transmission through a permeable breakwater.

An important contribution by Witting [1984] allowed the extension of these equations into deeper water. The approach of Boussinesq [1872] gives a Taylor series approximation for the

velocity potential; Witting [1984] instead derived expressions for the velocities at the bed and at the surface in terms of a velocity defined at an arbitrary depth, allowing the wave dispersion relation to be expressed as a Pade approximation. Pade approximations express a function as a rational fraction, i.e:

$$f(x) = \frac{p_0 + p_1 x + p_2 x^2 + \dots}{q_0 + q_1 x + q x^2 + \dots} \tag{2.29}$$

and are more accurate than the equivalent Taylor expansion.

According to Madsen and Schäffer [1999], although the equations of Witting [1984] have very good linear dispersion characteristics, their nonlinear behaviour is not so good, and his methodology was not suited to two horizontal dimensions. However, subsequent researchers built on this work to develop what are generally known as the extended Boussinesq equations. Madsen et al. [1991] used the equations of Peregrine [1967] (modified with the assumption of a horizontal bed), but included an extra expression that would approximate to zero in shallow water and improve the linear dispersion characteristics in deeper water. The expression was controlled by a parameter, B, that could be optimised (by comparison with linear wave theory) for the best dispersion properties throughout a range of depths. Also, unlike the equations of Witting [1984], the derivation was valid in two horizontal dimensions. Madsen and Sorensen [1992] extended the work of Madsen et al. [1991], again using Peregrine's equations as a starting point, but including the effects of a mildly sloping bed. One important feature of this method is that when $B = 0$, the equations reduce to the nonlinear shallow water equations (2.25).

Nwogu [1993] used a different approach to derive equations with similar linear dispersion properties. Instead of using depth-averaged velocities, the derivation made use of the fluid velocity at a fixed level above the bed, which could be set to produce the best linear dispersion. The resulting equations are of a similar form to Peregrine's [1967], with extra terms in the continuity equation to modify the linear dispersion. Despite a different approach from Madsen and Sorensen [1992], the equations give similar linear dispersion properties, again allowing the celerity to be expressed as a Pade approximation. The reference velocity level, z_α, employed by Nwogu [1993] is closely related to the parameter, B, of Madsen and Sorensen [1992]. Schäffer and Madsen [1995] made two further improvements: firstly removing the mild-slope bed assumption with an additional free parameter; and secondly developing a new set of equations based on Nwogu [1993], but further improving the linear dispersion, allowing accurate modelling of wave celerity up to the deepwater limit.

Until now, nonlinear effects have been neglected. Although the equations described above have increased the range of d/L for which they are valid, nonlinearity must still be small (i.e. $\varepsilon \ll 1$). Madsen and Sorensen [1993] carried out a further analysis of their previous equations

in comparison with third-order Stokes waves and found that nonlinear properties are not so well modelled. For example when $kh = 2$, the linear phase celerity has an error of less than 2% whereas the correction factor for third-order dispersion is about 90% too small; also the amplitude of the bound harmonics is considerably underestimated. Equations by Wei et al. [1995] and Madsen and Schäffer [1998] incorporated higher-order nonlinear terms, making the assumption that ε is of the order of 1, rather than μ^2. Agnon et al. [1999] devised a method to ensure that the nonlinear properties are to the same level of accuracy as the linear dispersion properties, although the method requires the solution of six coupled equations with six unknown variables (rather than two equations with two unknowns for other methods).

The horizontal velocity profile associated with the weakly nonlinear models ($\varepsilon \ll 1$) is a quadratic polynomial, as is the pressure profile. The profiles for the so-called fully nonlinear equations ($\varepsilon = \mathcal{O}(1)$) contain higher order terms. Gobbi et al. [2000] developed a set of equations, similar to those of Wei et al. [1995], with higher-order dispersion terms, and included an analysis of the resulting velocity profiles. Madsen et al. [2002] extended the methodology of Agnon et al. [1999], showing good linear dispersion properties for kh of up to 40 as well as accurate velocity profiles for kh of up to 12. Madsen et al. [2006] modified this method to take account of a rapidly varying bathymetry.

It is apparent that a considerable amount of work has been carried out extending and improving equations that have their origins in Boussinesq's work. One may have noticed that none of the more recent equations have been quoted in this review. The extended equations of Madsen and Sorensen [1992] and Nwogu [1993] look similar to those of Peregrine [1967], with terms of up to third-order. However, the more modern equations contain many more terms, of up to fifth order, and are not straightforward to examine, manipulate or discretise. The Boussinesq-type equations will be discussed later with reference to numerical modelling.

2.2 Irregular Waves

2.2.1 Random waves and wave spectra

With the analytical wave theories discussed in Sections 2.1.1 and 2.1.2 waves were either *monochromatic* or contained harmonics bound in phase to the main wave. These waves are known as *regular waves*, and very rarely (if ever) occur in real seas. Real seas consist of waves of different amplitudes and frequencies travelling in different directions. Although much of the mathematical basis to the theory of regular waves was developed in the 19th century, the study of *random waves* and real seas is much more recent, with its origins in the military requirements of World War II.

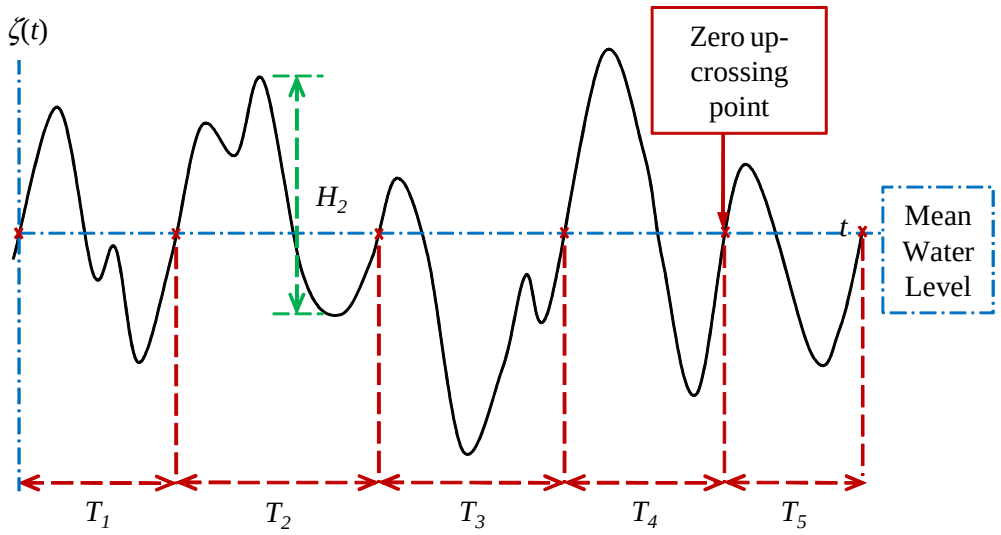

Figure 2.2: Random waves in the time domain

There are two main analytical approaches to the study of random waves: statistical calculations in the time domain; and calculations in the frequency domain. In the time domain, one can separate a time-series in individual waves and calculate probability distributions of wave heights or other properties. In the frequency domain, one can split a signal into component sine-waves of different frequencies and analyse properties of the wave spectrum. In fact, these statistical methods were developed at the same time, and are closely linked. Before continuing further, it is important to apply some definitions to a random wave train. Figure 2.2 shows a sequence of five waves; the start and end point of each wave is defined when the water level crosses upward through the mean (a zero up-crossing point). The use of zero down-crossing points is also common, and gives the same statistical results. The height of a wave is defined as the difference between its maximum and minimum water level.

It is convenient to represent these waves of different heights and periods by some universal parameters. One would expect the larger waves to be of more importance to a coastal engineer; Sverdrup and Munk [1947] developed the concept of the *significant wave*, defining it as the highest third of waves. This concept was based as much on visual recording methods as it was on statistical importance. The significant wave height is therefore the mean height of the highest third of waves, $H_{1/3}$, and the signifcant wave period ($T_{1/3}$) is the mean period of these waves (note it is not the mean of the longest third of wave periods). Sverdrup and Munk [1947] also developed a method for calculating significant wave heights as a function of wind speeds and fetch length.

Calculations in the frequency domain, based on Fourier analysis, were first developed in the 1940s; analysis of random noise in electrical devices by Rice [1944, 1945] formed the basis

of subsequent applications to water waves. Rice [1944] introduced the expression of a wave train as:

$$\zeta(t) = \sum_{n=1}^{N} a_n \cos(2\pi n f t - \phi_n) \tag{2.30}$$

where ϕ_n are uniformly distributed random phases (hence the term random wave) and the component amplitudes a_n are related to the energy spectrum $S(f)$ such that:

$$\sum_{f}^{f+\Delta f} \frac{a_n^2}{2} = S(f)\Delta f \tag{2.31}$$

For a non-repeating wave train, N approaches infinity and Δf approaches zero. Rice [1944, 1945] also derived certain statistical properties of such a wave train, including showing that ζ itself has a Gaussian distribution. Note that the energy density spectrum, $S(f)$ is the variance of the amplitude components. The sum of the variance is equal to the variance of the sum; therefore the variance of the water level about the mean, ζ, is equal to the integral of the energy density spectrum [Holthuijsen, 2007]:

$$\bar{\zeta^2} = E\{\zeta^2\} = \sum_{n=1}^{N} E\left\{\frac{a_n^2}{2}\right\} = \int_0^\infty S(f)\mathrm{d}f = m_0 \tag{2.32}$$

where m_0 is the zero-th moment (or the integral with respect to f) of the energy density spectrum. Longuet-Higgins [1952] (cited in Longuet-Higgins [1980]) showed that for a narrow spectrum, the distribution of wave heights has a Rayleigh distribution:

$$p(H) = \frac{H}{4m_0} \exp\left(-\frac{H^2}{8m_0}\right) \tag{2.33}$$

thus giving a relationship between a parameter in the time domain (H) with one in the frequency domain. Using equation (2.33) one can derive the significant wave height in terms of m_0:

$$H_{m_0} = 4.004\sqrt{m_0} \approx H_{1/3} \tag{2.34}$$

Wave period parameters can be derived; the mean zero-crossing period is [Rice, 1945]:

$$\bar{T} = T_{m_{02}} = \sqrt{\frac{m_0}{m_2}} \tag{2.35}$$

where m_2 is the second moment of the frequency spectrum:

$$m_2 = \int_0^\infty f^2 S(f)\mathrm{d}f \tag{2.36}$$

Unfortunately, higher-order moments become very dependent on high-frequency components and are therefore affected by noisy data or the cut-off frequency in the analysis [Holthuijsen, 2007]. More commonly used are the significant wave period, $T_{1/3}$, or the peak wave period (i.e. corresponding to the maximum in the energy spectrum), T_p. A mathematical derivation of $T_{1/3}$ from the wave spectrum is not straightforward to obtain and T_p is obviously directly related to the spectrum; therefore the relationship between these parameters is more realistically determined from field data. Goda [2000] contains a considerable amount of useful information on these parameters.

2.2.2 Models of spectral shape

The equations described above give certain statistical properties and parameters associated with wave energy spectra. However, they give no description of what type of spectrum one would expect to find in the field. Indeed, the Rayleigh distribution of wave heights relies on the assumption that a spectrum is narrow; can we be certain that the spectra found in real seas conform to this restraint? The properties of real waves are determined by the mechanics of wave formation by the wind and are out of the scope of this thesis; however, the resulting wave spectra are very important and some background information will be described here.

In the previous section, the method of Sverdrup and Munk [1947] for calculating properties of significant waves from the wind speed and fetch was mentioned; this method does not allow additional calculations on spectral properties. Phillips [1958] showed that for a well-developed sea, the spectral energy of the high frequency components is proportional to $g^2 f^{-5}$. Bretschneider [1959] introduced a complete spectral shape and an empirical method for calculating wave period and wave height parameters from the wind speed and fetch length. Pierson and Moscowicz [1964] analysed wind and wave data for fully developed seas, finding the spectral shape has the form, in terms of angular frequency ω:

$$S(\omega) = \frac{\alpha g^2}{\omega^5} \exp\left(-\beta \left(\frac{\omega_0}{\omega}\right)^4\right) \tag{2.37}$$

where α and β are parameters with the values 8.1×10^{-3} and 0.74 respectively and ω_0 is a frequency parameter:

$$\omega_0 = \frac{g}{U_{19.5}} \tag{2.38}$$

where $U_{19.5}$ is the wind speed 19.5 m above the water level.

The JONSWAP spectrum was developed by Hasselmann et al. [1973] to take account of fetch-limited seas. Its shape is similar to that of the Pierson-Moscowicz spectrum, with the addition of a peak-enhancement factor, γ^q. The JONSWAP spectrum in terms of frequency f

is:

$$S(f) = \frac{\alpha g^2}{(2\pi)^4 f^5} \exp\left(-\frac{5}{4}\left(\frac{f_p}{f}\right)^4\right)\gamma^q \tag{2.39}$$

where q is:

$$q = \exp\left(-\frac{1}{2}\left(\frac{f/f_p - 1}{\sigma}\right)^2\right) \tag{2.40}$$

with the parameter σ having average values of 0.07 for $f \leq f_p$ and 0.09 for $f > f_p$.

All the spectral shapes described above make the assumption that the water is deep. The TMA spectrum [Bouws et al., 1985] is based on wave measurements in water depths from 5 m to 42 m. The spectrum is based on the proposition that the high frequency part of the spectrum is proportional to a function of the wave number, rather than the frequency. In deep water, this gives the same f^{-5} proportionality of Phillips [1958], becoming f^{-3} in shallower water. The spectral shape can be expressed as a modification to the JONSWAP spectrum, with an additional transformation factor, Φ_k:

$$S(f)_{\text{TMA}} = S(f)_{\text{JONSWAP}}\Phi_k(\omega_d) \tag{2.41}$$

where the transformation factor Φ_k is:

$$\Phi(\omega_d) = \frac{(k(\omega,d))^{-3}\,\frac{\partial k(\omega,d)}{\partial f}}{(k(\omega,\infty))^{-3}\,\frac{\partial k(\omega,\infty)}{\partial f}} \tag{2.42}$$

and:

$$\omega_d = 2\pi f\sqrt{\frac{d}{g}} \tag{2.43}$$

Bouws et al. [1987], based on calibration against their data, also proposed modifications to the parameters α and γ in the JONSWAP spectrum as functions of $k(f_p,d)U_{10}/g$. Note that, although the TMA spectrum is derived for use in all water depths, it does not take account of non-random phases or wave shoaling (to be described in Sections 2.2.5 and 2.3). Also, despite the TMA spectrum's greater range of applicability, the JONSWAP spectrum remains the most widely used, and the most widely tested.

2.2.3 Spectral energy models

Numerical wave modelling can be divided into two distinct categories: phase-averaged and phase-resolving [Battjes, 1994]. A phase-resolving type of model is based on a form of the continuity and momentum equations (such as those described in Section 2.1.3), which describe the instantaneous state of motion of the fluid. Therefore, time-series outputs for parameters such as free suface level or flux can be obtained. Spectral energy or phase-averaged mod-

els do not calculate individual waves; instead they predict the evolution of a wave energy spectrum across deep water, taking account of energy inputs and losses due to wind, white capping, bottom friction and nonlinear interactions. From these models, integrated parameters such as significant wave height can be obtained. Several phase-averaged models are in use, such as the WAM model [WAMDI Group, 1988], which models the evolution of waves across oceans, the finite element based TOMAWAC [Benoit et al., 1996], and SWAN (Simulating WAves Nearshore, Booij et al. [1999]), which is better suited to the modelling of nearshore waves than the WAM model.

Spectral energy models such SWAN calculate the spectral action balance equation; unlike the spectral energy density, the action density is also conserved with currents. The spectral action balance equation is given as [Booij et al., 1999]:

$$\frac{\partial N}{\partial t} + \frac{\partial c_x N}{\partial x} + \frac{\partial c_y N}{\partial y} + \frac{\partial c_f N}{\partial f} + \frac{\partial c_\theta N}{\partial \theta} = \frac{S_{in}}{f} \tag{2.44}$$

where the action density, N, is related to the spectral energy density by:

$$N = \frac{S(f, \theta)}{f} \tag{2.45}$$

c_x and c_y are the action propagation celerities in the x and y directions; c_f represents the propagation velocity of the shifting of frequencies due to variations in depths and currents; the terms with wave direction θ represent refraction, with propagation velocity c_θ; and the term S_{in} represents the source terms in terms of spectral energy density. The source terms include a range of wave processes: wave generation due to the wind; dissipation due to white-capping (deepwater wave breaking), bottom friction and shallow-water wave breaking; and nonlinear wave interactions.

Phase-averaged models such as SWAN are a highly efficient method of modelling waves over large areas of water. SWAN has been widely tested over a range of scales and for a wide variety of wave conditions (e.g. Ris et al., 1999, Jin and Ji, 2001, Rusu et al., 2008). In recent years, improvements have been made to the model to incorporate more phenomena, such as wave reflection and diffraction; for more information, see the SWAN website [Office of Naval Research and Rijkswaterstaat, 2011].

2.2.4 Focussed wave groups: NewWave

In the laboratory, the components of spectral waves need not be randomly phased. For a focussed group the components are such that they all come into phase at a defined location and time. If it is possible to represent the waves of a long random wave train by a short group

of focussed waves, this would be a very useful tool. The NewWave method by Tromans et al. [1991] is such a focussed group, aiming to represent the average free-surface shape around an extreme crest or trough; their approach states that the expected waves around the extreme crest or trough are equal to the auto-correlation function of the free surface level. The free surface level of an irregular wave is calculated as:

$$\zeta = \sum_{n=1}^{N} a_n \cos(k_n x - \omega_n t + \phi_n) \tag{2.46}$$

with N component amplitudes, a_n, being calculated according to the equation:

$$a_n = \frac{A_N S_n \Delta\omega_n}{\sum_{n=1}^{N} S_n(\omega)\Delta\omega_n} \tag{2.47}$$

where A_N is the specified maximum amplitude of the extreme wave, S_n is the spectral energy density at angular frequency ω_n, spaced in steps of $\Delta\omega_n$. The phases ϕ_n are calculated such that:

$$\phi_n = \omega_n t_{\text{focus}} - k_n x_{\text{focus}} + \begin{cases} \pi & \text{for trough-focussed wave} \\ 0 & \text{for crest-focussed wave} \end{cases} \tag{2.48}$$

where x_{focus} and t_{focus} are the defined position and time at which the crests (crest-focussed wave) or troughs (trough-focussed wave) of each of the N component waves come into phase (i.e. the focal point). The maximum amplitude can be specified from a certain exceedance probability from a Rayleigh distribution, or from some other extreme value analysis. NewWave groups have been used to calculate extremes in deep water; for example the work of Cassidy et al. [2001] to calculate wave forces on offshore platforms. Their use in the nearshore is not so well established; the method is based on linear random wave theory, and nonlinear effects in shallow water are considerably greater. However, experiments carried out by Stansby et al. [2007] have aimed to simulate extreme wave overtopping with NewWave groups; although this is a useful dataset, it does not make a comparison with overtopping from random waves.

2.2.5 Nonlinear waves and other limitations

It should be emphasised that important assumptions were made in the derivation of the equations described in Section 2.2.1. Firstly, the Rayleigh distribution for wave heights relies on the assumption that the spectrum is relatively narrow; Cartwright and Longuet-Higgins [1956] showed that the proportion of crest heights below the mean water level, r, is related to the

spectral width parameter ϵ, such that:

$$\epsilon = 1 - (1 - 2r)^2 \tag{2.49}$$

where:

$$r = \frac{1}{2}\left(1 - \frac{m_2}{\sqrt{m_0 m_4}}\right) \tag{2.50}$$

A Rayleigh distribution is approached when the proportion of negative crests, r, approaches zero; this is true when the spectral width is narrow and ϵ approaches zero. Although in deep water a Rayleigh distribution can be assumed as a rule of thumb, and field data confirms that real waves nearly conform to this, the width of wave spectra does lead to small discrepancies. Longuet-Higgins [1980] concluded that wave data fit more closely to such a distribution if the rms wave height, determined in the time domain, is substituted for the zero-th spectral moment into equation (2.33). Goda [2000, Section 2.4] and Holthuijsen [2007, Section 4.2.2] discuss how the Rayleigh distribution should be modified for greater spectral widths, and how the relationships between spectral and temporal parameters (for example equation (2.34)) are altered by this.

Secondly, it has been assumed that waves are linear; if waves are nonlinear, some component phases are no longer random. Therefore the water level will not have a Gaussian distribution; nonlinear waves are characterised by shorter, higher crests and longer, shallower troughs, skewing the distribution. Also, nonlinear interactions occur between components. If N second-order Stokes waves are superimposed, the resulting wave will have the form [Baldock et al., 1996]:

$$\zeta = \sum_{n=1}^{N} \zeta_{(n)} + \sum_{n=1}^{N} \sum_{m=n+1}^{N} \zeta_{(n,m)} \tag{2.51}$$

where $\zeta_{(n)}$ is the second-order Stokes solution for the nth wave component and $\zeta_{(n,m)}$ is the second-order interaction between the nth and mth component, such that [Longuet-Higgins and Stewart, 1960]:

$$\zeta_{(n,m)} = \frac{a_n a_m}{2g}\left(C\cos(\psi_n - \psi_m) - D\cos(\psi_n + \psi_m)\right) \tag{2.52}$$

where the phase angles ψ_n (and ψ_m) are:

$$\psi_n = k_n x - \omega_n t + \phi_n \tag{2.53}$$

and C and D are functions of the frequencies of the component waves. Therefore two additional waves are generated, neither satisfying the linear dispersion relation (equation (2.10))

but with phases equal to the sum and difference of the first order waves. These higher order interactions have been demonstated in laboratory tests on focussed groups by Baldock et al. [1996]; they found that due to these interactions, amplitudes at the focal point were greater than those predicted by linear theory, with the effect increased with larger (hence more non-linear) waves.

In general, interactions between two components are usually small in comparison to the primary waves. However, Phillips [1960] demonstrated that when three waves interact it is possible for resonance to occur, and the tertiary component can grow, with energy being transferred from the primary wave component. These interactions are known as *triads* and can be important in shallow and intermediate water depths (in deep water, four wave interactions, known as *quadruplets*, are more important). The SWAN model has the option of incorporating triads into its calculations, using a modified version of the method developed by Eldeberky and Battjes [1995].

Another related nonlinear phenomenon is that of *parasitic free waves*. For example, if a first order wave is propagated into water but is not a correct solution in the conditions, the necessary bound components will form, but will also release the parasitic free wave. According to Hunt [2003], at the point of generation the free waves will be equal to the bound components but of negative amplitude (i.e. of equal magnitude but π rad out of phase), therefore having the same frequency as the bound waves. Unlike the bound waves, they will travel according to the linear dispersion relation, thereby becoming "free". Such waves will also occur in a numerical model if the waves are not generated correctly.

2.3 Nearshore Waves and Wave Transformation

Water waves are affected by changes in the bed level, and interact with coastal structures. Despite the assumptions made in the formulation of linear wave theory, it can be used to explain many of these transformations. Dean and Dalrymple [1991] provide a thorough explanation of all the transformations described below.

As waves move into shallower water, according to equation (2.10) they slow down. For a steady state, the rate of change at which energy is transferred by the waves - the *energy flux* - remains constant. Therefore, if a wave travels from deep water to shallower depths:

$$Ec_{g0} = Ec_g \tag{2.54}$$

where E is the wave energy, c_g is the group celerity, or the velocity at which wave energy is transmitted, and c_{g0} is the deepwater group celerity. Because the wave energy is proportional

to H^2:

$$\frac{H}{H_0} = \sqrt{\frac{c_{g0}}{c_g}} = K_s \tag{2.55}$$

which results in an increase in wave height - or *wave shoaling* - as waves move towards the shore. K_s is the shoaling coefficient; in transitional water depths K_s is less than one, but increases above one in shallow water.

Additionally, waves travelling obliquely into varying water depths are subject to *wave refraction*. Wave refraction can be explained by the fact that the number of waves leaving an area per unit time must be the same as the number of waves entering (principle of conservation of waves). For straight and parallel bed contours, this leads to Snell's law:

$$\frac{\sin\theta}{\sin\theta_0} = \frac{c}{c_0} \tag{2.56}$$

Therefore, the wave fronts bend towards the shoreline as the water depth decreases. In addition, because energy flux is conserved, the equation for shoaling is modified, such that:

$$\begin{aligned} \frac{H}{H_0} &= \sqrt{\frac{c_{g0}}{c_g}}\sqrt{\frac{\cos\theta_0}{\cos\theta}} \\ &= K_s K_r \end{aligned} \tag{2.57}$$

where K_r is the refraction coefficient, and its value is always less than one. Because the work in this thesis will consider waves travelling perpendicular to the shore, wave refraction will not be considered. Additionally, *wave diffraction* will not be considered; this is the phenomenon whereby waves propagate into the shadow of an obstacle such as a breakwater. Wave diffraction is important in the design of ports and harbours; once again the interested reader is referred to Dean and Dalrymple [1991].

Wave reflection is important when considering the interaction of waves with structures, whether or not they are submerged. By considering a wave propagating towards a seawall, the combined incident and reflected wave will be:

$$\zeta_i + \zeta_r = a_i \cos(kx - \omega t) + a_r \cos(kx + \omega t) \tag{2.58}$$

If it is assumed there is no energy loss (i.e. $a_i = a_r = a$), then the incident and reflected waves will combine to form a standing wave:

$$\zeta = 2a \cos kx \cos \omega t \tag{2.59}$$

However, this is an idealised situation, and there will usually be energy loss and a change

in phase as the wave interacts with and reflects from a structure. Various techniques have been developed to separate the incident and reflected waves in a wave record; the method of Frigaard and Brorsen [1995] will be discussed in Section 5.3.1.

An important concept, with its origins in linear wave theory, is that of *radiation stress* (alternatively known as *momentum flux*). The theory and its application was developed by Longuet-Higgins and Stewart [1964] and describes many nonlinear phenomena associated with waves. The radiation stress is defined by Longuet-Higgins and Stewart [1964] as, "the excess flow of momentum due to the presence of waves", which can be expressed as (in the x direction):

$$\begin{aligned} S_{xx} &= \overline{\int_{-d}^{\zeta} p + \rho u^2 dz} - \int_{-d}^{0} p_0 dz \\ &= E\left(\frac{2kd}{\sinh 2kd} + \frac{1}{2}\right) \end{aligned} \tag{2.60}$$

There is also a radiation stress in the y direction, S_{yy}:

$$S_{yy} = E\left(\frac{2kd}{\sinh 2kd}\right) \tag{2.61}$$

which reduces to zero in deep water. Radiation stress can be used to explain wave *setup*, which is an increase in the mean water level in the surf zone. As waves break and lose energy, the loss of radiation stress is balanced by an increase in mean water level; this is the phenomenon of wave *setup.* There is also a lowering of mean water level in the location of shoaling waves seaward of the surf zone (wave *set-down*), which is also explained by the concept of radiation stress.

When the concept of radiation stress is applied to groups of waves, low frequency *infragravity* waves result (at the shoreline they are known as *surf beat*). Under higher waves, where the radiation stress is larger, the mean water level is lower than in regions of lower wave energy. This low frequency wave is bound to wave groups travelling at the group celerity; however in the surf zone Longuet-Higgins and Stewart [1964] argued that these waves are released as the higher frequency waves break, and are reflected offshore. However, there is another mechanism for the generation of surf beat; Symonds et al. [1982] showed that these long waves can be generated by the variation in break-point over time. Schäffer et al. [1993] showed that wave groups can still exist inside the surf zone, and that these can contribute to the low frequency waves, alongside the varying break point. An analysis of laboratory data by Baldock et al. [2000] suggested that the varying break-point generation was the predominant cause of surf beat, although Battjes et al. [2004] concluded that there is a strong dependence on the bed slope, with the low frequency bound waves making a greater contribution for milder

slopes.

2.4 Wave Breaking

2.4.1 Regular waves

Breaking is a well-known but little-understood phenomenon. Stokes [1880] calculated a theoretical maximum wave steepness, where the angle at the crest is 120°. McCowan [1894], in a mathematical analysis of solitary waves, first established a relationship between maximum wave height and water depth, deriving the expression:

$$\frac{H_{max}}{d} = 0.78 \tag{2.62}$$

which is still used as a rule of thumb for determination of the initiation of wave breaking. Miche (1944, referenced in Battjes [1974]) calculated a criterion for the propagation of waves in constant depth without change in form, given as:

$$\left(\frac{H}{L}\right)_{max} = 0.14 \tanh \frac{2\pi d}{L} \tag{2.63}$$

which, in shallow water reduces to:

$$\left(\frac{H}{d}\right)_{max} \approx 0.88 \tag{2.64}$$

There have been a consderable number of experimental studies on breaking waves. Galvin [1968] performed tests on a range of regular wave conditions breaking on slopes of 1/20, 1/10 and 1/5, and categorised the breaking waves into four types: spilling, plunging, collapsing and surging. Spilling breakers consist of turbulent water "spilling" down the front face of the breaking wave; plunging breakers are the typical breaking wave of one's imagination, with the wave crest curling over the wave and colliding into the preceeding trough; surging waves do not break by the time they reach the shore, with waves surging up the slope and being reflected back offshore. Collapsing breakers are a transition between surging and plunging waves, with a little turbulence on the front face of the wave but without the overturning associated with plunging breakers. A range of parameters are considered as a means for distinguishing these types, one of which is equivalent to an offshore surf similarity parameter:

$$\xi_0 = \frac{\tan \beta}{\sqrt{H_0/L_0}} \tag{2.65}$$

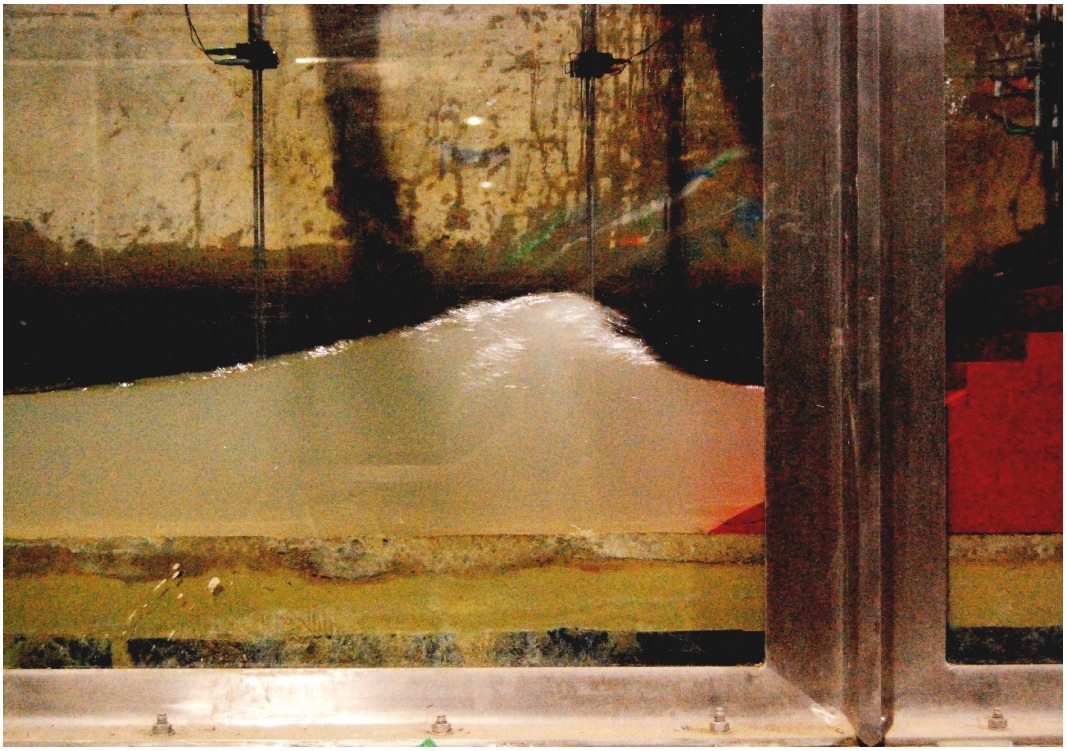

Figure 2.3: A spilling breaker approaching a seawall in a wave flume

According to Galvin [1968], spilling breakers would occur when $\xi_0 < 0.46$, plunging breakers would occur when $0.46 < \xi_0 < 3.3$, and collapsing or surging waves would occur when $\xi_0 > 3.3$.Battjes [1974] also re-analysed the data of Galvin [1968] in terms of a surf similarity parameter based on the waves at their break point, noting that there is in fact a gradual transition between these breaker types.

Weggel [1972] examined laboratory data and proposed a criterion for the onset of breaking that is dependent on beach slope:

$$\frac{H_b}{h_b} = \frac{1.56}{1.0 + \exp(-19.5m)} - 43.8(1.0 - \exp(-19m))\frac{H_b}{gT^2} \tag{2.66}$$

where m is the beach slope. Others, such as Goda [2000], have proposed different formulae for the break point location, also dependent on beach slope. These criteria are also based on laboratory tests, for regular waves, and with considerable scatter of data. Svendsen and Veeramony [2001] state that there is still no definitive wave breaking criterion.

2.4.2 Random waves

For random waves, breaking does not start at a fixed location. In this case, statistical models have been developed to determine the proportion of broken waves across the surf zone, and the associated energy loss. Battjes and Janssen [1978] developed one such model; they

assumed that the proportion of breaking waves could be determined by assuming a Rayleigh distribution of wave heights in the surf zone, cut off for heights above a limiting wave height. Their expression for depth-limited waves is similar to that of Miche (2.63), giving an expression for the proportion of breaking waves, Q_b:

$$\frac{1 - Q_b}{-\ln Q_b} = \left(\frac{H_{rms}}{H_{max}}\right)^2 \tag{2.67}$$

where H_{max} is the depth-limited wave height. Their calculation for the dissipation associated with breaking waves, $\bar{D}$, assumed similarity to that associated with a bore, giving the expression:

$$\bar{D} = \frac{1}{4}\alpha Q_b f_p \rho g H_{max}^2 \tag{2.68}$$

where α is a constant of order 1. The expression for dissipation was assumed to be equal to the rate of change of energy flux as the waves move inshore, allowing calculation of the change in significant wave height to be calculated numerically. Battjes and Stive [1985] carried out additional testing of this model against laboratory and field data, concluding that it performed well over a wide range of conditions. This model is still widely used today as part of the spectral energy model SWAN [Booij et al., 1999].

Thornton and Guza [1983] took a similar approach to Battjes and Janssen [1978], but aimed to increase the accuracy of calculated height distributions for breaking waves. Instead of cutting off the Rayleigh distribution for wave heights above H_{max}, a certain proportion of waves in each part of the distribution were assumed to be breaking; this proportion was determined by empirical formula, with larger proportions for higher waves. Thornton and Guza [1983] made a small modification to the energy dissipation model of Battjes and Janssen [1978], with $\bar{D}$ proportional to H^{2H}/h, rather than simply H^2. Baldock et al. [1998] also modified the model of Battjes and Janssen [1978], to improve results for steep beaches and Alsina and Baldock [2007] have made improvements to the calculation of energy dissipation.

2.4.3 Wave breaking in Boussinesq-type models

Such energy dissipation models are a useful addition to spectral energy models such as SWAN, but do not give information on the breaking of individual waves. The Boussinesq-type equations were derived for solitary waves, where the nonlinearity and dispersion parameters are balanced, giving steady state (i.e. non-breaking) solutions. Additional nonlinear terms such as those used by Wei et al. [1995] improve the accuracy of shoaling waves prior to breaking, but make no allowance for the turbulence and energy losses associated with breaking waves. A Boussinesq-type model for breaking waves must therefore contain some type of "trigger"

to initiate breaking, after which the model must change to incorporate the breaking process. So two questions are posed: when does breaking start; and what happens during the breaking process?

The first question has partly been answered above, giving criteria as functions of wave heights, wavelengths, water depths and beach slopes (equations (2.63) and (2.66)). It is possible, but not especially convenient in a model based in the time domain, to calculate such parameters from outputs such as free surface level or water velocity. Therefore, this type of criterion is rarely used in a Boussinesq-type model. One approach towards determining the onset of breaking is to use some type of limiting wave steepness. The approach first used by Schäffer et al. [1993] sets a maximum angle of the free surface of the front face of the wave, beyond which breaking occurs. Kennedy et al. [2000] instead used a limiting rate of change of the free surface on the front face of the wave, and is related to the gradient through the wave celerity. Breaking starts when:

$$\frac{\partial \zeta}{\partial t} > C_b \sqrt{gh} \tag{2.69}$$

where C_b is an empirical parameter (Kennedy et al. [2000] used $C_b = 0.65$ but this will vary depending on the model). The use of other parameters has been proposed. Zelt [1991] employed one related to the acceleration ($\partial u/\partial x$) of the flow; acceleration limits are more common for deepwater breaking or whitecapping (e.g. Srokosz [1986]). A rather different approach was proposed by Okamoto and Basco [2006], who compared breaking waves to a hydraulic jump. Their relative trough Froude number is based on the proposition that waves start to break in a similar way to an undular hydraulic jump changing to a fully developed surface roller hydraulic jump. However, their method relies on calculating wave celerities using a cross-correlation of free surface levels, which is rather more complex than calculating a simple gradient. D'Alessandro and Tomasicchio [2008] have improved their method with a new parameter, the Breaking Celerity Index (BCI), which combines the relative trough Froude number with the $\partial \zeta/\partial t$ criterion, such that breaking occurs when:

$$\frac{\partial \zeta}{\partial t} > \frac{\sqrt{g h_{crest}} - u_{BCI}}{1.47} \tag{2.70}$$

where u_{BCI} is a horizontal water velocity, which will depend on the type of Boussinesq equations being used. D'Alessandro and Tomasicchio [2008] used the equations of Nwogu [1993]; for their derivation u_{BCI} corresponds to the velocity at level z_α(see Section 2.1.3). According to D'Alessandro and Tomasicchio [2008] the value of 1.47 in the denominator may be a function of bed slope; it will also change depending on the definition of u_{BCI}.

With a range of available breaking criteria, what happens when the waves break? Battjes

[1988] reviewed the available research on surf zone processes, describing in detail the formation and development of breaking waves. When the crest of a plunging breaker overturns, a jet of water impacts onto the preceeding trough. Battjes [1988] states that this is similar for spilling breakers except that this jet is confined to a small region near the crest. The impacting jet forms a cavity that collapses allowing air to mix with the water causing the formation of vortices. Splashing water from the jet impacts again on the water surface leading to more violent motion; a sequence of vortices leads to high shear stresses and energy dissipation. Eventually, the vortices become more disordered, resulting in the formation of a "roller" associated with breaking waves propagating towards the shore. In this region there is a continuous transfer of wave motion into turbulent motion; Battjes [1988] states that the momentum flux associated with this turbulent motion is considerably less than that of the wave motion, leading to the wave setup described in Section 2.3. Usually the water depth decreases sufficiently to maintain the turbulent bore; if the slope is too shallow, or the water depth increases, the bore Froude number will decrease causing the bore to become an undulating hydraulic jump and the breaking process ceases. Beji and Battjes [1993] analysed experimental data of waves propagating over a submerged bar, examining the effects of the cessation of the breaking process as waves propagate back into deeper water.

It is apparent that a Boussinesq-type model cannot (and possibly should not) aim to model all of these processes. The equations make assumptions on the vertical structure of the water velocity and pressure, which becomes rather more complex in the surf zone. Additionally, the equations have been derived with the assumption that water is irrotational (i.e. $\partial u/\partial z - \partial w/\partial x = 0$); this is most certainly not the case with breaking waves. Therefore, any such numerical model will greatly simplify these processes.

There are two main methods for incorporating the breaking process into a Boussinesq-type model. Schäffer et al. [1993], building on previous work by Svendsen [1984], used what is called a roller approach, whereby the breaking wave carries a body of water on the wave front, at the local wave celerity. Therefore, the velocity profile is effectively divided in two, with the bottom portion consisting of a Boussinesq-type velocity (usually either the depth-averaged horizontal velocity, or the horizontal velocity at a pre-defined location), and the top portion (the roller) having a velocity equal to the wave celerity. According to Dingemans [1997], this breaking model gives good results for spilling breakers but does not agree so well for plunging breakers. It also requires some geometric calculations on the front face of the wave, to determine the size of the roller.

The second method makes use of an eddy viscosity term for the breaking waves; this method was employed by Zelt [1991] for breaking solitary waves, with a similar but slightly

improved method in the model of Kennedy et al. [2000]. The stresses caused by the turbulence in breaking waves are simply represented as an additional horizontal diffusion term. The use of such a model also controls the change of breaking waves into the bores produced by the nonlinear shallow water equations. This method has a less sound physical basis than the previous method but is simpler to implement.

An extension to the roller method is that developed by Veeramony and Svendsen [2000], who solve the vorticity transport equation under the breaking waves. They revisit the Boussinesq-type equations, without the irrotational flow assumption. This represents the most physically correct representation of breaking waves, although the resulting equations are considerably more difficult, without great improvement in results.

2.5 Wave Runup and Overtopping

2.5.1 Experimental and field studies of wave runup

Wave *runup* is the maximum level to which the water travels up a beach or coastal structure. Breaking waves lose their energy as they approach the shore; if there is any energy remaining in the individual waves, the waves propagate up and down the beach or structure. However, runup is also composed of the surf beat described in Section 2.3. Some authors, such as Guza and Thornton [1982], make a distinction between swash and runup, with swash being the oscillations about the mean setup level, and runup being the level of swash combined with setup. For other authors swash is the same as runup; to avoid confusion the word "runup" will be preferred in this thesis.

Hunt [1959] (cited in Bowen et al. [1968]) carried out laboratory tests of breaking regular waves, finding that the runup is a function of the surf-similarity parameter:

$$\frac{R}{H_0} = C_p \frac{\tan\beta}{\sqrt{H_0/L_0}} \tag{2.71}$$

where C_p is a porosity factor, which would be equal to 1 for impermeable slopes. Bowen et al. [1968] also carried out laboratory tests with regular waves on a beach of slope $\tan\beta = 0.082$, and found good agreement with equation (2.71). Battjes [1974] used analytical reasoning and physical model tests to establish whether Hunt's formula is applicable to random waves. It was found that any percentile runup could be estimated using a form of this formula, multiplied by a factor that is a function of the spectral width. Battjes [1974] also suggested that if the incident wave heights are Rayleigh distributed and the wavelengths are correlated with the wave height (i.e. $H/L =$ constant), the runups will also be Rayleigh distributed.

Guza and Thornton [1982] analysed field data on gently sloping beaches (with slopes, $\tan\beta$, from 0.03 to 0.05 at the shoreline) showing that the magnitude of the high frequency runup was unaffected by offshore wave heights (i.e. all waves in the surf zone are depth limited - a saturated surf zone) but the low frequency motion made a greater contribution, which was proportional to the offshore wave heights. Holman and Sallenger [1985] had a larger and more reliable set of field data than Guza and Thornton [1982], using time-lapse photography to measure runup levels, with a steeper beach slope ($\tan\beta = 0.1$). They also found that the surf similarity parameter, ξ_0, was a good measure of runup, and that low frequency waves started to dominate when $\xi_0 < 1.75$.

Mase [1989] published a large range of experimental runup tests on slopes, $\tan\beta$, ranging from 0.033 to 0.2. Some of this data had previously been analysed by Mase [1988], firstly showing that the number of individual runups is a function of the surf similarity parameter; for shallower slopes, individual runups effectively merge, while for steeper slopes, there is a runup corresponding to almost every incident wave. Mase [1988] also analysed the data in the frequency domain; like others he found saturation in the surf zone, showing that it would manifest itself in the high frequency part of the spectrum as:

$$S(f)\mathrm{d}f \sim 4g\tan^4\beta f^{-4} \tag{2.72}$$

He proposed that the low frequency part of the runup spectrum could be generated by the superimposition of runups from the incident waves, without the effect of surf beat. Further analysis on experimental data with bichromatic waves [Mase, 1995] suggested that both phenomena can cause low frequency runup, with surf beat becoming more dominant for lower surf similarity parameters.

Mase [1989] concentrated on developing empirical formulae for runup parameters, all of form:

$$\frac{R}{H_0} = a_R\left(\frac{\tan\beta}{\sqrt{H_0/L_0}}\right)^{b_R} \tag{2.73}$$

where a_R and b_R are empirical constants. The commonly used runup parameters are: $R_{2\%}$, which is the 98th percentile runup; $R_{1/10}$, which is the mean of the highest tenth of runups; $R_{1/3}$, which is the mean of the highest third; and also $\bar{R}$, the mean runup level. Mase [1989] also derived formulae of a similar form for the ratio of runups to incident waves. Hedges and Mase [2004] used the same dataset to make a further modification to Hunt's equation, with an additional term to represent wave setup.

Analysis of data on dykes was carried out by van Gent [2001]. The same processes control runup on coastal structures as they do on beaches, though slopes are generally steeper, the

water level on the foreshore determine whether or not breaking occurs, and such structures may have armour units or other mechanisms to increase roughness and dissipate energy. The objective of this research was to determine which representative wave period should be used to calculate L_0 in the surf similarity parameter; the spectral peak period, T_p, is most common, but van Gent [2001] suggested that $T_{m-1,0}$, which is based on the spectral moments m_0 and m_{-1}, should be preferred. This period, $T_{m-1,0}$ will also come up in research on wave overtopping; it does have the disadvantage of being over-affected by low frequency motion, and a low frequency cut-off is essential when calculating $T_{m-1,0}$.

Mase et al. [2004] performed tests on slopes with a seawall, in addition to an offshore bar, over which the waves break. It was shown that previous empirical methods were not ideal for predicting runup in this situation, despite the runups being Rayleigh distributed, as before. This is a useful additional dataset to go alongside the previous research.

2.5.2 Experimental and field studies of wave overtopping

A large number of laboratory experiments have taken place to measure waves overtopping various forms of coastal structures. One of the aims of the CLASH (Crest Level Assessment of coastal Structures by full scale monitoring, neural network prediction and Hazard analysis on permissible wave overtopping [!]) project [Steendam et al., 2004] was to develop a database of the various experiments that have taken place. The database is an invaluable resource for a researcher looking for previous overtopping measurements. It contains information on over 10 000 overtopping tests, including wave heights and periods, model bathymetry and mean overtopping rates. It also gives an index on the reliability of the data, and in some cases a reference to the original model tests. It does not, however, present detailed parameters on wave spectra, distributions of overtopping events (including the number of overtopping waves), and some of the data may be open to interpretation. Obviously, not all of the studies that have taken place can be described here, but a few important ones will be outlined.

Owen [1980] (cited in Besley [1999]) performed physical model tests on seawalls with and without berms, to derive a formula for the design of seawalls. The equation is expressed in terms of dimensionless overtopping discharge, q^*_{Owen}:

$$q^*_{\text{Owen}} = \frac{q}{T_m g H_s} \tag{2.74}$$

and dimensionless freeboard, R^*_{Owen}:

$$R^*_{\text{Owen}} = \frac{R_c}{T_m \sqrt{g H_s}} \tag{2.75}$$

where q is the mean overtopping discharge (in $m^3\,m^{-1}\,s^{-1}$), R_c is the freeboard (i.e. vertical distance between the still water level and crest of the structure) and T_m is the mean wave period. Owen's [1980] formula was expressed as:

$$q^*_{\text{Owen}} = A \exp\left(-\frac{BR^*_{\text{Owen}}}{r}\right) \tag{2.76}$$

where A and B are empirically derived functions of seawall slope, and r is a roughness coefficient. Besley [1999] built upon this work, revising the empirical coefficients, incorporating new formulae for vertical seawalls, guidance for estimating the maximum overtopping discharge as well as estimates of the maximum mean discharges a structure can tolerate. Their guidance for mean overtopping on sloping seawalls is valid for values of R^*_{Owen} between 0.05 and 0.3.

Van der Meer and Janssen [1995] performed similar analyses of tests on dykes, with and without a berm. Their empirical formulae were in a different dimensionless form; with a dimensionless discharge q^*_{VJ}:

$$q^*_{\text{VJ}} = \frac{q}{\sqrt{gH_s^3}}\sqrt{\frac{H_s/L_0}{\tan\beta}} \tag{2.77}$$

and a dimensionless freeboard R^*_{VJ}:

$$R^*_{\text{VJ}} = \frac{R_c}{H_s}\frac{\sqrt{H_s/L_0}}{\tan\beta} \tag{2.78}$$

For non-breaking waves, the second term on the right hand side of the two equations above (i.e. $\sqrt{\frac{H_s/L_0}{\tan\beta}}$ and $\frac{\sqrt{H_s/L_0}}{\tan\beta}$) is set to 1. The resulting relationship between these two dimensionless parameters is similar to equation (2.76), though the parameters A and B are constants, without variation due to bed slope; the equations are presented for values of R^*_{VJ} beween 0.2 and 1.8 for breaking waves and between 0.5 and 3.5 for non-breaking waves. They also published additional guidance, including a similar method to Besley [1999] to estimate the maximum overtopping volume.

It is apparent that different researchers have derived a range of formulae for a range of structures with different restrictions on their validity. The EurOtop Manual [Pullen et al., 2007] aimed to combine these different sets of empirical formulae, and to update them using the information generated by CLASH. The resulting manual gives comprehensive empirical guidance on the overtopping of (almost) any coastal structure, as well as recommending which tools are best suited to calculating overtopping for the structure. These tools include similar formulae to those shown above; a web-based overtopping calculator that was developed from a previous Dutch overtopping manual [PC-Overtopping, 2007]; and a neural network devel-

oped as part of the CLASH project [van Gent et al., 2007], which is also available online [Overtopping Neural Network, 2007]. According to EurOtop, neural networks are used where a process is affected by a large number of parameters and a large volume of data is available for the network to calculate the influence of these parameters. The CLASH database contains data from over 10 000 tests on a variety of structures, which therefore means that estimates for overtopping rates can be given for almost any structure.

These tools and formulae can be very useful, but they do have their limitations. The immediate apparent weakness is the scatter of data shown on the charts from which the empirical formulae are derived. For example, by taking the 95% confidence intervals either side of the mean for the chart for non-breaking waves of Van der Meer and Janssen [1995], for a dimensionless freeboard of 3.5, the dimensionless discharge can range from just over 10^{-6} to nearly 10^{-3}. Some of this scatter is real, in that one wave train with the same significant wave height and period can differ noticeably from another, and when few waves overtop the structure, this can make a large difference to mean overtopping rates. Other scatter can be due to a variety of effects - these can include: not every possible shape or feature on a structure can be parameterised; different methods may have been used to measure overtopping; the wave conditions, which are generally meant to be calculated at the toe of the structure, may have been recorded differently. Additionally, wave-by-wave overtopping cannot be predicted; maximum overtopping volumes can be estimated, but only in a probabilistic way. The tools, especially the neural network, operate in a "black box" way; one enters the required parameters and receives an output for mean overtopping rate, without any available way of observing how overtopping occurs. These limitations make the numerical modelling of overtopping more desirable.

2.5.3 Numerical modelling of overtopping and runup

Until fairly recently, numerical modelling was impossible, and then impractical. Analytical solutions for non-breaking wave runup of solitary waves were derived by Carrier and Greenspan [1958]; these are now sometimes used as a test case for solitary wave runup in numerical models. Also Shen and Meyer [1963] used the nonlinear shallow water equation (2.25) to give an analytical solution to the path of a bore running up a slope. However, analytical solutions cannot be derived for the range of structures and random wave conditions encountered in reality.

Numerical modelling of nearshore waves has its own difficulties; wave breaking has already been discussed, but wave input and the seaward boundary present their own problems, as does the shoreline boundary. There is also a problem with steep bed slopes; both the nonlinear shallow water equations and most Boussinesq-type equations have been developed for

mild slopes. Nevertheless, Shiach et al. [2004] have shown that a nonlinear shallow water model can give reasonable results for the overtopping of vertical seawalls.

A numerical model based on the nonlinear shallow water equations were used by Kobayashi et al. [1987] and Kobayashi et al. [1989] to investigate surf zone processes for regular and solitary waves. The results were promising, though use of Boussinesq-type equations was suggested as an improvement for non-breaking waves. Also, the available computer power was such that calculations in the time domain would be impractical for random waves. However, Kobayashi and Raichle [1994] later used a similar model to investigate the overtopping of random waves. The model of van Gent [1994] was similar to Kobayashi's, but included terms for the flow through permeable structures. Dodd [1998] developed a finite volume nonlinear shallow water model and tested it against physical model tests for random wave overtopping. At the seaward boundary, these models allow reflected waves to leave using the method of characteristics, but wave input requires calculating both an input velocity and and input depth. The shock-capturing numerical solution of Dodd [1998] allows the tracking of any number of moving shorelines; for the other models, only one shoreline can be tracked and any water leaving the "wet" part of the domain is no longer solved. One common feature of these models is that they are only valid for breaking waves, which means the seaward boundary must be close to the shore.

With the greater computer power required, Boussinesq-type models started to become popular a little later. The model of Zelt [1991] made use of Boussinesq-type equations for breaking and non-breaking solitary waves, suggesting that the non-hydrostatic effects improved the runup predictions. Being a Lagrangian method, no special treatment was required to track the shoreline; however, the seaward boundary required an algorithm to separate the incident and reflected waves. Madsen et al. [1997a] and Madsen et al. [1997b] analysed surf beat and runup with their model based on the equations of Madsen and Sorensen [1992], using a roller method for breaking waves, and a "slot" method for a shoreline boundary. This method, also employed by Kennedy et al. [2000], represents the sloping bed as a nearly impermeable structure, almost preventing any flow through it; it has the advantage of being simple to implement, and is ideal modelling for permeable structures, but is unsuitable for modelling complex geometries where overtopping water may be collected, and it can be problematic in practice - Kirby [2003] described its use as "something of an art form".

An improved form of shoreline boundary was developed by Lynett et al. [2002], whereby the depth and velocity variables are linearly extrapolated into the "dry" part of the domain. One must select a minimum depth where the extrapolation must start, and the shoreline may well lie between two nodes. All relevant derivatives which require values from the dry do-

main use these extrapolated variables. It is unlikely that this method could be used where more than one "wet" region exists.

At the shoreline boundary, the nonlinear shallow water equations, without third-order (or higher) derivatives, present fewer problems; in these regions a Boussinesq-type formulation is unnecessary anyway. Therefore, some models, such as those by Stansby et al. [2007], Borthwick et al. [2006], Lynett et al. [2010] and Roeber et al. [2010] use Boussinesq-type equations for non-breaking waves, and nonlinear shallow water equations for breaking waves. At this stage, it is worth mentioning the work of Stelling and Zijlema [2010]; their model equations are similar to the nonlinear shallow water equations, but include vertical acceleration terms. The finite-difference grid is split into multiple layers, and the governing equations are integrated over each layer. Because non-hydrostatic pressure is accounted for, their model is valid for non-breaking and breaking waves, without requiring any algorithm to start the breaking process. It also has the advantage over Boussinesq-type models in that it does not contain higher-order derivatives. The model of Stelling and Zijlema [2010] performed well against experimental results from breaking and non-breaking regular and random waves. It is not clear how much computation power is needed to run such a model.

At the seaward boundary, Larsen and Dancy [1983] developed a method where the wave input takes place inside the model domain (no wave paddle is required); this allows the region offshore from the wave input location to contain a sponge layer, with an algorithm that absorbs all outgoing waves. To generate waves, all that is required is a displacement of the free surface, which is in one horizontal dimension:

$$\Delta\zeta = 2\zeta^I c_g \frac{\Delta t}{\Delta x} \tag{2.79}$$

where $\Delta\zeta$ is the free-surface displacement, ζ^I is the incident wave train, and c_g is the wave group velocity; note that Larsen and Dancy [1983] specified wave speed, c, but Lee et al. [2001] and Kim et al. [2009] have confirmed that the wave energy velocity, or c_g, is correct. The main disadvantage of this method is that recorded wave conditions contain incident as well as reflected waves. Strictly speaking, only the incident waves are wanted for wave generation; therefore to produce a numerical wave train from field or laboratory data one should remove the reflected waves from the time-series - a non-trivial exercise.

Studies of the Boussinesq-type modelling of wave overtopping have not yet been mentioned; there are few of them. Lynett et al. [2010] used a shallow-water Boussinesq-type to calculate regular and solitary wave overtopping of dykes. Stansby et al. [2007] compared shallow-water Boussinesq model simulations with results of overtopping from focussed wave

groups. Stansby et al. [2008] tested the commercial STAR-CD code, which solves the Reynolds-Averaged Navier-Stokes (RANS) using a volume of fluid method for tracking the free surface, and SPHysics, an open-source smoothed particle hydrodynamics (SPH) model, in comparison with the same shallow-water Boussinesq model. The commercial software underestimated overtopping volumes for a solitary wave by about 30 %, whereas the other two models were within 10 % of the experimental data. The main difference between the models was in terms of computation time; the Boussinesq-type model required 30 s to simulate the solitary wave, whereas the SPH model required 18 hours and the commercial code needed 20 days. Therefore, only the Boussinesq-type model would be fast enough to simulate the hundreds of waves required for a random wave analysis. However, there do not yet appear to be any tests or analyses of Boussinesq-type models for random wave overtopping. It would be of great use for coastal engineers to have a validated tool with a high level of confidence, which would enable more detailed and reliable analysis of wave overtopping and coastal flooding.

Chapter 3

The Shallow Water and Boussinesq Model

This chapter includes a description of the Shallow Water and Boussinesq (SWAB) model being used in the thesis, including the following: the model equations; the numerical solution method; the wave breaking models; the wave input mechanism; absorbing and shoreline boundary algorithms; the means of producing output, including determination of runup levels and overtopping volumes; and the algorithm developed for modelling vertical walls. Some tests of the model's range of validity are also presented. The model was originally written in Fortran 77 by Prof Peter Stansby (SWAB 1.0), this being the Boussinesq model described by Stansby et al. [2008] and similar to the one used by Stansby [2003]. The model was rewritten in Fortran 90/95 by Dr David Apsley (SWAB 2.0); some of the model runs were performed with various versions of SWAB 2.

Most model runs used the latest version of the model, which is described here. It will be described as SWAB 3.0 and uses the same solver and subroutines as SWAB 2, but has a very different model input. Whereas previously most model parameters were written into the Fortran code, in SWAB 3.0 they are read from input files; this allows multiple runs with different parameters to be set up.

3.1 Model Equations and Solution

The SWAB model uses the equations of Madsen and Sorensen [1992], in one horizontal dimension. They consist of a continuity equation (3.1) and a momentum equation (3.2):

$$\frac{\partial h}{\partial t} + \frac{\partial hu}{\partial x} = 0 \tag{3.1}$$

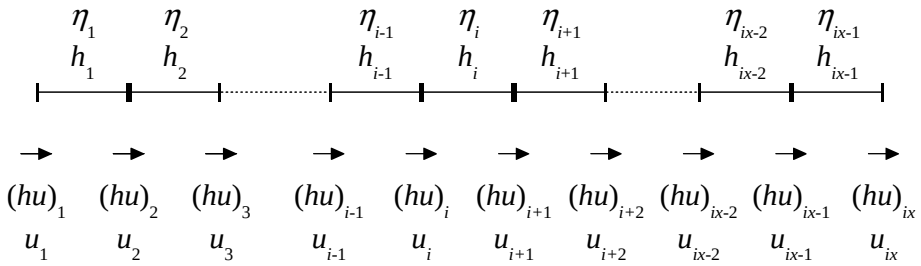

Figure 3.1: Diagram of staggered finite volume mesh for SWAB model

$$\frac{\partial hu}{\partial t} + \frac{\partial hu^2}{\partial x} = -gh\frac{\partial h}{\partial x} - gh\frac{\partial z_b}{\partial x} - \frac{\tau_b}{\rho} + \left\{ \left(B + \frac{1}{3} \right) d^2 \frac{\partial^3 (hu)}{\partial x^2 \partial t} + Bgd^3 \frac{\partial^3 \eta}{\partial x^3} + d\frac{\partial d}{\partial x} \left(\frac{1}{3} \frac{\partial^2 (hu)}{\partial x \partial t} + 2Bgd \frac{\partial^2 \eta}{\partial x^2} \right) \right\}_{\text{pre-break}} + \left\{ \frac{\partial}{\partial x} \left(h(\nu + \nu_e) \frac{\partial u}{\partial x} \right) \right\}_{\text{post-break}} \tag{3.2}$$

The Boussinesq terms are the pre-breaking part of the second line of equation (3.2), where B is a constant that controls the linear dispersion characteristics. The horizontal diffusion terms are the post-breaking part on the third line. Madsen and Sorensen [1992] found that $B = 1/15$ gives the best linear dispersion. The model calculates numerical solutions for h using a Crank-Nicolson semi-implicit method. This has the advantage of being more stable than fully explicit methods, without the dampening effects of fully implicit methods. A staggered mesh finite volume scheme is used; the mesh is shown in Figure 3.1. The continuity equation (3.1) becomes:

$$h_i^{n+1} = h_i^n - \theta \frac{\Delta t}{\Delta x} \left((hu)_{i+1}^{n+1} - (hu)_i^{n+1} \right) - (1 - \theta) \frac{\Delta t}{\Delta x} \left((hu)_{i+1}^n - (hu)_i^n \right) \tag{3.3}$$

where θ represents the degree of "implicitness" (i.e. fully implicit where $\theta = 1$ and fully explicit where $\theta = 0$) and is set to $1/2$. The subscripts n and i represent the temporal and spatial steps respectively.

The momentum equation (3.2) can be manipulated to give $(hu)^{n+1}$ in terms of h^{n+1}:

$$(hu)_i^{n+1} = \frac{f_i^*}{g_i^*} - \theta g \frac{\Delta t}{\Delta x} b_i^* \left(h_i^{n+1} - h_{i-1}^{n+1} \right) \tag{3.4}$$

where f_i^*, g_i^* and b_i^* are:

$$\begin{aligned} f_i^* &= (hu)_i^n - \Delta t\Bigg((\text{adv})_i + (\text{Bous})_i + (\text{dif})_i \\ &\quad - (1-\theta)\, g h_{i-1/2}^n \frac{h_i^n - h_{i-1}^n}{\Delta x} - g h_{i-1/2}^n \frac{z_i^n - z_{i-1}^n}{\Delta x} \Bigg) \end{aligned} \tag{3.5}$$

$$g_i^* = 1 + \frac{\Delta t}{2} C_f \frac{|u_i^n|}{h_{i-1/2}^n} \tag{3.6}$$

$$b_i^* = \frac{h_{i-1/2}^n}{g_i^*} \tag{3.7}$$

where $(\text{adv})_i$ represents advection and $(\text{Bous})_i$ represents the Boussinesq terms and $(\text{dif})_i$ represents the horizontal diffusion. $(hu)^{n+1}$ in equation (3.3) is substituted using equation (3.4) to give an expression for h^{n+1} in the following form:

$$A_1 h_{i-1}^{n+1} + A_2 h_i^{n+1} + A_3 h_{i+1}^{n+1} = f\left(h_i^n,\, (hu)_i^n,\, (hu)_{i+1}^n\right) \tag{3.8}$$

where A_1, A_2 and A_3 are functions of h^n and u^n. Equation (3.8) gives a tridiagonal matrix, from which solutions for h_{i-1}^{n+1}, h_i^{n+1} and h_{i+1}^{n+1} can be obtained using a tridiagonal equation solver. $(hu)^{n+1}$ and u^{n+1} are calculated using equation (3.4).

The advection ($\partial(hu^2)/\partial x$) terms, Boussinesq terms and horizontal diffusion terms are all calculated at the beginning of a time-step; the advective and horizontal diffusion terms are calculated explicitly first, followed by the Boussinesq terms. The advection is calculated using a linear upwind differencing scheme (LUDS) that is first-order in time, though different schemes could easily be implemented. The break point, or break points, are also calculated at the beginning of the time-step. Methods used for these will be described in Section 3.2.2. To calculate the Boussinesq terms, equation (3.2) can be rewritten by gathering all the $\partial(hu)/\partial t$ terms on the left-hand side:

$$\begin{aligned} \frac{\partial(hu)}{\partial t} - \left(B + \frac{1}{3}\right) d^2 \frac{\partial}{\partial x^2}\left(\frac{\partial(hu)}{\partial t}\right) - \frac{d}{3}\frac{\partial d}{\partial x}\frac{\partial}{\partial x}\left(\frac{\partial(hu)}{\partial t}\right) \\ = -\frac{\partial hu^2}{\partial x} - gh\frac{\partial \eta}{\partial x} - \frac{\tau_b}{\rho} + \frac{\partial}{\partial x}\left(h(\nu + \nu_e)\frac{\partial u}{\partial x}\right) \\ + Bgd^3\frac{\partial^3 \eta}{\partial x^3} + 2gd^2\frac{\partial d}{\partial x}\frac{\partial^2 \eta}{\partial x^2} \end{aligned} \tag{3.9}$$

with the Boussinesq terms being the last two terms on either side of the equation. From equation (3.9) a discretised equation of similar form to equation (3.8) is derived, giving a solution

for $\partial(hu)/\partial t$, for time-step $n+1$, using a tridiagonal solver.

$$A_4\left(\frac{\partial(hu)}{\partial t}\right)_{i-1}^{n+1} + A_5\left(\frac{\partial(hu)}{\partial t}\right)_{i}^{n+1} + A_6\left(\frac{\partial(hu)}{\partial t}\right)_{i+1}^{n+1} = F_i^n \tag{3.10}$$

where A_4, A_5 and A_6 are functions of B, d and $\partial d/\partial x$ and F_i^n represents all the terms on the right-hand side of equation (3.9), using the values for these terms at timestep n. To maintain stability with a moving break point, the Boussinesq terms are calculated throughout the domain, with post-breaking values set to, or phased towards zero. To prevent sawtooth numerical instability in non-breaking waves, a digital filter was applied to the water level η, of the form effectively used by Longuet-Higgins and Cokelet [1976] in their boundary-integral computations; the same filter has been used for Boussinesq modelling by Stansby [2003].

The third term on the right hand side of equation (3.2), τ_b/ρ, represents the bed shear stress. Using the Darcy-Weisbach equation, this can be expressed as:

$$\frac{\tau_b}{\rho} = \frac{C_f u|u|}{2} \tag{3.11}$$

where C_f is the friction coefficient. The bed shear stress is always in the opposite direction from the flow. The SWAB model calculates this term explicitly, featuring in the expression for g_i^* (equation (3.6)), using values of u from the previous time-step. The SWAB 3.0 model allows C_f to have varying values across the domain, though these values remain constant over a model run. Bed friction has little effect on surface gravity waves over the distances simulated by the SWAB model. However, it can affect runup levels and will be discussed in Sections 6.1.2 and 6.2.2.

3.2 Wave Breaking

3.2.1 Wave breaking model

The SWAB model has a similar breaking formualtion as those of Zelt [1991] and Kennedy et al. [2000], who used an additional horizontal diffusion term. In general, for breaking waves, the Boussinesq terms are set to zero and the horizontal diffusion is calculated. The horizontal diffusion is represented by the last term in equation (3.2), with the eddy viscosity associated with the breaking waves, ν_e, calculated using a similar method to Kennedy et al. [2000]:

$$\nu_e = \delta^2 h\left|\frac{\partial \eta}{\partial t}\right| \tag{3.12}$$

where δ is a mixing length coefficient. For the SWAB model $\delta = 0.5$ was used throughout; other values can affect the model stability, and Kennedy et al. [2000] found results fairly insensitive to varying this coefficient.

There is no definitive advice on how the Boussinesq terms should be switched off after the break point (this type of combined shallow-water and Boussinesq is relatively new); both an instant switch-off and a phasing-out algorithm have been tested.

3.2.2 Initiation of wave breaking

In Chapter 2, a range of wave breaking criteria were discussed; when some parameter exceeds a certain value, the breaking process is initiated. For the main criterion used by the SWAB model, this parameter is $\partial\eta/\partial t$; breaking occurs when:

$$\frac{\partial \eta}{\partial t} > C_{bt}\sqrt{gh} \tag{3.13}$$

where C_{bt} is a breaking coefficient. Values of C_{bt} between 0.2 and 0.3 were tested; these will be described in Chapter 5. Note that breaking is only initiated when $\partial\eta/\partial t$ is positive, as breaking starts on the front face of a wave. Another criteria is:

$$\frac{\partial \eta}{\partial x} > C_{bx} \tag{3.14}$$

which is related to the previous criterion (equation (3.13)) by the following:

$$c = -\frac{\partial\eta/\partial t}{\partial\eta/\partial x} \tag{3.15}$$

However, it was found to not work as well in practice as the $\partial\eta/\partial t$ criterion, probably because the time-step, dt/T, is smaller than the spatial step, dx/L, for all the model testing that has been done so far; $\partial\eta/\partial x$ will not be considered in subsequent chapters as a breaking parameter.

One can also use a wave height to water depth ratio, such that breaking occurs when:

$$\frac{H}{h} > C_{bh} \tag{3.16}$$

This condition requires an algorithm to separate individual waves before calculating their heights and the mean depth for each wave. Figure 3.2 shows how this is done. The mean water level, calculated from the start of the run, is used to find the zero up-crossing points (in a spatial sense - temporally, they are down-crossing points) in the domain; each wave therefore consists of a crest with a preceeding trough. Note that for the first four periods of a model run

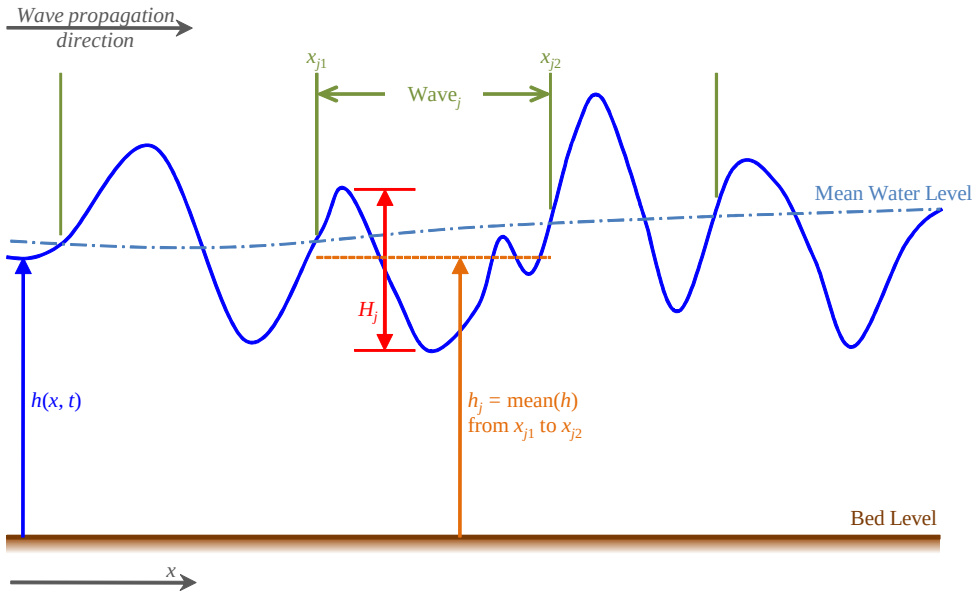

Figure 3.2: Separation of individual waves, for calculating H/h

the still water level is used instead, because the mean water level will take time to appear. The wave height, H, is therefore the difference between the minimum and maximum level of each wave; the mean depth, h, is the mean depth of water over the wave for that particular time-step.

None of the above conditions are perfect. The third of these conditions (equation (3.16)) requires the algorithm to separate the waves, which may cause problems where the wave setup is large. The other two conditions do not require such calculations. However, for these conditions there is no criterion available to stop the breaking process (for example, if the waves return into deeper water); the H/h condition will do so automatically as h increases; this will be investigated in later chapters.

Another possible drawback with the wave breaking model is the assumption that the Boussinesq model immediately (or over a short distance) becomes a shallow water model without any frequency dispersion. Therefore, if one is using the $\partial\eta/\partial t$ or the $\partial\eta/\partial x$ breaking criterion all waves inshore from the break point will be assumed to be shallow water waves; this is not necessarily true, and for random waves some breaking can occur in relatively deep water. The breaking of an intermediate depth wave in a wave flume is shown in Figure 3.3a. In Figure 3.3b the same wave is ceasing to break (the turbulence at the crest appears to be in the process of being overtaken by the crest of the wave itself), and will continue towards shallower water as a non-breaking wave; this highlights how the breaking model and the transfer to the nonlinear shallow water equations may be inappropriate in such a case.

Therefore, the following double break point was proposed. In deeper water, where $\partial\eta/\partial t >$

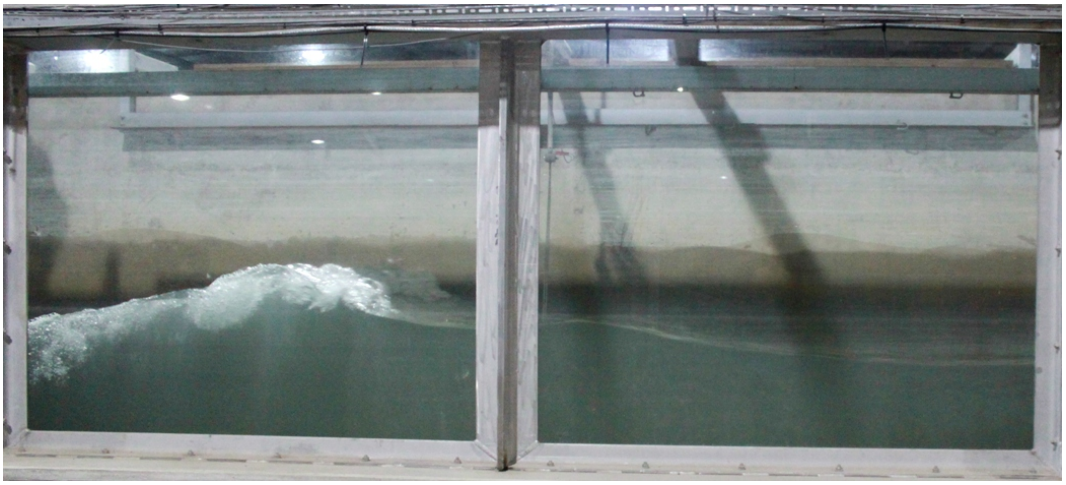

(a) Breaking wave

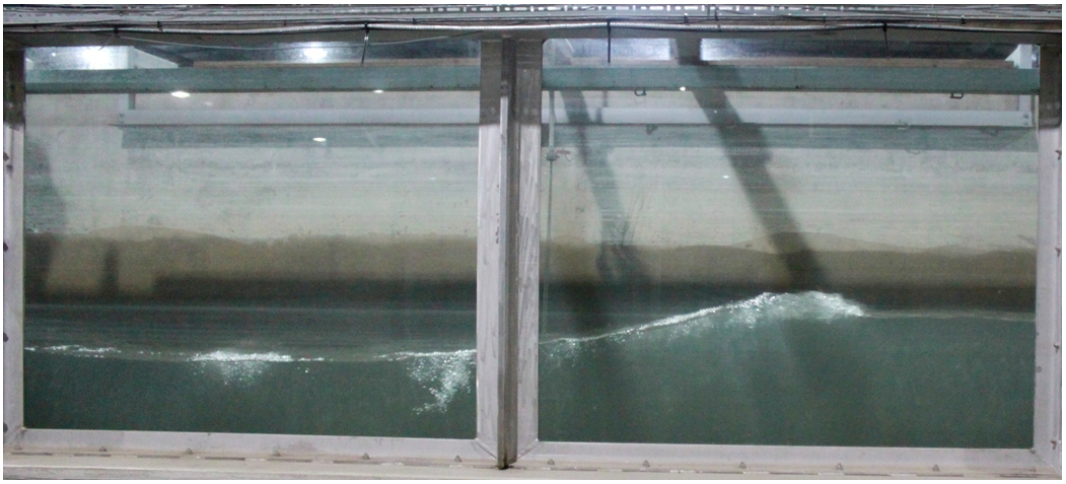

(b) Cessation of breaking of the same wave

Figure 3.3: Intermediate depth wave breaking: $d \approx 0.6\,\mathrm{m}$, $T_p \approx 2\,\mathrm{s}$, ${}^{d}/_{L_p} \approx 0.14$

$C_{bt}\sqrt{gh}$ the horizontal diffusion terms are applied, but the Boussinesq terms are not switched off; this will result in some energy loss associated with waves starting to break, without the loss of frequency dispersion. This is only applied in those locations where the limit is exceeded, and not all the way to the shoreline. Further inshore, at the wave where $H/h > C_{bh}$ all waves shoreward from this point are breaking; i.e. the horizontal diffusion is applied and the Boussinesq terms are switched off. Although there may be some logic behind this double breaking algorithm, it is not necessarily theoretically valid; nevertheless, it will be discussed further in Section 7.2.

3.3 Seawalls

The nonlinear shallow water equations and the Boussinesq-type equations used in the SWAB model were derived for mild bed slopes. However, in using the model, especially with overtopping modelling, one would expect to encounter steep slopes, vertical walls, and recurve walls with slopes beyond the vertical; Shiach et al. [2004] tested a model based on the nonlinear shallow water equations to simulate violent wave overtopping of vertical seawalls, with promising results. The model equations take account of the gravitational effects of a slope; that is, water will flow down a slope and reflection from a beach will occur due to wave rundown. However, the equations do not take account of the force imposed by a wall when a flow is directed perpendicularly towards it. If a jet of water impacts against a wall (Figure 3.4 a), the wall imposes a force in the opposite direction, reducing the x momentum to zero. Therefore:

$$F_{\text{wall}} = \rho A v_x^2 \tag{3.17}$$

where A is the cross-sectional area of the jet of water. In Figure 3.4 b, the wall re-directs the jet of water backwards at the same speed. Therefore:

$$F_{\text{wall}} = \rho A v_x^2 + \rho A v_x^2 = 2\rho A v_x^2 \tag{3.18}$$

When a wave impacts against a seawall the situation is not quite so simple. Firstly, the wall may not be as high as the depth of the flow, in which case it can only impose a force on a proportion of the depth. Also in this case, the flow is not uniform over the depth; therefore, a wall that only affects the bottom part of the flow will have a proportionally smaller effect than one that is higher. Secondly, a wall may absorb some of the flow, may partially reflect the flow and may allow some transmission. In addition, flow that has been affected by the seawall may interact with flow that has been unaffected, thus further complicating the situ-

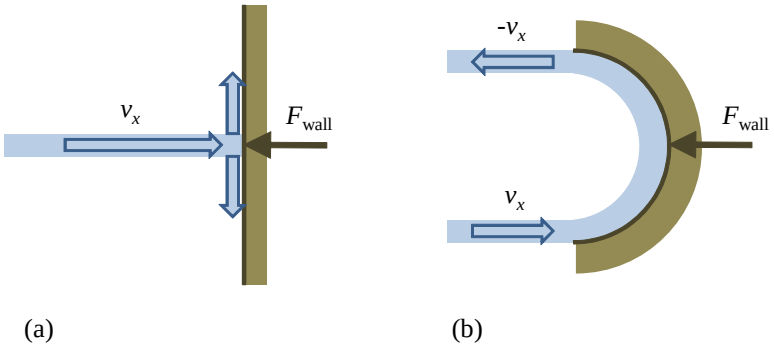

Figure 3.4: Forces imposed by a wall on a jet of water

ation, especially where a structure has a complex profile. Therefore, it may be that SWAB is not suitable for seawall modelling; nevertheless, a simple modification to equations (3.17) and (3.18) is proposed, with a force being proportional to $\rho A u^2$.

Figure 3.5 shows two adjacent cells in a SWAB 3.0 model, i and $i+1$. The SWAB momentum equation is in terms of force per unit bed area per unit density (i.e. $F/(\rho\, dy\, dx)$); in all following references to force and F_{wall}, it will be factored by $(\rho\, dy\, dx)^{-1}$. When the flow is directed towards the wall, the force is applied to cell i; the force must be applied to the bed area of the cell (i.e. dx; it is effectively applied as a shear stress). If the depth of the flow is less than the height of the wall (i.e. $h_i < dz$) then the representative height h_F is equal to h_i; otherwise it is equal to dz. Therefore:

$$F_{\text{wall},i} = \frac{k_{\text{wall}} h_{F,i} u_i^2}{dx} \tag{3.19}$$

where:

$$h_F = \min(h_i,\, dz) \tag{3.20}$$

and k_{wall} is an empirical constant; $k_{\text{wall}} = 1$ will be commonly used in the overtopping analysis. Note that u_i is used as the velocity; it was thought that u_i is more representative of the deeper flow below the wall than $u_{i+1/2}$ or u_{i+1}. When the flow is in the other direction F_{wall} is zero. A similar algorithm was also derived for cases where dz is negative. To specify where this wall force is calculated and applied in the model, a text file input is required specifying which cells are located adjacent to a wall, and what k_{wall} should be at each wall location. The effectiveness of this algorithm will be discussed in Chapters 6 and 8.

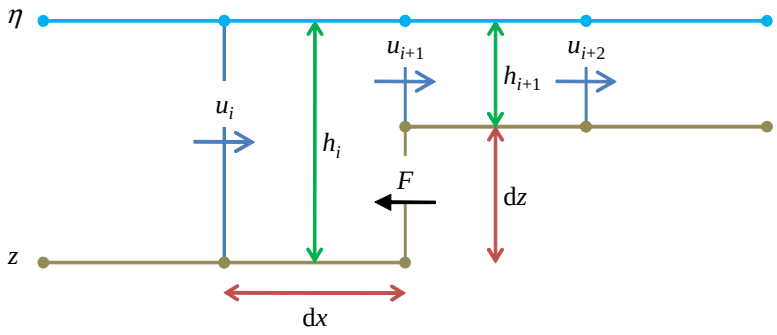

Figure 3.5: Wall force in the SWAB 3.0 model

3.4 Wave Input

The method of Larsen and Dancy [1983] is employed; its advantages are discussed in Section 2.5.3. Equation (2.79), repeated below, is used to calculate the change of free-surface level required to generate the necessary wave:

$$\Delta\eta = 2\eta^I c_g \frac{\Delta t}{\Delta x} \tag{3.21}$$

The wave group velocity is that corresponding to the Boussinesq equations of Madsen and Sorensen [1992], given by Lee et al. [2003] as:

$$c_{g,\text{Bous}} = c_{\text{Bous}} \left(1 - \frac{(kh)^2}{3(1+(B+1/3)(kh)^2)(1+B(kh)^2)}\right) \tag{3.22}$$

where the wave celerity, c_{Bous}, is:

$$c_{\text{Bous}} = \frac{L}{T} = \sqrt{gh\frac{1+B(kh)^2}{1+(B+1/3)(kh)^2}} \tag{3.23}$$

with $B = 1/15$ as the linear dispersion parameter. Unfortunately waves are usually specified in terms of wave period rather than wavelength, $L = 2\pi/k$. However, equation (3.23) can be rearranged to give a quadratic equation for L^2 in terms of h and T^2:

$$(L^2)^2 + \left((B+1/3)(2\pi h)^2 - ghT^2\right) L^2 - ghT^2 B(2\pi h)^2 = 0 \tag{3.24}$$

One root of this equation is always positive (for positive h and T) and the other is always negative; therefore there is always only one real and positive value for wavelength, L, which

is:

$$L = \frac{1}{\sqrt{2}}\sqrt{-\left(B+\frac{1}{3}\right)(2\pi h)^2 - gT^2 + \sqrt{\left(\left(B+\frac{1}{3}\right)(2\pi h)^2 - gT^2\right)^2 + 4ghT^2B\,(2\pi h)^2}} \tag{3.25}$$

From the wavelength, the wave celerity and group velocity can be calculated.

The SWAB 3.0 model has been set up to run a range of wave types; these are described in Table 3.1. Each wave input type is distinguished by a three-character code (e.g. "FS1", in the Option Code column); this must be included in the SWAB code input file, as it specifies what other parameters are required (the Required Wave Parameters column) and how the waves are calculated (the Calculation Information column). The first letter of this code (i.e. "F", "A" or "N") states what type of wave input is being specified: "F" requires waves from an input file; "A" gives automatically generated waves, requiring input wave parameters such as wave height or wave period; and "N" refers to the generation of a NewWave focussed group, described in Section 2.2.4. For example, using Table 3.1 on the following page, if the "FS1" wave type is specified, an input file is required with component frequencies, amplitudes and phases, which is used to calculate the waves and the length of the model run. In addition to the wave type parameter, a still water level must be specified for all wave conditions, and the number of time-steps per wave must be specified for most wave types. To calculate the displacement at the wave input location, the SWAB model must calculate $c_{g,\text{Bous}}$ for each component at the beginning of a each time-step; however, $\eta^I(t)$ for each component is calculated at the start of the model run. This method for calculating wave input can become time consuming, especially with many waves and many spectral components. Therefore, a maximum cut-off frequency can also be specified; this is effective in reducing run times.

The original versions of the SWAB 2 code, which will be called SWAB 2.0, used a simple spectral wave input; one value of c_g was calculated using linear wave theory at the beginning of the model run, based on the still water level at the input location. The wave input was not separated into its spectral components; instead equation (3.21) was applied once to the entire input time-series. Most references to SWAB 2 runs will refer to SWAB 2.0. Later versions of SWAB 2 (SWAB 2.1) incorporated the Boussinesq wave celerity (equations (3.23) and (3.22)), followed by the separate input celerities for each spectral component (SWAB 2.2). The SWAB 2.2 spectral wave input method is the same as that used by the SWAB 3 model.

Waves should be input onto a horizontal bed. Therefore, at least five spatial steps of horizontal bed should be specified either side of the wave input location; in fact, the bed should be horizontal all the way to the offshore boundary.

Table 3.1: Description of Wave Input Types

Option Code	Description of Wave Type	Required Wave Parameters	Calculation Information
FS1 FS2 FS3	Wave spectrum from file	• Component frequencies • Component amplitudes (FS1, FS2) or spectral energy density (FS3) • Component phases (FS1)	• Length of run is determined by minimum component frequency (FS1, FS2) • Model frequency step is determined from specified number of waves, with a linear interpolation used to find spectral energy at these frequencies (FS3) • Calculates component amplitudes using equation (2.31) (FS3) • Calculates $c_{g,\text{Bous}}$ for each component frequency • Uses random seeding routine to calculate random phase for each component (FS2, FS3)

Option Code	Description of Wave Type	Required Wave Parameters	Calculation Information
FW1 FWG FB1 FBG	One wave from file (FW1, FB1) Group of waves from file (FWG, FBG)	• Time • Water level time-series	• Fourier transfrom of water levels to calculate component frequencies, amplitudes and phases • Calculates $c_{g,\text{Bous}}$ for each component frequency (FW1, FWG) (note, this may not be correct as some components may be bound) • Calculates $c_{g,\text{Bous}}$ for main component frequency (FB1, FBG) (note, this does not take account of free components of different frequency) • Number of waves (FW1, FB1) or wave groups (FWG, FBG) must be specified
FWT FWE	Wave train from file (FWT) Larsen and Dancy [1983] wave input from file (FWE)	• Time • Water level time-series (FWT) • Wave input displacement time-series (FWE)	• Fourier transfrom of water levels to calculate component frequencies, amplitudes and phases (FWT) • Calculates $c_{g,\text{Bous}}$ for each component frequency (FWT) • Time-series directly input to model (FWE)

Option Code	Description of Wave Type	Required Wave Parameters	Calculation Information
A1O A2O	Linear (Airy) wave theory (A1O) Stokes 2nd order wave theory (A2O)	• Amplitude (of main component - A2O) • Frequency (of main component - A2O)	• Calculates $c_{g,\text{Bous}}$ for input frequency (for both input frequences - A2O) • Number of waves must be specified
ABI	Bichromatic waves	• Amplitude • Mean frequency • Frequency difference	• Calculates $c_{g,\text{Bous}}$ for both input frequencies • Number of waves must be specified
ASP	Generated wave spectrum, with random phases	• Wave height parameter • Wave height • Frequency parameter • Frequency • Spectral shape • Spectral shape variables	• Run time or number of waves must be specified, to calculate minimum component frequency • Component amplitudes are calculated from specified wave height and spectral shape • Calculates $c_{g,\text{Bous}}$ for each component frequency • Uses random seeding routine to calculate random phase for each component

Option Code	Description of Wave Type	Required Wave Parameters	Calculation Information
NWF	NewWave group, with spectrum from file	• Frequencies • Corresponding spectral shape from file • Number of spectral components • Either maximum amplitude, or number of waves represented by group • Focal point • Focal time	• If representative number of waves is specified, calculates maximum expected amplitude • Calculates component amplitudes from equation (2.47) • Calculates $c_{g,\text{Bous}}$ for each component frequency • Calculates component phases to focus at specified time and location
NWS	NewWave group, with generated wave spectrum	• Wave height parameter • Wave height • Frequency parameter • Frequency • Spectral shape • Spectral shape variables • Focal point • Focal time	• Calculates spectral shape from peak frequency and other input variables • If representative number of waves is specified, calculates maximum expected amplitude • Calculates component amplitudes from equation (2.47) • Calculates $c_{g,\text{Bous}}$ for each component frequency • Calculates component phases to focus at specified time and location

Option Code	Description of Wave Type	Required Wave Parameters	Calculation Information
000	No waves	• Run time	• Runs model without input waves for specified time

3.4.1 Variable water level

The SWAB 3 code has incorporated the facility to vary the still water level during a model run, for the modelling of tides. An extra input file is required for the specifiation of the still water level at certain times within the run. The SWAB code then linearly interpolates between these specified levels. At the beginning of each time-step water levels throughout the domain (except in the "dry" region, and landward of any seawall) are adjusted by the required amount. As the water level changes the wave input method, which requires calculation of $c_{g,Bous}$ (Section 3.4), remains valid as it uses the water level at the current time-step to perform these calculations. No modification to velocity or flux is included; this should be acceptable because the modification to the level at each time-step is very small. The SWAB model has no facility to include tidal currents. Also, it does not allow any modification to wave conditions within a model run.

3.5 Sponge Layer

With the Larsen and Dancy [1983] wave input, a sponge layer can be used at the seaward boundary. In the sponge layer, at the end of each time-step, the resulting excursion, η, flux, hu, and velocity, u, are all multiplied by a damping factor, ν^*. By doing this, all the outgoing wave energy is absorbed in this zone and no wave reflection occurs at the boundary. The performance of the sponge layer derived by Larsen and Dancy [1983] is dependent on the model grid resolution; Yoon and Choi [2001] have therefore improved upon this derivation. The damping factor, ν^*, is given by Yoon and Choi [2001] as:

$$\nu^* = \exp\left(-\left(b^{-x^*/\Delta x} - b^{-x_s/\Delta x}\right)\ln\Lambda\right) \tag{3.26}$$

where x^* is the position inside the sponge layer ($x^* = 0$ at the boundary), x_s is the width of the sponge layer, Λ is a damping factor (kept as $\Lambda = 2$) and b is given as:

$$b = 1 + r_s + \exp\left(\frac{-1}{r_s}\right) \tag{3.27}$$

where:

$$r_s = \frac{10}{i_s} \tag{3.28}$$

with i_s being the number of points inside the sponge layer.

Yoon and Choi [2001] recommend that the width of the sponge layer be equal to one wavelength. In the SWAB model, the size of the sponge layer is automatically set to be equal to one wavelength at the still water depth, based on the peak frequency. This requires, in the bathymetry input file, specification of a horizontal bed long enough to contain the sponge layer. Also, the wave input location should be far enough from the seaward boundary to not overlap the sponge layer (this would result in a dampened wave input).

3.6 Shoreline Boundary

A similar shoreline boundary to that described by Stansby [2003] is used here. The bed is impermeable (unlike the "slot" technique (Section 2.5.3)) and the "dry" part of the domain is actually covered by a very small depth of water, $h_{\min}$. Strictly speaking, the entire domain is "wet", enabling any number of shorelines to exist. In the "dry" part of the domain the pressure head and velocity is set to zero. However a "dry" cell will fill if it is adjacent to a "wet" cell and there is inward flux across the boundary.

At the shoreline, the first two terms on the right hand side of equation (3.2) are important; they represent hydrostatic pressure. In Figure 3.6, in both cases cell $i-1$ is "wet" and cell i is "dry". However, in Figure 3.6 (a), the free surface level in the wet cell is lower than that in the dry cell; it is therefore assumed that there is no pressure differential at the cell boundary. In Figure 3.6 (b), the wet cell has a higher free surface level; therefore, it imposes pressure on the dry cell. If this rule were not imposed, the water in the "dry" part of the domain would start to slide down a sloping bed.

3.7 Model Output

It is possible to select a range of variables for output from the SWAB model. The possible outputs are given in Table 3.2. Note that two additional variables can be output, for sediment

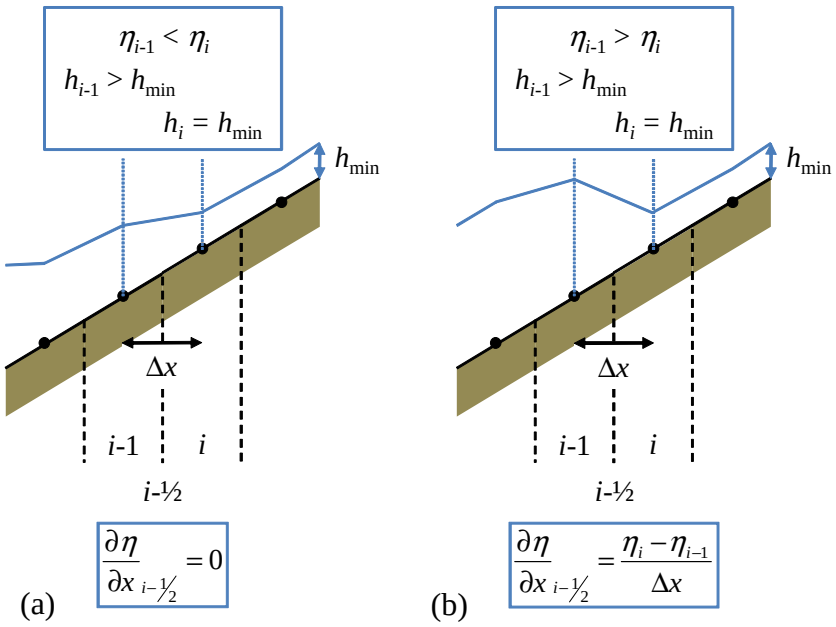

Figure 3.6: Pressure at the shoreline boundary

transport rate and change in bed level. However, the sediment transport module has not been tested and is out of the scope of this thesis. For many variables, there are two options for writing to the output file: either values for the entire domain can be written at set times, or values for selected locations can be written throughout the model run (for this case the the number of time-steps between outputs can also be specified). Other variables such as swash level are functions of time only, and therefore this option is not available. Output files are ASCII text files; most post-processing of results was done using MATLAB.

3.8 SWAB Model Range

In this section, a range of tests are presented to demonstrate the range of validity of the SWAB model. For these tests the model domain shown in Figure 3.7 is used; the domain is ten wavelengths long with a sponge layer of one wavelength at each end. The bed is horizontal throughout. For most tests, the domain consisted of 2000 spatial steps; 1000 steps was also tested. Breaking is not being investigated here; therefore, breaking is switched off (i.e. there is no trigger to set the Boussinesq terms to zero or to calculate horizontal diffusion). Time-series outputs of free surface level were at half wavelengths across the domain. Also for each test, twenty outputs of free surface level over the entire domain were taken 1.1 wave periods apart, giving an envelope of water levels across the domain. Three types of wave input were tested: a simple Airy wave input; a regular wave input with waves calculated using the method of

Table 3.2: SWAB output variables

Variable Code	Variable Description	Output Type	Notes
E	$\eta(x,t)$: free surface level	Set times Set locations	
E0	$\eta(x,t)$, at end of previous time-step	Set times	Required when using a run to provide initial conditions for a subsequent run
EAV	Mean value of $\eta(x,t)$ over time	Set times Set locations	
U	$u(x,t)$: depth averaged velocity	Set times Set locations	
H	$h(x,t)$: water depth	Set times Set locations	
HU	$hu(x,t)$: flux	Set times Set locations	
ADV	Advection term	Set times Set locations	
DIF	Horizontal diffusion term	Set times Set locations	
BOU	Boussinesq terms, see equation (3.2)	Set times Set locations	
DHU	$\frac{\partial hu}{\partial t}$: rate of change of momentum	Set times Set locations	
DEX	$\frac{\partial \eta}{\partial x}$	Set times Set locations	
BRK	Breaking flag: 0, 1, 2 or 3, respectively for not breaking, offshore breaking, shallow water breaking, or both	Set times Set locations	Unless double breaking is used (Section 3.2.2), value will either be 0 or 3
BED	$z_b(x,t)$: bed level	Set times Set locations	No sediment transport has been modelled. Therefore $z_b(x,t) = z_b(x,0)$.
BREAK	$x_{break}(t)$, $i_{break}(t)$: location of break point	Output as function of time	
SWASH	$\eta_{swash}(t)$: free surface level at shoreline	Output as function of time	
EIN	$\Delta\eta(t)$: input change in water level, see equation (3.21)	Output as function of time	
TRAIN	$\eta^I(t)$: input wave train, see equation (3.21)	Output as function of time	
SF	$S(f)$: input wave energy spectrum	Output as function of frequency	
AF	$a(f)$, $\phi(f)$: input wave amplitude spectrum, with component phases	Output as function of frequency	
FORCE	$F_{wall}(t)$: wall force, see Section 3.3	Output as function of time	One column of output for each cell where F_{wall} is calculated
VOLUME	$V(t)$: volume overtopping the seawall	Output as function of time	$V^n = V^{n-1} + hu^n_{itop}.dt$, where hu_{itop} is flux at seawall crest

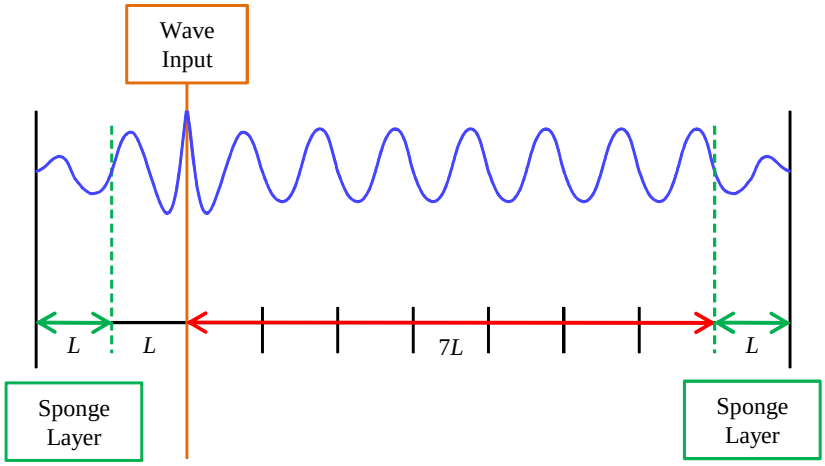

Figure 3.7: Model range test domain

Rienecker and Fenton [1981]; and a random wave input with a JONSWAP spectrum. The code used to calculate the Rienecker and Fenton [1981] method is called "SAWW.FOR"; therefore these waves will be referred to as SAWW waves. Note that the accuracy of the SAWW waves is dependent on the number of Fourier components used in the calculations; with a suitable number of components the calculated solution should be very close to the exact solution for a real fluid.

3.8.1 Regular wave tests

The wave input will prevent a uniform output if there are parasitic free waves; that is, if the input wave is not of the correct form. For example, if the input wave is sinusoidal:

$$\zeta_{\text{in}} = a\cos(kx - \omega t) \tag{3.29}$$

and the output wave has a second-order bound wave, there will be a corresponding parasitic free wave:

$$\zeta_{\text{out}} = a_1\cos(kx - \omega t) + a_{2b}\cos(2kx - 2\omega t) + a_{2f}\cos(k_2 x - 2\omega t) \tag{3.30}$$

where a_{2b} is the amplitude of the bound component, and a_{2f} is the aplitude of the parasitic free component. If we take the wave input location as $x = 0$ and $\zeta_{\text{out}} = \zeta_{\text{in}}$ at this location,

then $a_{2f} = -a_{2b}$. Manipulation of equation (3.30) gives:

$$\zeta_{\text{out}} = a_1 \cos(kx - \omega t) - 2a_{2b} \sin\left(\frac{2kx - k_2 x}{2}\right) \sin\left(\frac{2kx + k_2 x}{2} - 2\omega t\right) \tag{3.31}$$

giving a second order wave, which travels through the domain, but with a fluctuating amplitude as it propagates. Note that in most cases, the output waves will contain higher order components, so the resultant waves will not have a form as simple as that of equation (3.31); nevertheless the fluctuating amplitude of the higher-order components across the domain will remain true.

The Airy waves were input using wave input type "A1O" (see Table 3.1). The SAWW waves could be input using either input type "FB1", where the group velocity of the first order component is applied to all components, or "FG1", where a group velocity is calculated for each frequency component. For Figures 3.8 and 3.9 the wave dispersion (or water depth) parameter, kd, is 0.2, with nonlinearity (H/d) increasing from bottom to top of each figure. Figure 3.8 shows water levels across the domain at several time-steps, with the Airy wave input. It is apparent that even for $H/d = 0.01$, the presence of parasitic free waves causes a slight increase in crest and trough levels towards the right edge of the domain. With increasing H/d the uniform waveform differs even further from the linear form, leading to increased fluctuations across the domain. In Figure 3.9, the "FG1" type SAWW wave input was used instead. A waveform calculated by SAWW should be very close to that found in a real fluid; therefore the parasitic free waves are considerably reduced. However, the equations used by the SWAB model are an approximation of real fluid motion; therefore as H/d increases up to 0.5, the parasitic free waves return. For the "FB1" type wave input, the parasitic free waves were found to be larger than for the "FG1" method; therefore it will not be considered for subsequent tests.

When the wave input is in deeper water, the Ursell number drops significantly (being inversely proportional to $(kd)^2$). Therefore, Airy waves become suitable for higher values of H/d (see Hedges [1995], for example, on the range of validity of analytical wave theories). Figure 3.10 shows, that for $kd = 0.5$, the size of the parasitic free waves is fairly small as long as $H/d < 0.1$. Although the linear properties of Madsen and Sorensen [1992] are quite suitable for such water depths, Madsen and Sorensen [1993] showed that the amplitudes of nonlinear components are underestimated; therefore in deeper water the SWAB model effectively becomes more linear. Figure 3.11 shows that when H/d is increased above 0.05, the SAWW waves become too nonlinear for the SWAB model resulting in large fluctuations across the domain; therefore, for more nonlinear waves in transitional water depths, the Airy wave input

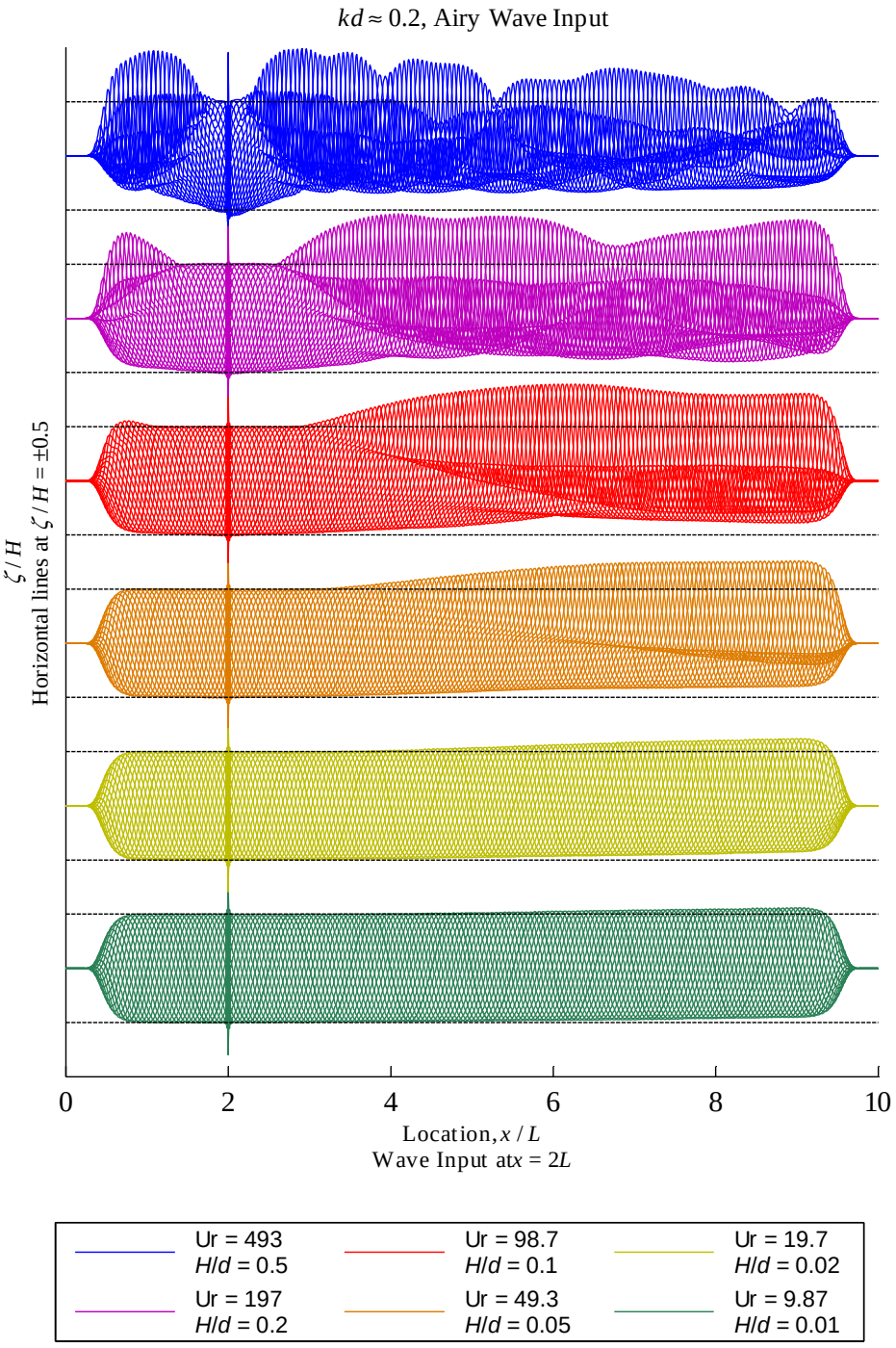

Figure 3.8: Free surface level outputs with varying H/d: Airy wave input, $kd = 0.2$

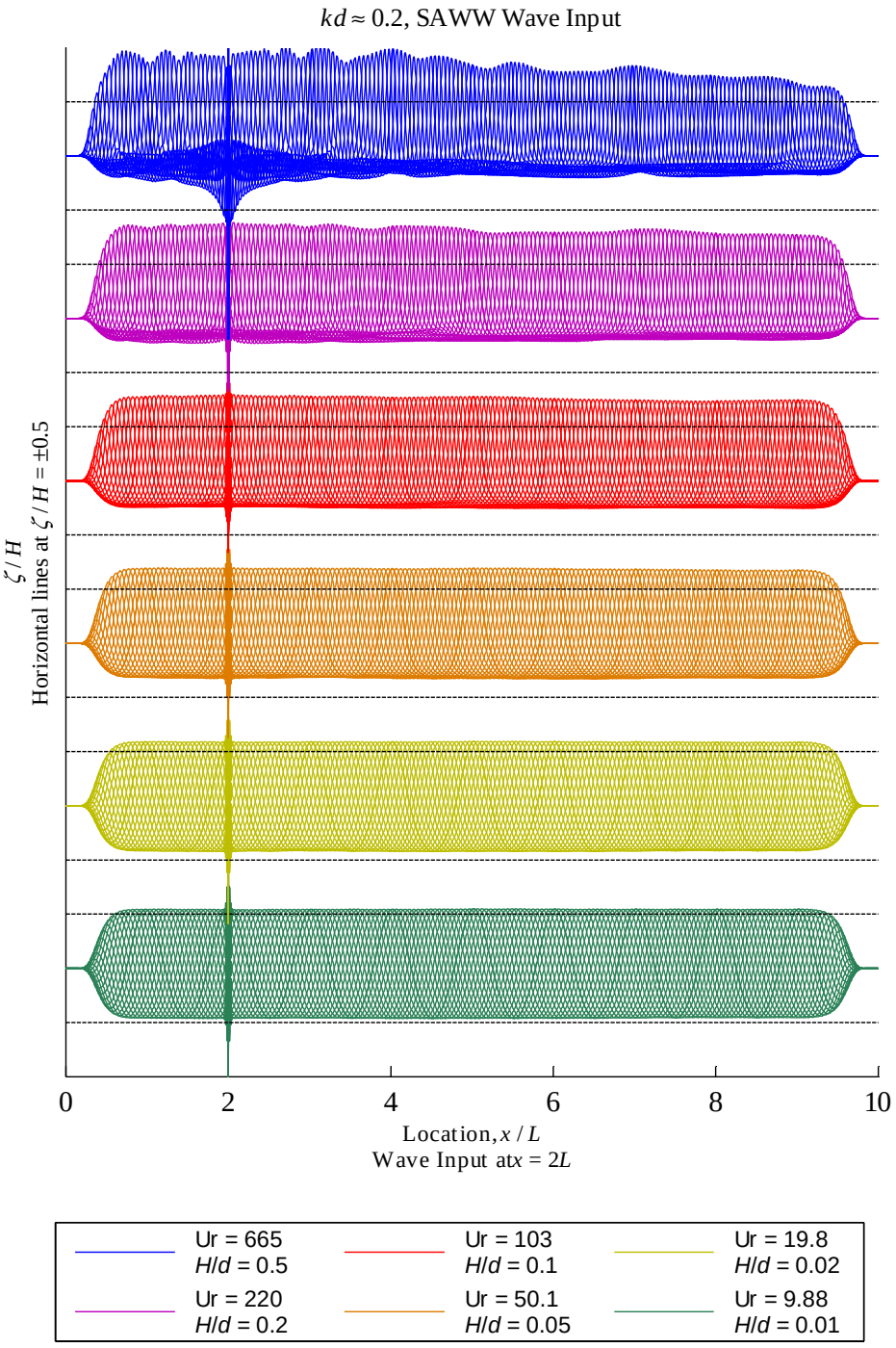

Figure 3.9: Free surface level outputs with varying H/d: SAWW wave input, $kd \approx 0.2$

is more appropriate for the SWAB model.

When kd is even larger, a damping effect starts to occur. This was noticed by Madsen et al. [1991], who stated that in deeper water the Boussinesq effect becomes a balance between relatively large terms, leading to a significant loss of wave energy if the time-step is too large. Figure 3.12 shows outputs for $kd = 5.00$; over only six wavelengths the wave amplitude declines to little more than half the input amplitude. Figure 3.13 summarises the effect of increasing kd on wave heights; with 500 time-steps per period, the SWAB model should not be used to model large distances with $kd > 1$. As Figure 3.14 shows, by reducing the time-step, good wave heights can be achieved even when kd is as high as 2. However, this does increase the model running time. These model runs used a domain consisting of 2000 spatial steps. To test the influence of spatial step size on this loss in wave height, the same domain was tested with half the number of spatial steps (i.e. dx/L is doubled). Figure 3.15 is virtually identical to Figure 3.13; therefore this damping is almost entirely due to the time-step being too large. Note that according to Madsen and Sorensen [1992], the equations used by SWAB are suitable for h/L_0 of up to 0.5; this equates to local values of kd of over 3.

3.8.2 Random waves

With random waves, most components will be free waves. Some interactions between components will occur, which will increase with nonlinearity; this will be demonstrated here, but a full analysis is out of the scope of this research. Madsen and Sorensen [1993] studied the nonlinear properties of the equations used in the SWAB model, comparing the amplitudes of bound subharmonics and superharmonics with theoretical values, showing that their Boussinesq equations generally underestimate the amplitude of these superharmonics. When analysing spectral waves, there is obviously no single wave height, period or wavelength; in general wave heights refer to the spectral significant wave height, H_{m0} (equation (2.34)) and periods, wavelengths and wave numbers are those corresponding to the peak frequency, f_p. There is also a spectral mean wave period, T_{m02} (see equation (2.35)), which is used here, firstly as the basis for determining the time-step (i.e. dt as a fraction of T_{m02}), and secondly for the analysis of damping across the spectrum. Note that the spatial step, dx, is expressed here as a fraction of L_p, i.e. the wavelength corresponding to the peak frequency.

With free wave components, it should be pointed out that even when the peak wave frequency has a corresponding value of kd within the limits of the equations' suitability, this may not be true for higher frequency components. Firstly, there will be damping due to the time-step being too large, and secondly, the linear dispersion properties of these components may become quite inaccurate. Lee et al. [2003] showed that when $kd = 2$, the wave celerity will

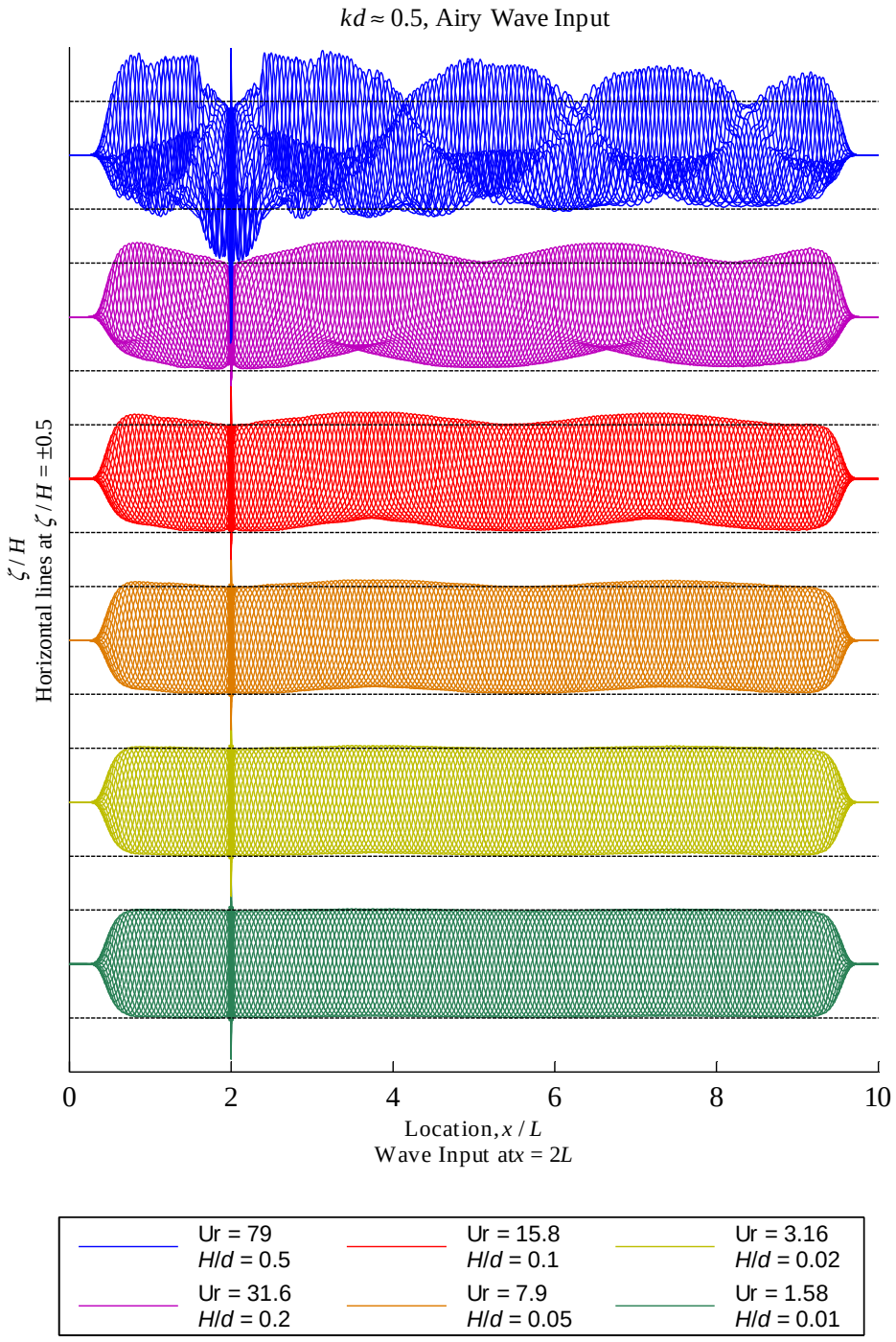

Figure 3.10: Free surface level outputs with varying H/d: Airy wave input, $kd = 0.5$

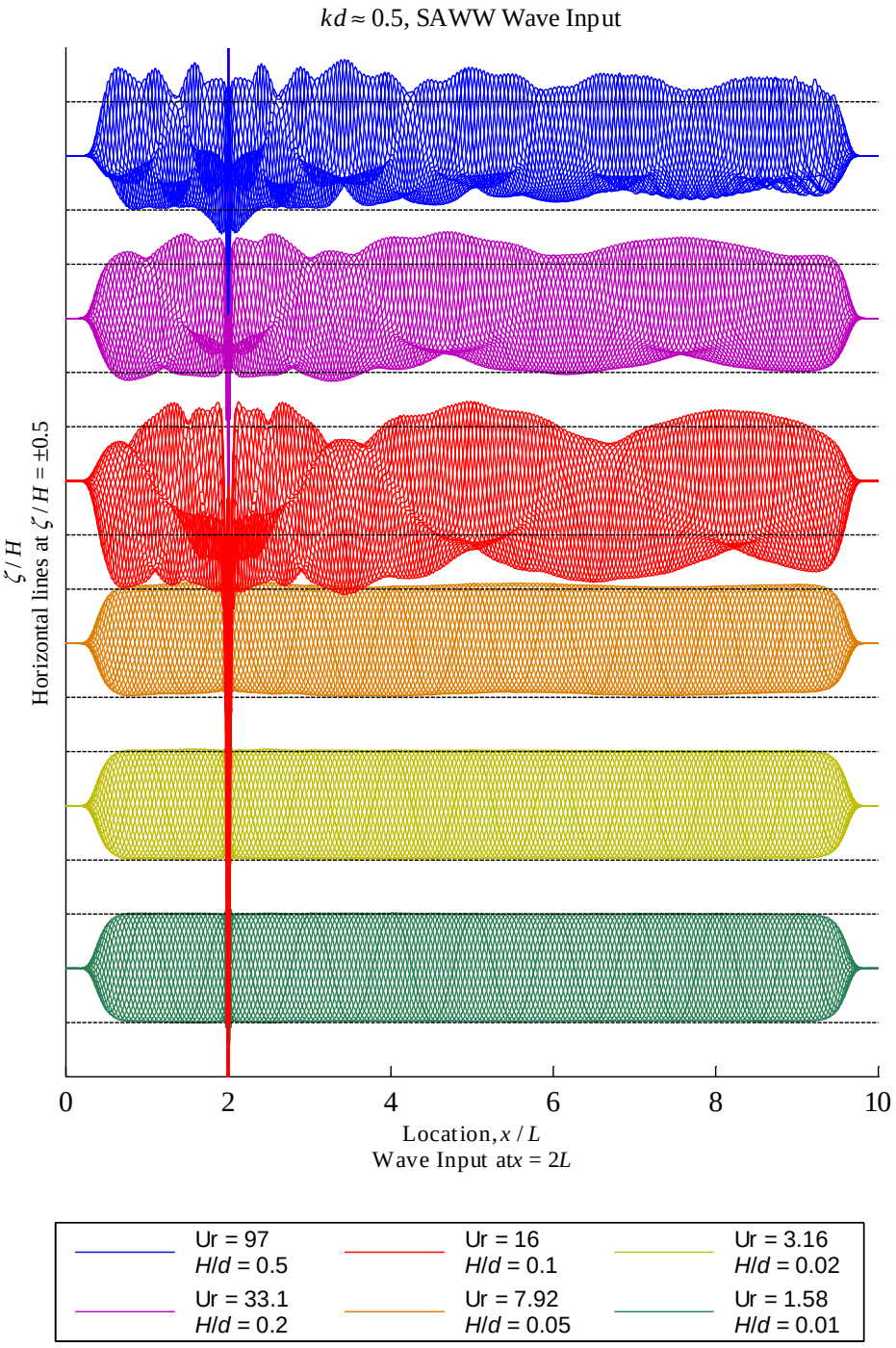

Figure 3.11: Free surface level outputs with varying H/d: SAWW wave input, $kd \approx 0.5$

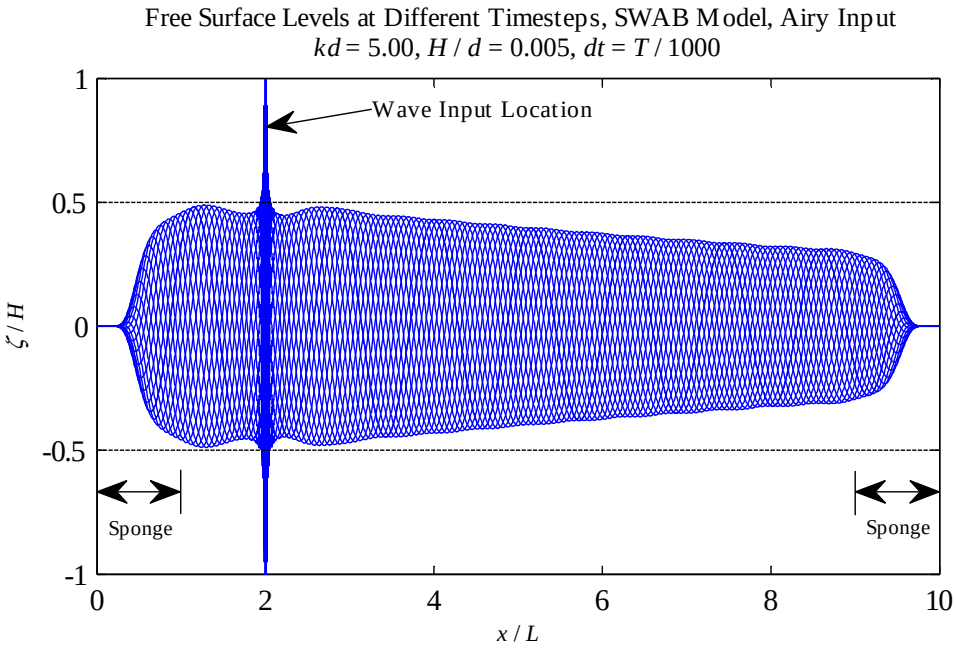

Figure 3.12: Water levels across the domain - deeper water ($kd = 5.0$)

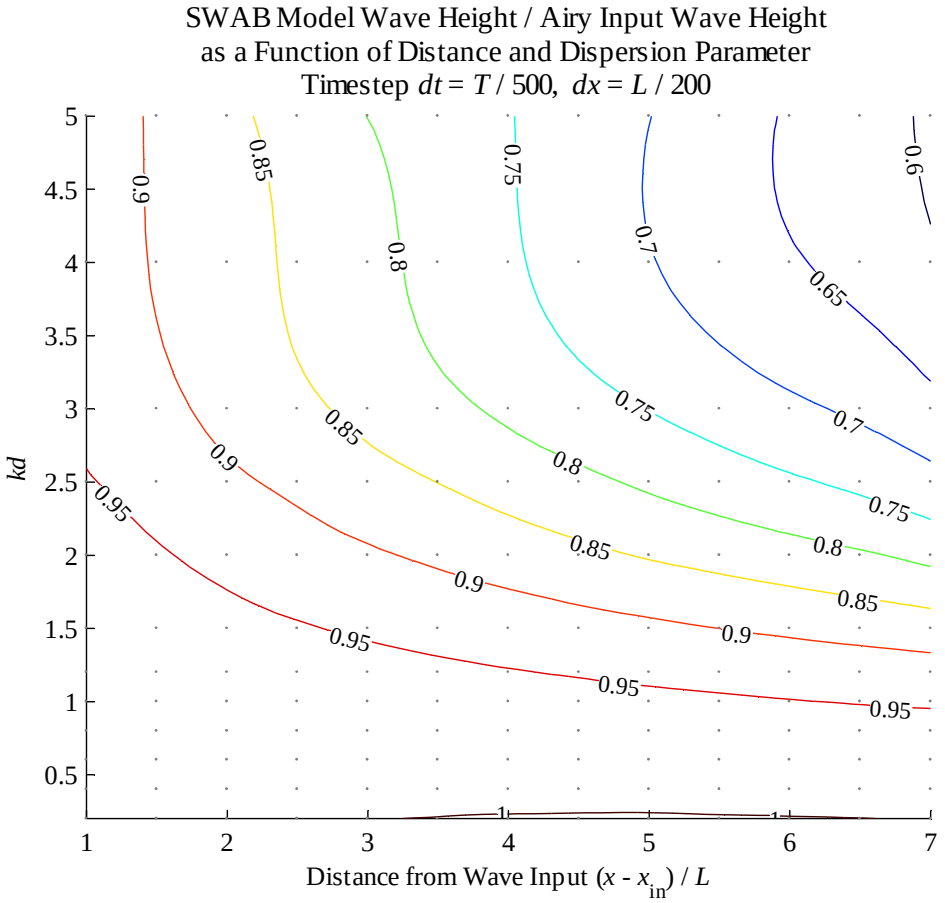

Figure 3.13: Contours of H/H_{in} as a function of distance from wave input and dispersion parameter, kd; Airy wave input, $H/d = 0.005$, $HL^2/d^3 < 5$, with $dt = T/500$. Grey dots indicate SWAB model run outputs

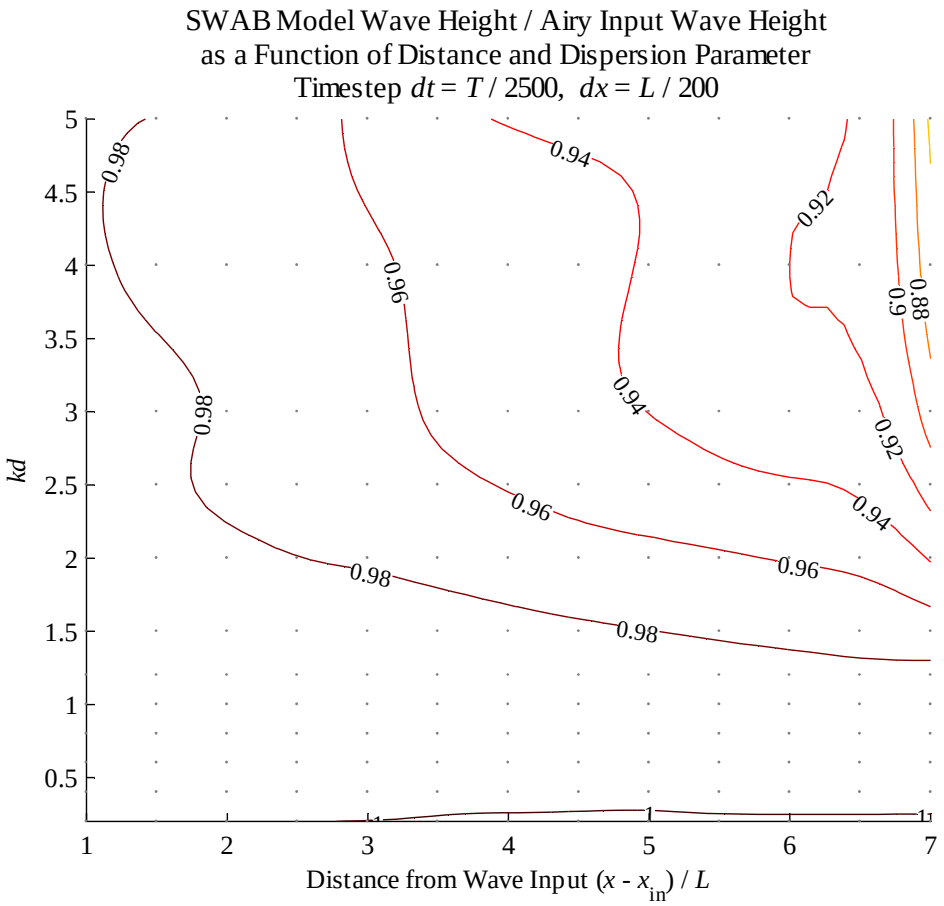

Figure 3.14: Contours of H/H_{in} as a function of distance from wave input and dispersion parameter, kd; Airy wave input, $H/d = 0.005$, $HL^2/d^3 < 5$, with a reduced time-step ($dt = T/2500$). Grey dots indicate SWAB model run outputs

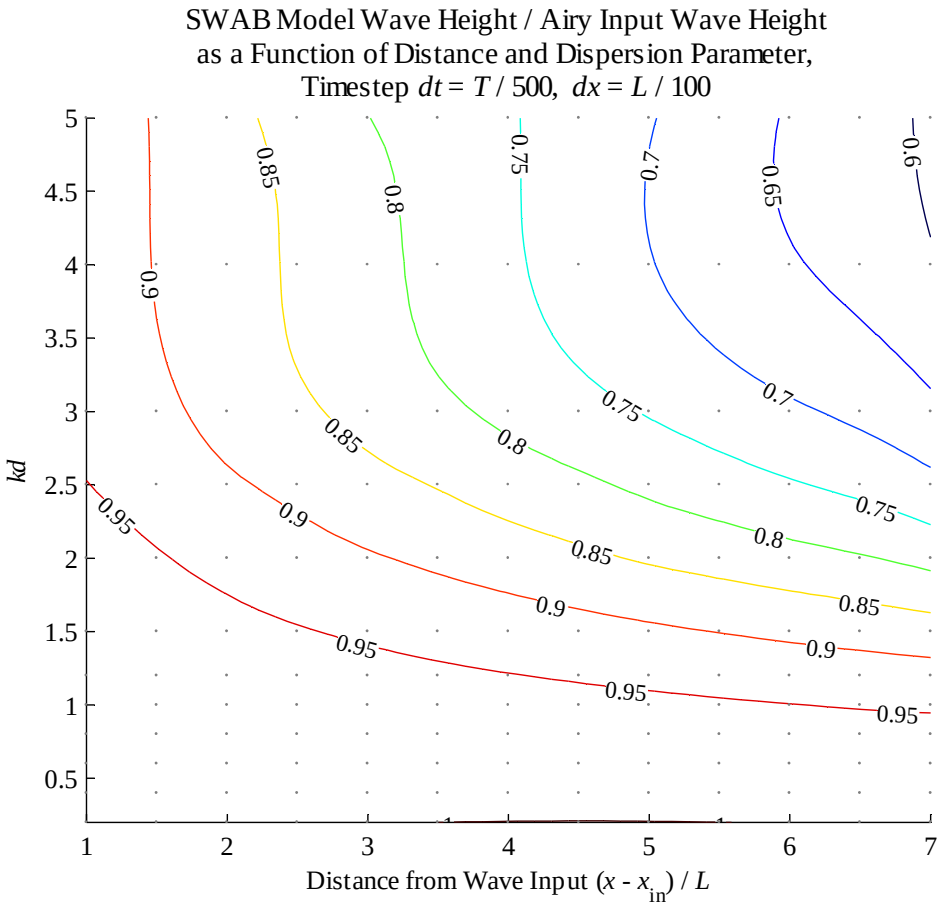

Figure 3.15: Contours of H/H_{in} as a function of distance from wave input and dispersion parameter, kd; Airy wave input, $H/d = 0.005$, $HL^2/d^3 < 5$, $dt = T/500$, with an increased spatial step ($dx = L/100$). Grey dots indicate SWAB model run outputs

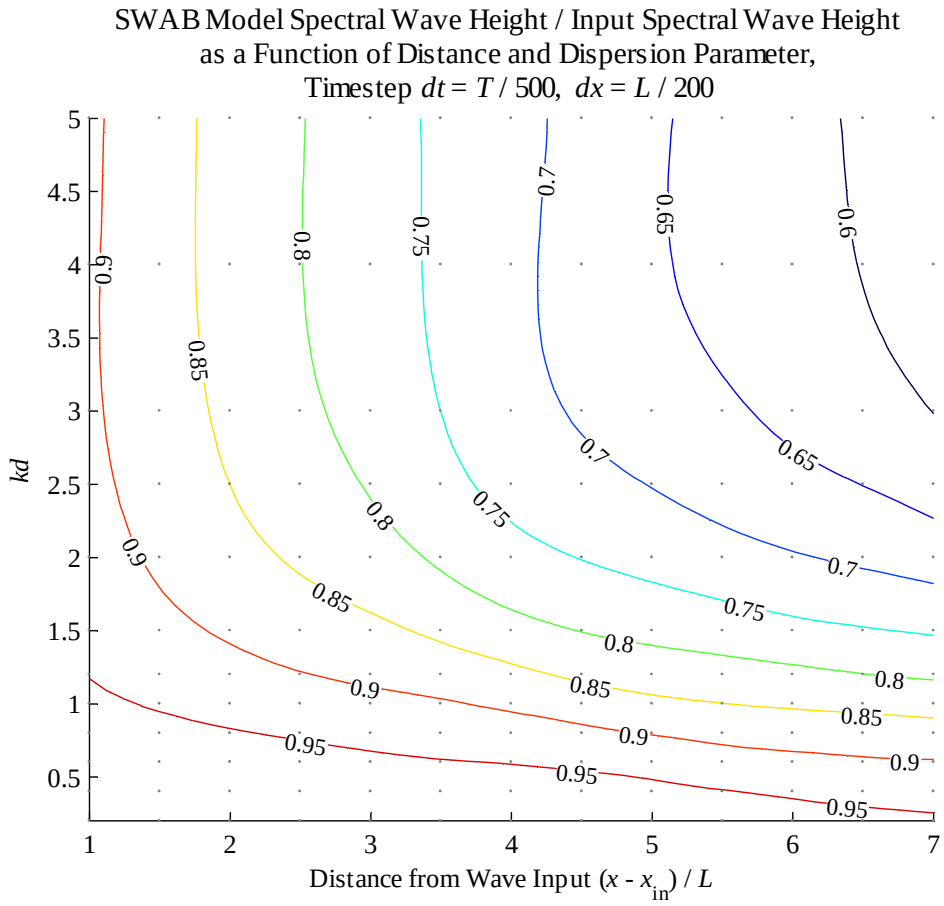

Figure 3.16: Contours of $H_{m0}/H_{m0,\text{in}}$ as a function of distance from wave input and dispersion parameter, kd, where k is based on the peak frequency; JONSWAP wave input, $H_{m0,\text{in}}/d = 0.005$, with $dt = T_{m02,\text{in}}/500$

be overestimated by 20 %; this will lead to component phases becoming incorrect. Figure 3.16 shows that the damping effect is slightly more severe than that for the regular wave tests. The spectral mean wave period, T_{m02}, is a useful parameter to demonstrate changes to the wave spectrum. Because of its dependence on f^2, a relatively greater loss of energy at higher frequencies will result in an increase in the value of T_{m02}. This can be seen in Figure 3.17, where a peak kd of 1.5 results in a 20 % increase in T_{m02} across the domain.

As with regular waves, decreasing the time-step has a considerable effect on reducing the damping. Figures 3.18 and 3.19 show that this greatly improves the range of conditions at which the SWAB model becomes useful. Note that there are actually some reductions in mean wave period in Figure 3.19; this may be due to nonlinear transfers of energy to harmonic frequencies.

The effect of nonlinearity on wave conditions in the SWAB model is harder to quantify. If H_{m0}/d is 0.1, as the waves travel across the domain some of the free wave energy is transferred to bound wave components. Figure 3.20 shows how energy at the peak frequency is

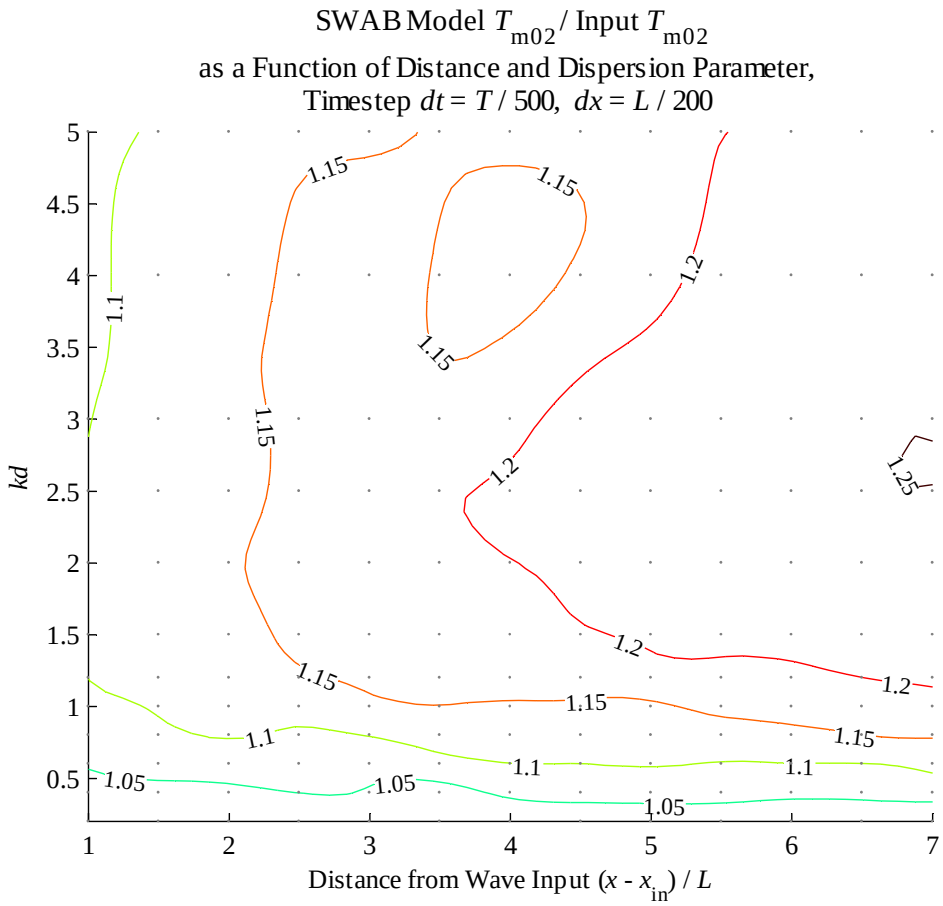

Figure 3.17: Contours of $T_{m02}/T_{m02,\text{in}}$ as a function of distance from wave input and dispersion parameter, kd, where k is based on the peak frequency; JONSWAP wave input, $H_{m0,\text{in}}/d = 0.005$, with $dt = T_{m02,\text{in}}/500$

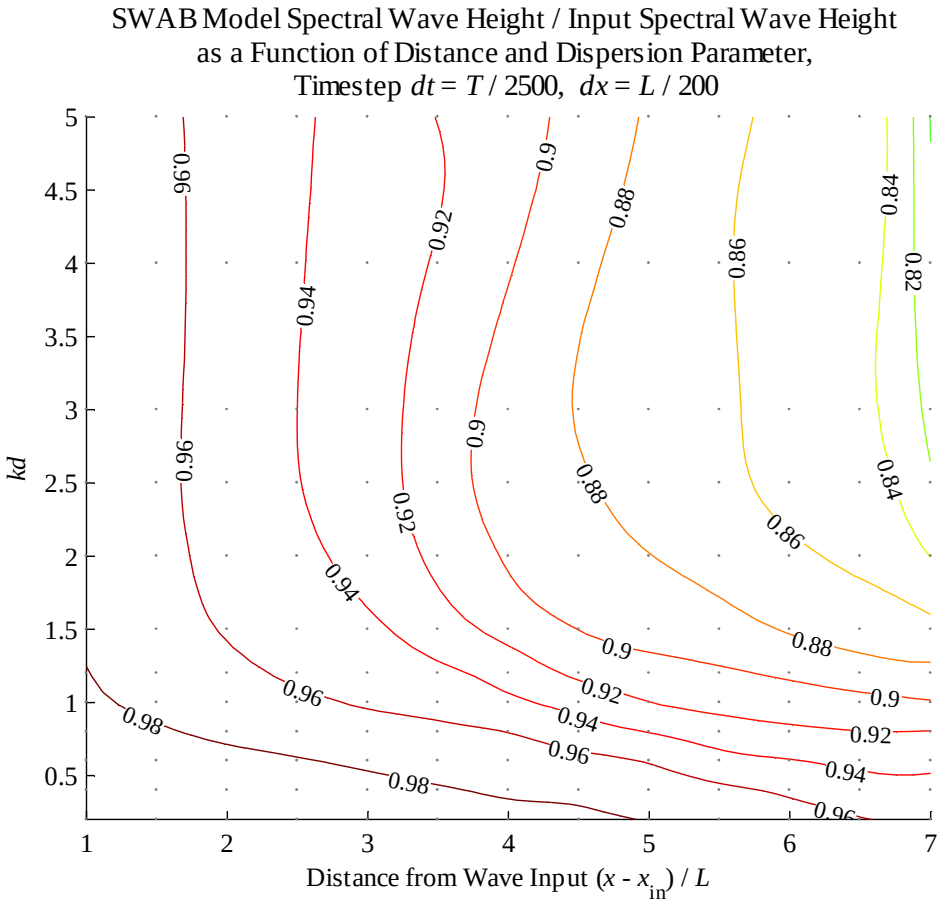

Figure 3.18: Contours of $H_{m0}/H_{m0,\text{in}}$ as a function of distance from wave input and dispersion parameter, kd, where k is based on the peak frequency; JONSWAP wave input, $H_{m0,\text{in}}/d = 0.005$, with $dt = T_{m02,\text{in}}/2500$

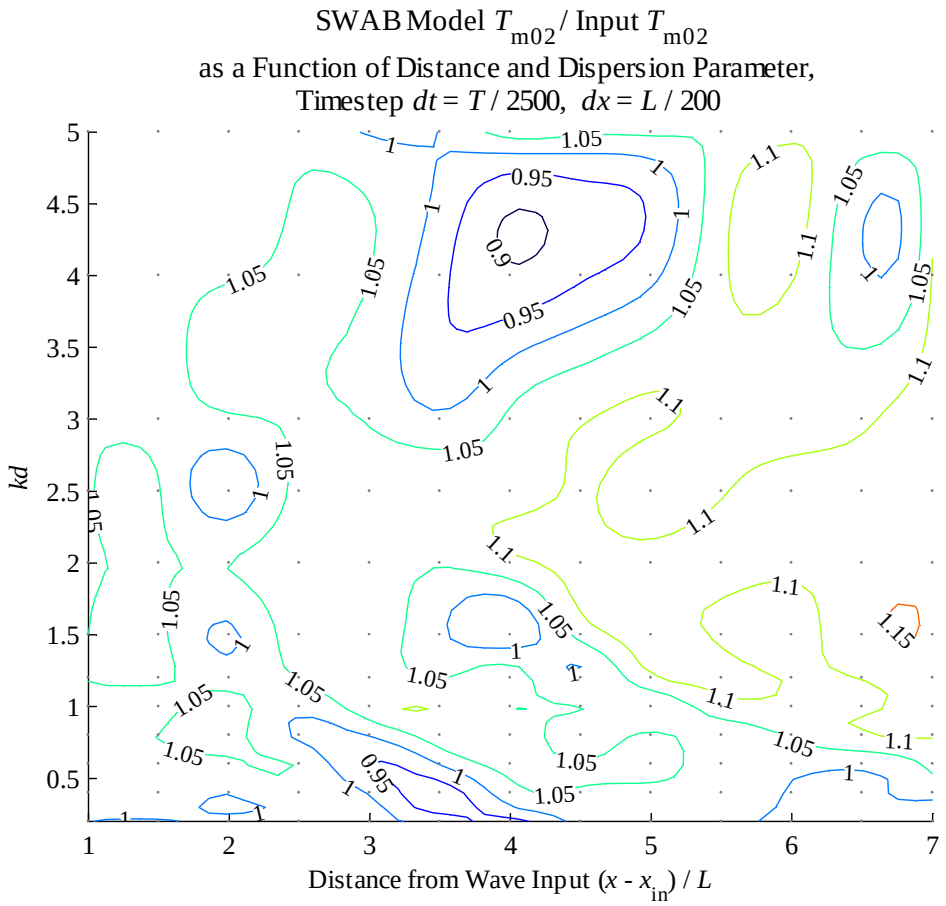

Figure 3.19: Contours of $T_{m02}/T_{m02,\text{in}}$ as a function of distance from wave input and dispersion parameter, kd, where k is based on the peak frequency; JONSWAP wave input, $H_{m0,\text{in}}/d = 0.005$, with $dt = T_{m02,\text{in}}/2500$

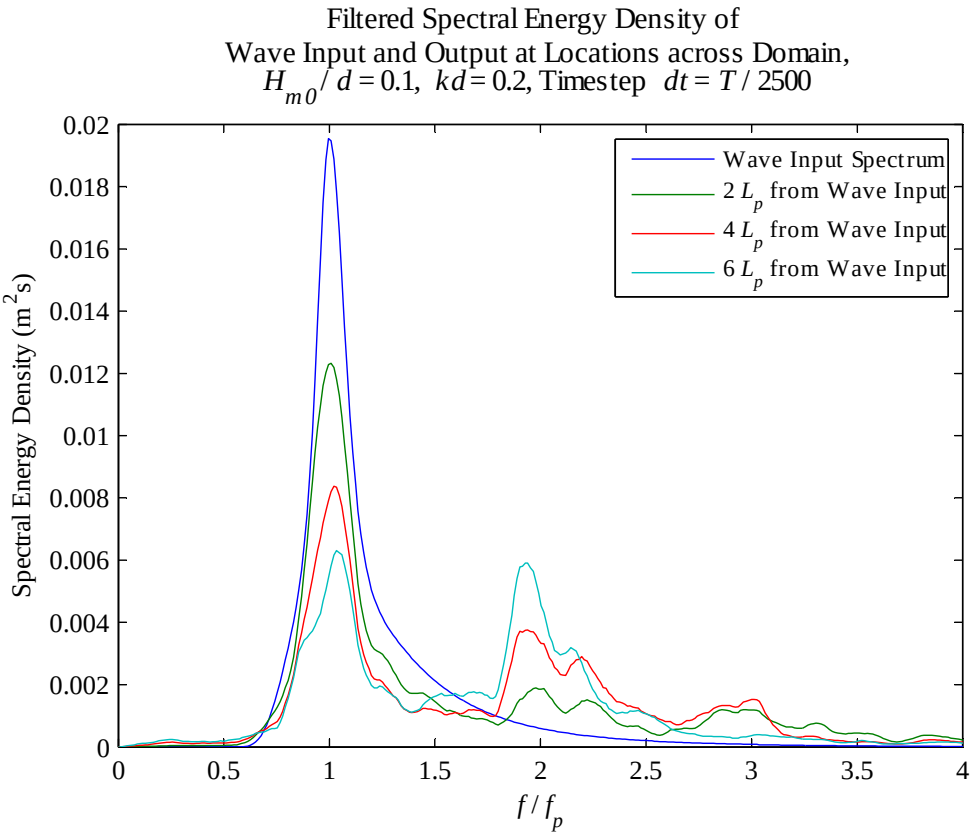

Figure 3.20: Wave input spectrum and filtered spectral energy curves across the domain, $H_{m0,\text{in}}/d = 0.1$, $kd = 0.2$ and $dt = T_{m02,\text{in}}/2500$

transferred to second and third order harmonics. When watching non-breaking waves approaching a beach, one notices how they appear to be reasonably regular, but not sinusoidal. The formation of such waves is being demonstrated here. The rate of generation of these harmonic components is dependent on H_{m0}/d; this is demonstrated by Figure 3.21.

3.8.3 Concluding remarks

The tests described above show quite effectively some of the properties of the SWAB model. The model equations are well suited to situations where $kd < 3$. As kd is increased, not only are the linear dispersion characteristics less valid, but the solver produces a damping effect. For regular waves, when $dt/T = 1/2500$, very little damping occurs over 5 wavelengths for $kd < 1.5$; when $dt/T = 1/500$, little damping occurs over 5 wavelengths for $kd < 1$. For random waves, damping occurs for all values of $k_p d$, where k_p is based on the peak frequency of the spectrum; however, most of this damping will affect high frequency components.

For regular waves, the type of wave input is important. Airy waves are not suitable for high Ursell numbers ($Ur > 20$). The SAWW-type wave input is suitable for all Ursell numbers, except in conditions where the model nonlinearity is less than it should be for real waves.

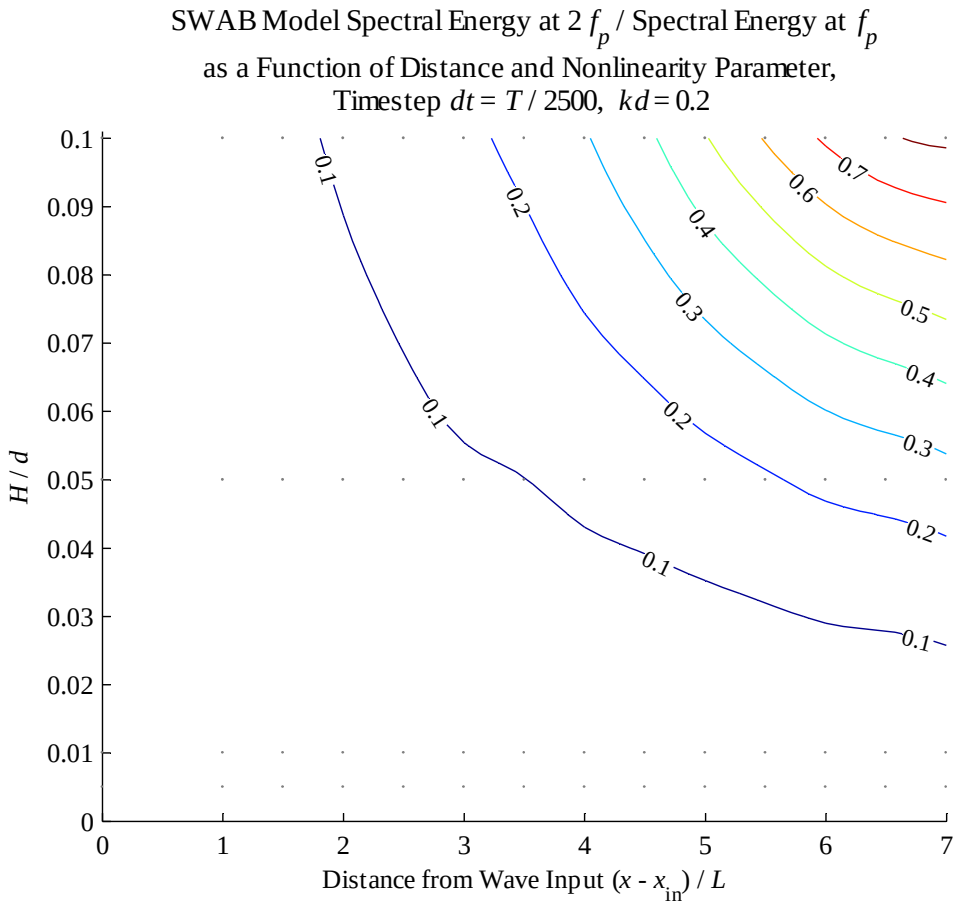

Figure 3.21: Contours of spectral energy density at $2f_p$ as a proportion of spectral energy at f_p as a function of nonlinearity parameter, $H_{m0,\text{in}}/d$, and distance from wave input; JONSWAP wave input, $kd = 0.2$, with $dt = T_{m02,\text{in}}/2500$

Therefore, in deeper water ($kd = 0.5$), when $H/d > 0.05$ the SWAB model is insufficiently nonlinear to allow a SAWW wave input to propagate correctly; in such situations the Airy input gives better results.

For random waves, although some high frequency damping occurs, the SWAB model also allows the nonlinear transfer of energy to harmonic frequencies. To assess the accuracy of the SWAB model for random waves, testing against physical model data will be more appropriate.

Chapter 4

Description of Data Sources

4.1 Regular Waves

Data from experiments using regular waves were used as the first test of the SWAB model's validity for nearshore waves. They were used to calibrate breaking parameters, and to investigate the phasing out of the Boussinesq terms after breaking. The SWAB model can generate regular waves (linear, or 2nd order Stokes); however, many wave conditions in intermediate depths are better suited to cnoidal wave theory and linear or Stokes generated waves will produce parasitic free waves. A Fortran code based on the method of Rienecker and Fenton [1981] was also used to generate regular waves. Table 4.1 summarises the regular wave conditions used in this study.

Stive [1985] carried out a study on regular and random waves, using small-scale (55 m long flume) and large-scale (233 m long flume) to investigate scale effects in breaking waves. Test ST in Table 4.1 uses results from a small-scale regular wave test; Stive [1985] presented values for wave height and wave setup throughout the experimental domain.

Regular wave tests carried out by Hansen and Svendsen [1979] are described by Kennedy et al. [2000]. Measurements were taken for shoaling and breaking waves using an automated continuously moving trolley. Small sample sizes resulted in a large amount of scatter; therefore Kennedy et al. [2000] averaged results over adjacent measurement locations, reducing the scatter, but still leaving a considerable number of measurement locations. Loss of water to an inactive part of the flume affected the data for wave setup; therefore Kennedy et al. [2000] adjusted the measured setup by a fixed amount to match their computed set-down offshore. Kennedy et al. [2000] presented data for wave heights and wave setup for shoaling and breaking waves (including spilling and plunging breakers) from five of the tests of Hansen and Svendsen [1979].

Table 4.1: Regular wave conditions. $\cot\beta$ is the bed slope

Condition Code	Experimental Data	H_{in} (m)	T (s)	d_{in} (m)	$(kd)_{\text{in}}$	ξ_0	$\cot\beta$
ST	Stive [1985]	0.15	1.79	0.70	1.099	0.138	40
HS1	Hansen and Svendsen [1979] cited by Kennedy et al. [2000]	0.043	3.33	0.36	0.370	0.646	34.26
HS2	Hansen and Svendsen [1979] cited by Kennedy et al. [2000]	0.039	2.50	0.36	0.501	0.480	34.26
HS3	Hansen and Svendsen [1979] cited by Kennedy et al. [2000]	0.036	2.00	0.36	0.641	0.384	34.26
HS4	Hansen and Svendsen [1979] cited by Kennedy et al. [2000]	0.067	1.67	0.36	0.789	0.230	34.26
HS5	Hansen and Svendsen [1979] cited by Kennedy et al. [2000]	0.067	1.00	0.36	1.578	0.136	34.26
TK1	Ting and Kirby [1994]	0.125	2.00	0.40	0.680	0.200	35
TK2	Ting and Kirby [1994]	0.128	5.00	0.40	0.257	0.596	35

Ting and Kirby [1994] generated cnoidal waves for their experiments on undertow and surf zone turbulence. Two tests were run, one with spilling and the other with plunging breakers. They presented results for maximum, minimum and mean water levels for shoaling and breaking waves.

4.2 Random Wave Tests

Stive [1985] carried out full-scale and small-scale random wave tests for a plane slope beach, recording root mean square (rms) wave heights and mean wave setup in the nearshore. Unfortunately, the spectral shape is not described; however, initial SWAB and SWAN model runs for these wave conditions showed little difference in results between using a JONSWAP or a Pierson-Moscowicz spectrum. Therefore, for all subsequent model runs for these waves a Pierson-Moscowicz spectrum was assumed. Ting [2001] also carried out tests on a plane slope, using a TMA spectrum, with a spectral peak enhancement factor (γ) of 3.3. Wave height distributions, wave periods and proportions of breaking waves were all recorded in the nearshore. Recording took place over 307.2 s periods, giving test runs of approximately 200 waves.

Mase [1989] carried out an extensive series of tests on random wave runup, for a range of wave conditions and plane slopes, using a Pierson-Moscowicz spectrum. The test parameters were presented in terms of offshore wave conditions; these parameters were transformed using linear wave theory to give wave input conditions for the model runs. Wave runup was measured using a capacitance gauge installed in a groove running up the beach slope. Individual runups were recorded by measuring the maximum level of each runup crest in a time-series. However, Mase [1989] did not publish time-series or any information on nearshore waves; instead, runup parameters such as the mean of the highest third of runups ($R_{1/3}$) were presented. Nevertheless, the extensive range of conditions of this dataset is most useful; four tests on a 1 in 20 slope have been selected here. Test parameters for these plane slope random wave experiments are given in Table 4.2.

Mase et al. [2004] performed tests for the runup of random waves on a seawall fronted by a submerged breakwater. Figure 4.1 shows the experimental set-up for which time-series are available. Experiments were also performed without the reef, and for a different reef bathymetry; however time-series data are not available for these additional tests. Additionally, a seawall with a slope of $\cot\beta = 0.5$ was also tested. Mase et al. [2004] performed tests with seven significant wave periods and two different still water levels; however, time-series are only available for $T_{1/3}$ of 1.1 s and 2.1 s for a water depth of 0.425 m. Table 4.3 contains the incident wave conditions for these tests. In the flume there were six wave gauges; the

Table 4.2: Random wave conditions. Surf similarity parameters are based on offshore wave steepness using peak period, T_p, and significant wave height, H_{m0}. $\cot\beta$ is the bed slope. The subscript $_{in}$ refers to conditions at the wave input location

Condition Code	Experimental Data	$H_{m0,\text{in}}$ (m)	T_p (s)	d_{in} (m)	L_{0p} (m)	$(k_p d)_{\text{in}}$	ξ_0	$\cot\beta$
ST1	Stive [1985]	1.414	5.41	4.19	45.70	0.840	0.138	40
ST2	Stive [1985]	0.198	2.93	0.7	13.40	0.606	0.207	40
ST3	Stive [1985]	0.198	1.58	0.7	3.90	1.307	0.106	40
TI	Ting [2001]	0.152	2.00	0.4572	6.25	0.735	0.180	35
MA1	Mase [1989]	0.049	2.50	0.45	9.76	0.566	0.715	20
MA2	Mase [1989]	0.062	2.00	0.45	6.25	0.728	0.494	20
MA3	Mase [1989]	0.074	1.67	0.45	4.35	0.906	0.370	20
MA4	Mase [1989]	0.091	1.25	0.45	2.44	1.332	0.247	20

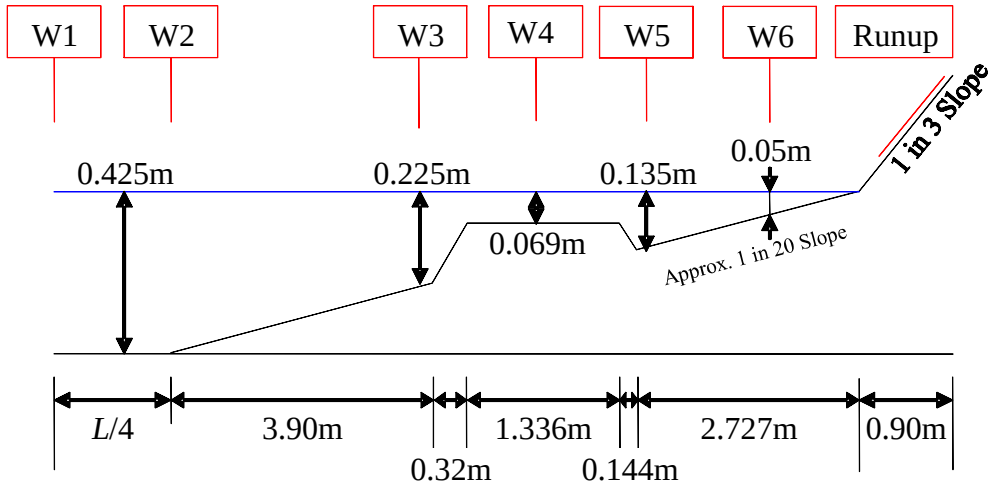

Figure 4.1: Mase et al. [2004] experimental set-up

second, W2, was placed at the base of the slope, with the first, W1, being $L/4$ further offshore (with L based on the significant wave period). A runup meter was placed 3 mm above the face seawall; the lower end of the runup meter was placed approximately 10 cm distance from the base of the wall. This means the base of the runup meter was located 3.45 cm above the still water level.

Mase [2008] provided the time-series data for all six wave gauges and the runup meter for the tests described in Table 4.4, as well as data on wave heights and runup parameters from all their model tests. However, the SWAB modelling that will be described in Chapters 5 and 6 will only make use of the time-series data.

Table 4.3: Incident wave data for selected Mase et al. [2004] tests

Condition Name	$H_{1/3}$ (m)	H_{m0} (m)	$T_{1/3}$ (s)	T_p (s)	Distance W1 - W2 (m)	$\xi_{0,p}$
T1	0.0709	0.0726	1.05	1.14	0.43	0.253
T2	0.0671	0.0739	2.11	2.25	1.00	0.519

Figure 4.2: Location of Anchorsholme Seawall

4.3 Blackpool Field Data and Model Tests

4.3.1 Introduction and location

Simultaneous wave and overtopping field data was collected at Anchorsholme, Blackpool by HR Wallingford for the Environment Agency [Bocquet et al., 2009]. By carrying out physical model tests using the conditions from the field data, this will provide a potentially very useful dataset. It will enable a three-way comparison between field data, physical model test results, and numerical modelling.

To establish the relationship between extreme waves and maximum overtopping rates, one additional run was carried out using a NewWave focussed group. NewWave groups [Tromans et al., 1991] aim to represent the free surface shape around an extreme crest or trough. They have been effective in predicting extreme loadings on offshore structures but their use has yet to be demonstrated nearshore. The running of a NewWave test equivalent to one of the random wave conditions will enable research into their nearshore applicability.

Anchorsholme seawall is located about 6 km north of central Blackpool (OS Grid Reference

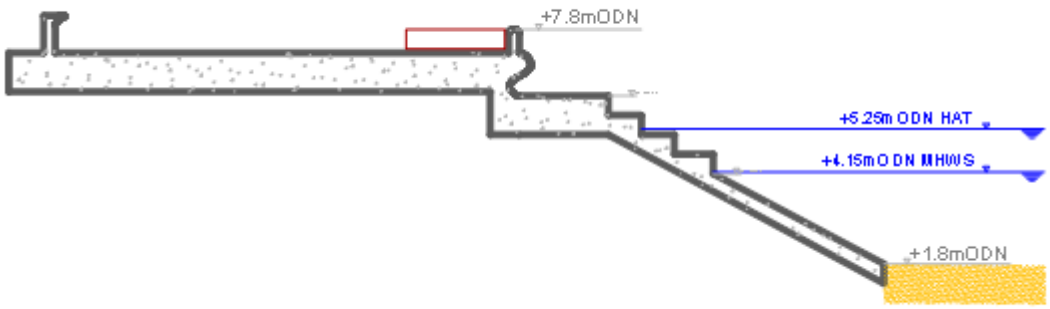

Figure 4.3: Cross-section of seawall (horizontal and vertical at same scale)

Figure 4.4: AWAC locations

SD 31185 42409). Figure 4.2 shows the location of the seawall. A cross-section of the seawall is shown in Figure 4.3. Two acoustic wave and current profilers (AWACs) were placed approximately 30 m and 450 m offshore from the base of the seawall; these locations are shown in Figure 4.4. Each AWAC has two methods for recording free surface levels: acoustic surface tracking (AST), which is effectively an inverted echo sounder, and a pressure sensor. Datasets from the AWACs were recorded from 23rd January 2008 to 25th January 2008 in 1024 s "bursts". These bursts were collected at 20 minute intervals. 147 bursts were recorded offshore, and 144 inshore. However, the inshore recording was started before the offshore recording. In this report, burst numbers (or test numbers) refer to offshore bursts; therefore offshore Burst Number 1 is simultaneous with the fourth inshore burst.

The bathymetry between the offshore AWAC and the shore was not measured. The bed level at the inshore AWAC location was measured relative to an Ordnance Survey Benchmark. To calculate the level of the offshore AWAC, the difference in mean water depth between the two AWACs was used; this was done separately for each burst. This method assumes that the wave setup is minimal.

4.3.2 Analysis of field data

The field wave data was analysed for the following reasons: firstly to check the quality of the data and whether the offshore and inshore datasets match; and secondly to select a suitable set of wave conditions and water levels for the physical model tests.

The AST gives a direct measurement of the free surface, at a frequency of 4 Hz. The pressure sensor records at 2 Hz. Using Airy wave theory, the relationship between the pressure, p, and the free surface level is given as [Reeve et al., 2004]:

$$p = -\rho g z + \rho g \zeta K_p \tag{4.1}$$

where $K_p(z)$ is the pressure attenuation factor:

$$K_p(z) = \frac{\cosh k(d+z)}{\cosh kd} \tag{4.2}$$

and ζ is the free surface excursion (i.e. level above still water level), d is the still water depth, and z is the vertical distance above the still water level (i.e. $z = -d$ at the bed). Note that errors will occur where Airy wave theory is not suitable, in the presence of currents, and for high frequency components, which will be recorded as near-zero pressures with near-zero attenuation factors.

Equation (4.2) shows the attenuation factor is a function of kd, and therefore frequency.

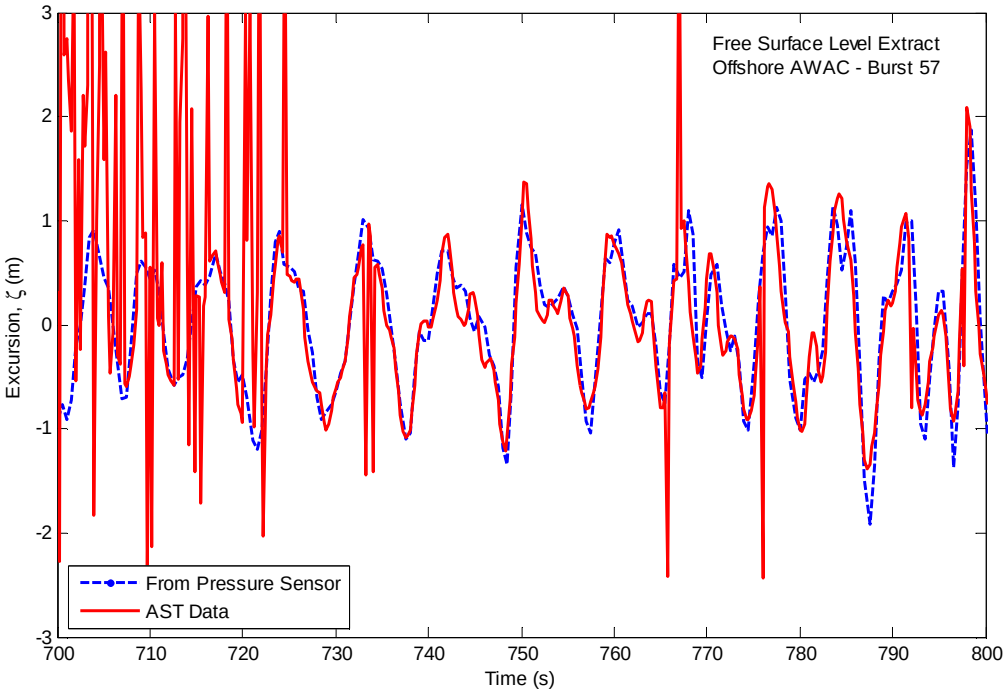

Figure 4.5: Extract of free surface levels; AST data compared to pressure sensor data

Therefore, for spectral waves, different components need to be factored differently. To do this, the pressure time-series were converted using discrete Fourier transforms into their component frequencies and phases, each component was factored, and the time-series were reformed with the factored components and original phases. To avoid errors with high frequency components, the magnitudes of deepwater components (i.e. where $kd > \pi$) were limited by using the same value of K_p as the deepest intermediate depth component.

The AST-based time-series were found to contain some messy signals (Figure 4.5); almost all the inshore AST data was messy. This may be due to wave breaking or some other reason. Therefore it was decided to use the pressure sensor data to calculate water level time-series.

The phase-averaged spectral wave model SWAN [Booij et al., 1999] was used to model the transformation of the offshore data to the inshore AWAC location (in one horizontal dimension). The bed level was assumed to have a constant gradient between the offshore and inshore AWACs. Results show a poor agreement between the SWAN-transformed inshore wave heights and the recorded wave heights inshore (Figure 4.6). It is likely that, especially for the more severe wave conditions, breaking occurs, and the Airy wave theory used to calculate the free surface level may well be invalid. Therefore, it was decided that the offshore data would be used to select wave conditions for the physical model tests.

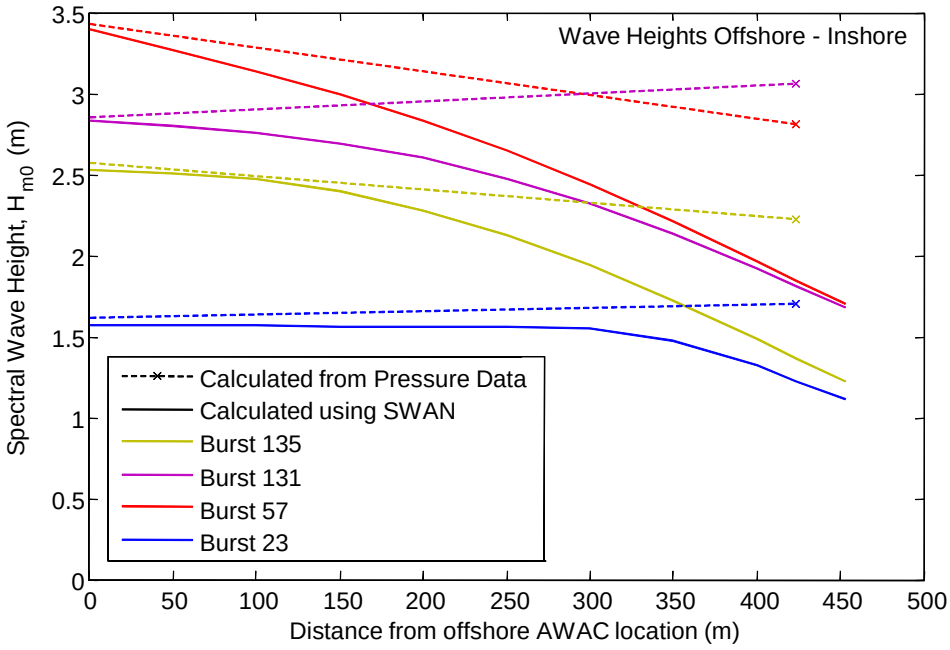

Figure 4.6: SWAN transformations compared with field data

4.3.3 Selection of wave conditions for physical modelling

Six "storm" wave conditions and water levels were selected from the offshore field data. It was intended to use a wide variety of conditions from those that produce very little overtopping to the most severe. Equation (5.9) from the EurOtop Manual [Pullen et al., 2007] was used to provide estimates of the expected overtopping discharges. Spectral energy curves were calculated from the time-series for these wave conditions; these spectra were used to create time-series for the wave paddle in the flume.

Six more "parametric" wave conditions were selected to provide combinations of wave heights, periods and water levels not found in the field data. Figure 4.7a shows wave heights and wave periods for these conditions and Figure 4.7b shows wave heights and water levels (relative to Ordnance Survey Datum, Newlyn). For these parametric conditions, a JONSWAP spectrum was adopted, with a peak enhancement factor, γ, of 3.3.

Table 4.4 shows all the parametric and storm wave and water level conditions; the storm wave spectra are shown in Figures 4.14 to 4.20. One of the storm conditions (Test 131) was chosen as the basis for a test using a NewWave group. Test name "Parametric 05" was never run because it was estimated not to give sufficient overtopping. It was replaced with "Parametric 07". "Parametric 07" was repeated twice: firstly, an exact re-run to check the repeatability of the tests; and secondly, with the gain to the paddle reduced, to test the model's sensitivity to small changes in wave height. Wave trains generated in the flume consisted of 1024 waves.

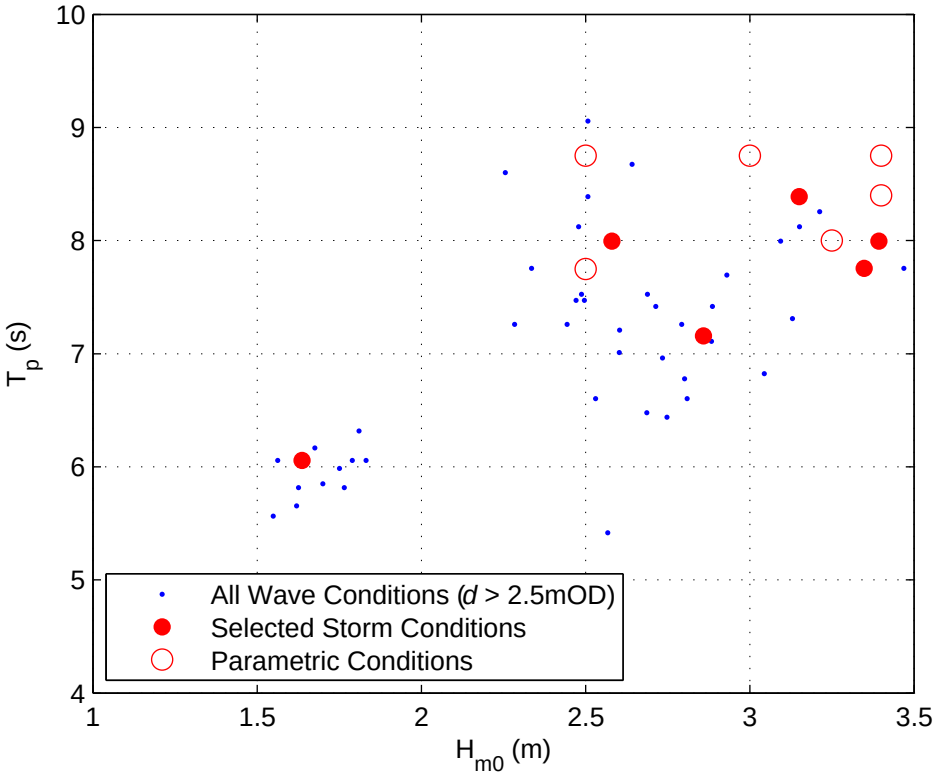

(a) Wave periods and wave heights

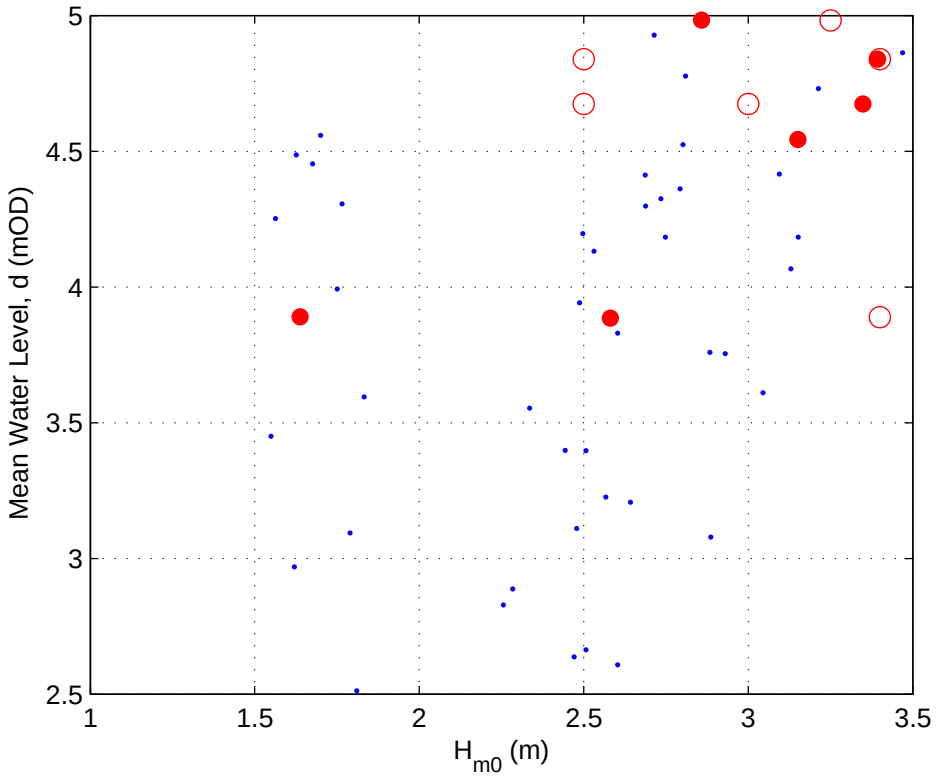

(b) Water levels and wave heights

Figure 4.7: Wave and water level conditions recorded by the offshore AWAC, with selected conditions and parametric conditions

Table 4.4: Specified wave and water level conditions at prototype scale, for all tests

Test Name	Spectral Wave Height, H_{m0} (m)	Peak Wave Period, T_p (s)	d (m) at toe	d (m) at paddle	Water Level (mOD)
Storm 23	1.637	6.056	2.089	8.779	3.889
Storm 55	3.349	7.754	2.874	9.564	4.674
Storm 57	3.393	7.996	3.039	9.729	4.839
Storm 59	3.151	8.389	2.743	9.433	4.543
Storm 131	2.859	7.157	3.182	9.872	4.982
Storm 135	2.581	7.996	2.085	8.775	3.885
Parametric 01	3.4	8.75	3.039	9.729	4.839
Parametric 02	2.5	8.75	3.039	9.729	4.839
Parametric 03	2.5	7.75	2.874	9.564	4.674
Parametric 04	3.4	8.4	2.089	8.779	3.889
Parametric 06	3.0	8.75	2.874	9.564	4.674
Parametric 07	3.25	8.0	3.182	9.872	4.982

4.3.4 Model bathymetry

The model tests used the existing bathymetry in the wave flume at HR Wallingford. A 1:15 scale was chosen as the best at which to carry out the model tests. Figure 4.8 shows the model bathymetry (at prototype scale) alongside the estimated field bathymetry. Unfortunately, the level of the wave paddle is at -4.99 mOD (where mOD is metre above Ornance Datum, Newlyn - maOD and mODN are also sometimes used), instead of the -3.4 mOD level of the offshore AWAC. Therefore, the input waves were modified using the following method. SWAN was used with the field bathymetry to model the transformation of each storm wave condition from the offshore AWAC to the toe of the seawall. Then, again using SWAN, but instead using the flume bathymetry at prototype scale, the wave spectra at the toe of the seawall were transformed offshore to the wave paddle location, giving the required wave spectra for the model tests. These revised wave conditions are very similar to the original conditions; Table 4.5 shows spectral significant wave heights for the original and revised wave conditions.

Figure 4.9 shows the model set-up. The seawall is shown in Figure 4.10. The toe of the seawall was located 5.18 m from the back wall of the flume. To ensure the seawall was placed horizontally, the bed on which it was placed was raised approximately 7 mm (or 0.1 m at model scale) and levelled. Therefore, the bed on the horizontal part of the flume, where Wave Probes

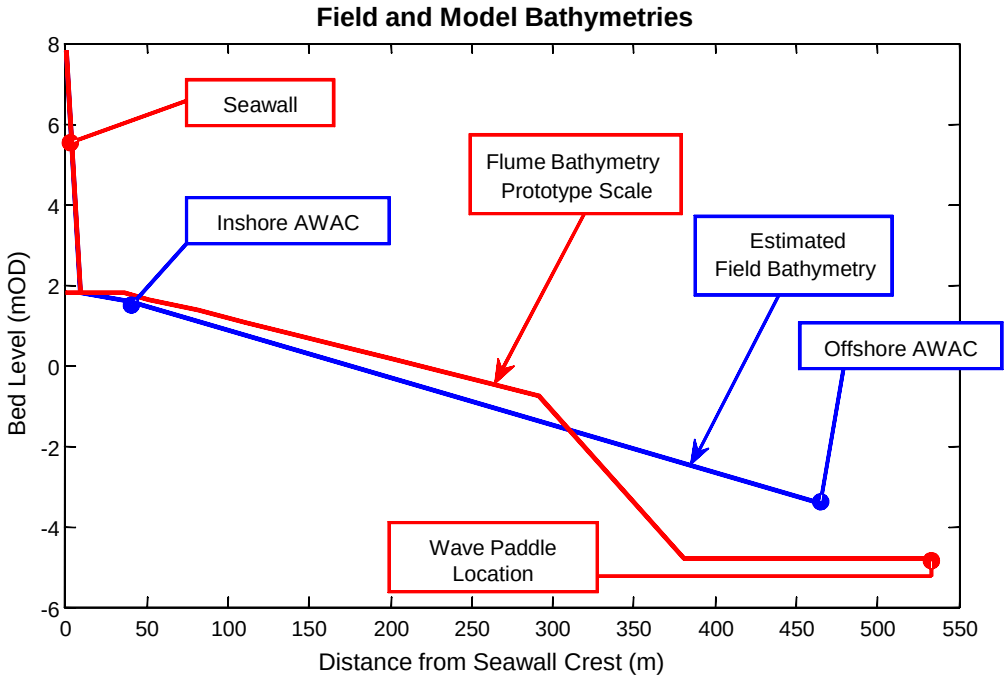

Figure 4.8: Flume bathymetry at prototype scale, compared to estimated field bathymetry

Table 4.5: Spectral significant wave heights for the field conditions compared to revised wave heights for the flume bathymetry

	Spectral Significant Wave Height, H_{m0} (m)	
Test Name	At Offshore AWAC	At Wave Paddle, after SWAN transformation
Storm 23	1.587	1.590
Storm 55	3.356	3.361
Storm 57	3.369	3.371
Storm 59	3.117	3.113
Storm 131	2.848	2.849
Storm 135	2.536	2.535

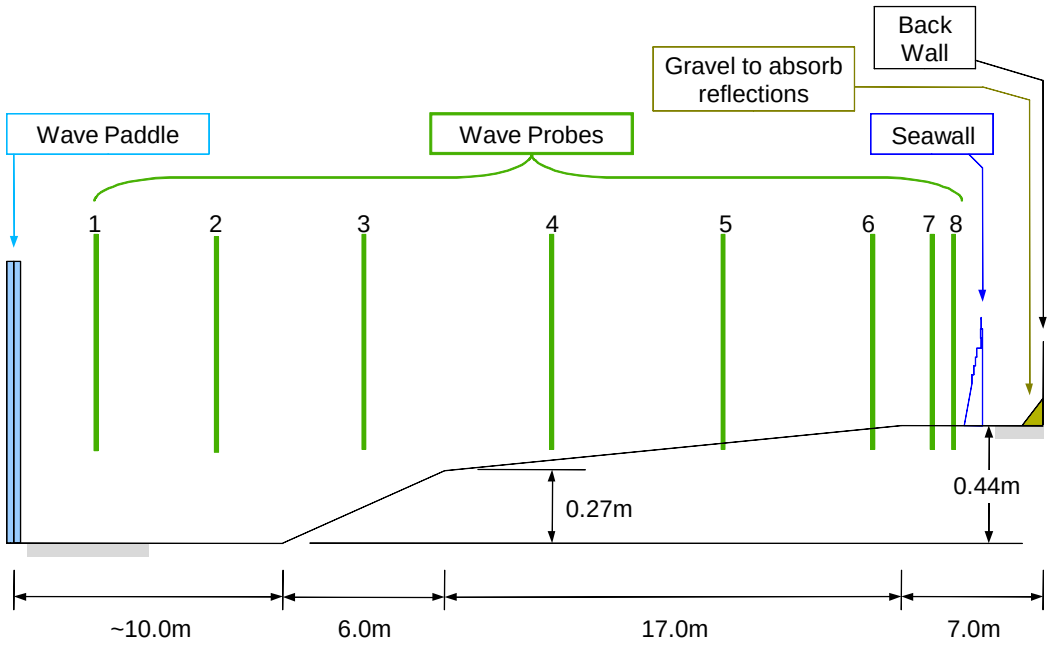

Figure 4.9: Wave flume layout. Vertical scale in figure is 10 times horizontal scale

7 and 8 are located, is actually at a level of +1.7 mOD (instead of +1.8 mOD).

Before starting testing the flume bathymetry was re-surveyed. This bathymetry is slightly different from the given flume bathymetry (Figure 4.11). The analysis of results in subsequent chapters will use this revised bathymetry as it is expected to be more accurate. The horizontal part of the bed, near the seawall, is still given a level of +1.7 mOD. Therefore the horizontal bed level adjacent to the paddle has a lower revised level (-4.99 mOD instead of -4.9 mOD).

4.3.5 Instrumentation and data measurement

Table 4.6 gives a summary of the instrumentation in the flume. Wave probes 1 to 8, shown in Figure 4.9, were used to measure water levels along the flume. Wave probes 1 to 5 remained in the same location throughout testing; alternative locations of probes 6 to 8 are described in Table 4.6.

To measure overtopping, a tank was placed some distance behind the seawall. A chute of known width was placed between the seawall and the collection tank. The chute was always placed after the waves had started to avoid recording overtopping from potential abnormally high waves at the start of the wave train; the placement time was recorded for each test. Inside the collection tank was a wave probe, placed inside a tube to protect it from high-frequency movements. The overtopping tank was emptied after each test; if it filled during a test, this time was also recorded. A photograph of the flume set-up from behind the seawall is shown

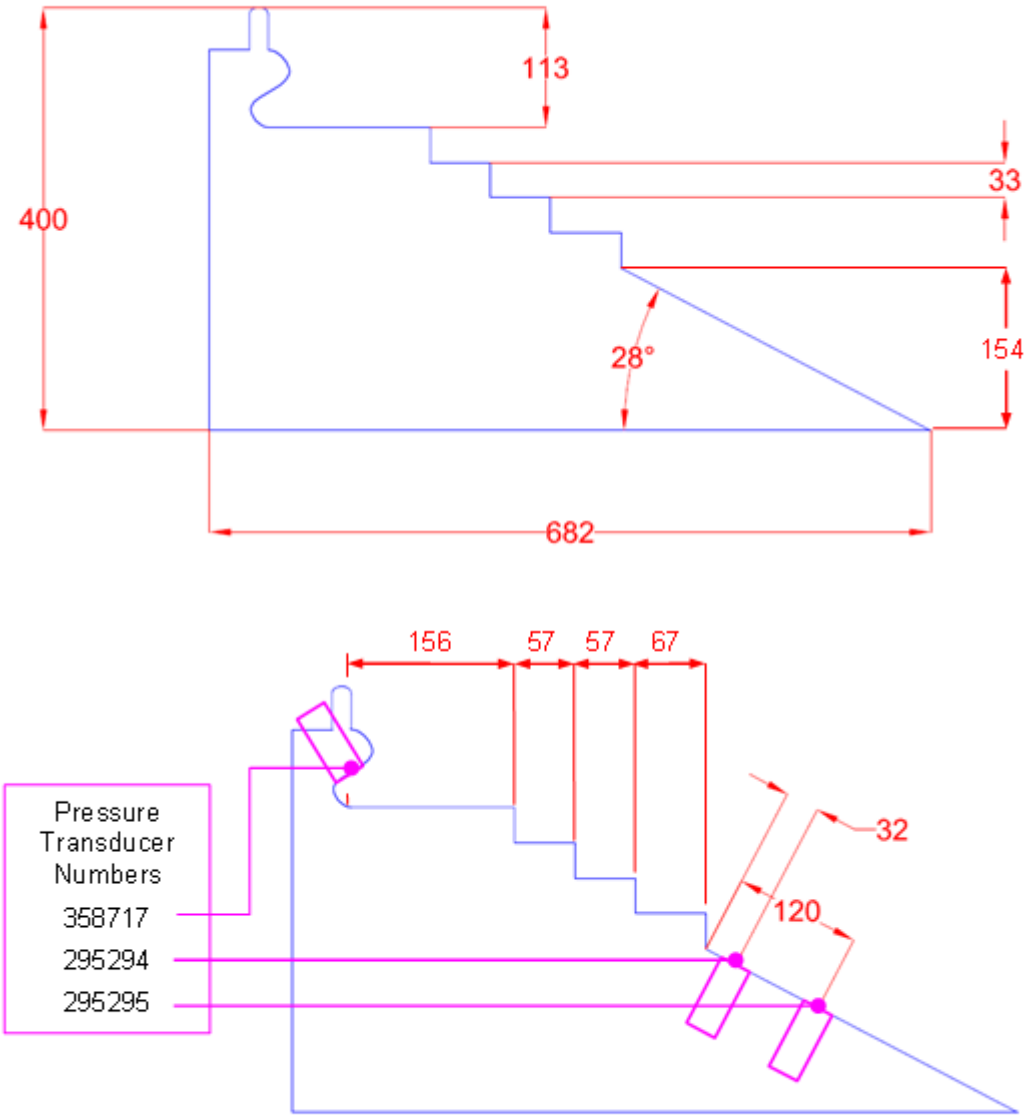

Figure 4.10: Model seawall, with dimensions and locations of pressure transducers. Lengths in mm

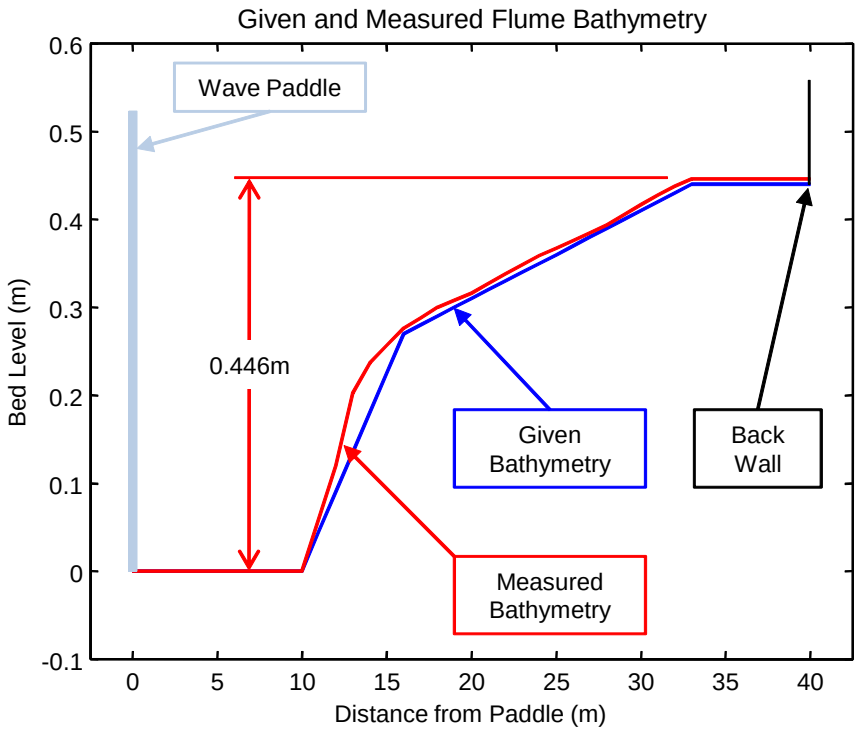

Figure 4.11: Measured flume bathymetry, compared with given bathymetry

in Figure 4.12 and another photograph of the wave flume in the nearshore region is shown in Figure 4.13.

Two additional wave probes, set to high gain, were placed immediately behind the seawall, one closely positioned behind the other. This was an attempt to record the velocity of the overtopping wave fronts. Unfortunately, due to the presence of the recurve wall, the overtopping flow does not form a clean wave front, and the data from these probes will be of little use.

All these wave probes (including the overtopping and the high gain probes described above) were calibrated using three known water levels to calculate calibration factors; the wave probes' response can be assumed to be linear.

Four pressure transducers were used in the experiments, three on the seawall (Figure 4.10) and one on the bed below Wave Probe 6. At prototype scale, the bed level at Wave Probe 6 is at +1.57 mOD, equivalent to the inshore AWAC. Therefore a direct comparison can be made between the inshore AWAC readings and the waves and pressures in the flume. (Note, for test Storm 57, Wave Probe 6 was placed 1.06 m closer to the paddle than the pressure transducer; the pressure transducer was in its correct location). The pressure transducers were pre-calibrated in a series of known water levels. The four pressure transducers used had a response that is very close to linear; the processed data assumes it is linear.

Data collection for the wave probes, pressure transducers and the overtopping tank probe

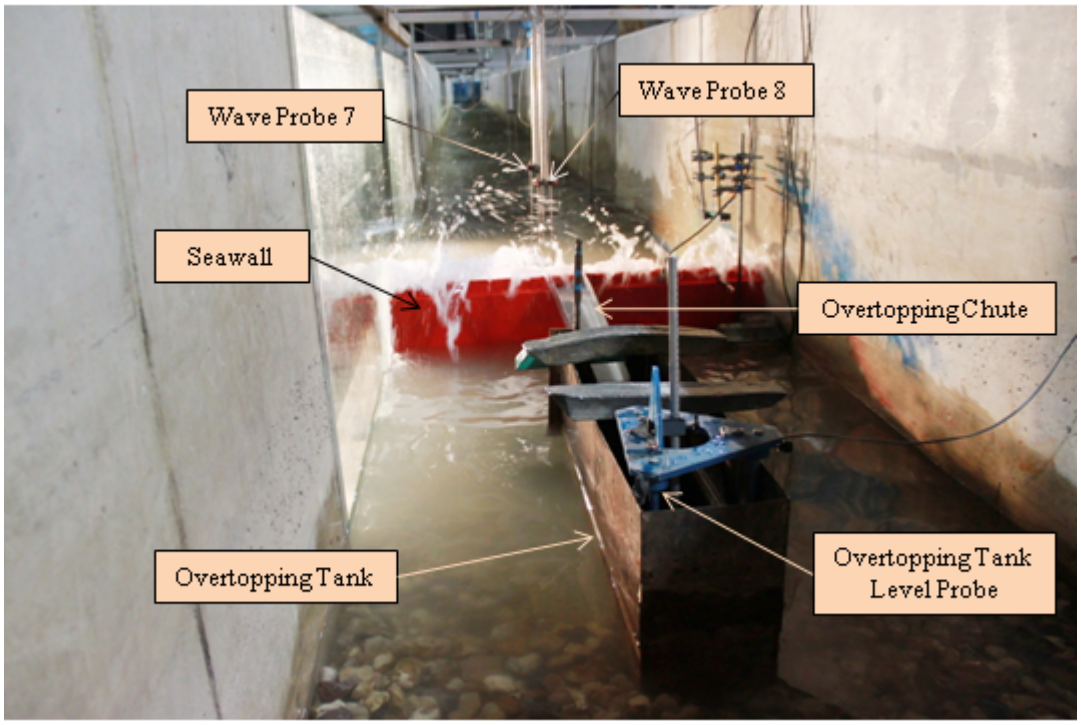

Figure 4.12: Experimental set-up from behind the seawall

was done at a 100 Hz sampling rate. However, the calibration of the storm waves used a 50 Hz sampling rate and some tests were re-run at a 1000 Hz sampling rate.

4.3.6 Wave paddle calibration

The selected spectra, at prototype scale, were automatically converted into random wave time-series using HR Wallingford's in-house software. Input files require values for spectral energy at 24 frequency steps, df, with the peak energy being at $8df$. Therefore they are a smoothed version of the spectra created using a Fourier transform of the storm waves recorded in the field, which appear to be more "spiky". Figures 4.15 to 4.20 show the actual storm wave spectra alongside the input file spectra. The parametric conditions used a JONSWAP spectrum, for which the software requires specification of H_{m0} and T_p.

Although the software calculates paddle signals from the wave spectra, calibration is required to obtain the required wave heights. Where wave heights are incorrect, the gain on the paddle signal can be increased or decreased as required.

Paddle calibration was carried out for each wave condition, as well as the NewWave condition; the NewWave calibration will be described in the next section. To keep wave reflections to a minimum, calibration took place without the seawall in place. For each test, calibration was carried out in two stages. Firstly, short bursts of 400 to 500 s were run, and the gain was adjusted to obtain the correct significant wave height. Once the wave height was within

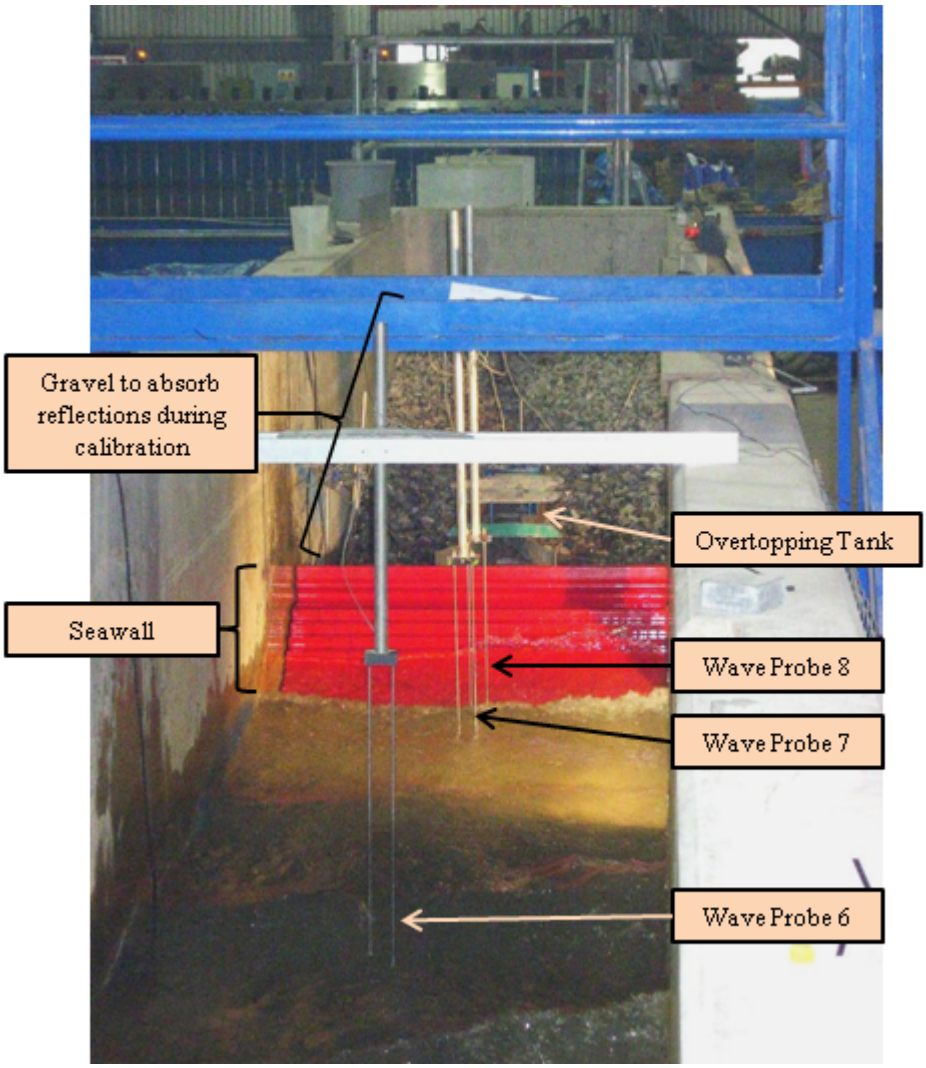

Figure 4.13: Experimental set-up from in front of the seawall

Table 4.6: Wave probes and pressure transducers

Channel Number	Description	Distance from Back Wall at Model Scale (m)	Bed Level at Prototype Scale (mOD)	Notes
1	Wave Probe 1	36.94	-4.99	
2	Wave Probe 2	32.45	-4.99	
3	Wave Probe 3	26.99	-2.91	
4	Wave Probe 4	20.00	-0.25	
5	Wave Probe 5	13.61	+0.70	
6	Wave Probe 6	7.00	+1.70	During calibration and Storm 57 test.
6	Wave Probe 6	8.07	+1.57	For all other tests and post-calibration. This is equivalent to the inshore AWAC position.
7	Wave Probe 7	5.85	+1.70	For pre-calibration, including NewWave calibration
7	Wave Probe 7	5.46	+1.70	For post-calibration
7	Wave Probe 7	6.35	+1.70	For all tests, approximate location
8	Wave Probe 8	4.54	+1.70	For pre-calibration, including NewWave calibration
8	Wave Probe 8	4.46	+1.70	For post-calibration
8	Wave Probe 8	5.85	+1.70	For all tests, approximate location
9	Overtopping Probe 1	Behind seawall crest		Data available but of little use
10	Overtopping Probe 2	Behind seawall crest		Data available but of little use
11	Overtopping Tank	In overtopping tank		Level of water in overtopping tank
12	Pressure Transducer 1 (no. 295294)	4.915	+3.887	Pressure transducer on seawall – see Figure 4.10
13	Pressure Transducer 2 (no. 295295)	4.993	+3.273	Pressure transducer on seawall – see Figure 4.10
14	Pressure Transducer 3 (no. 358717)	4.55	+6.70	Pressure transducer in recurve wall – see Figure 4.10
15	Pressure Transducer 4 (no. 358718)	8.07	+1.57	Pressure transducer at location equivalent to inshore AWAC

2.5% of the target, a storm (of 1024 waves) was run. Calibrated wave statistics were taken from these runs; for all cases, Wave Probe 2 was used as the calibration probe. Table 4.7 summarises these calibrated wave heights and periods. Figure 4.14 shows the calibrated wave conditions alongside the range of conditions recorded in the field (Figure 4.7 shows the target wave conditions).

Although Wave Probe 2 was used to calibrate the test conditions, all eight wave probes were in place for the calibration runs. The data from these probes will be a useful dataset for waves without reflection due to the seawall. It can be assumed that the incident waves from the calibration runs are approximately identical to the incident waves from the test runs.

For the parametric conditions, when the seawall was in place the wave paddle was unable to dampen as required the reflections from the seawall, causing it to crash. This was solved by reducing the gain on the wave paddle input. Therefore, these conditions were post-calibrated, after the seawall had been removed. Two different gain values were used for the Parametric 07 test, to test sensitivity to small changes in wave height; these were all post-calibrated.

It should be noted that the post-calibrated conditions are not within 2.5% of their target values, with wave heights generally considerably higher. However, it is most important that the wave conditions are known, and less important that they are within their target values.

4.3.7 NewWave tests

The NewWave group by Tromans et al. [1991] was described in Section 2.2.4. They represent the average free-surface shape around an extreme crest or trough. Like conventional spectral waves, the surface elevation is expressed as the sum of its component harmonics. However, the constituent amplitudes are calculated using equation (2.47). The phases of these wave components are not random, but are instead calculated to come into phase at the focal point, using equation (2.48).

Storm 131 (Table 4.4) was chosen as the wave spectrum for a NewWave group. This spectrum, with frequencies of up to $3f_p$, was divided into 48 spectral components; however components with a frequency of less than $0.5f_p$ were not used, leaving a total of 41 components, incorporating 99% of the total energy spectrum. For a NewWave group to correspond to the highest wave in a wave train, if a Rayleigh distribution of wave heights is assumed, then the sum of the amplitudes, A_N, can be calculated by integrating equation (2.33) with respect to H and assuming an exceedance probability of $1/N$. This gives the following:

$$A_N = \sqrt{2m_0 \ln N} \tag{4.3}$$

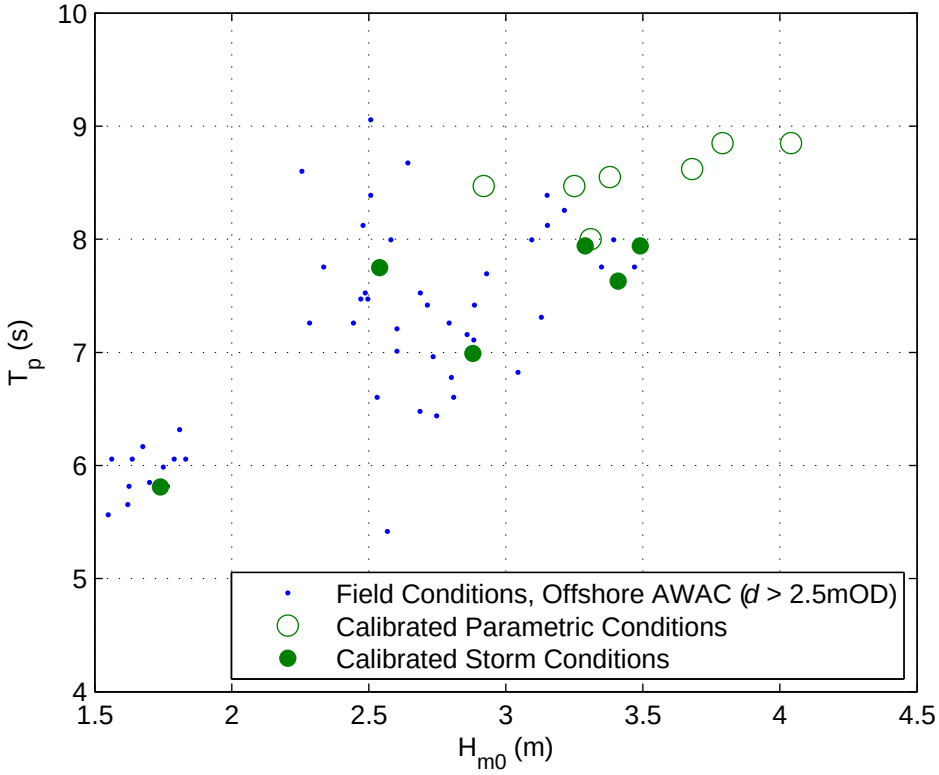

(a) Wave periods and wave heights

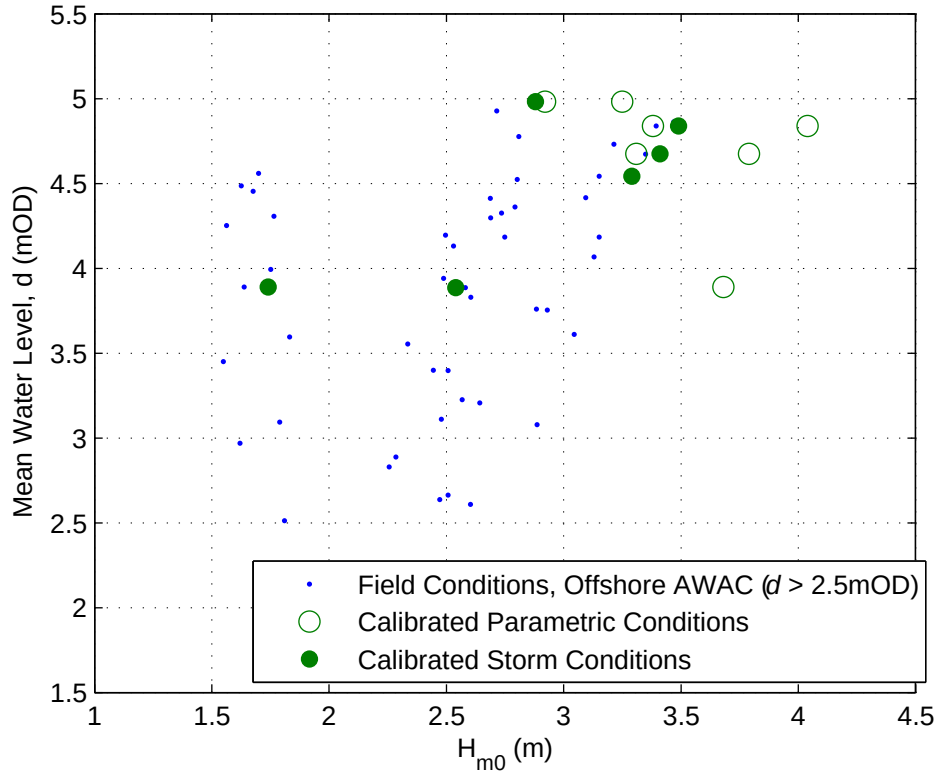

(b) Water levels and wave heights

Figure 4.14: Calibrated wave and water level conditions in the flume (prototype scale) alongside those recorded by the offshore AWAC

Table 4.7: Calibrated wave conditions, compared to target conditions. All values at prototype scale

	Target Values		Model Values from Calibration			
Test Name	H_{m0} (m)	T_p (s)	H_{m0} (m)	T_p (s)	% Error in Model H_{m0}	Notes
Storm 23	1.637	6.056	1.74	5.81	6.3	
Storm 55	3.349	7.754	3.41	7.63	1.8	
Storm 57	3.393	7.996	3.49	7.94	2.9	
Storm 59	3.151	8.389	3.29	7.94	4.4	
Storm 131	2.859	7.157	2.88	6.99	0.7	
Storm 135	2.581	7.996	2.54	7.75	-1.6	
Parametric 01	3.400	8.750	4.04	8.85	18.8	Post-calibration
Parametric 02	2.500	8.750	3.38	8.55	35.2	Post-calibration
Parametric 03	2.500	7.750	3.31	8.00	32.4	Post-calibration
Parametric 04	3.400	8.400	3.68	8.62	8.2	Post-calibration
Parametric 06	3.000	8.750	3.79	8.85	26.3	Post-calibration
Parametric 07 G75	3.250	8.000	2.92	8.47	-10.2	Post-calibration Gain = 0.75
Parametric 07 G85	3.250	8.000	3.25	8.47	0.0	Post-calibration Gain = 0.85 This test was repeated

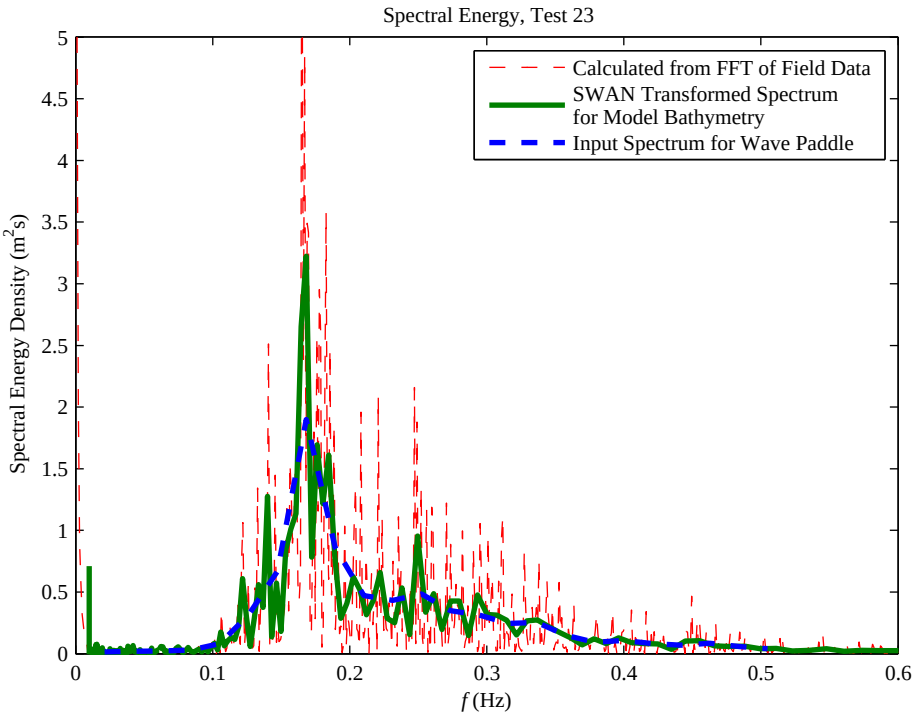

Figure 4.15: Spectral energy density for Storm 23

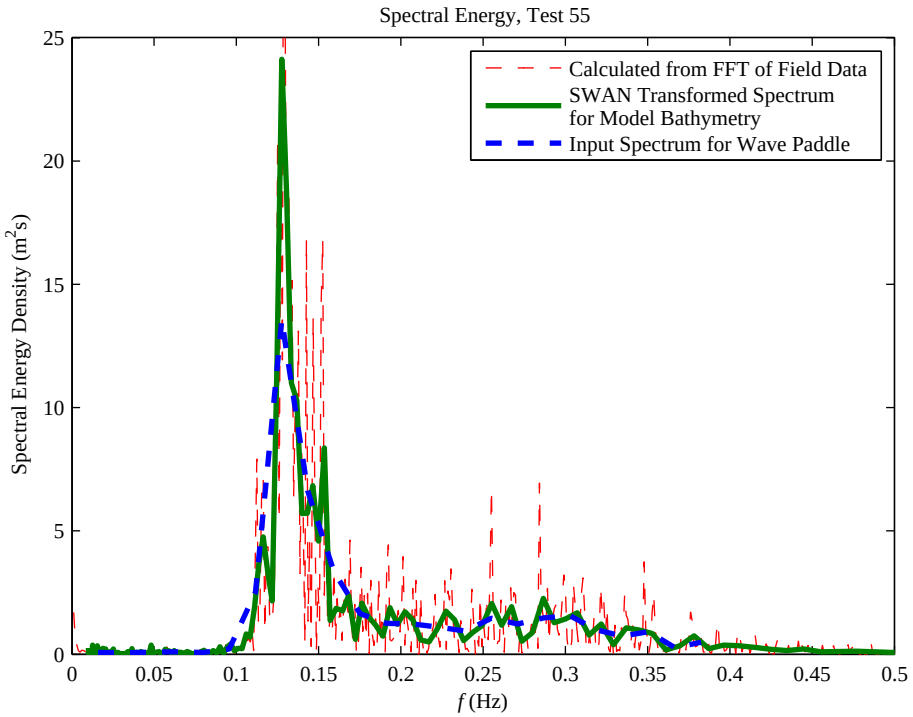

Figure 4.16: Spectral energy density for Storm 55

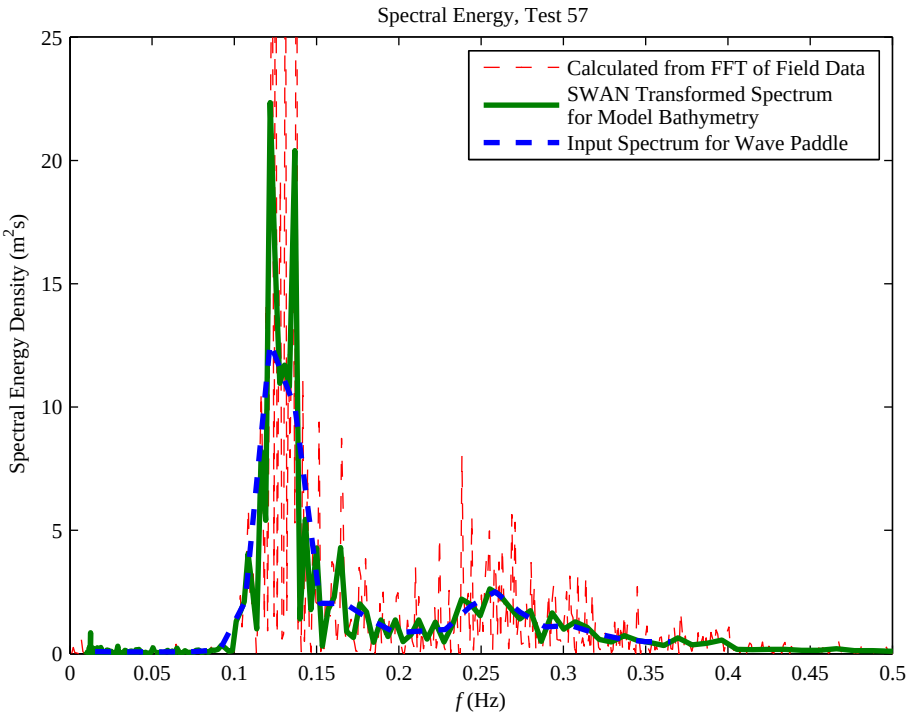

Figure 4.17: Spectral energy density for Storm 57

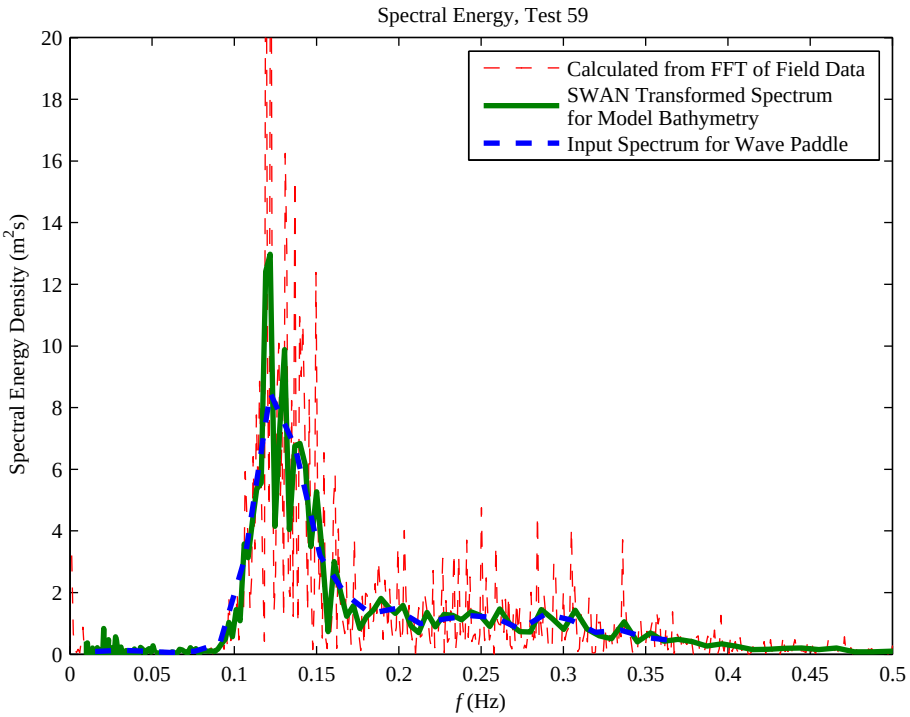

Figure 4.18: Spectral energy density for Storm 59

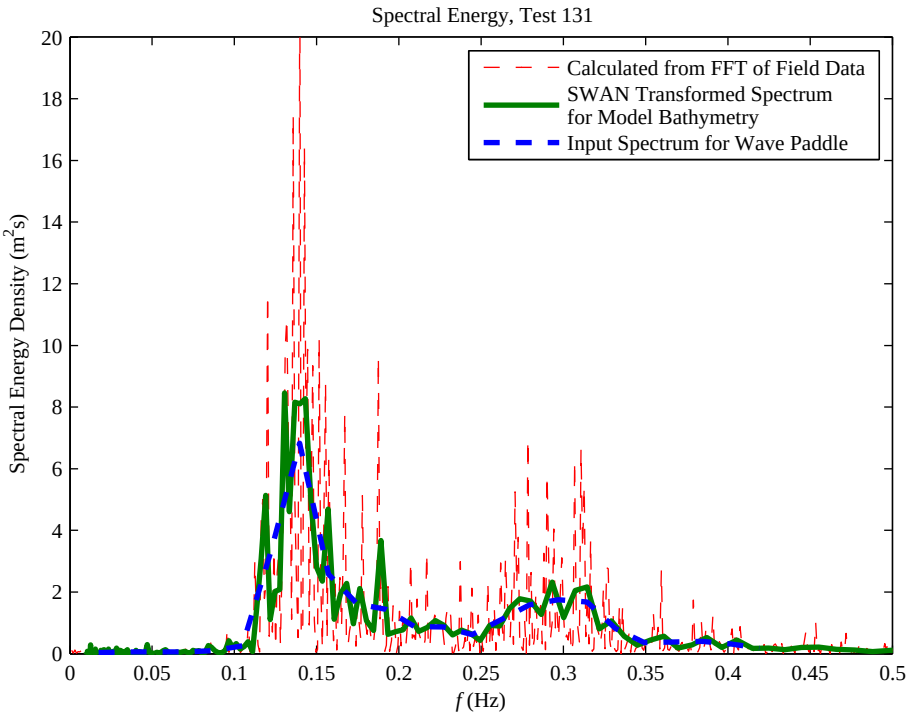

Figure 4.19: Spectral energy density for Storm 131

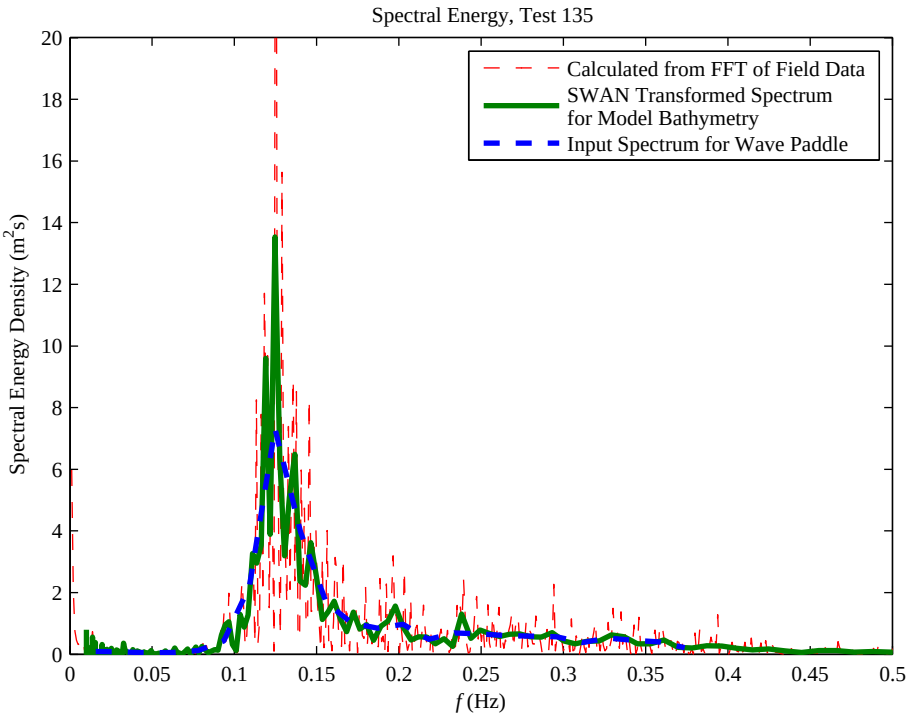

Figure 4.20: Spectral energy density for Storm 135

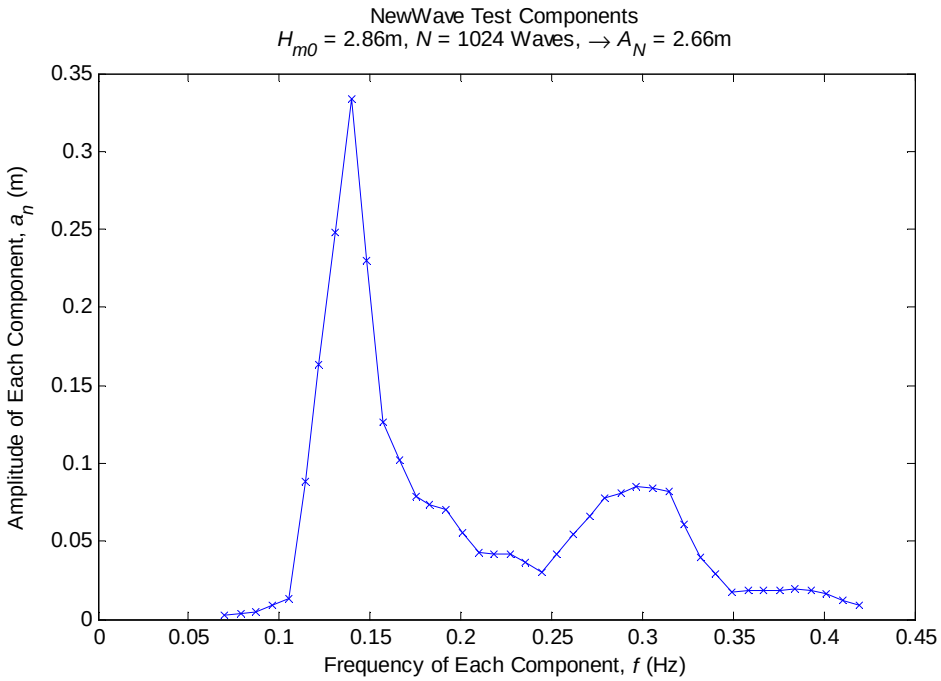

Figure 4.21: Amplitudes of the NewWave components based on the spectrum of Storm 131

where N is the number of waves, which is 1024 in this case. Figure 4.21 shows the amplitudes and frequencies of the 41 components.

For the initial calibration, 21 components (i.e. every second component, including the lowest and highest frequency components) were run separately as regular waves, with free surface outputs at each wave probe. For this stage of calibration the amplitude of each of these components is not important. Because these calibration wave trains were not perfectly monochromatic, Fourier transforms were performed to extract the required frequency output. From each of these calibration runs, the change in phase between each wave probe was calculated and extrapolated to estimate the phase change between the paddle and Wave Probe 1. For the 20 components not calibrated, the change in phase between the paddle and the focal point was calculated by interpolation with respect to component frequency. From these calculations, any wave probe location could be selected as a focal point. Figure 4.22 helps to explain this methodology.

The second stage of calibration combined the components with their required amplitudes and phases at the paddle, to check that the components come into focus at the focal point. The focal point was chosen to be at the location of Wave Probe 8, or Wave Probe 7 during calibration (Table 4.6). The wave paddle software converts the time-series for free surface level at the paddle into paddle movements. The target value of A_N is 2.66 m, representing the expected highest wave over the 1024 waves of the Storm 131 test. However, this value of A_N will not be exactly reproduced, and it depends on the gain to the paddle signal. Four values

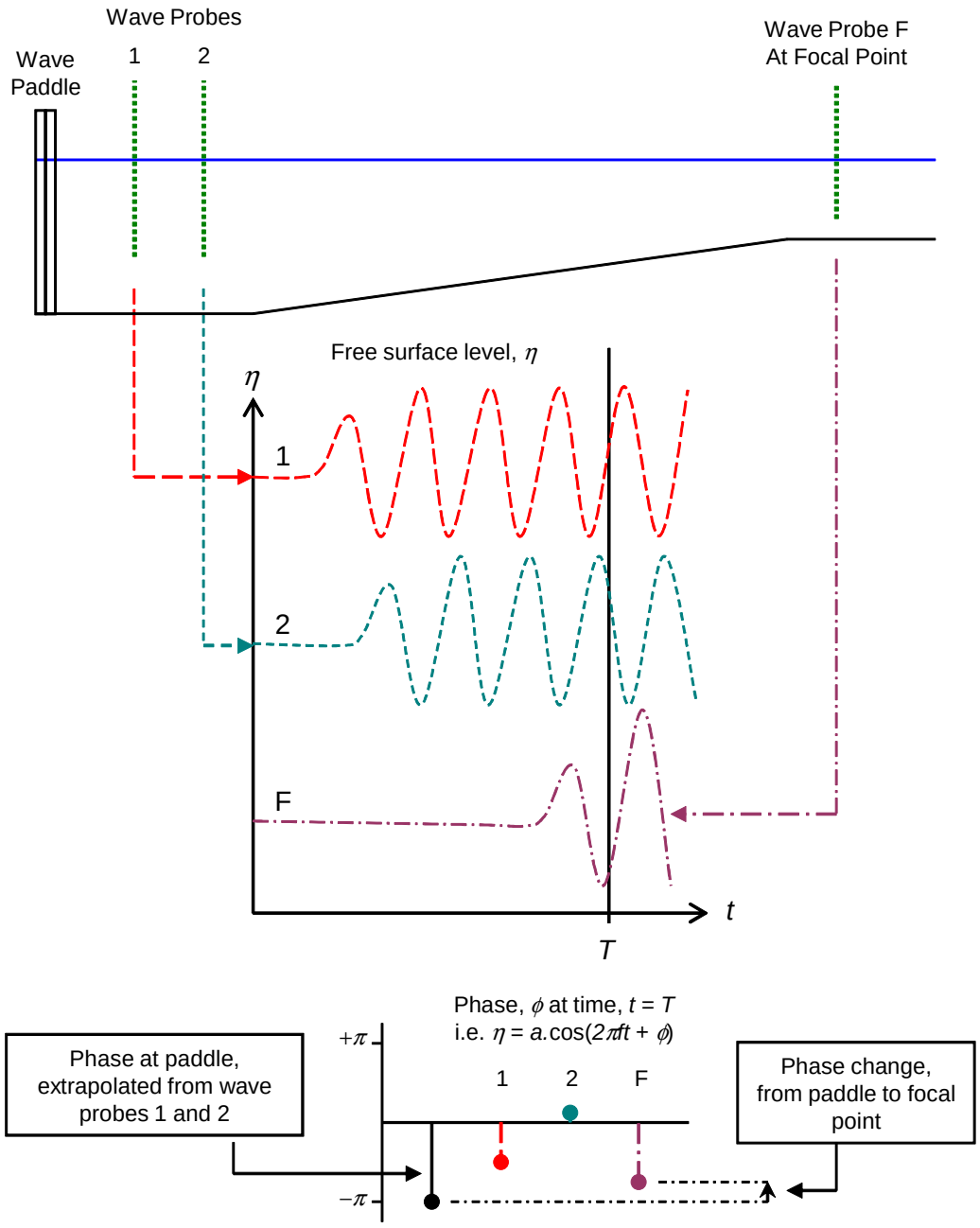

Figure 4.22: NewWave calibration – calculation of phase change between wave paddle and focal point

Table 4.8: Maximum excursions from NewWave calibrations

NewWaveTest Name	Gain on Signal	Maximum excursion (m)	Equivalent H_{m0} (m), if $N = 1024$	Equivalent N, if $H_{m0} = 2.86\,\mathrm{m}$
7V3G2a	2.0	1.544	1.659	10.3
7V3G25a	2.5	1.648	1.771	14.2
7V3G3a	3.0	1.591	1.709	11.9
7V3G35a	3.5	2.046	2.198	60.2

for the gain were tried for these NewWave tests: 2, 2.5, 3 and 3.5.

Table 4.8 shows the values of maximum excursion at the focal point (Wave Probe 7) for each NewWave calibration test. Note that this will be slightly less than A_N, firstly because the components may not exactly focus at the correct location at the correct time, and secondly due to a loss of wave energy, either through friction or breaking. Unfortunately, none of these tests correspond well to the Storm 131 test; better calibration would be required to produce a NewWave group which produces the extreme wave from this test. Despite this, their results may still be useful, but not for comparison with the Storm 131 test itself.

Chapter 5

Shoaling and Breaking Waves

5.1 Regular Waves

5.1.1 Test runs and SWAB input

The aim of this chapter is to determine how well SWAB models shoaling and breaking waves and to optimise the breaking model to give the best results in the nearshore. Random wave modelling is more important for practical uses, and will be studied in detail later in the chapter, but one can gain much from firstly looking at regular waves. Based on the analysis in Section 3.8, the results will be affected by the wave input type (either linear Airy waves, or stream-function SAWW waves). Which is best is dependent on the Ursell number and the dispersion parameter kd. The Airy wave input is preferred for $Ur < 20$ and the SAWW for $Ur > 40$, where the Airy input is unsuitable. For the values of Ur between 20 and 40, the preferred input will be chosen using kd, with Airy preferred where $kd > 0.4$. However, both input types were tried for all regular wave tests.

Table 5.1 shows the relevant test parameters. In addition to the eight tests described in Section 4.1, it was noted that the wave height to depth ratio (H/d) at the input for tests TK1 and TK2 was relatively high (i.e. very nonlinear and close to breaking). Therefore, two additional tests were set up (TK11 and TK21), extending the slope for twice the distance offshore (i.e. into water of twice the depth). Linear wave theory was used to transform the input wave conditions from tests TK1 and TK2 into new input wave conditions for these additional tests. Figure 5.1 shows that most wave conditions are best suited to the Airy wave input. However, it should be noted that the ratio H/d is above 0.1 for all conditions, which is relatively high.

Each SWAB model test run consisted of 50 waves, with the time-step, dt, set to 1500 per wave period; this value was used to ensure run-times were fast, but minimising the damping

Table 5.1: Regular wave test parameters. Note, kd and Ur were calculated using linear wave theory

Test Name	kd at Input	H/d at Input	Ur at Input	ξ_0	Preferred Wave Input Type
ST	1.099	0.214	7.0	0.138	Airy
HS1	0.370	0.119	34.5	0.646	SAWW
HS2	0.501	0.108	17.0	0.480	Airy
HS3	0.641	0.100	9.6	0.384	Airy
HS4	0.789	0.186	11.8	0.230	Airy
HS5	1.578	0.186	3.0	0.136	Airy
TK1	0.680	0.313	26.7	0.200	Airy (note high Ur)
TK2	0.257	0.320	192.0	0.596	SAWW
TK11	1.037	0.146	5.4	0.200	Airy
TK21	0.366	0.137	40.1	0.596	SAWW

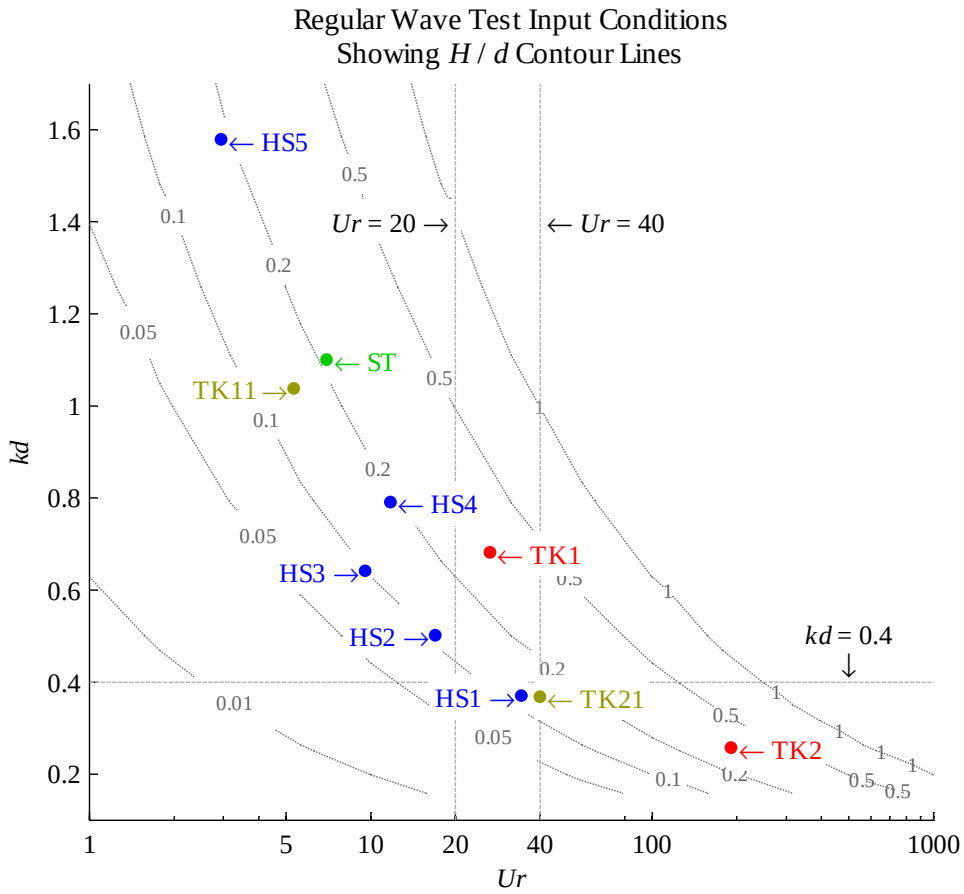

Figure 5.1: Regular wave test input conditions

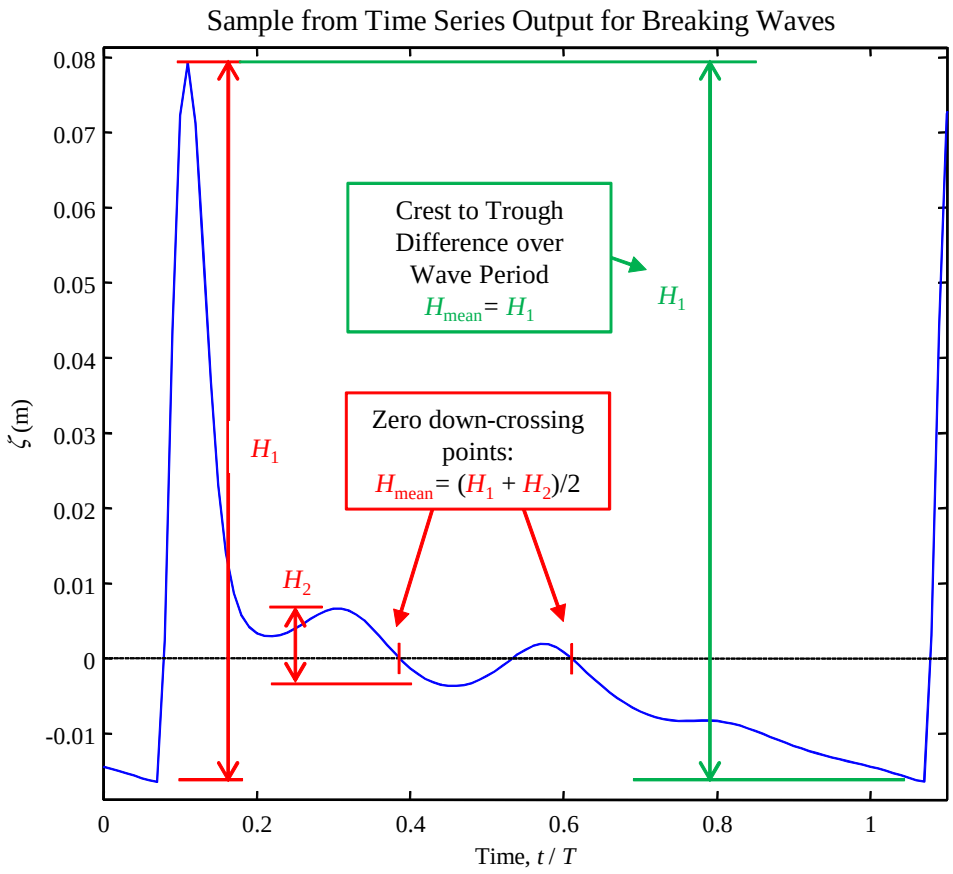

Figure 5.2: Wave height calculation methods

that occurs for large kh, discussed in Section 3.8.1. Time-series outputs of free-surface level were obtained at 40 points across each model domain, between the wave input location and the shore; these were used to determine wave heights. It was found that calculating wave heights using a zero up- or down-crossing method led to some anomalous results while waves were breaking; higher-order harmonics could lead the formation of minor crests and troughs, leading to smaller than expected wave heights. Therefore, each time-series was split into lengths of time, T (the wave period), and the wave height was calculated from the difference between the maximum and minimum levels. Figure 5.2 shows the difference between these two calculation methods, with a sample from one of the output time-series.

5.1.2 SWAB breaking criteria

Possible breaking criteria were discussed in Section 3.2.2. In this study, the difference between using $\partial\eta/\partial t$ and H/h to determine the break point will be investigated. Also, the post-breaking role of the Boussinesq terms will be considered. In this section, we will look at the difference between switching off the Boussinesq terms immediately at the break point and phasing them

out linearly over a distance of h_{br}, where $h_{br}(t)$ is the water depth at the break point. That is:

$$Bous_{ph} = K_{ph}.Bous_{calc} \tag{5.1}$$

$$K_{ph} = \begin{cases} 1 & \text{for } x < x_{br} \\ 1 - \frac{x - x_{br}}{h_{br}} & \text{for } x_{br} \leq x \leq x_{br} + h_{br} \\ 0 & \text{for } x > x_{br} + h_{br} \end{cases} \tag{5.2}$$

where *Bous* represents the sum of the Boussinesq terms (see equation (3.2)); K_{ph} is the phasing out factor; and x_{br} is the location of the break point (landward direction is positive). This type of phasing out was only considered for the $\partial\eta/\partial t$ criterion. When the H/h criterion is applied to random waves, breaking is determined on a wave-by-wave basis, such that it could theoretically commence and cease many times in the nearshore; therefore, the phasing in or out of the Boussinesq terms was thought to be inappropriate in this case.

Figures 5.3 to 5.8 show wave heights in the nearshore for the ST test and the HS tests. When the surf similarity parameter, ξ_0, is low (according to Galvin [1968], spilling breakers occur for $\xi_0 < 0.46$), the $\partial\eta/\partial t$ breaking criterion models shoaling and breaking waves very effectively. There is some discrepancy as the waves approach their maximum height, probably due to the weak nonlinearity associated with the Boussinesq equations being used. As ξ_0 increases, the optimal breaking coefficient, C_{bt}, starts to decrease; in other words, C_{bt} needs to decrease to prevent the waves from breaking too close to the shore. At some point between $\xi_0 = 0.230$ (Figure 5.5) and $\xi_0 = 0.384$ (Figure 5.6), the waves lose their height too close to the shore no matter what the breaking coefficient. The phasing out of the Boussinesq terms appears to make little difference for these high surf similarity parameters; it could be partly because h at the break point becomes very small, and the phasing-out distance becomes negligible.

The H/h criterion makes a significant difference to the results; although it seems to be unable to model the highest waves approaching the break point, causing breaking to occur too soon, once these breaking waves approach the shore, their heights are very similar to those measured experimentally. Moreover, the surf similarity parameter appears to have little effect on the accuracy of these nearshore waves, which is a considerable improvement over the $\partial\eta/\partial t$ criterion. A breaking coefficient of 0.6 appears to give the best results for all cases.

The phasing out of the Boussinesq terms did not appear to make much improvement to wave heights in the surf zone. However, an analysis of the wave setup for these tests shows that there is a considerable difference (Figures 5.9, 5.10 and 5.11). The wave setup is caused by the loss of momentum stress associated with the breaking waves. When the Boussinesq terms are not phased out, there is too great a loss occurring too far offshore. Therefore the

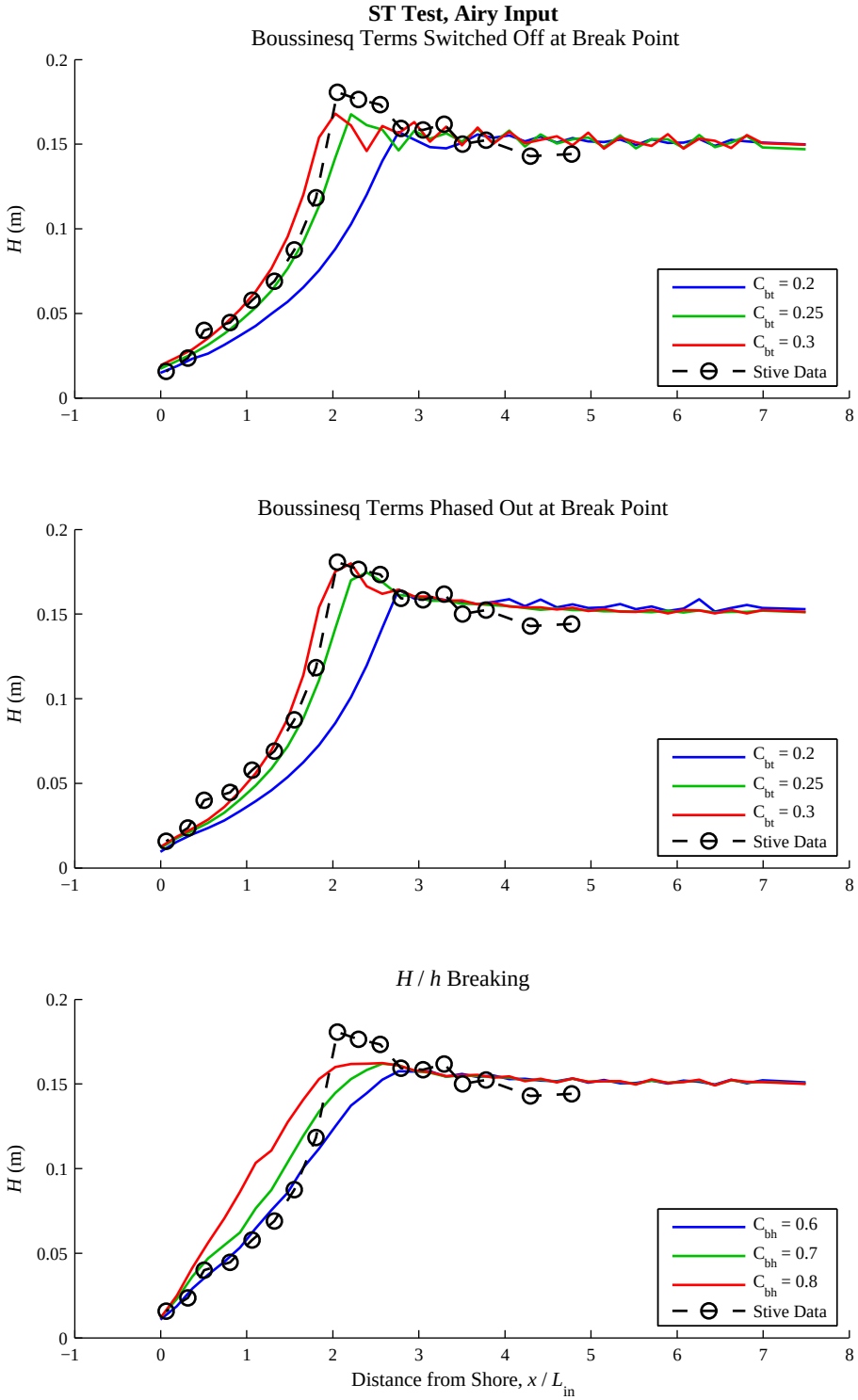

Figure 5.3: Wave heights in the nearshore: SWAB runs compared with experimental data. ST Test, Airy wave input, $\xi_0 = 0.138$

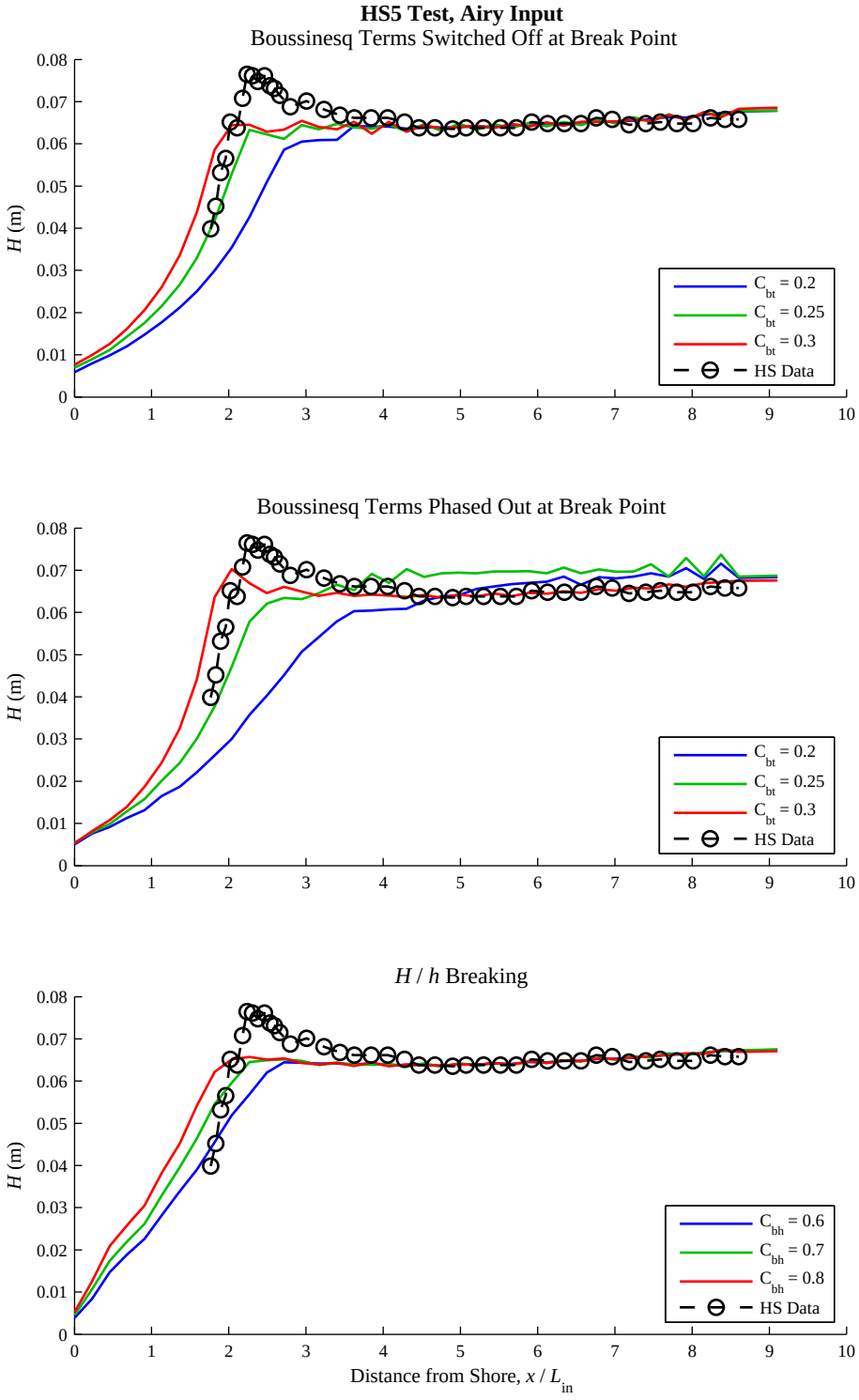

Figure 5.4: Wave heights in the nearshore: SWAB runs compared with experimental data. HS5 Test, Airy wave input, $\xi_0 = 0.136$

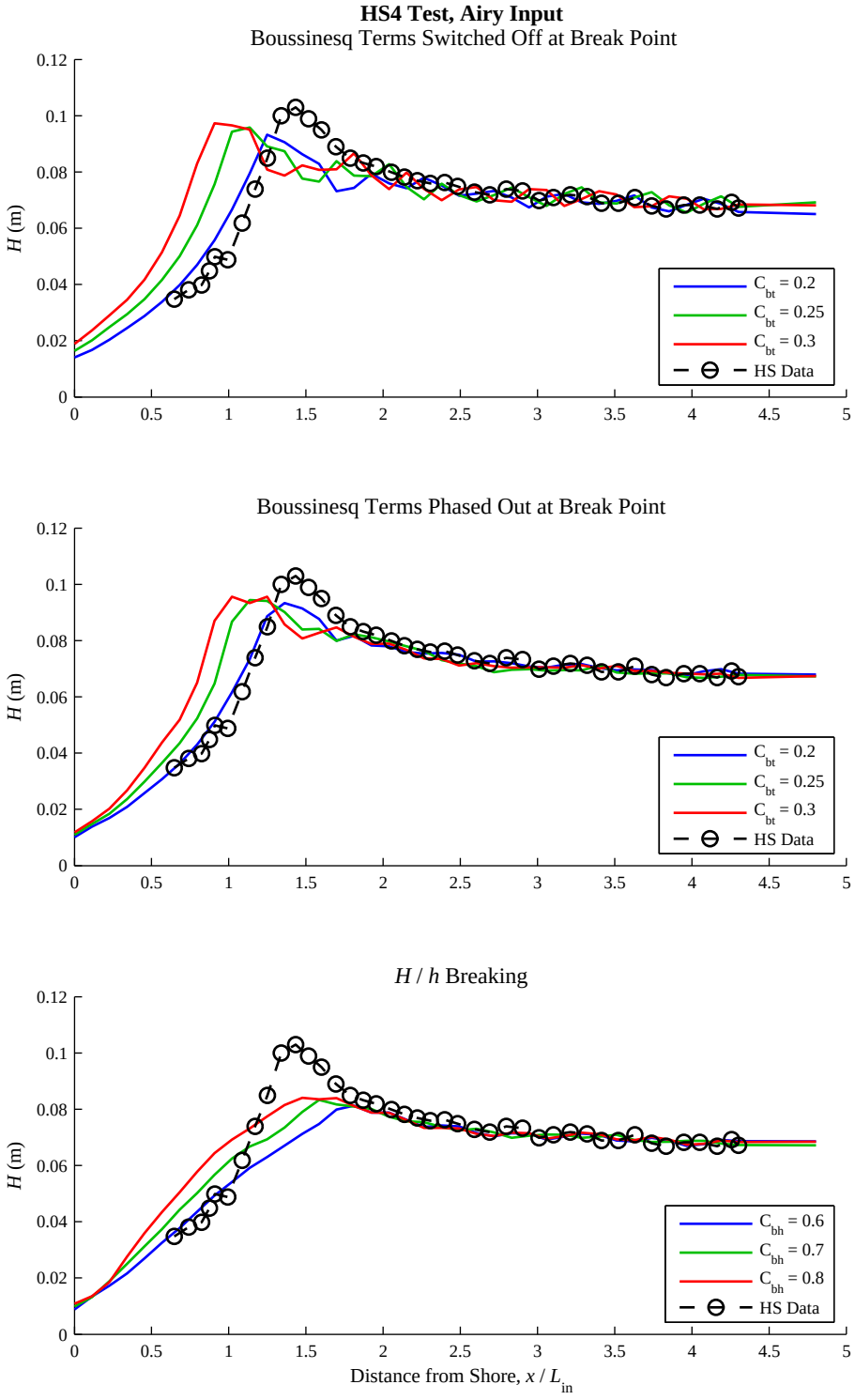

Figure 5.5: Wave heights in the nearshore: SWAB runs compared with experimental data. HS4 Test, Airy wave input, $\xi_0 = 0.230$

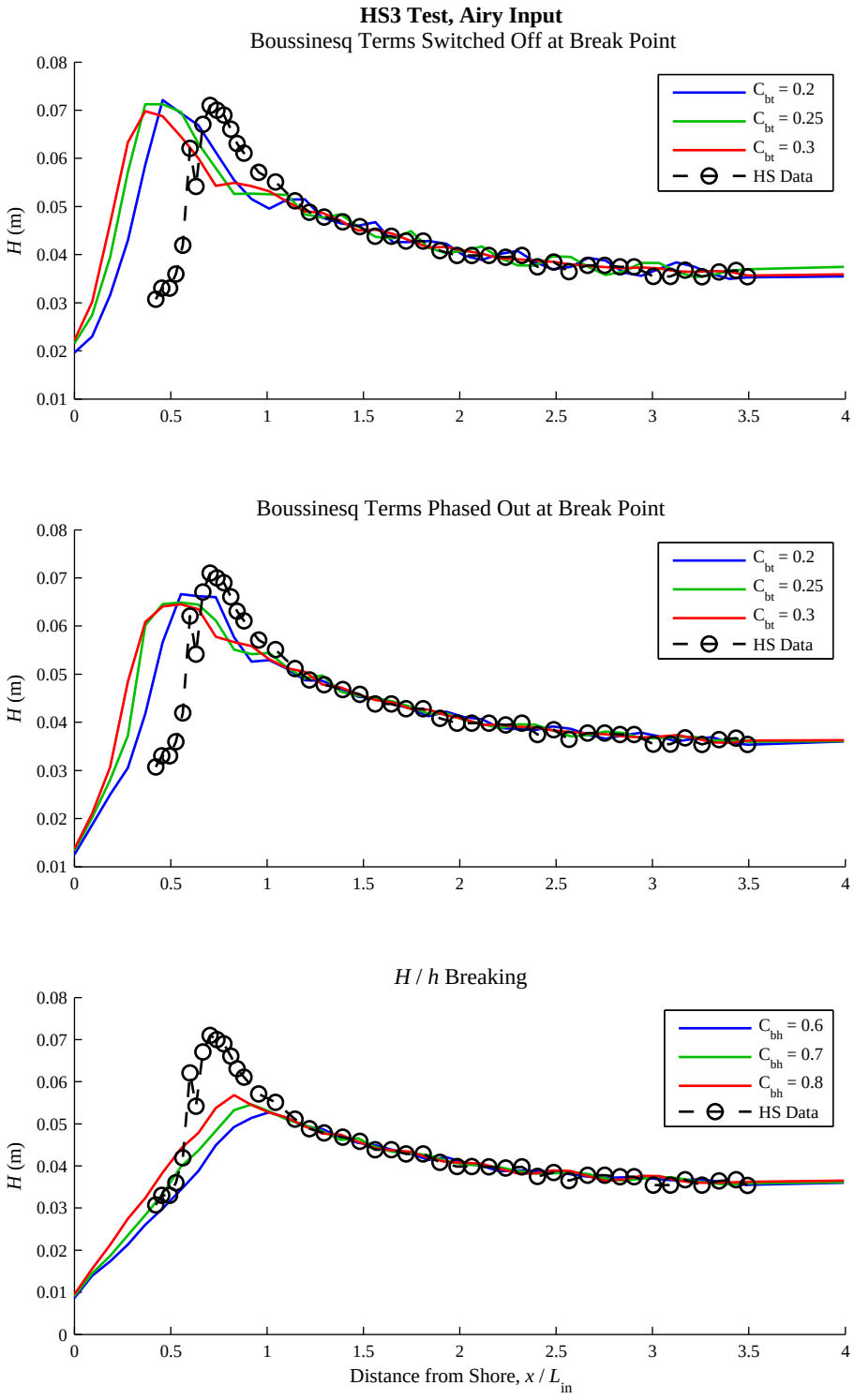

Figure 5.6: Wave heights in the nearshore: SWAB runs compared with experimental data. HS3 Test, Airy wave input, $\xi_0 = 0.384$

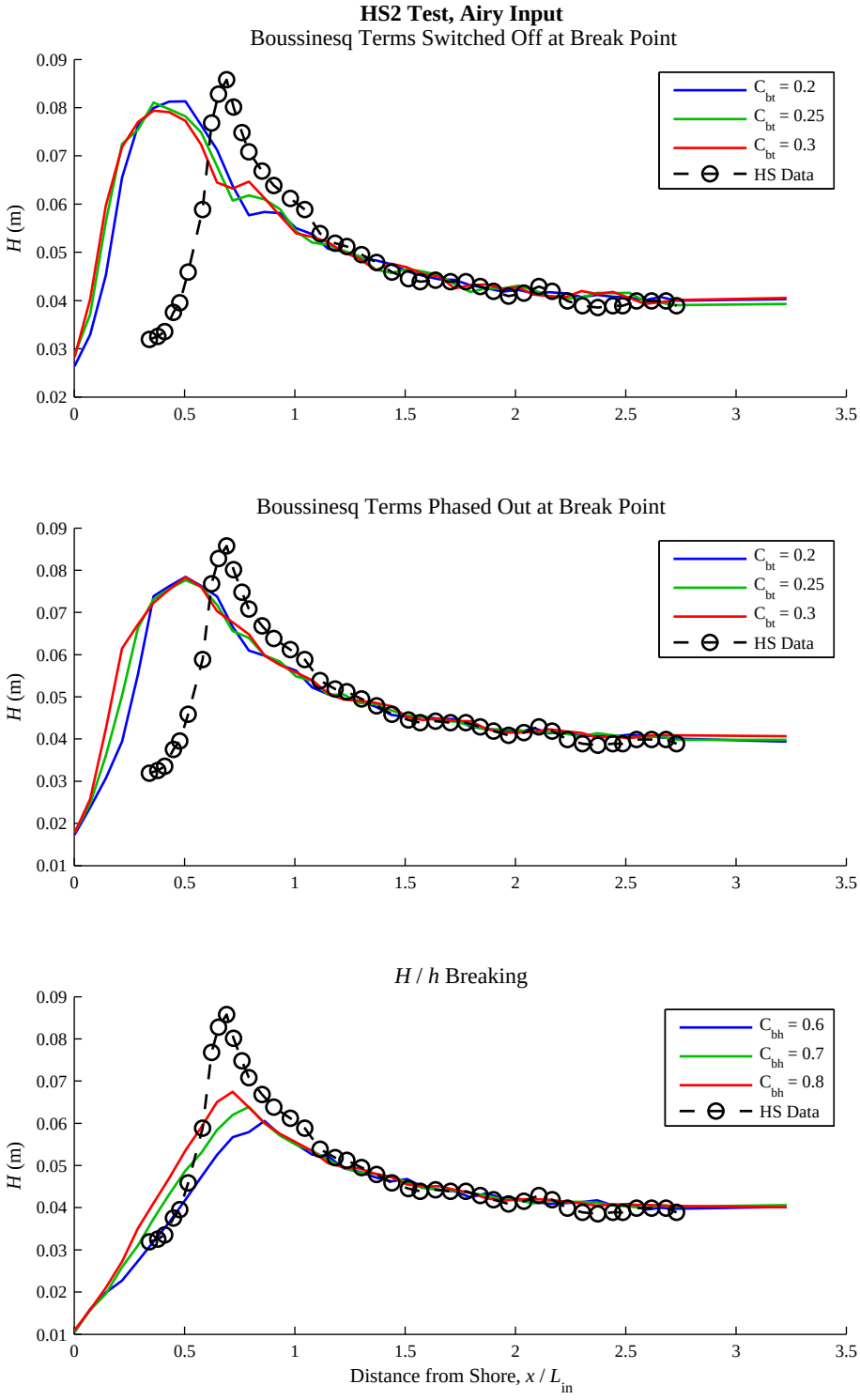

Figure 5.7: Wave heights in the nearshore: SWAB runs compared with experimental data. HS2 Test, Airy wave input, $\xi_0 = 0.480$

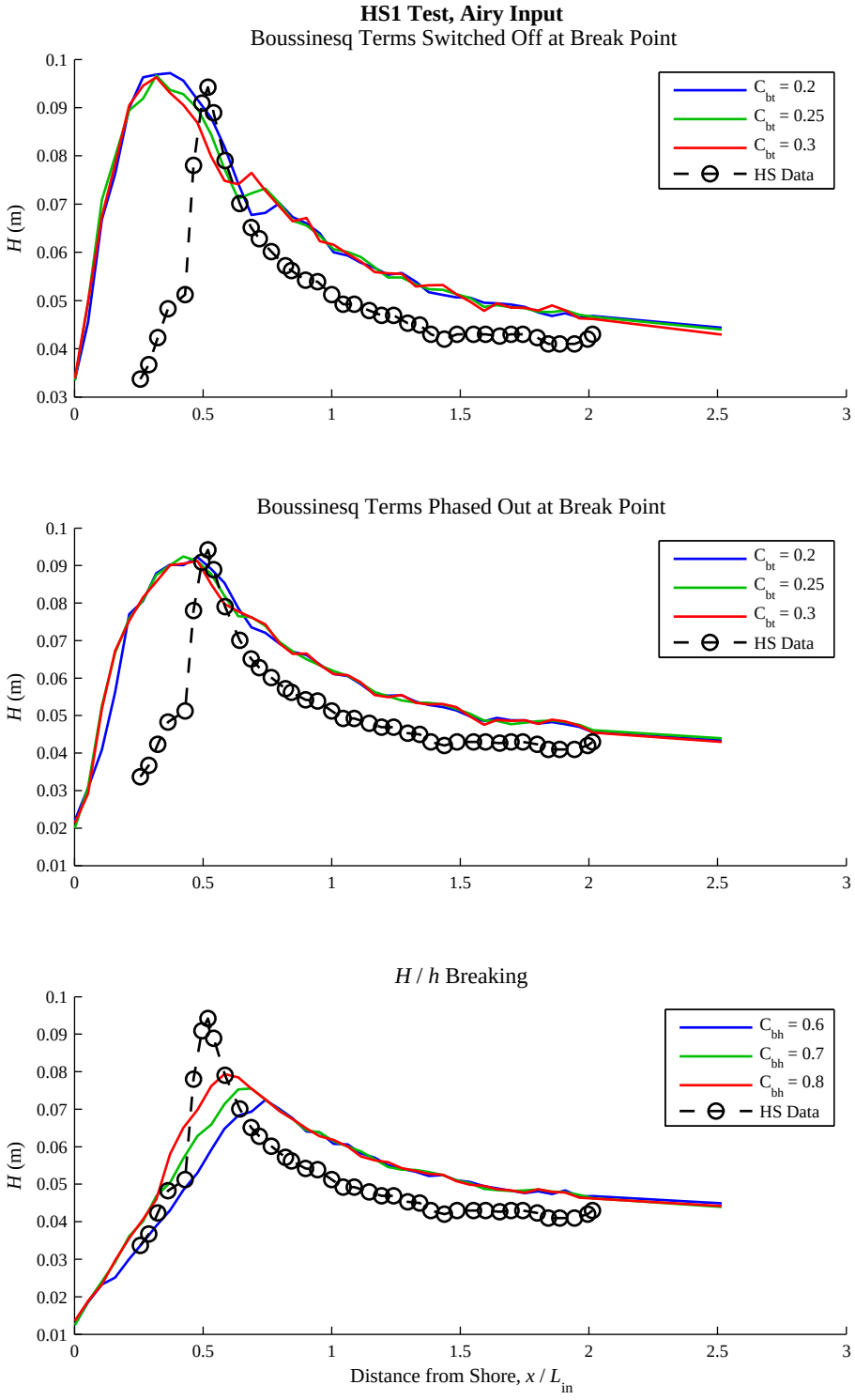

Figure 5.8: Wave heights in the nearshore: SWAB runs compared with experimental data. HS1 Test, Airy wave input, $\xi_0 = 0.646$

wave setup close to the shore is much too great. By phasing out the Boussinesq terms, the magnitude and location of the setup are much improved.

Outputs of the Boussinesq and horizontal diffusion terms pre- and post-breaking were also taken. Figures 5.12, 5.13 and 5.14 show values in the nearshore at two different times, approximately half of one period apart. For non-breaking waves, non-zero Boussinesq terms occur on the sloping free-surface between the crests and troughs, preventing the waves from steepening into shallow-water bores. For breaking waves the horizontal diffusion terms impose a force only on the front face of the wave; near the trough this force is towards the shore and near the crest it is offshore (positive Boussinesq and diffusion in Figures 5.12 to 5.14 represent an onshore force). Phasing out the Boussinesq terms results in larger offshore forces acting at the wave crest, resulting in the steepening of the crest, and a relatively smaller onshore force acting on the wave trough. This appears to have the effect of reducing the wave setup during the initial stages of breaking.

For the H/h breaking criterion, breaking initially takes place further offshore. As a breaking wave approaches the shore, it drops in height and becomes non-breaking again, until it once again exceeds the height-to-depth threshold and breaks again. Unfortunately, this prevents the waves from being able to reach their correct maximum pre-breaking height, but it does result in accurate depth-limited waves in the surf zone.

The TK2 test input contains very nonlinear waves. As Figure 5.15 (a) shows, the Airy input does not give a clean waveform, producing unwanted free components. However, the SAWW wave input produces little improvement (Figure 5.15 (b)), although it results in more accurate crest and trough levels near the shore. The TK21 test used linear wave theory to transform the input wave conditions of Ting and Kirby [1994] offshore into water of twice the depth; by using these transformed wave conditions as a wave input, there are fewer parasitic oscillations pre-breaking (Figure 5.15 (c)). Close to the shore, there is very little difference between the TK2 and TK21 test. For the comparison between different breaking criteria, Figure 5.15 (d) shows SWAB output using the $\partial\eta/\partial t$ criterion; as with the other tests with high surf similarity parameters (HS3, HS2 and HS1), wave crests in the surf zone remain too high, resulting in waves that are not sufficiently depth-limited. In comparison with Figure 5.15 (d), Figure 5.15 (c) (which uses the H/h criterion) shows the breaking process starting too soon; however as these waves approach the shore they match well to the experimental data.

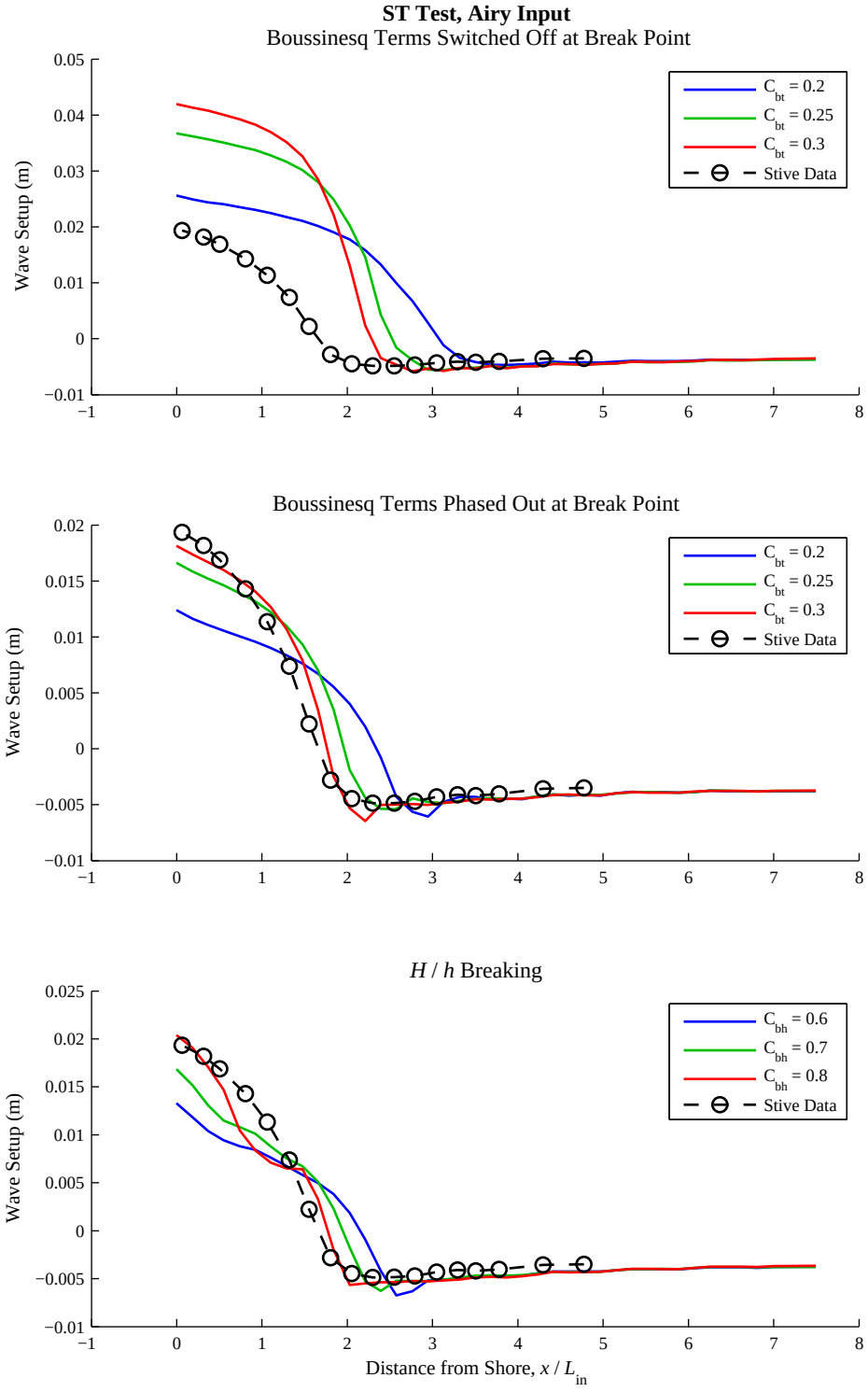

Figure 5.9: Wave setup in the nearshore: SWAB runs compared with experimental data. ST Test, Airy wave input, $\xi_0 = 0.138$

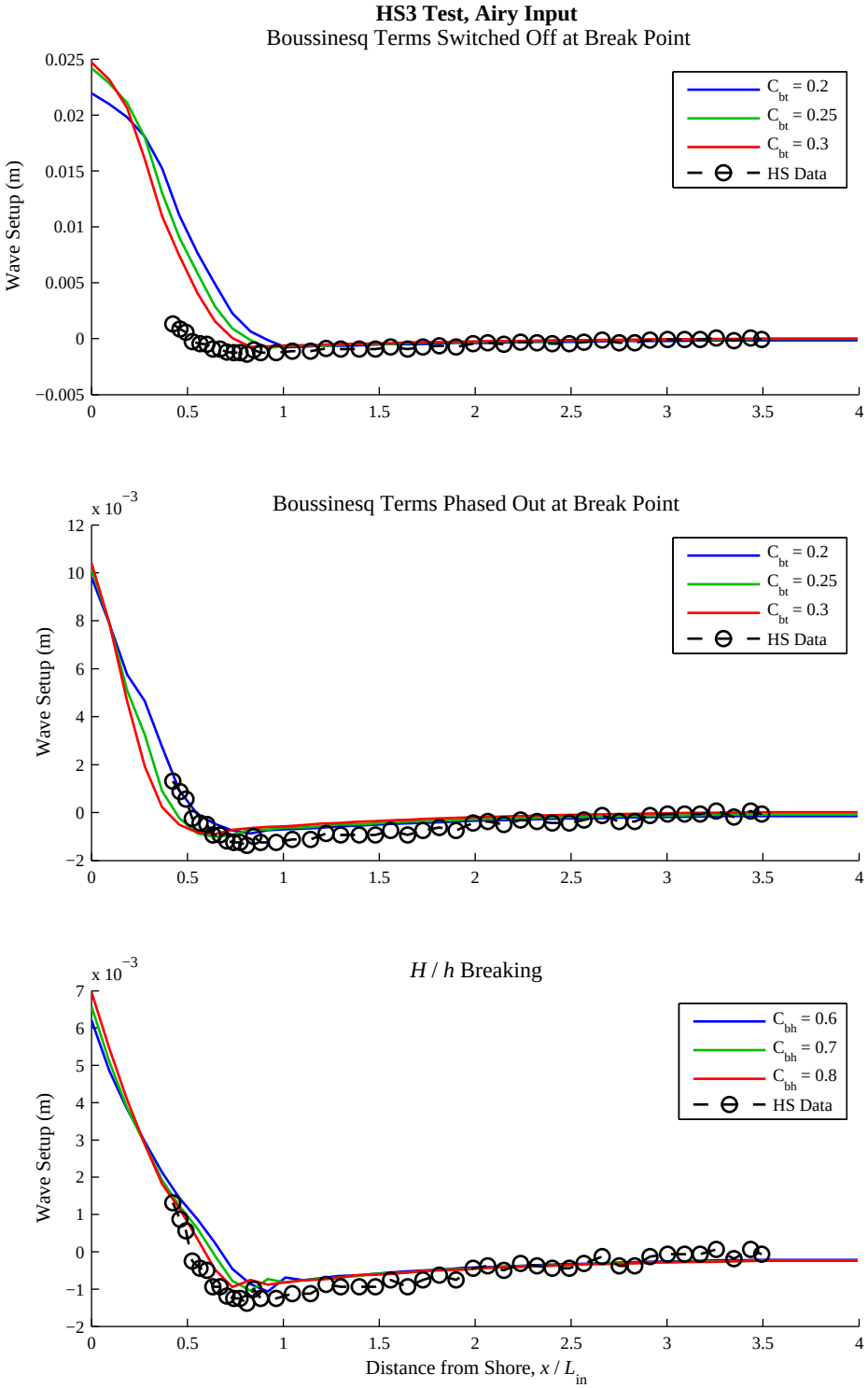

Figure 5.10: Wave setup in the nearshore: SWAB runs compared with experimental data. HS3 Test, Airy wave input, $\xi_0 = 0.384$

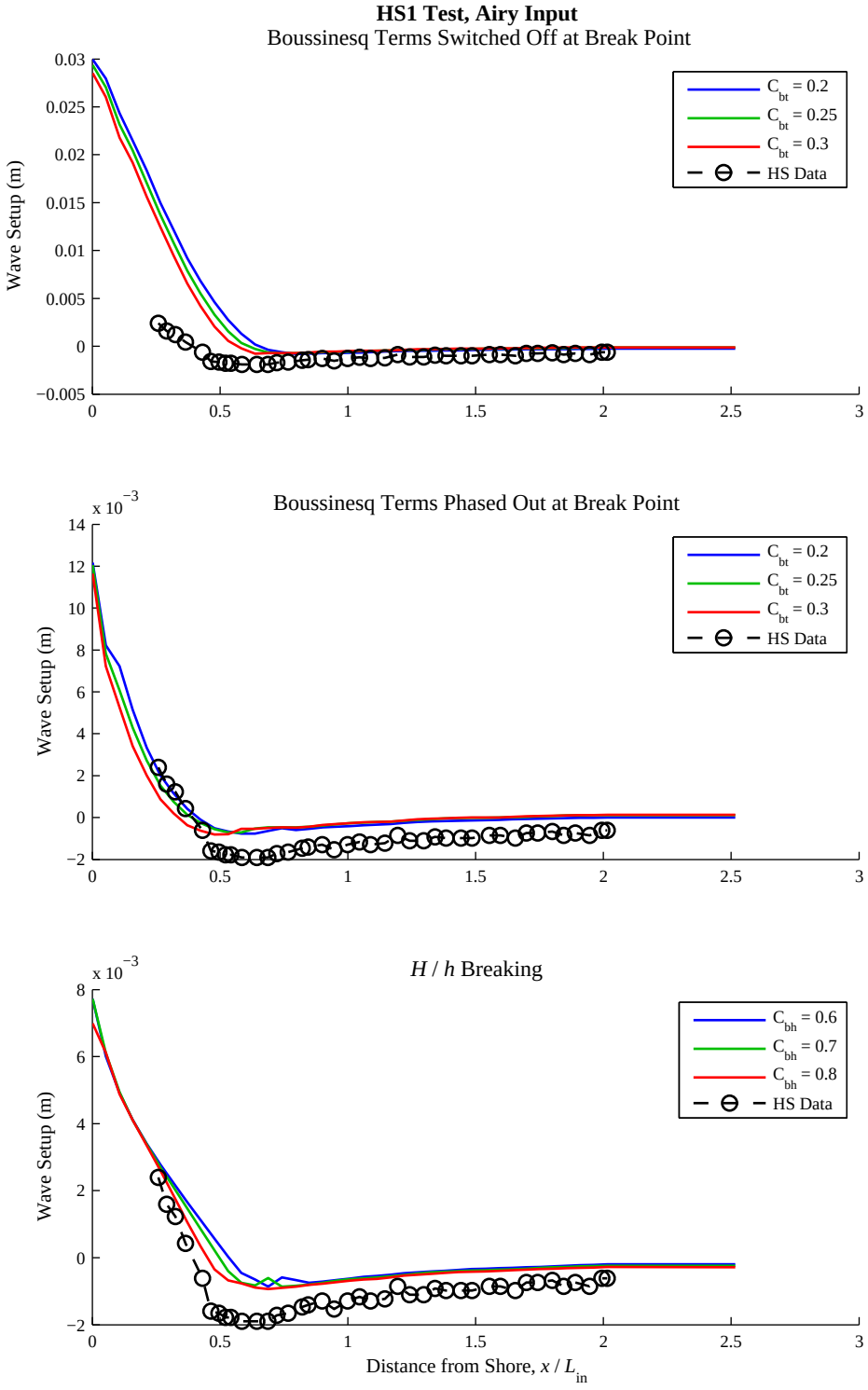

Figure 5.11: Wave setup in the nearshore: SWAB runs compared with experimental data. HS1 Test, Airy wave input, $\xi_0 = 0.646$

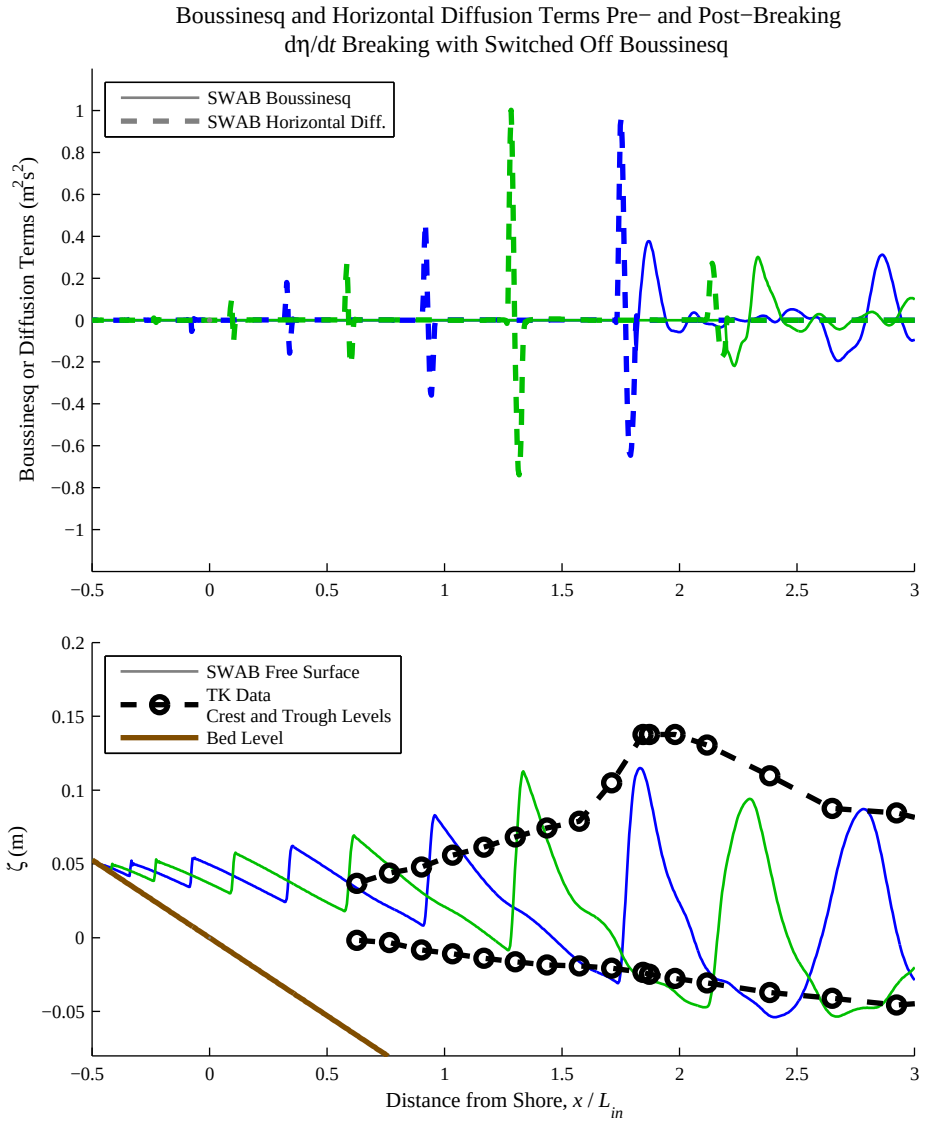

Figure 5.12: Boussinesq and horizontal diffusion terms across the nearshore at two time-steps approximately $T/2$ apart, with simultaneous free surface levels and Ting and Kirby [1994] mean crest and trough levels. TK1 test with SAWW wave input ($\xi_0 = 0.200$), $\partial\eta/\partial t$ breaking without phased-out Boussinesq terms, $C_{bt} = 0.25$

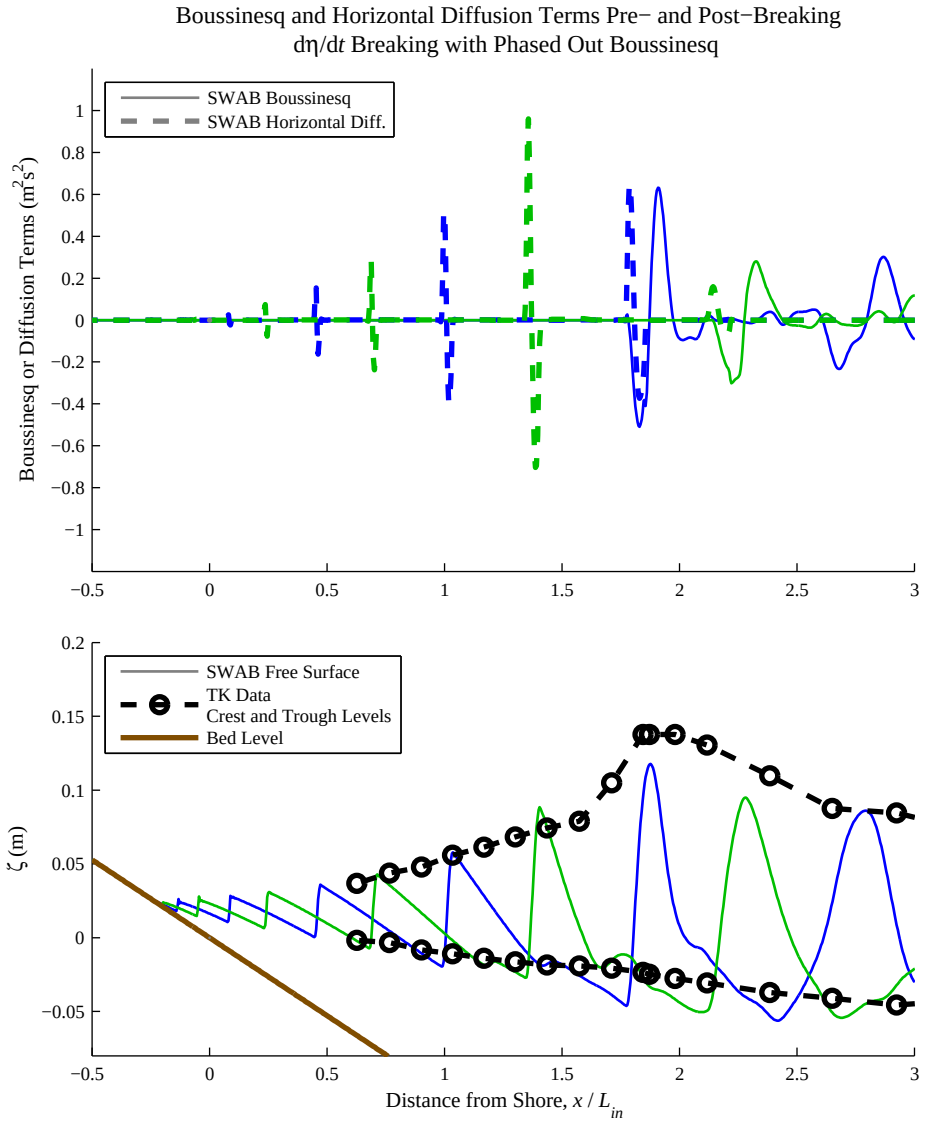

Figure 5.13: Boussinesq and horizontal diffusion terms across the nearshore at two time-steps approximately $T/2$ apart, with simultaneous free surface levels and Ting and Kirby [1994] mean crest and trough levels. TK1 test with SAWW wave input ($\xi_0 = 0.200$), $\partial\eta/\partial t$ breaking with phased-out Boussinesq terms, $C_{bt} = 0.25$

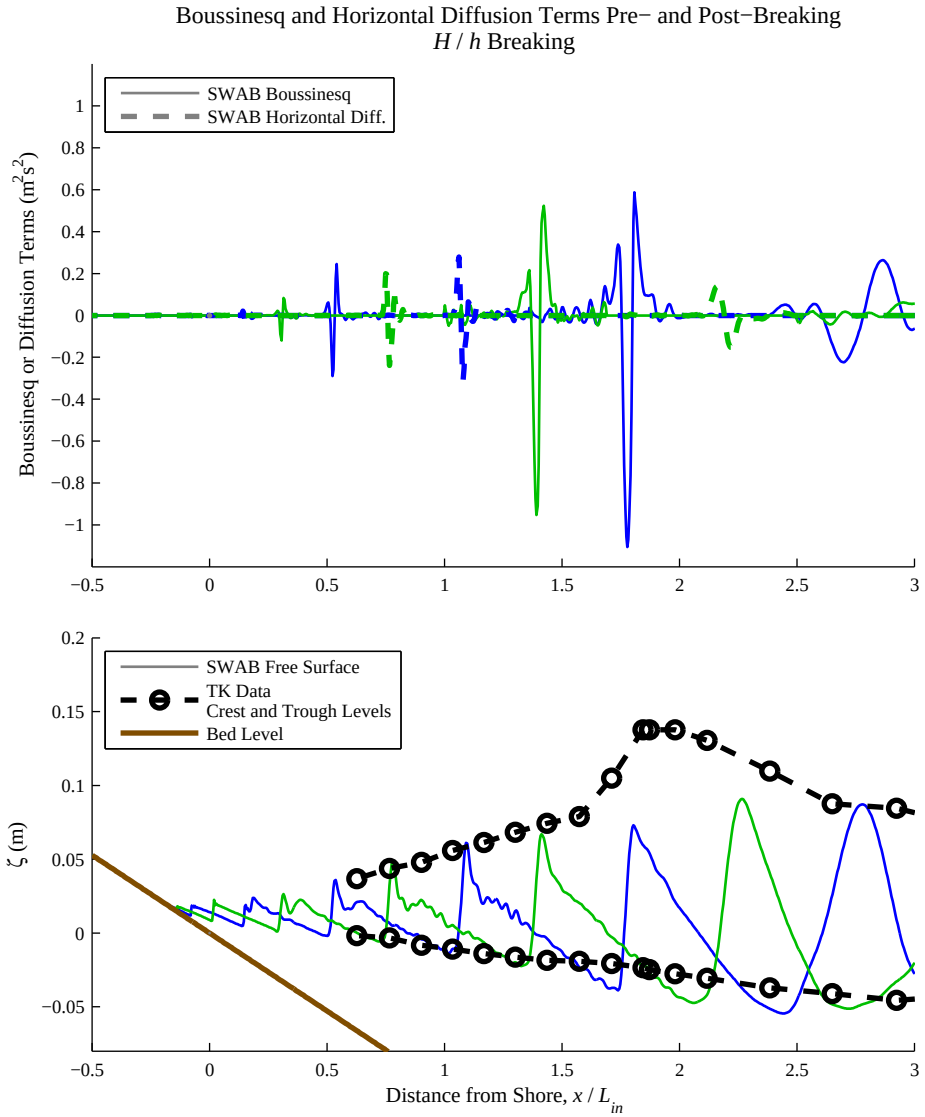

Figure 5.14: Boussinesq and horizontal diffusion terms across the nearshore at two time-steps approximately $T/2$ apart, with simultaneous free surface levels and Ting and Kirby [1994] mean crest and trough levels. TK1 test with SAWW wave input ($\xi_0 = 0.200$), H/h breaking, $C_{bh} = 0.6$

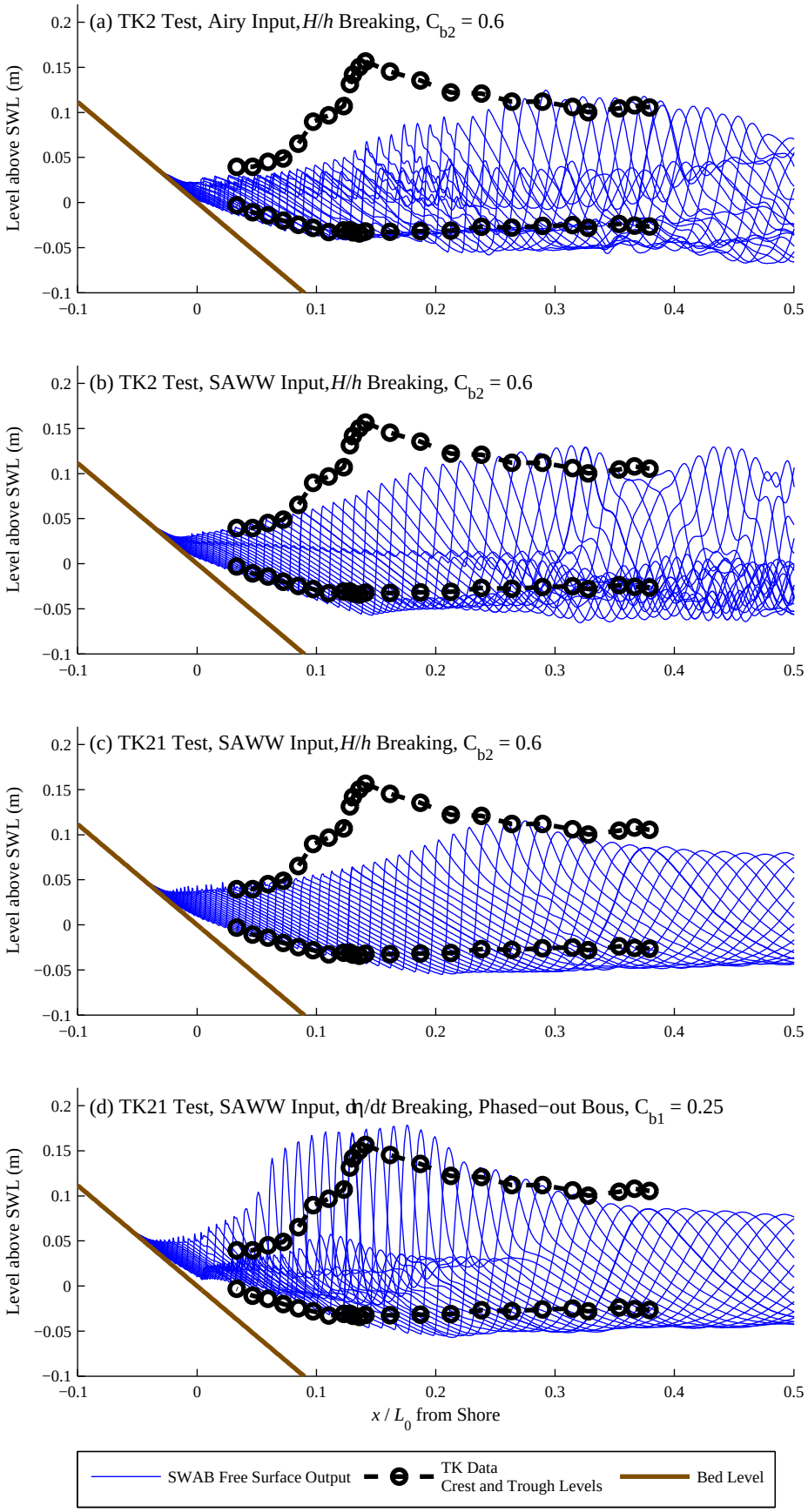

Figure 5.15: TK2 and TK21 model runs with SWAB output at several time-steps ($\xi_0 = 0.596$). Comparison between wave input types and breaking criteria

5.2 Random Waves on a Plane Slope

5.2.1 SWAB testing methodology

Results from the tests of Stive [1985] and Ting [2001] were used to check the SWAB model's ability to model random waves (Test Conditions ST1, ST2, ST3 and TI: Table 4.2). Two sets of SWAB 3.0 model tests were set-up with the same bathymetries used in the physical model tests: firstly using the $\partial\eta/\partial t$ breaking model with a breaking coefficient, C_{bt}, of 0.25; and secondly using the H/h breaking criterion with a coefficient, C_{bh}, of 0.60. Wave input type "ASP" was used for these tests (Table 3.1). Because these are random waves and time-series data from the experiments are not available, the TI tests (for which more detailed data on wave height distributions were available) were repeated with a different set of random phases. Each test run consisted of 150 waves, with a time-step, dt/T_{m02}, of $1/2000$.

5.2.2 Nearshore phase averaged parameters

Figure 5.16 shows spectral rms wave heights in the nearshore. The rms wave heights published by Stive [1985] were also calculated spectrally (i.e. $H_{rms} = \sqrt{8m_0}$ as opposed to $H_{rms} = \sqrt{\frac{1}{N}\sum^{N} H^2}$); Ting [2001] does not describe how their rms wave heights were calculated, although both methods should give similar results. The SWAB model generally gives excellent results. For random waves there is no fixed break point; instead waves will break at various points in the nearshore. Therefore, some of the errors that occur around the breaking point for regular wave tests (Figure 5.15, for example) are not as immediately apparent for random waves. For higher surf similarity parameters (the ST2 test), the $\partial\eta/\partial t$ breaking criterion does not work as well as the H/h criterion, with too little decay in the initial part of the surf zone.

Figure 5.17, showing wave setup in the nearshore, also gives some good results. For the TI test, the experimental pre-breaking set-down is zero; different to the SWAB model prediction. It is unclear why this difference exists, though for the H/h breaking the difference between maximum set-down and setup agrees well with the experiment. A difference between the length of the wave flume and the length of the domain in the SWAB model may also contribute; the volume of wave setup must be taken from elsewhere in a domain. Additionally, the magnitude of wave setup and set-down is of the order of millimetres; the instrumentation in the flume may not be sufficiently sensitive to give accurate results.

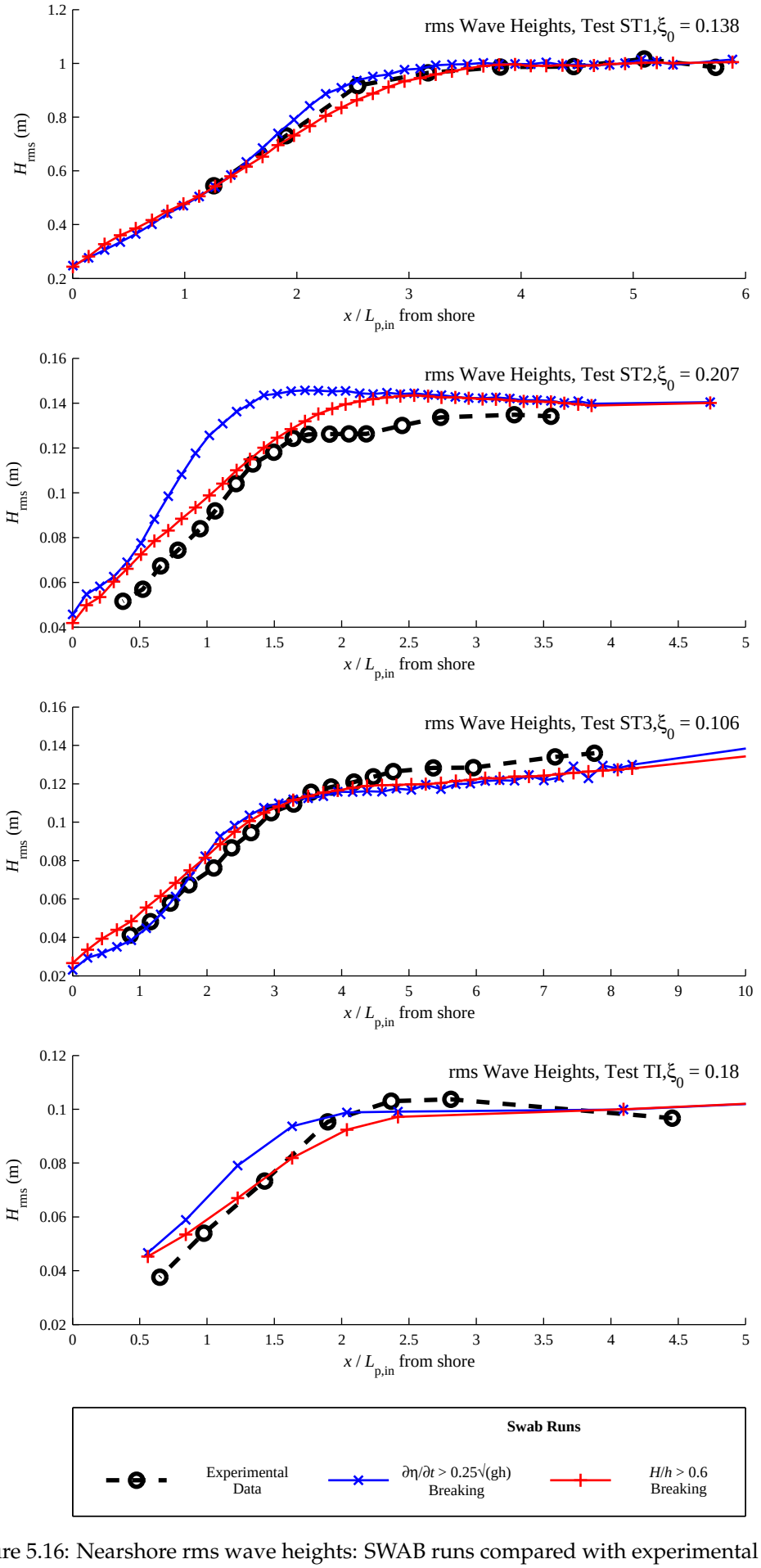

Figure 5.16: Nearshore rms wave heights: SWAB runs compared with experimental data

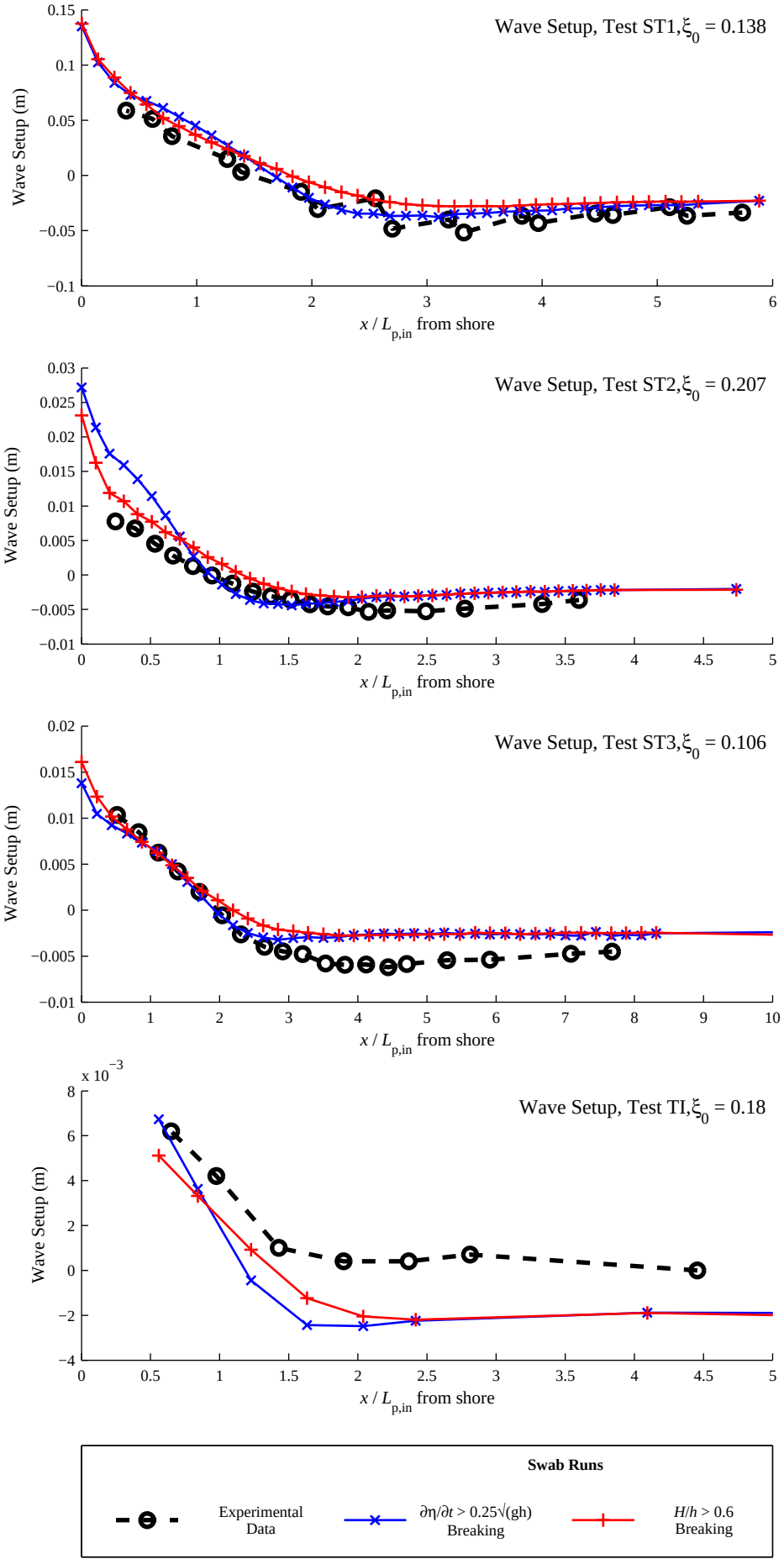

Figure 5.17: Nearshore wave setup: SWAB runs compared with experimental data

5.2.3 Wave breaking and wave height distributions

Figure 5.18 shows wave height exceedance probabilities at six locations in the nearshore for the TI run. The SWAB model performs well; however, closer to the shore it overestimates the proportion of smaller waves. For example, at $0.56L_{p,in}$ from the shore, the SWAB model predicts that 30 % to 40 % of waves have a height less than $0.5H_{1/3}$, whereas only 20 % of waves were below this height in the experiments. Firstly, the SWAB model overestimates the significant wave height in this region and the results are normalised relative to $H_{1/3}$; $0.5H_{1/3}$ for the SWAB model is therefore larger than $0.5H_{1/3}$ in the experiments, which partly explains why more waves are included at this end of the distribution. Also, as will be explained later in this section (see Figure 5.25), small differences in separating waves from a time-series (for example, by having a slightly different mean water level to separate the waves), can have a large effect on waves parameters and distributions in the nearshore region. There is little difference between the two breaking criteria, though the H/h type appears to be slightly closer to the experimental data.

Figure 5.19 shows that the SWAB model also underperforms in depth-limiting the highest waves very close to the shore. Although mean wave heights remain close to the experimental data, the highest waves become proportionally too large. Once again the two breaking criteria give similar results, although in the initial stages of breaking (where $1 < h/H_0 < 2$) the H/h criterion remains very close to the experiments.

Repeating the tests makes a small difference to the results, the difference between runs is less than the difference between the SWAB model and the experimental data. Figure 5.20 shows significant wave heights for the repeated runs. Note that the $\partial\eta/\partial t$ and H/h breaking runs used the same set of random phases for Run 1, but not the same set as each other for Run 2 (so effectively three sets of random phases can be seen in Figure 5.21). Figure 5.21 shows wave height exceedance proportions for two different SWAB runs, for each of the breaking criteria. Once again, the difference between runs is generally less than the error from the experimental data.

Modifying the breaking coefficient has a greater effect on the results. As expected, a lower breaking coefficient gives lower significant wave heights in the nearshore (Figure 5.22). However, the $\partial\eta/\partial t$ criterion appears to be more effective at depth-limiting the waves very close to the shore, although, as Figure 5.23 shows, the maximum waves in this region are still too large. Ting [2001] also published results on wave periods in the surf zone. Figure 5.24 shows that for both breaking criteria, the SWAB model overestimates nearshore wave periods. However, these results require some caution. Since there was no active absorption at the paddle for the

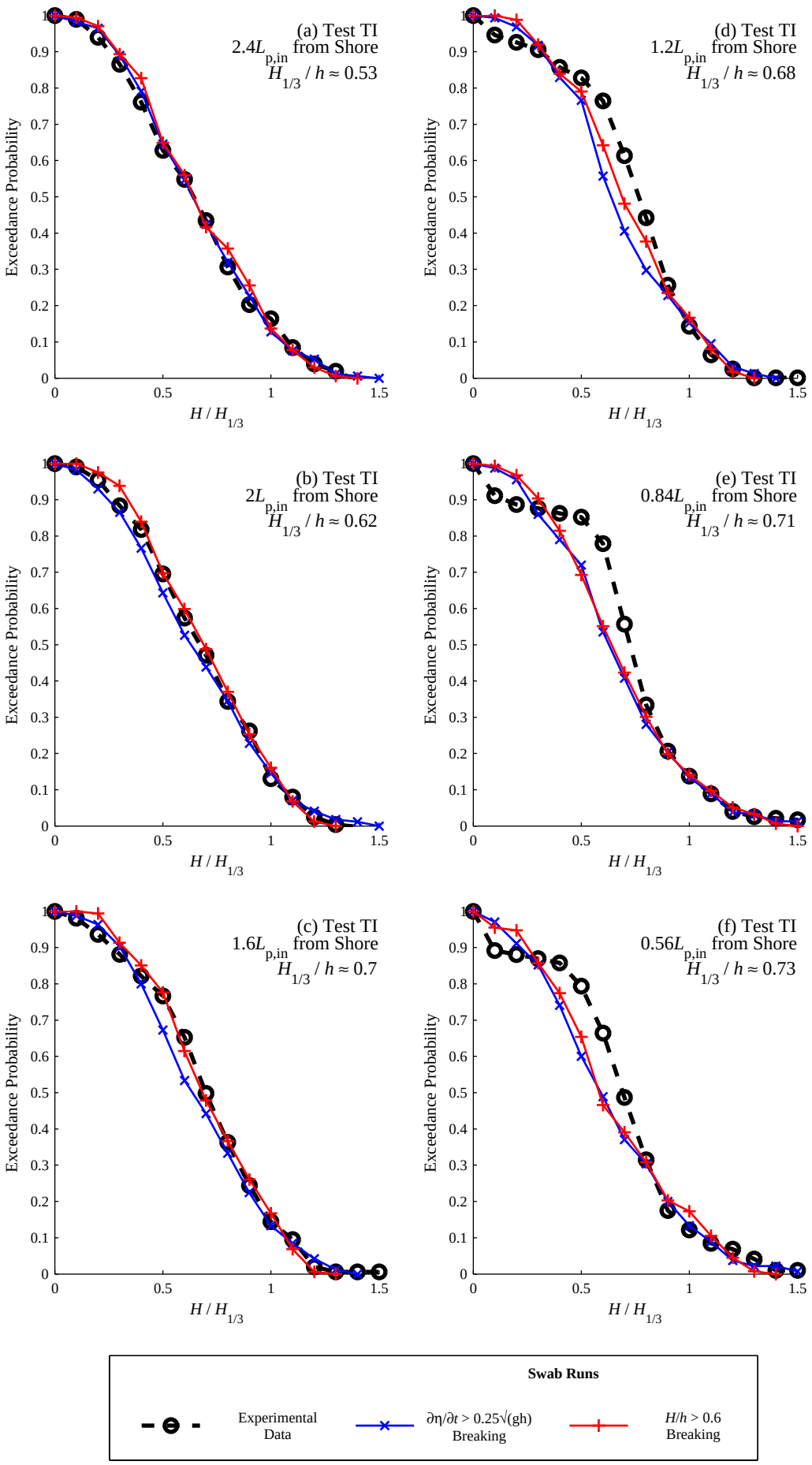

Figure 5.18: Wave height distributions in the nearshore: SWAB runs compared with Ting [2001] data

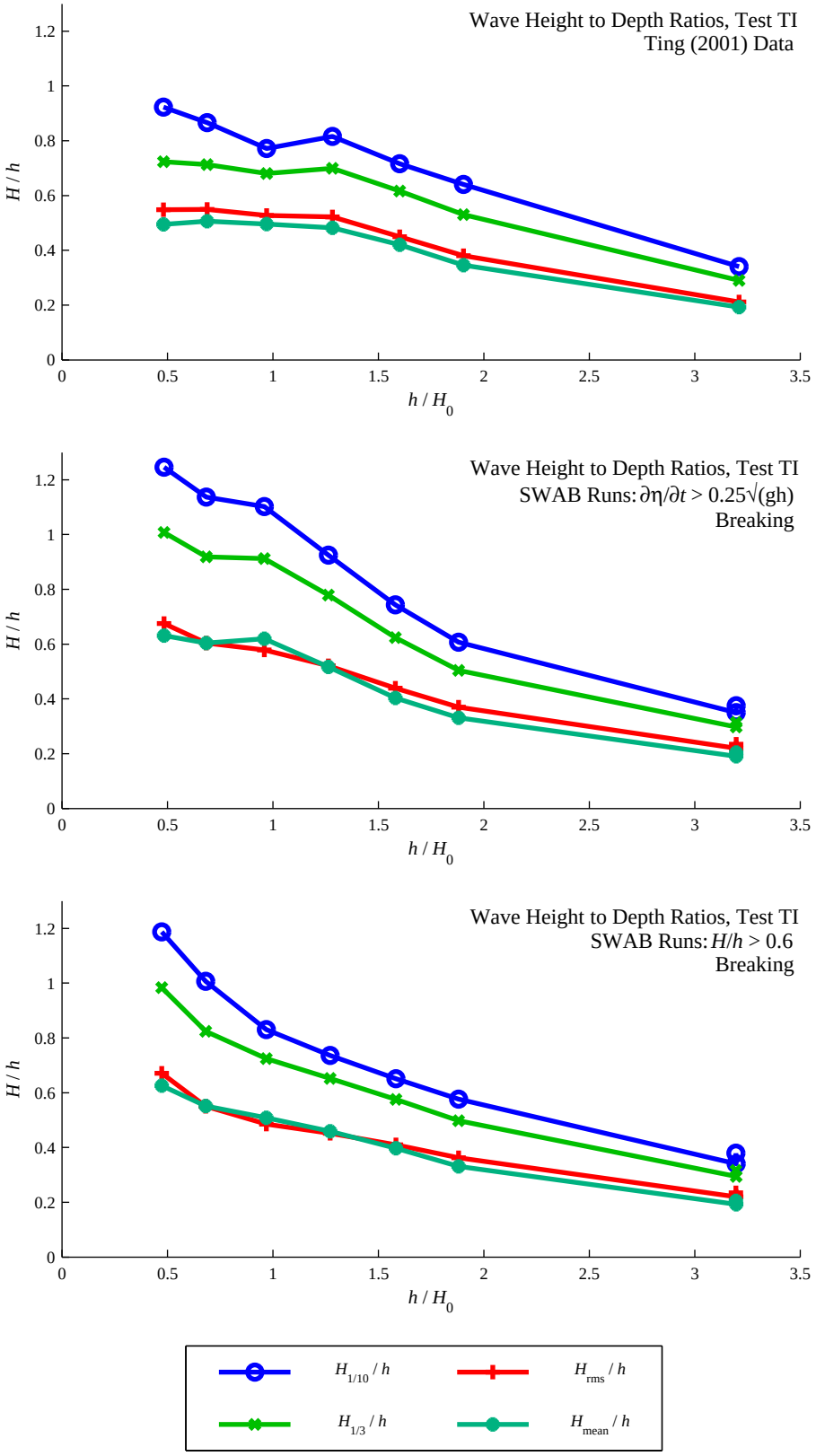

Figure 5.19: Nearshore normalised wave heights: SWAB runs compared with Ting [2001] data. The six data points nearest the shore ($h/H_0 < 2$) are at the same locations as the six wave height distributions shown in Figure 5.18

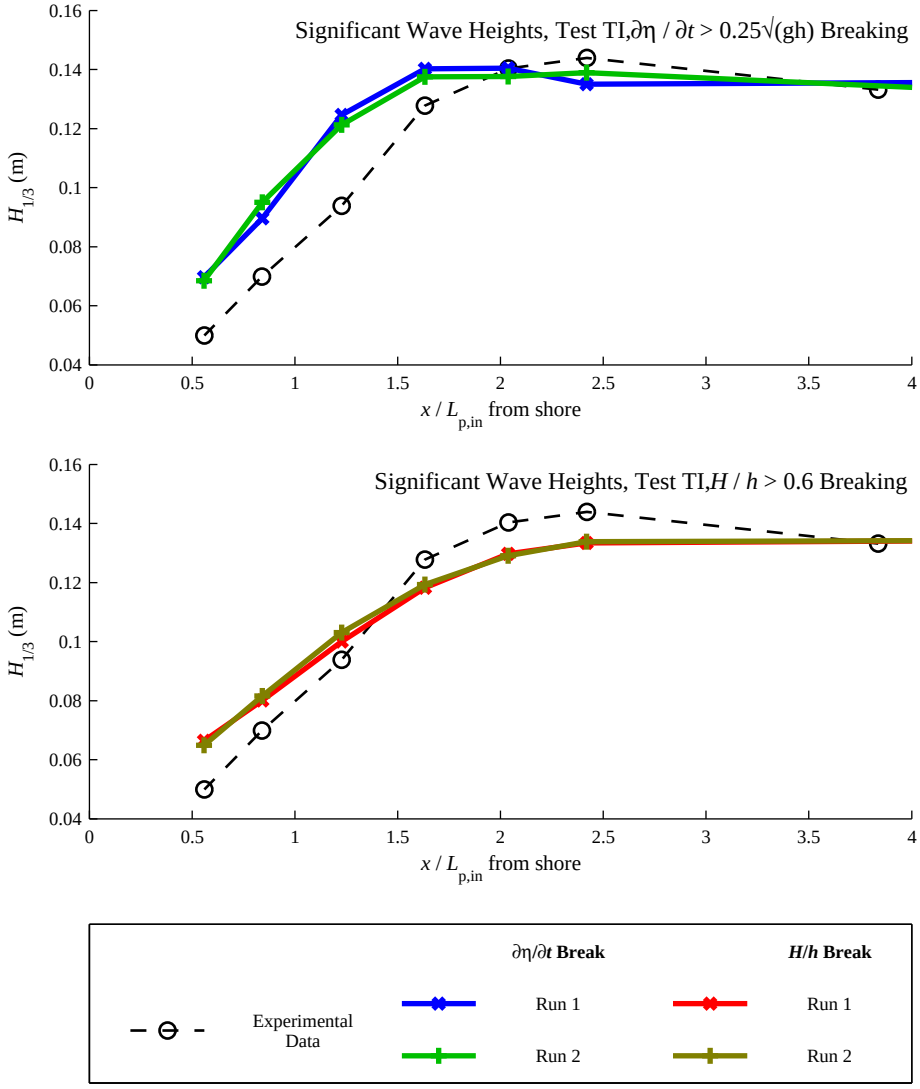

Figure 5.20: Nearshore significant wave heights: repeated SWAB runs and experimental data

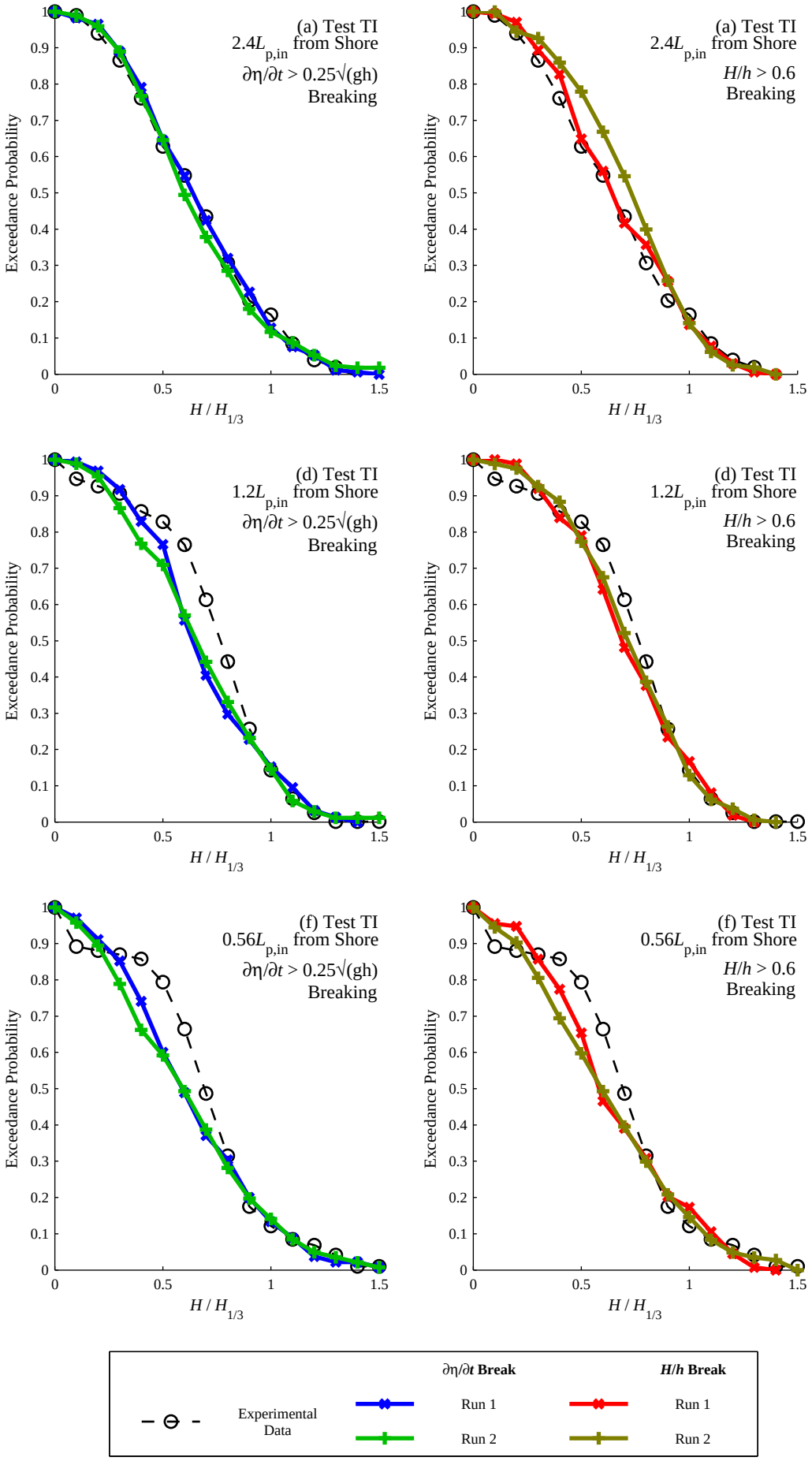

Figure 5.21: Wave height distributions in the nearshore: repeated SWAB runs and experimental data

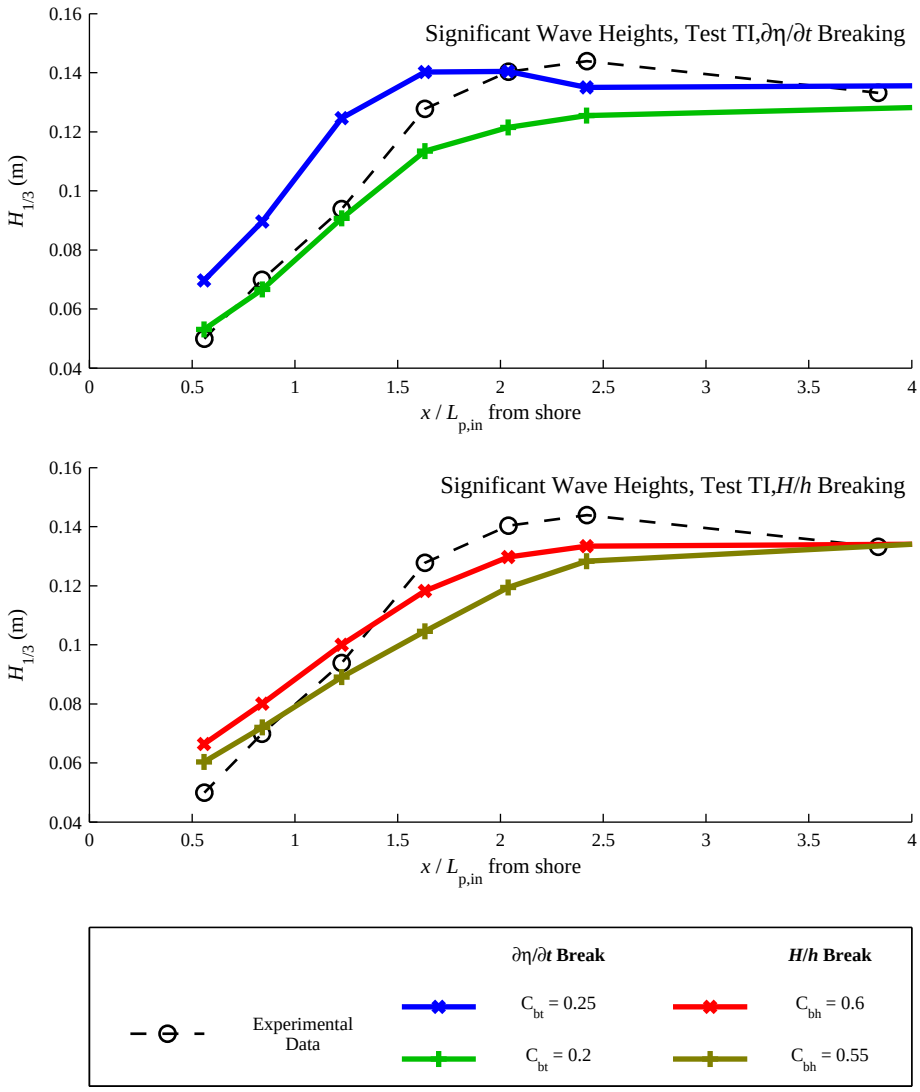

Figure 5.22: Nearshore significant wave heights: effect of changing breaking coefficient

experiments of Ting [2001], the data was subjected to low-pass filtering of long waves. Also, only the data from the second half of each experimental run was used for processing, due to the time required for it to reach a quasi-steady state. The relative amplitudes of long and short waves as well as the mean water level can make a large difference to the measurement of wave periods in the time domain. As an example of this, Figure 5.25 is an extract from the time-series closest to the shore from the SWAB model run with the $H/h > 0.6$ breaking criterion. Figure 5.25a shows only two waves in the 10 s long sample, based on upcrossing points about the mean water level. However, if this water level is raised by 0.01 m (Figure 5.25b), the same sample now consists of seven periods. Therefore, such time-domain analysis of nearshore wave periods may well be rather unreliable.

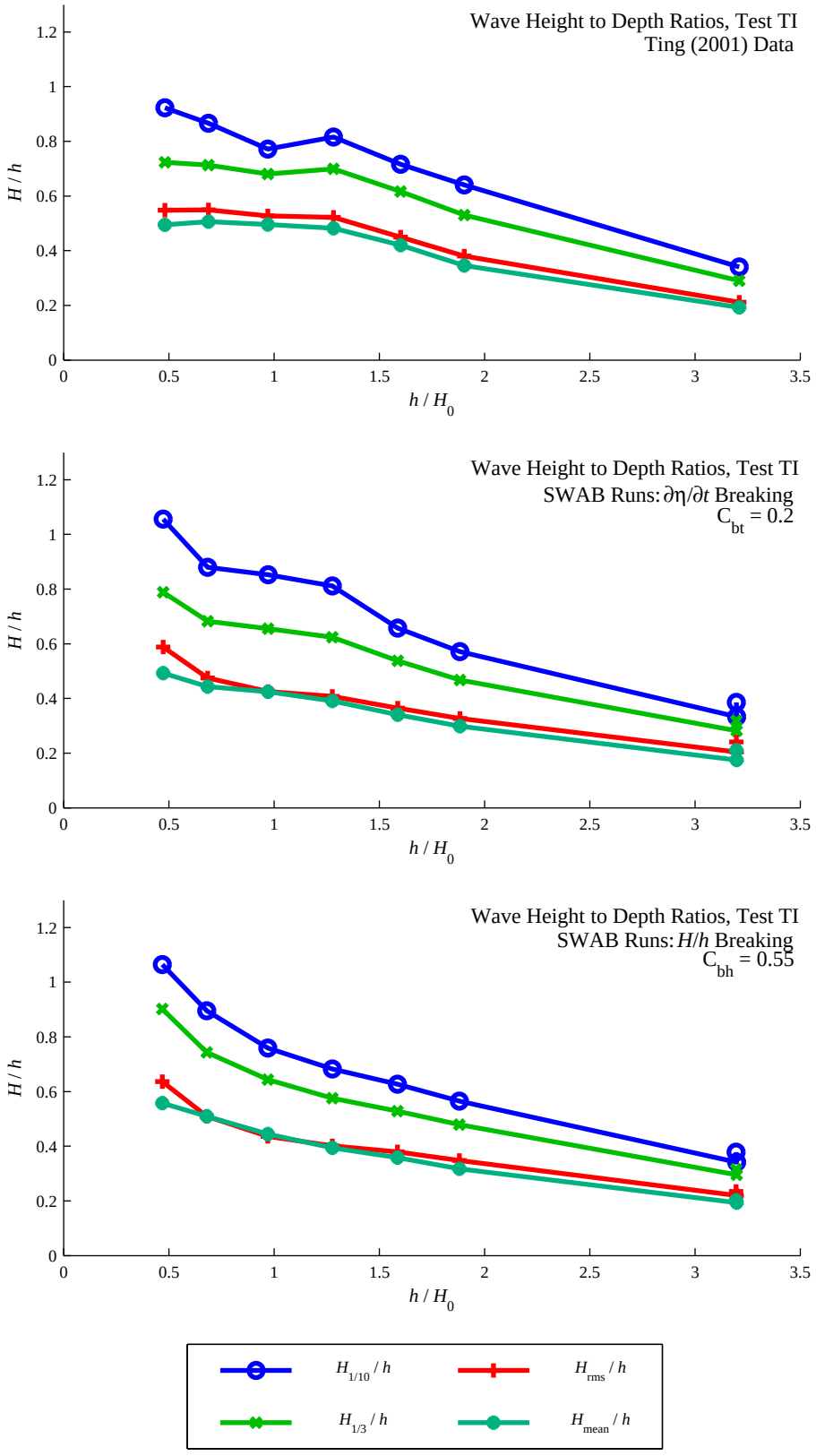

Figure 5.23: Nearshore normalised wave heights: SWAB runs with reduced breaking coefficients compared with Ting [2001] data

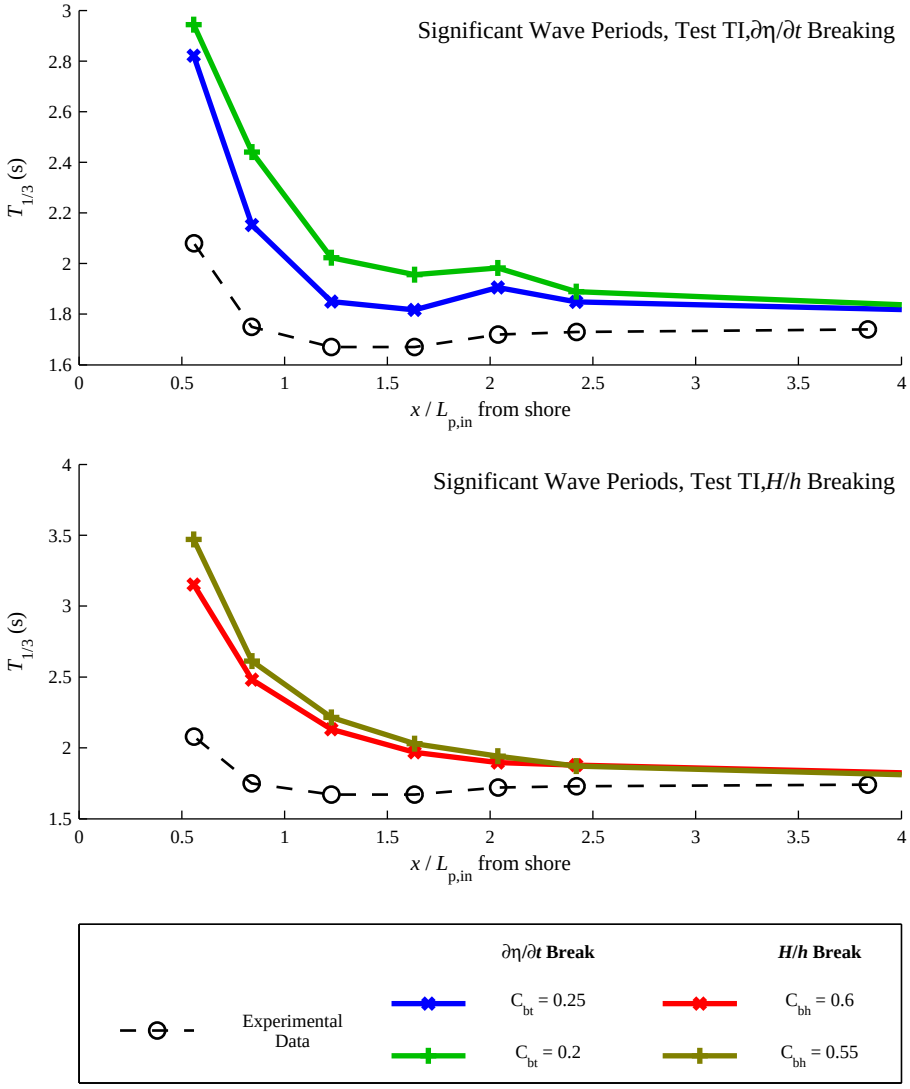

Figure 5.24: Nearshore significant wave periods: effect of changing breaking coefficient

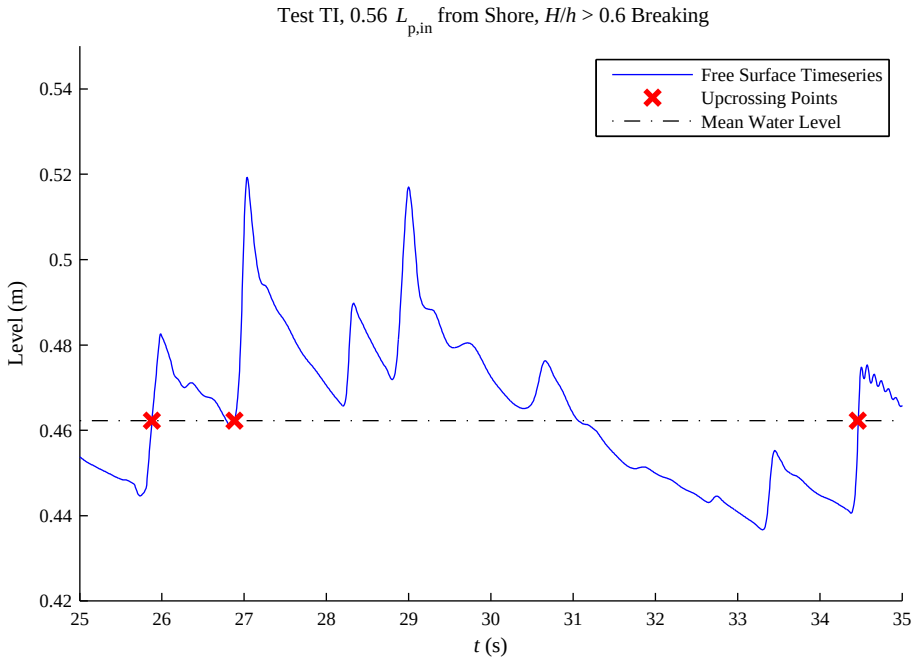

(a) Actual mean water level

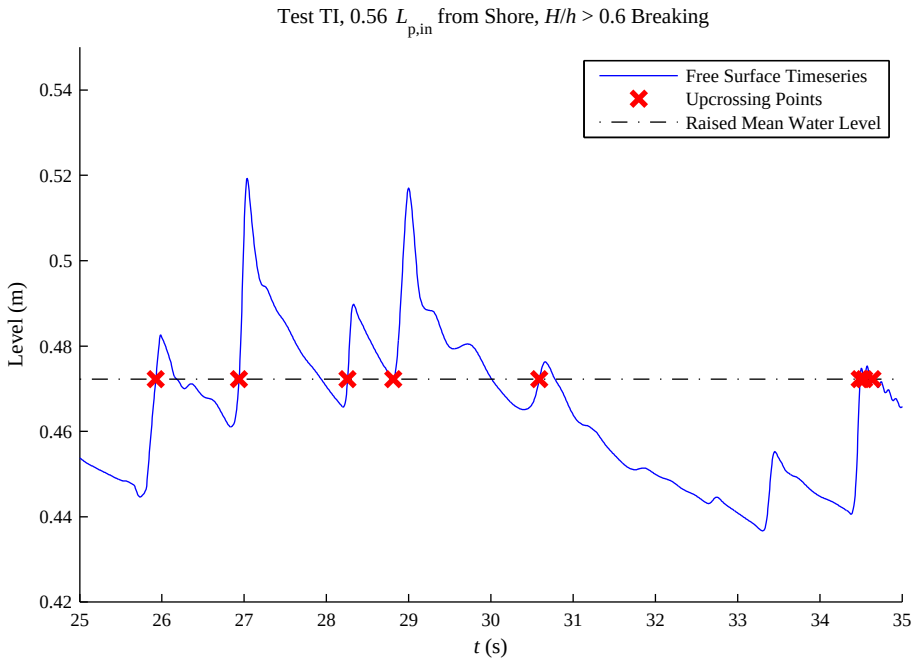

(b) Raised mean water level

Figure 5.25: Extract from nearshore time-series: sensitivity of wave period to mean water level

5.3 Random Waves with a Submerged Reef

5.3.1 SWAB testing methodology

Mase [2008] provided time-series from the tests for waves propagating over a submerged reef presented by Mase et al. [2004]. The experimental set up is as shown in Figure 4.1. The SWAB model was set up with the same dimensions. The location of W1 was used as the location of the wave input for the model, with a 10.0 m length sponge layer offshore. For the original SWAB runs, using the SWAB 2.0 code, the W1 time-series were input directly into the model. Some of the newer SWAB runs, performed using SWAB 3.0, used the method of Frigaard and Brorsen [1995] to separate the incident and reflected waves, with a Fourier transform of the incident wave train being used to provide a spectral wave input (Type "FS1", Table 3.1). The method of Frigaard and Brorsen [1995] requires two closely-spaced time-series (Δx apart), phase-shifting them such that the incident parts of the signals are in phase, and the reflected components are out of phase. Each component of each signal is transformed separately. The components of Signal 2 are phase-shifted by ϕ_1 and ϕ_2 respectively:

$$\begin{aligned} \phi_1 &= -k\Delta x + \frac{\pi}{2} + m\pi + 2n\pi && (5.3)\\ \phi_2 &= -\frac{\pi}{2} - m\pi - 2n\pi && (5.4)\\ m &\in (0, \pm 1, \pm 2, \ldots) \\ n &\in (0, \pm 1, \pm 2, \ldots) \end{aligned}$$

and amplified by C:

$$C = \frac{1}{2\cos\left(-k\Delta x - \frac{\pi}{2} - m\pi\right)} \qquad (5.5)$$

The incidient wave signal is obtained simply by adding the two transformed signals.

This method is not without its problems. For some components the denominator of equation (5.5) is close to zero. Fortunately wave gauges W1 and W2 were placed $L/4$ apart (based on the significant wave period) specifically for the purpose of separating incident and reflected waves; this means that for components near the peak frequency, equation (5.5) works well. However, for some higher frequency components (generally above $2.5f_p$), C does approach infinity. Therefore it was assumed that the part of the signal above $2.5f_p$ consisted of incident waves only and was not transformed in this way. Also, it is assumed that all components are free waves; that is, the principle of linear superposition is applied. There is no advice on how to take account of bound waves; this will introduce errors into the results, especially for steeper waves in shallow water. Therefore, to test the reliability of this means of separating in-

Table 5.2: Test runs

Run Name	Breaking Type (see Table 5.3)	Breaking Coefficient	C_f	Time-step T1 Condition	Time-step T2 Condition	SWAB Model
R1	1	0.3	0.005	$2.0 \times 10^{-3}\,s$	$2.0 \times 10^{-3}\,s$	2.0
R2	1	0.3	0.015	$2.0 \times 10^{-3}\,s$	$2.0 \times 10^{-3}\,s$	2.0
R3	1	0.2	0.005	$2.0 \times 10^{-3}\,s$	$2.0 \times 10^{-3}\,s$	2.0
R4	2	0.3	0.005	$2.0 \times 10^{-3}\,s$	$2.0 \times 10^{-3}\,s$	2.0
R5	2	0.3	0.010	4.7×10^{-4} s $= T_{m02}/2000$	8.8×10^{-4} s $= T_{m02}/2000$	3.0
R6	3	0.6	0.010	4.7×10^{-4} s $= T_{m02}/2000$	8.8×10^{-4} s $= T_{m02}/2000$	3.0

Table 5.3: Descriptions of breaking types. Unless specified otherwise, the Boussinesq terms are phased out after breaking and the diffusion terms immediately switched on

Breaking Type	Breaking Parameter	Description
1	$\frac{\partial \eta}{\partial t}$	Breaking occurs when $\frac{\partial \eta}{\partial t} > C_{bt}\sqrt{gh}$.
2	x, $\frac{\partial \eta}{\partial t}$	Breaking occurs automatically at seaward edge of reef; diffusion switched off and Boussinesq phased in at landward edge of reef. Breaking Type 1 applied landward of reef.
3	$\frac{H}{h}$	Breaking occurs when $H/h > C_{bh}$. Boussinesq terms switched off / on at commencement / cessation of breaking.

cident and reflected waves, SWAB 3.0 runs were carried out, firstly using a Fourier transform of the original W1 time-series, and secondly using the calculated incident waves; these tests are discussed in Section 5.3.2. All incident waves were input at the location of gauge W1.

Table 5.2 describes the SWAB model runs and Table 5.3 describes the different breaking types used for these runs. In this section, the results from the SWAB tests will be compared to the the data from Mase [2008], checking the accuracy of the SWAB model and the effect of the different breaking criteria. Run R2 was included to check the effect of the friction coefficient on runup levels; this will be discussed in Section 6.2. Two different model bathymetries were tested; these are described in Table 5.4. Mase et al. [2004] did carry out tests on two other bathymetries, B0 (without a reef) and B1 (a different reef from B2), but these will not be covered here. The second bathymetry in Table 5.4, B3, was added because in some cases the SWAB model would become unstable and it was thought the abrupt decrease in water depth over a small proportion of a wavelength was responsible. Reducing the seaward slope of the reef did stop the SWAB model from crashing.

Table 5.4: Descriptions of SWAB test bathymetries

Bathymetry Name	Description
B2	Same as Figure 4.1
B3	Similar to Figure 4.1. Seaward slope of reef has a reduced gradient: the previous slope (W2 to W3) is 3.749 m long (with same gradient), seaward slope of reef is 0.64 m long, top of reef is 1.176 m long (at same level as before).

The SWAB model test runs will be referred to by their names from Tables 4.4, 5.2 and 5.4. Therefore Test T1B2R5 would have the input waves T1, the bathymetry B2 and the R5 run condition. Those SWAB 3.0 runs carried out using the original W1 time-series will have an extra "-O" in their names, and those using the calculated incident waves will have an "-I"; all SWAB 2.0 runs used the original W1 time-series, so do not require a suffix. Note, that the time-series supplied by Mase [2008] consist of approximately 800 waves; for most testing only approximately the first 200 waves have been used.

5.3.2 Comparison between W1 input and incident wave input

The results from run R5, using each of the different wave inputs, were compared to the data supplied by Mase [2008]. Figure 5.26 shows smoothed wave spectra, firstly from the time-series at Wave Probe 1, and secondly from the incident waves calculated using the method of Frigaard and Brorsen [1995]. In this case, the method was applied up to $2.5f_p$. There are differences, both desirable and undesirable. Firstly, at the lower frequency end of the spectrum, there is a peak in the W1 part of the spectrum; this would be due to reflected long waves, and should not be part of the input to the SWAB model. The Frigaard and Brorsen [1995] method successfully removes these waves. However, especially for test T1, the method creates peaks in the higher frequency part of the spectrum. It is unlikely that the absence of reflected waves would cause these peaks; those in the region around $2f_p$ are most likely due to the presence of bound components.

Figure 5.27 shows smoothed spectra at Probe W3 (the first probe before significant breaking occurs). In the low frequency part of the spectrum, the incident waves show a clear improvement over using the waves from W1, giving results much closer to the experiment. It is also apparent that some of the discrepancies in the higher frequency part of the spectrum are much reduced by the time the waves reach Probe W3. It can therefore be concluded that using the calculated incident waves for the SWAB model wave input should produce more accurate results than using the time-series from Probe W1. For those runs performed using

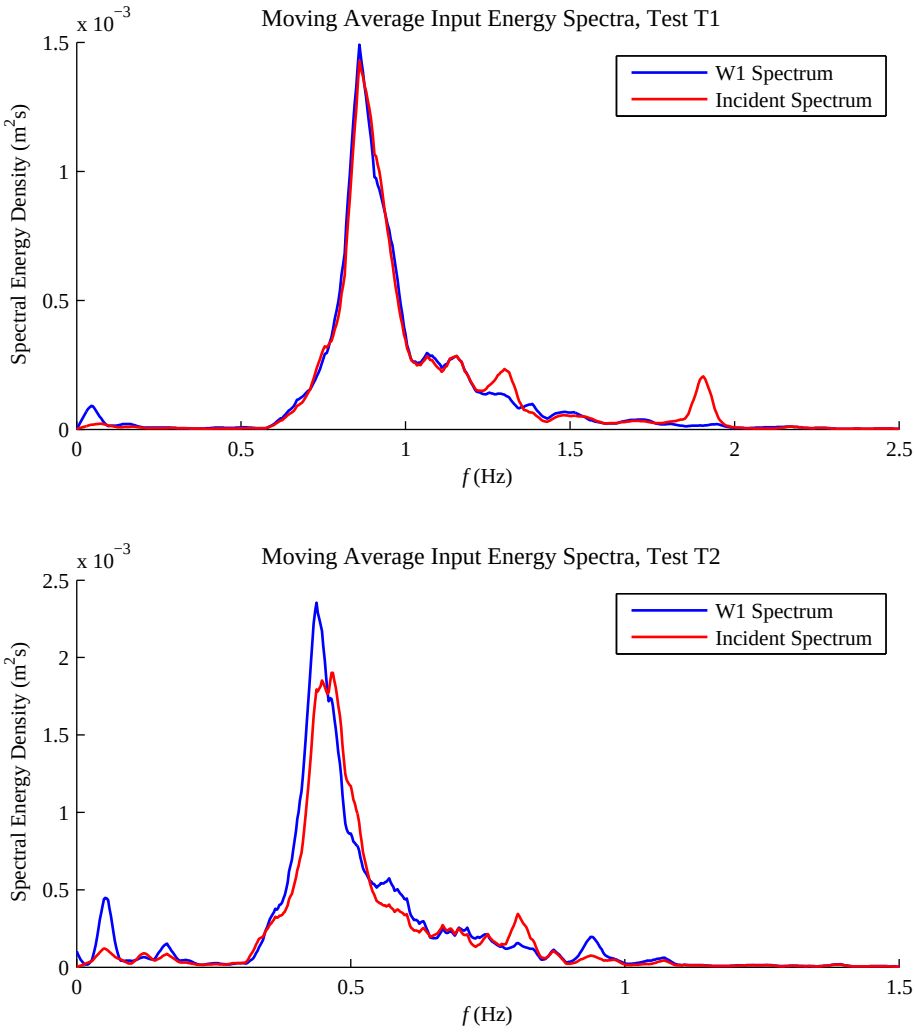

Figure 5.26: Wave spectra from Probe W1 and calculated incident input waves

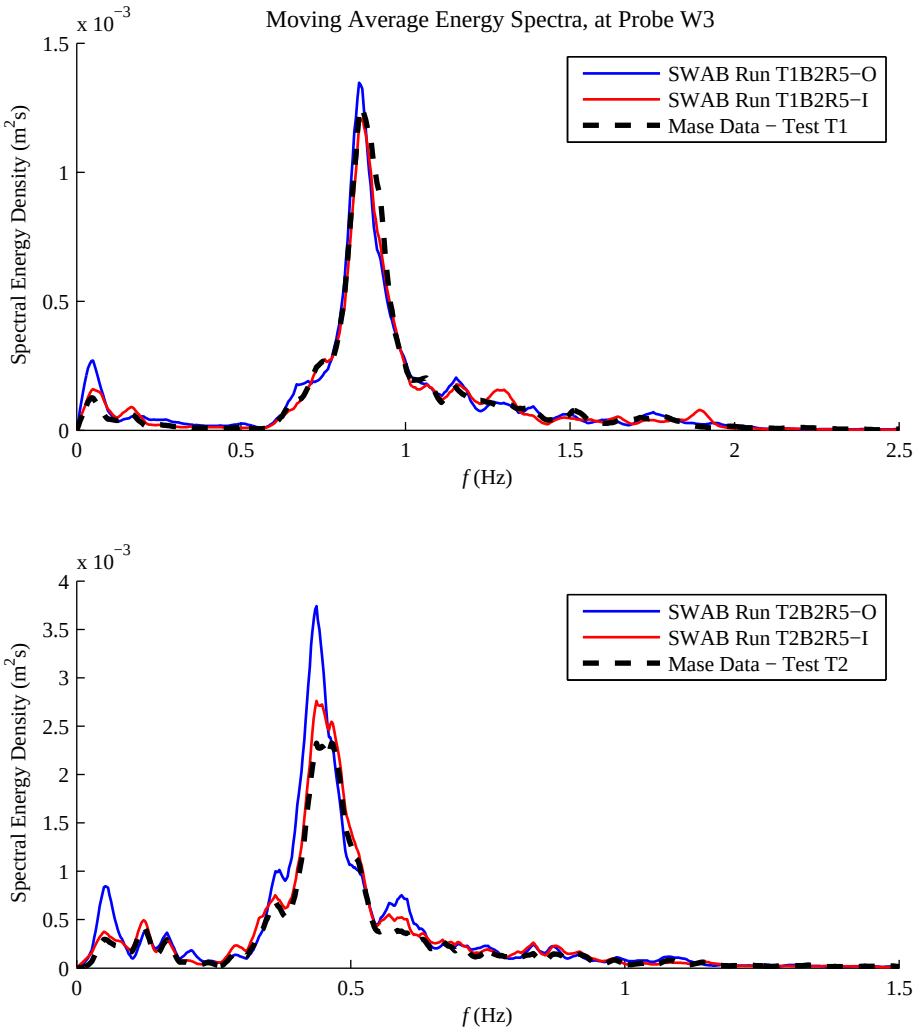

Figure 5.27: Wave spectra at Probe W3 - SWAB runs compared with experimental data

the SWAB 2.0 model, the W1 wave input was always used; these results are still valid, but the low frequency wave energy will be overestimated.

5.3.3 Comparison between SWAB 2.0 and SWAB 3.0

Runs R4 and R5 use identical breaking conditions, for the SWAB 2.0 and SWAB 3.0 models respectively. The differences between the results of these runs should highlight any differences between the older and newer model. Because the R4 runs all used the W1 based wave input, the R5 runs described here will do the same (i.e. runs TxB2R5-O, as opposed to TxB2R5-I).

Figure 5.28 shows wave group velocities calculated as a function of frequency, using Airy and Boussinesq theories. By applying a value of c_g based on the peak frequency to the whole wave train, the lower frequency components will be underestimated and higher frequency components overestimated. However, it is apparent that for a frequency of above 1 Hz (for the present water depth), the Boussinesq equations themselves give overestimates for the group

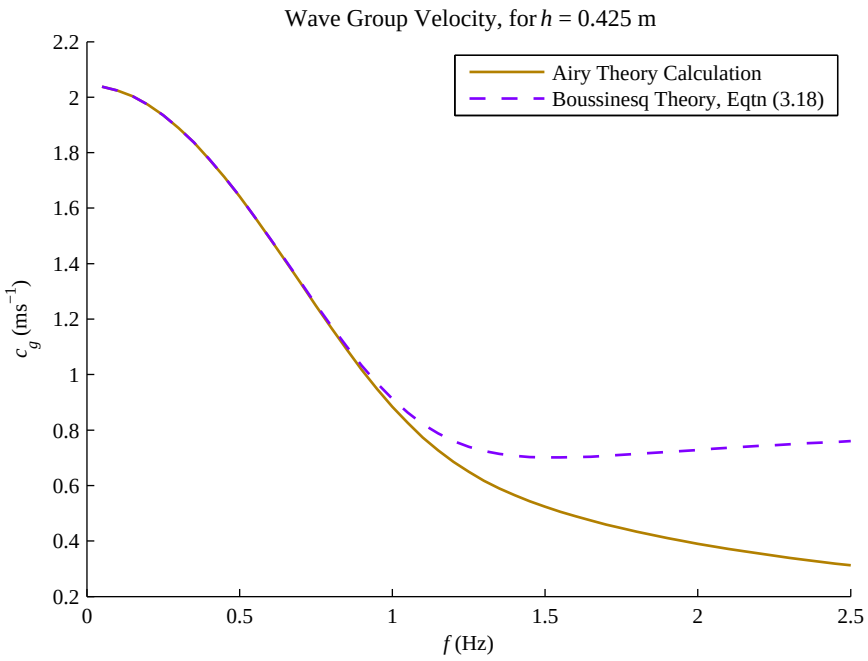

Figure 5.28: Wave group velocity as a function of frequency

velocity. Because the SWAB 2.0 model uses only the value of c_g based on the peak frequency to calculate the input waves, the difference between the SWAB 2.0 and SWAB 3.0 models will not actually be particularly large for higher frequencies. Unfortunately, erroneous wave celerities at higher frequencies for this type of Boussinesq model will result in inaccuracies in the relative phases of wave components, causing the time-series to differ from the experimenal data.

Figure 5.29 shows spectra at Probe W3, just before breaking occurs on the reef. To highlight the differences, the spectral energy density is shown on a log scale. As expected the higher frequency components are slightly overestimated by the SWAB 2.0 model (runs TxB2R4), though this is less apparent for the T1 test, where the high frequency ($f > 1$ Hz) Boussinesq c_g is rather similar to the peak frequency Airy c_g. In the lower frequency region, the SWAB 2.0 underestimates components relative to the SWAB 3.0 model (runs TxB2R5-O). However, because the SWAB 2.0 model used the W1 time-series for its wave inputs, which contains reflected waves (i.e. the amplitudes of the lower frequency part of the input are too large), the errors happen to approximately cancel each other out, and the SWAB 2.0 model is reasonably close to the experimental data.

Figure 5.30 shows energy spectra of the waves after they have broken on the reef and moved back into deeper water. In the high frequency region for test T1, the breaking process appears to have caused the generation of high frequency components. The SWAB 2.0 model used a larger time-step (about four times that used by the SWAB 3.0 runs) and this will result in

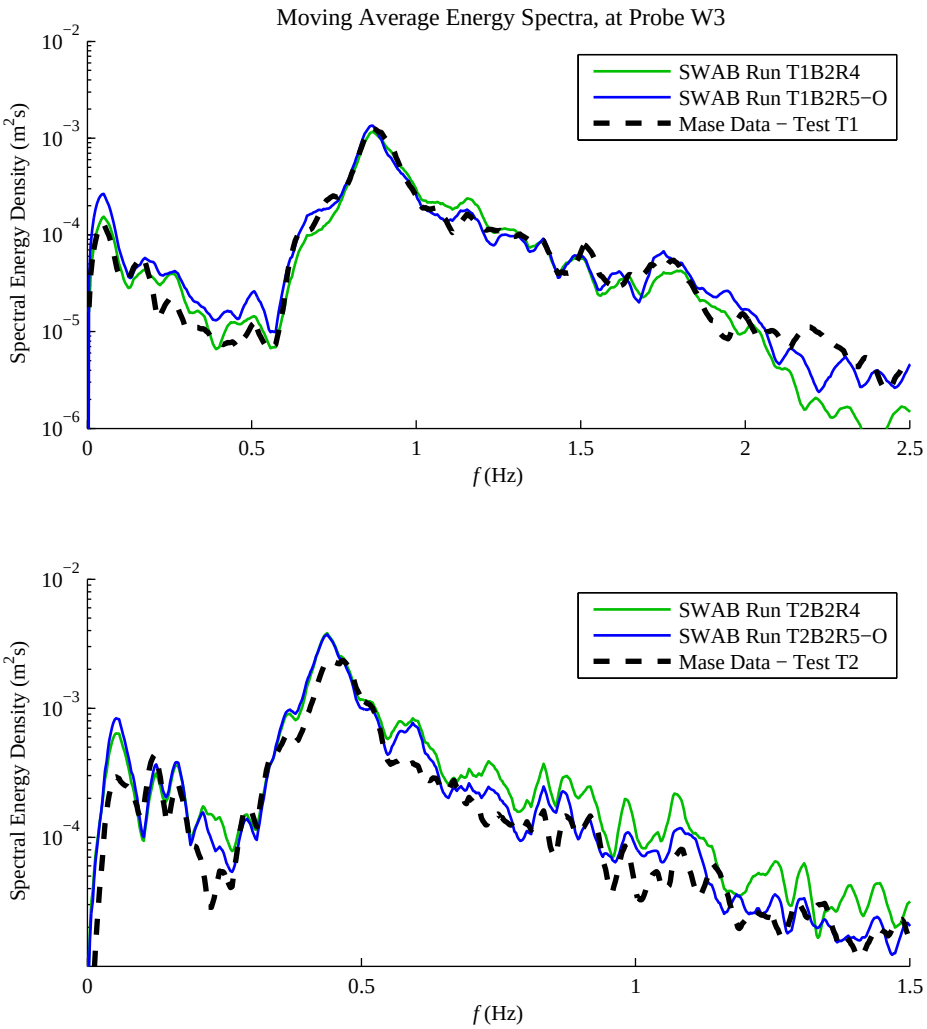

Figure 5.29: Wave spectra at Probe W3 - SWAB 2.0 and SWAB 3.0 runs compared with experimental data

increased damping of high frequency components (see Section 3.8 for tests on high-frquency damping).

In conclusion, the SWAB 2.0 model runs are valid for general comparison, with minor differences from the SWAB 3.0 model runs. All the discrepancies discussed above can be seen in Figure 5.31 with values of H_{m0} throughout the domain. For test T2, a large difference is apparent between the wave heights for the SWAB 2.0 and SWAB 3.0 run as the waves propagate onto the reef; this is mainly because very abrupt changes take place over a small distance. In this case, the SWAB 3.0 data point is approximately 0.5 cm closer to the shore than the SWAB 2.0 data point, leading to significant wave heights over 10 % smaller. Offshore, the overestimation of high frequency components means SWAB 2.0 wave heights are too large in test T2, and inshore the high frequency damping in test T1 results in wave heights that are too small. However, the offshore overestimation of the high frequency input is generally small due to the nature of the Boussinesq equations and the underestimation of the low frequency input is partly balanced by the use of raw time-series data without the removal of reflected waves.

5.3.4 Wave breaking on the reef

An important aspect of these tests is how the waves break on the reef and what happens when they propagate back into deeper water. Without the reef most waves would remain unbroken until they had moved closer to the shore. It has already been stated that the role of the Boussinesq terms for breaking waves is uncertain; therefore, we do not know what should happen to the Boussinesq terms if breaking waves move back into deeper water.

Relatively few studies have been done on the movement of waves into deeper water. Beji and Battjes [1993] performed experiments on regular waves propagating and breaking over a submerged reef before moving back into deeper water. Long waves travelling onto the reef become more nonlinear, with the generation of bound harmonic components. On the reef, even for non-breaking waves, there is a significant transfer of energy, creating free higher frequency components. As the waves move back into the deeper water, this transfer continues, in a process described by Beji and Battjes [1993] as “de-shoaling”, whereby these harmonic components become dispersive free waves. For higher frequency incident waves, this process is less apparent, with a smaller transfer of energy to harmonic components. Note that the group velocity will also increase as the waves de-shoal, resulting in a lower energy density.

A comparison was made between the different breaking types (Table 5.3) and the experimental data. Recalling Section 2.2.1 and equation (2.32), the variance of the free surface level

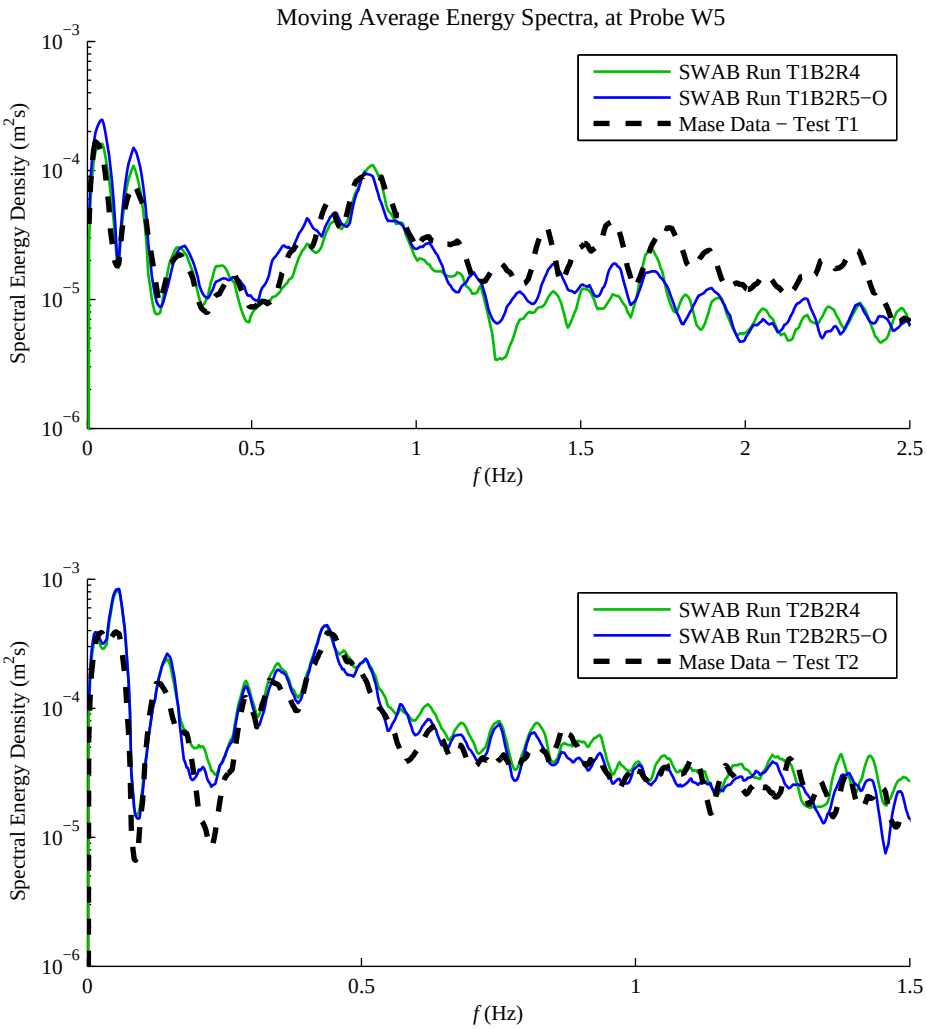

Figure 5.30: Wave spectra at Probe W5 - SWAB 2.0 and SWAB 3.0 runs compared with experimental data

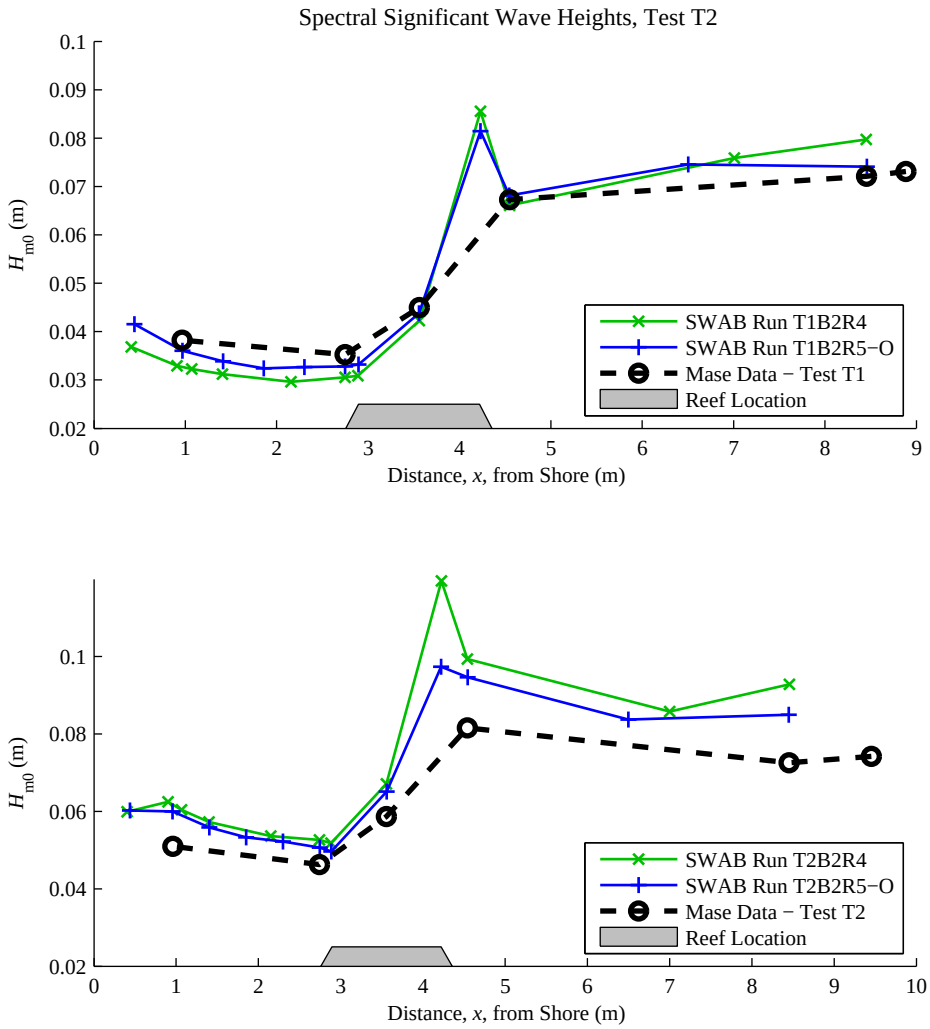

Figure 5.31: Spectral signficant wave heights across the domain - SWAB 2.0 and SWAB 3.0 runs compared with experimental data

is equivalent to the integral of the wave energy spectrum, m_0. Therefore $4\eta_{rms}$, where:

$$\eta_{rms} = \sqrt{(\eta - \bar{\eta})^2} \tag{5.6}$$

is equivalent to the significant wave height, H_{m0}. By plotting a moving average η_{rms}, a moving representative wave height over time is being presented. In Figures 5.32, 5.33, 5.34 and 5.35, the time-series of η_{rms} are normalised using the local still water depth, taking the moving average over $20T_p$. Comparing runs R1 and R3, it can be seen that changing the breaking coefficient from 0.3 to 0.2 makes little difference to the waves at the shoreline; because the reef causes almost all the waves to break, the initial breaking point remains almost unchanged. Stopping the breaking process landward of the reef (run R4), seems to make little improvement to the results for η_{rms}. However, run R6, where the breaking process is determined by H/h, gives a considerable improvement, especially for test T2. This breaking algorithm allows, if required, the automatic cessation of breaking landward of the reef, and it does not require a manual specification of breaking on the reef. Therefore the actual location of breaking waves may be more accurately modelled with this algorithm.

Goda [2000] gives two useful parameters for the study of nonlinear and breaking waves. Firstly, the skewness, γ_1, of the free surface level is given by Goda [2000] as:

$$\gamma_1 = \frac{1}{\eta_{rms}^3} \frac{1}{N} \sum_{i=1}^{N} (\eta_i - \bar{\eta})^3 \tag{5.7}$$

and secondly, the "atiltness" parameter, γ_3 is defined as:

$$\gamma_3 = \frac{\frac{1}{N-1} \sum_{i=1}^{N-1} (\dot{\eta}_i - \bar{\dot{\eta}})^3}{\left(\frac{1}{N-1} \sum_{i=1}^{N-1} (\dot{\eta}_i - \bar{\dot{\eta}})^2 \right)^{3/2}} \tag{5.8}$$

where $\dot{\eta} = \partial\eta/\partial t$. Notice that the atiltness parameter is effectively the skewness applied to $\dot{\eta}$ instead of η. Nonlinear waves are characterised by short steep crests with long shallow troughs; the skewness parameter will equal zero for linear waves but will become positive when the crests steepen and the troughs become shallower. If, as described by Beji and Battjes [1993], the nonlinear bound components are released when the waves move back into deeper water, the positive value of γ_1 will move closer to zero. Near-breaking and breaking waves are characterised by steepening of the front face of the wave; therefore a time-series of $\dot{\eta}$ will also contain short steep crests with long shallow troughs; according to Goda [2000], γ_3 will exceed 1.0 in the surf zone. As the breaking waves return to deeper water the value of γ_3 will also be expected to decrease, and then increase again as these waves move closer to the shore.

Figures 5.36 and 5.37 show part of the time-series for the skewness parameters for runs

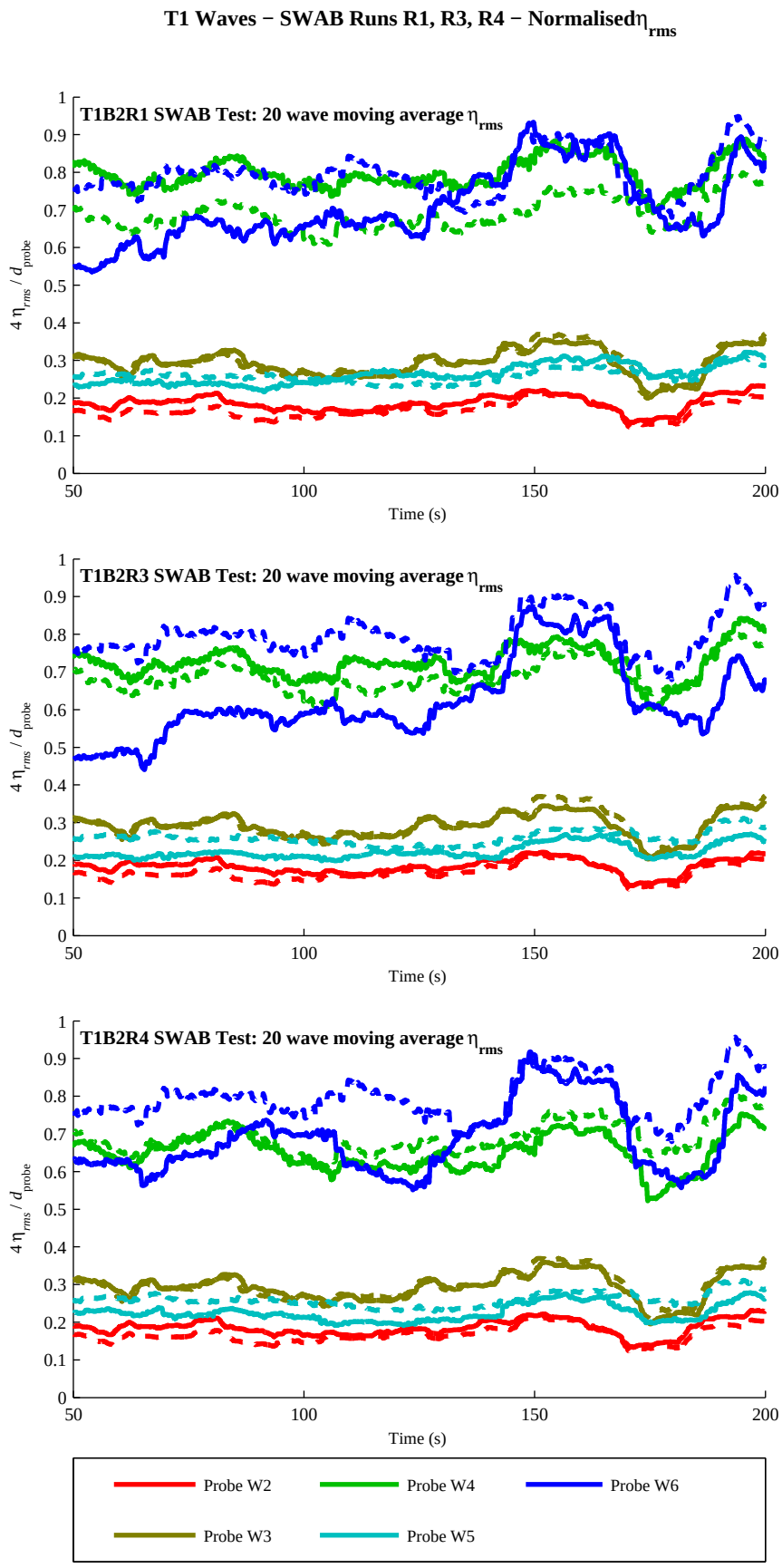

Figure 5.32: Time-series of $20T_p$ moving average normalised η_{rms}, at various wave probe locations, for T1 wave condition: Runs R1, R3 and R4. Experimental data shown as dotted lines and SWAB runs shown as solid lines

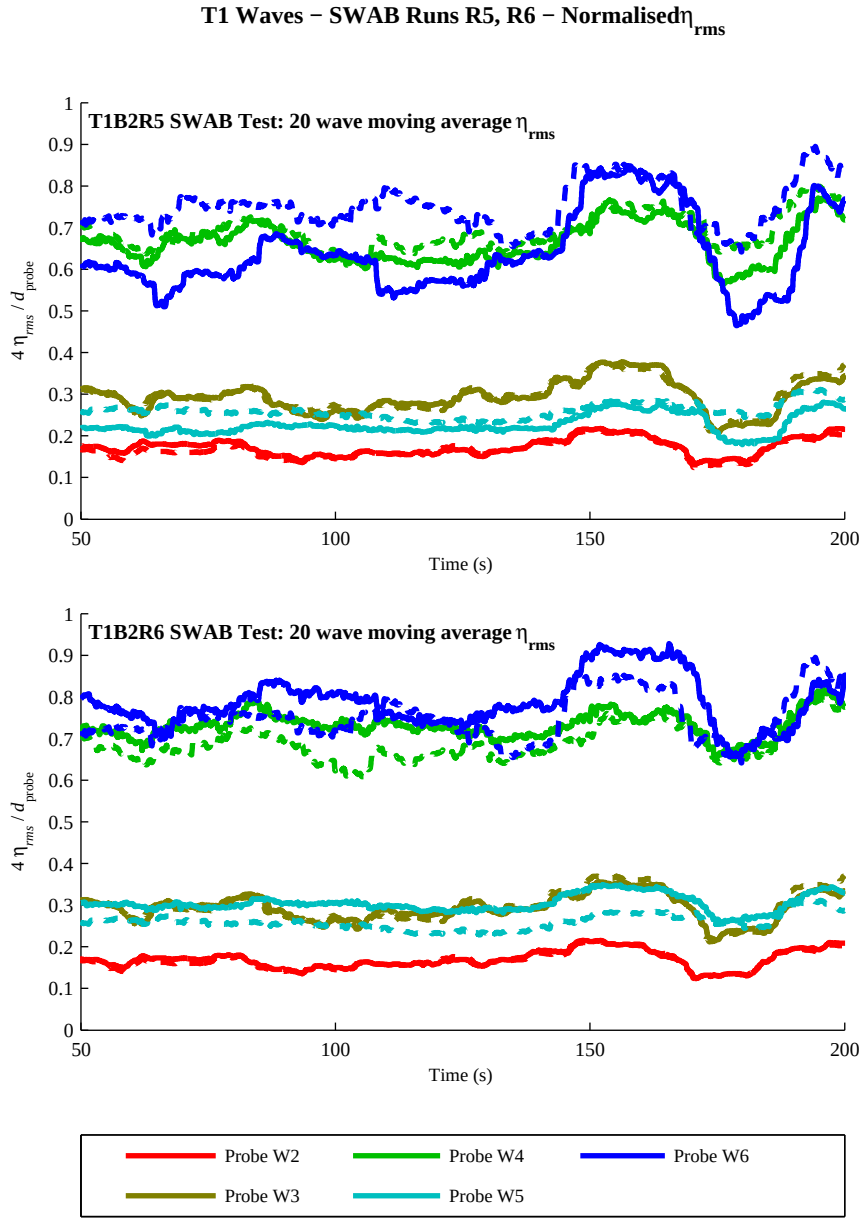

Figure 5.33: Time-series of $20T_p$ moving average normalised η_{rms}, at various wave probe locations, for T1 wave condition: Runs R5 and R6. Experimental data shown as dotted lines and SWAB runs shown as solid lines

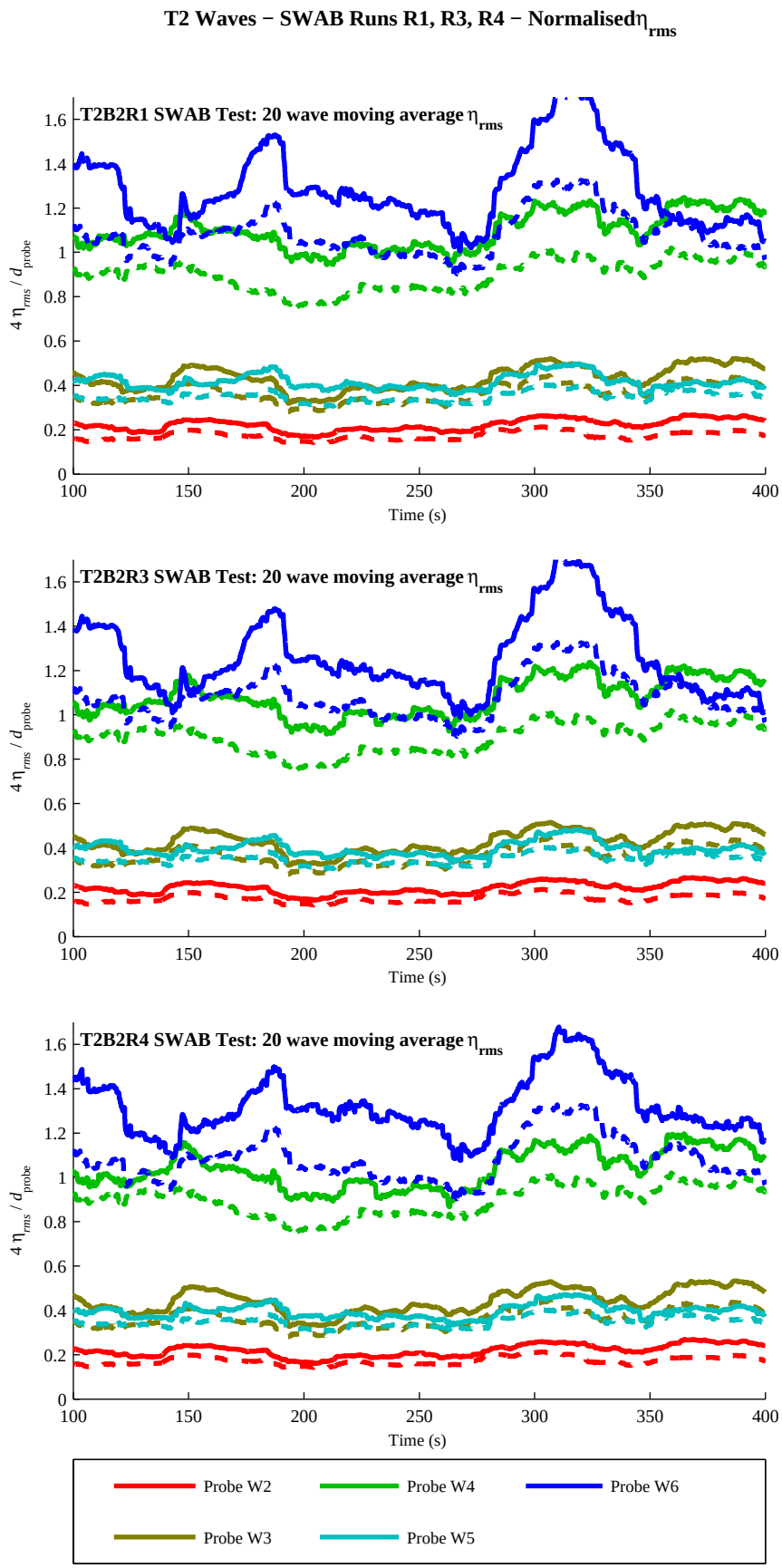

Figure 5.34: Time-series of $20T_p$ moving average normalised η_{rms}, at various wave probe locations, for T2 wave condition: Runs R1, R3 and R4. Experimental data shown as dotted lines and SWAB runs shown as solid lines

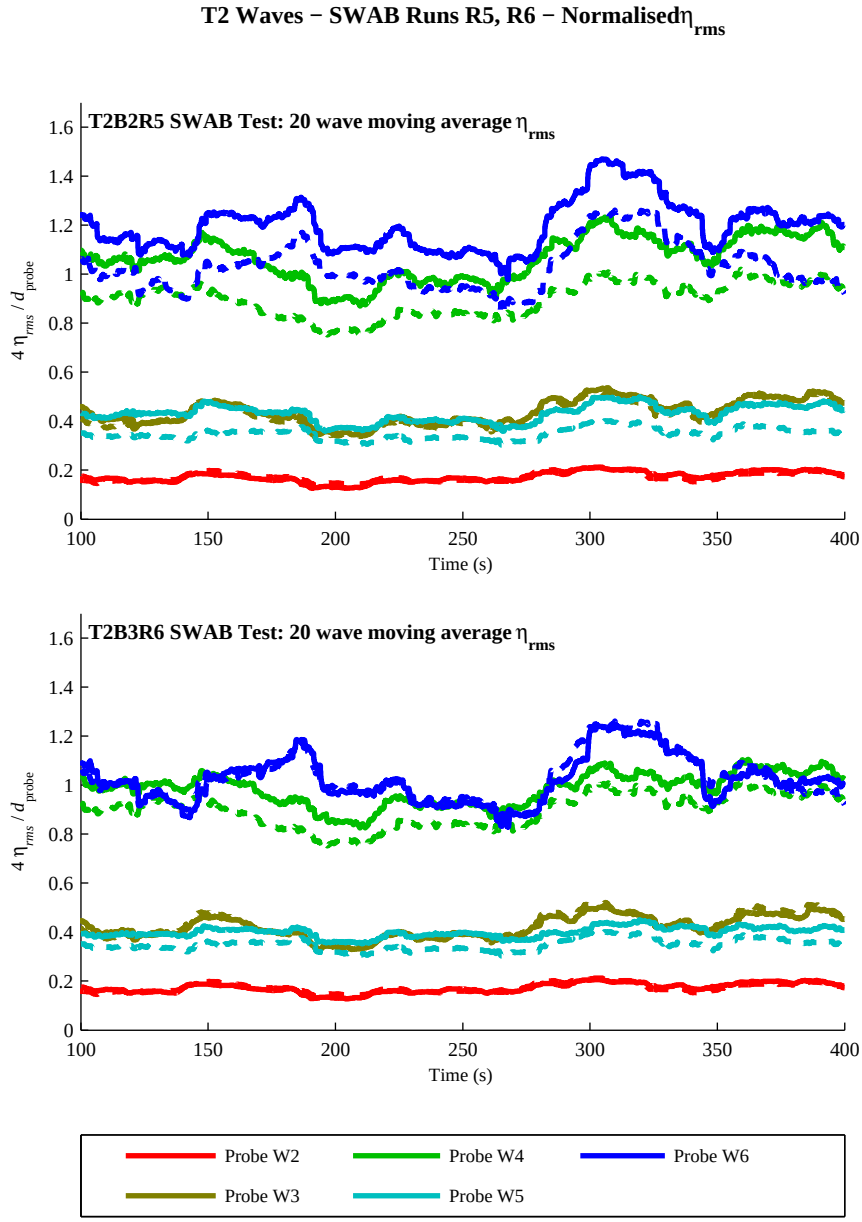

Figure 5.35: Time-series of $20T_p$ moving average normalised η_{rms}, at various wave probe locations, for T2 wave condition: Runs R5 and R6. Experimental data shown as dotted lines and SWAB runs shown as solid lines

R1, R5 and R6; for clarity, only approximately 25 periods of data have been shown in the figures. It appears that the skewness parameter increases between probes W4 (on the reef) and W5 (landward of the reef) before dropping as the waves move closer to the shore. The R6 run produces the closest match to the experimental data for both tests. The R5 run gives some rather inconsistent results; for the shorter waves (T1) it underestimates the skewness parameter on the reef, whereas for the longer waves (T2) it overestimates the same parameter. It is also interesting to note that the simpler breaking algorithm (R1, where the waves break once only and cannot stop breaking) produces better results landward of the reef than the R5 run.

Figures 5.38 and 5.39 show the moving average atiltness parameters from the reef (Probe W4) to the probe nearest the shore (W6). In this case, the experimental data shows the atiltness dropping as the waves move back into deeper water; at Probe W6, the parameter remains low. On the reef, at Probe W4, both the R1 and R6 runs produce better results than R5, which is once again inconsistent in its predictions. However, the R5 run does appear to give very good results landward of the reef for test T1, but not for test T2; it could be the case that forcing breaking to occur on the reef and stop again landward of the reef may be too simplisitc when applied to different wave conditions. Landward of the reef, the R6 breaking algorithm seems to overestimate the extent to which the breaking process ceases and starts again, with values for γ_3 that are too small at Probe W5 and too large at Probe W6; once again, it may be too simplistic to switch the breaking process off and on in this way, despite there being a parameter (H/h) that allows it to be done automatically. It may also be the case that the rather crude breaking model used by the SWAB model is not sufficiently accurate to give good results for γ_3; this atiltness parameter is a function of $\partial\eta/\partial t$, and will therefore be rather sensitive to errors in the shape of a modelled wave. It may require more sophisticated Navier-Stokes models to accurately replicate the shape of the waves travelling across the reef towards the shore.

Figures 5.40 and 5.41 show the energy spectra at these nearshore probes. It is apparent that all three runs give quite accurate results. However, the R1 run does slightly overestimate the low frequency energy, especially near the shore; this is probably due to not removing reflected waves from the wave input for this run. For the T1 conditions, there is also too little energy at the peak frequency (approx 0.9 Hz) for the R1 run; this may be because the breaking process continues between the reef and the shore. The R5 and R6 runs do not show this error. There appears to be little transfer of energy to higher frequency components, neither in the SWAB model results nor in the experimental data. The most apparent energy gain is at the lowest frequency part of the spectrum, where the SWAB results compare well with the experimental

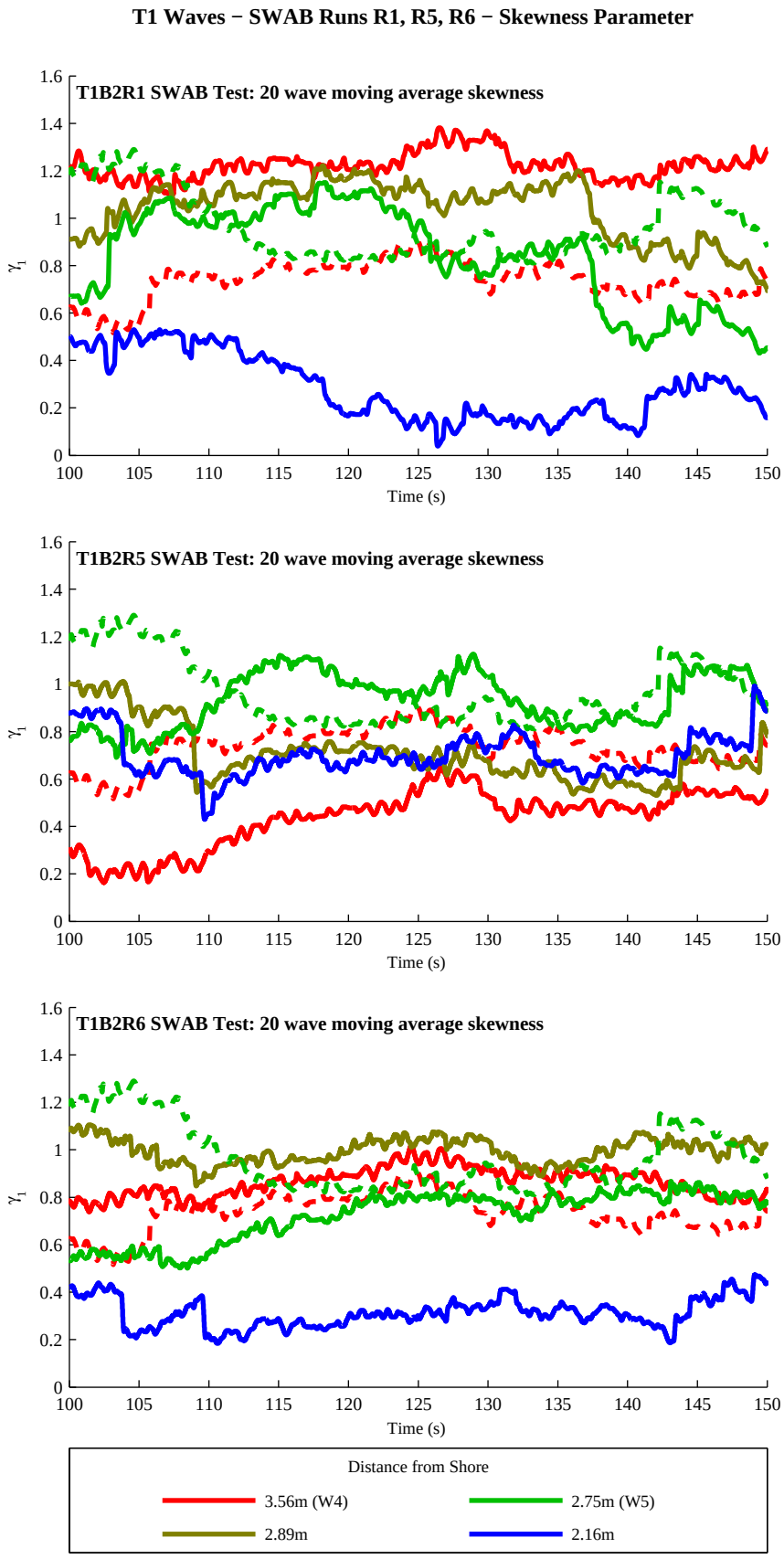

Figure 5.36: Time-series of $20T_p$ moving average skewness parameter, at various wave probe locations, for T1 wave condition: Runs R1, R5 and R6. Experimental data shown as dotted lines and SWAB runs shown as solid lines

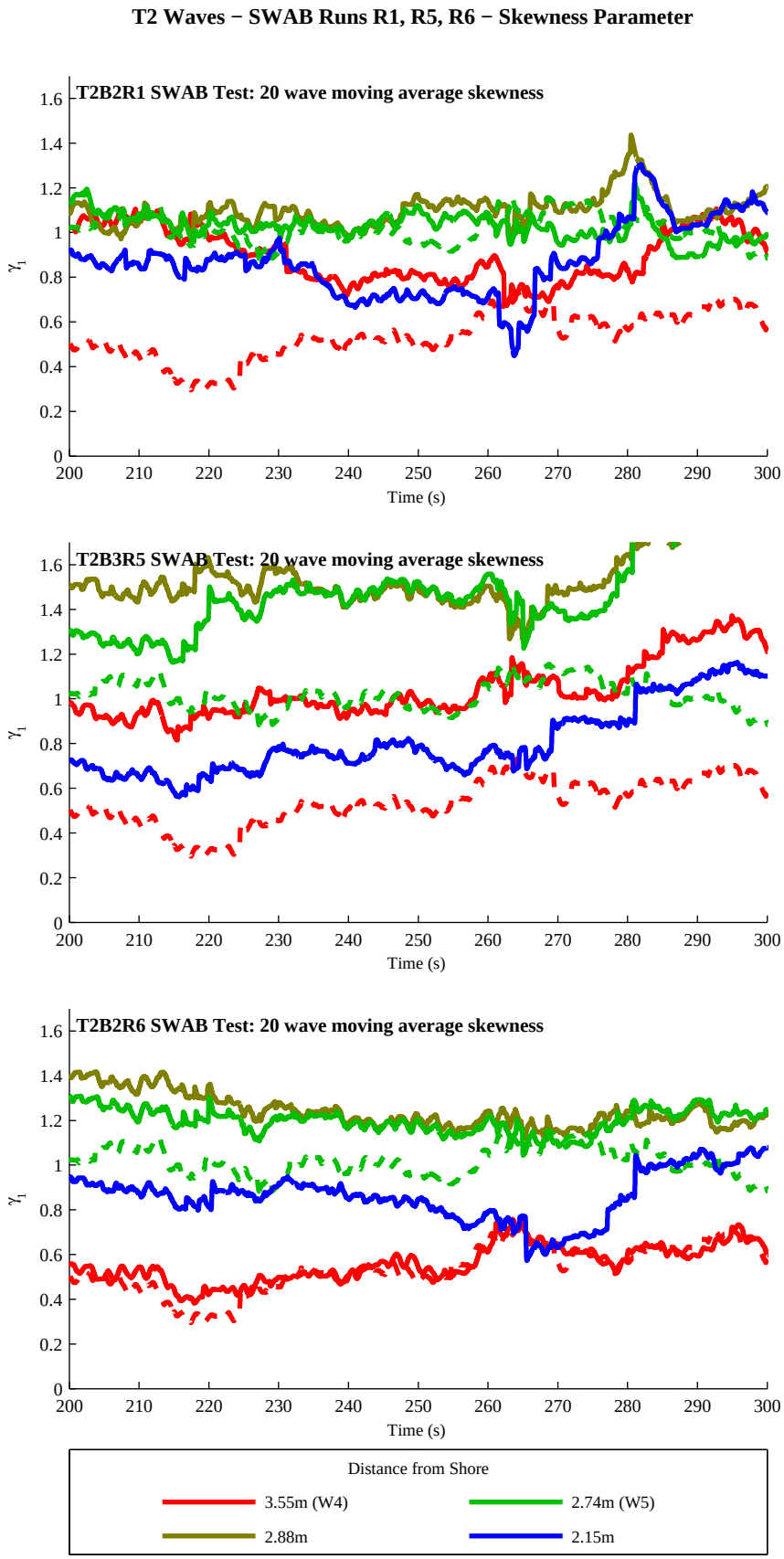

Figure 5.37: Time-series of $20T_p$ moving average skewness parameter, at various wave probe locations, for T2 wave condition: Runs R1, R5 and R6. Experimental data shown as dotted lines and SWAB runs shown as solid lines

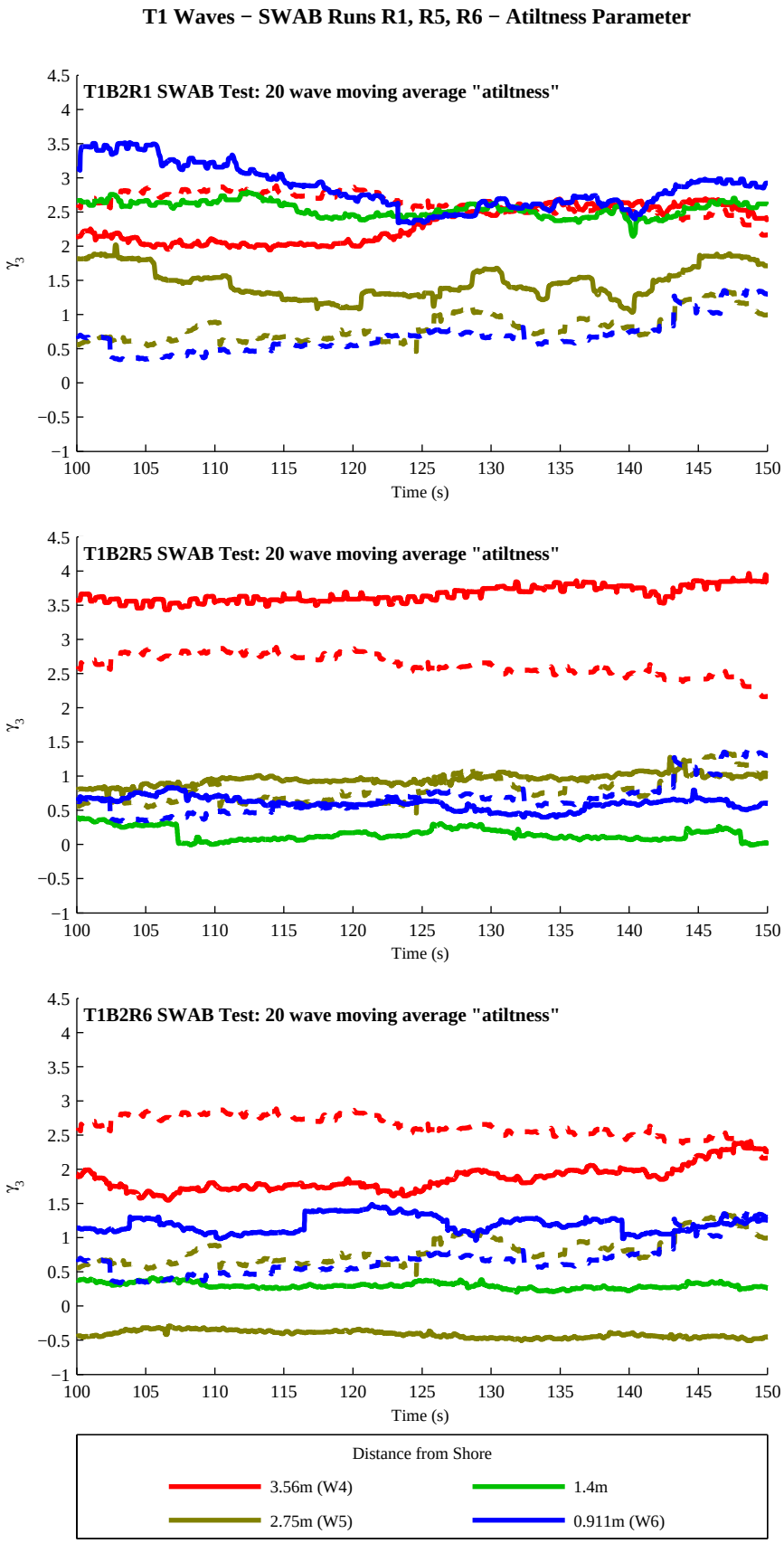

Figure 5.38: Time-series of $20T_p$ moving average atiltness parameter, at various wave probe locations, for T1 wave condition: Runs R1, R5 and R6. Experimental data shown as dotted lines and SWAB runs shown as solid lines

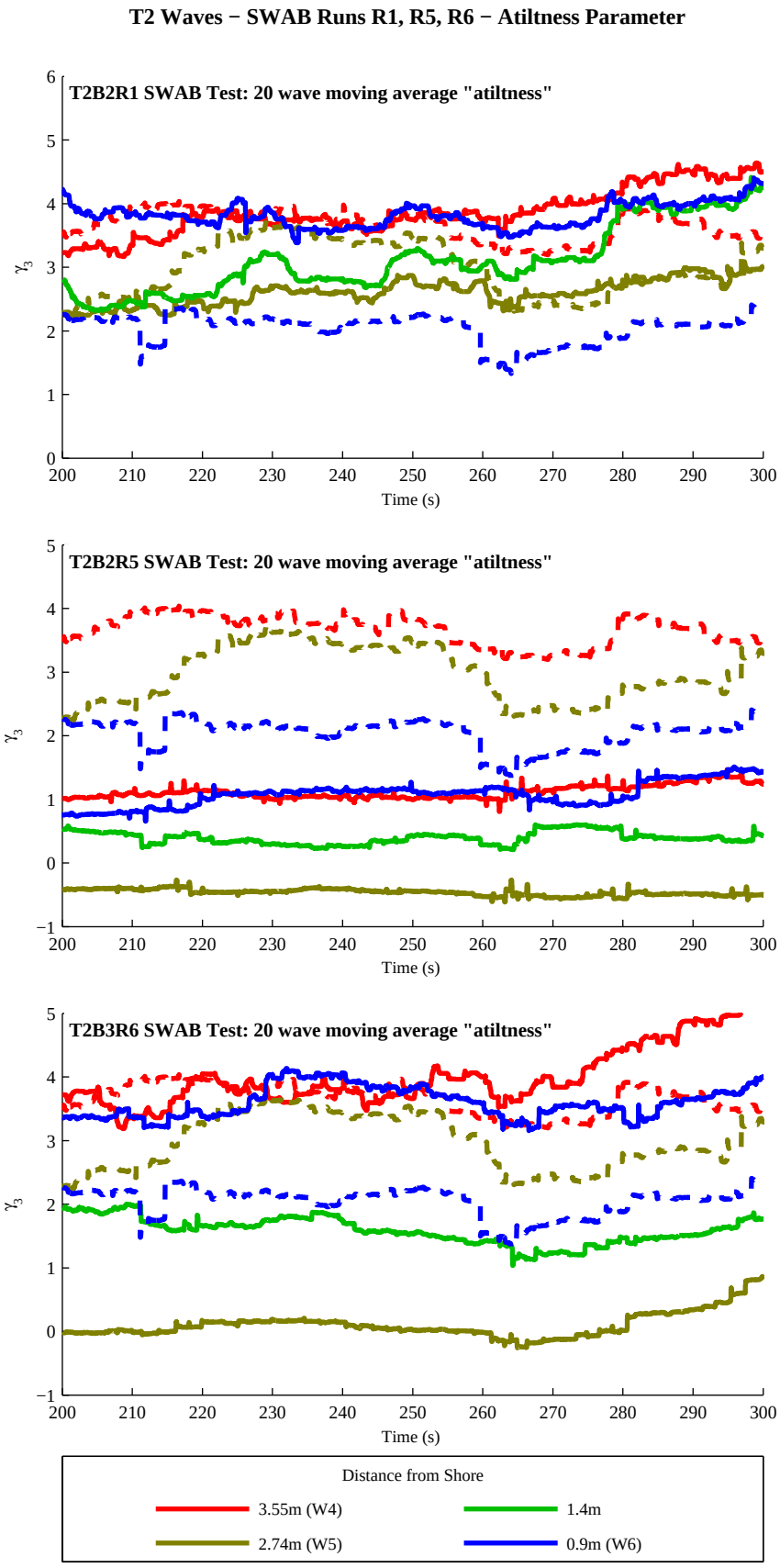

Figure 5.39: Time-series of $20T_p$ moving average atiltness parameter, at various wave probe locations, for T2 wave condition: Runs R1, R5 and R6. Experimental data shown as dotted lines and SWAB runs shown as solid lines

data.

5.4 Conclusions

This chapter has concentrated on the SWAB model's ability to simulate the shoaling of nearshore waves, and how to most effectively model the breaking process. The SWAB model has been tested against results from experiments with regular waves, random waves on a plane slope, and random waves propagating over a submerged reef. The following points summarise the main findings from this investigation:

- For regular waves with low surf similarity parameters, the SWAB model gave good predictions of nearshore wave heights. However as the surf similarity parameter is increased, the $\partial\eta/\partial t$ type breaking algorithm requires decreasing values of breaking coefficient C_{bt}, to give good results. For $\xi_0 \geq 0.38$ no breaking coefficient was low enough. Therefore, this type of breaking criterion was not suitable for plunging breakers. A similar conclusion can be drawn for random waves, where for higher values of ξ_0, rms wave heights are overestimated in the surf zone.

- The H/h type breaking algorithm applies the breaking process to the whole wave. The optimal breaking coefficient, C_{bh}, did not depend on the surf similarity parameter for regular waves. However, wave heights around the break point (i.e. just pre- and post-breaking) are underestimated when this algorithm is used; this is because breaking begins too soon;

- For random waves on a plane slope, nearshore wave heights appear to be overestimated. Analysis of wave parameters such as $H_{1/10}$ showed that the largest waves were too large. Increasing the breaking coefficient (C_{bt} or C_{bh}) improves the results to a certain extent;

- Different sets of random phases have little effect on wave heights and wave height distributions in the nearshore. However (as will be discussed later in this thesis), this is not necessarily true for wave runup or wave overtopping;

- The SWAB model performs rather well at modelling random waves propagating over a reef. Waves break on the reef, then move into deeper water before reaching the shore. Spectral analysis showed good results for all types of breaking criterion. Forcing the waves to break on the reef, then manually stopping breaking, before using the $\partial\eta/\partial t$ type criterion near the shore, gives little improvement over using a simple $\partial\eta/\partial t$ criterion. The best results are achieved using the H/h breaking algorithm, which does not need any manual input to stop the waves breaking as they move into deeper water. This algorithm

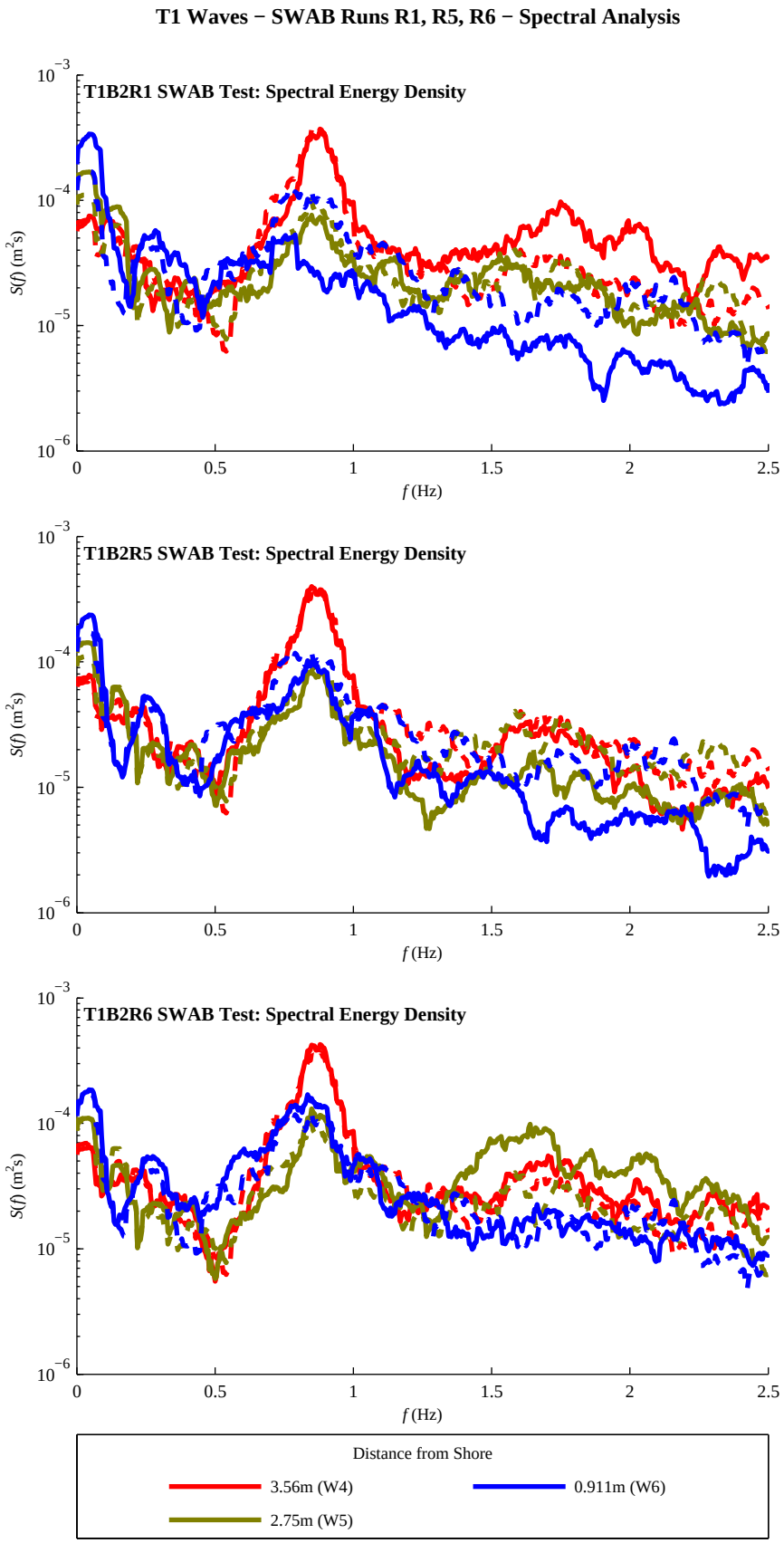

Figure 5.40: Spectral analysis for T1 wave condition at probes W4, W5 and W6: Runs R1, R5 and R6. Experimental data shown as dotted lines and SWAB runs shown as solid lines

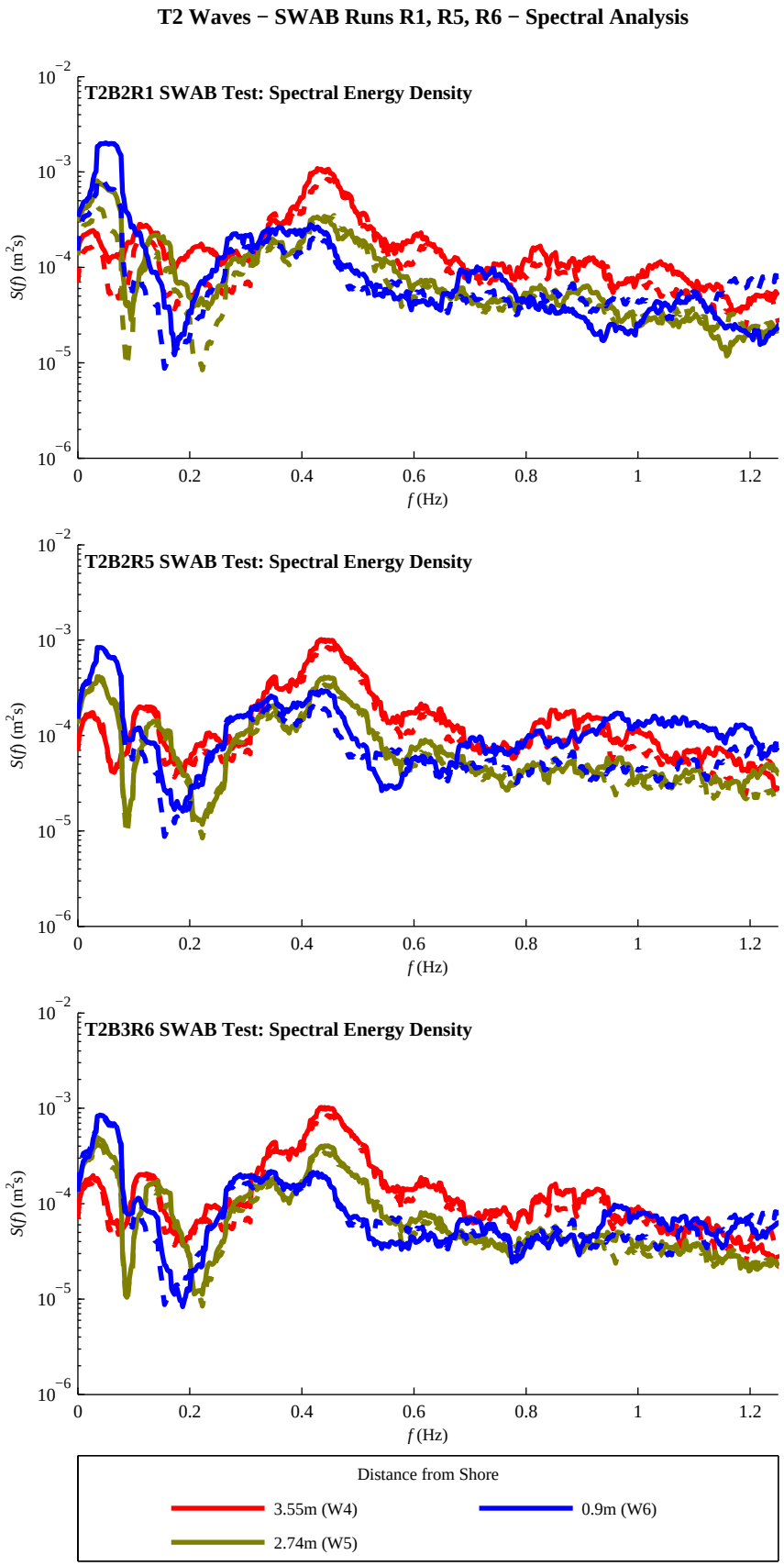

Figure 5.41: Spectral analysis for T2 wave condition at probes W4, W5 and W6: Runs R1, R5 and R6. Experimental data shown as dotted lines and SWAB runs shown as solid lines

produced very good simulations of 20 wave moving averaged η_{rms} (and hence wave energy) in the nearshore, with mean absolute errors of 7.6 % for the T1 wave conditions and 2.4 % for the T2 wave conditions. However, the SWAB model did not perform so well at reproducing results for skewness (measure of wave nonlinearity) and atiltness (asymmetry between front and rear face of the wave); it may be that the crudeness of SWAB's breaking model may have an influence.

Chapter 6

Wave Runup

6.1 Random Wave Runup on a Plane Slope

6.1.1 Methodology

The experiments of Mase [1989] were used for comparison against the SWAB model. These tests, designated MA1, MA2, MA3 and MA4, are described in Section 4.2, with test parameters given in Table 4.2. They have a range of surf similarity parameters from 0.25 to 0.72, which includes spilling as well as plunging breakers (see Section 2.4.1). The SWAB model was set up the same as the wave flume set-up, with the addition of a 10 m section offshore of the wave input location, to incorporate the sponge layer. To measure wave runup in the SWAB model, the shoreline position was measured as the first point in the domain (from offshore to inshore) where the water depth is less than a certain value. The initial limit used was 1.0×10^{-4} m. The SWAB model outputs a time-series of the absolute free-surface level at this shoreline. Runup parameters, such as the 98th percentile runup, require the separation of a time-series of runup levels into individual runups. Mase [1989] counted every runup crest as an individual runup. However, using the same method on the raw SWAB output can cause errors. As Figure 6.1 shows (around $t = 32$ s), it is not uncommon for the SWAB output to oscillate between two shoreline locations, one wavelength apart. Any algorithm to separate the crests directly from this raw data will be misleading; for example, between 30 s and 33 s there will be five crests recorded instead of the correct value of one. This problem was partly resolved by increasing the limiting depth for locating the shoreline to 1.0×10^{-3} m. This removes some (but not all) of the unwanted oscillations although it does have the effect of lowering the recorded runup crests.

To find the individual runup crests, the following method was used. Firstly, a moving av-

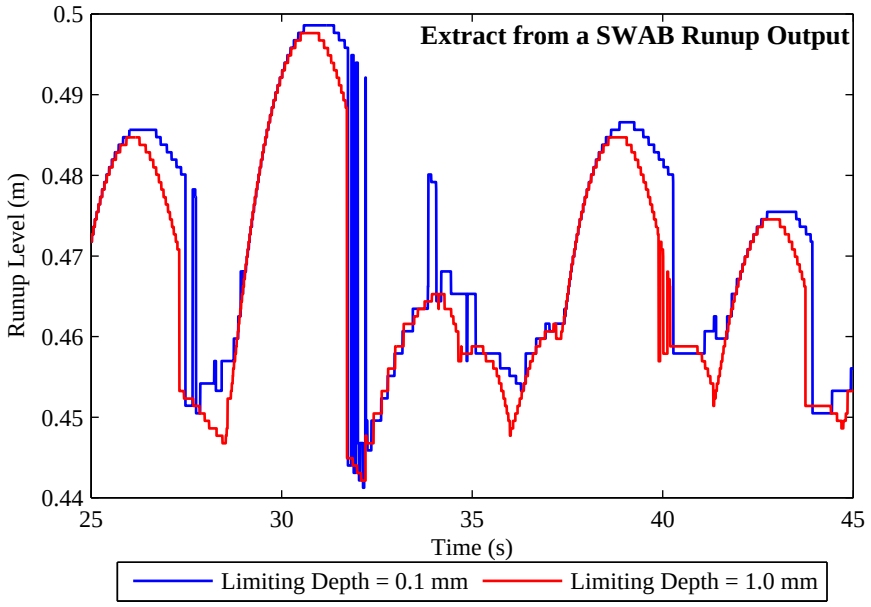

Figure 6.1: Extract from a runup time-series, showing oscillating swash level

erage filter over $T_p/4$ was applied; this smooths most of the remaining unwanted oscillations. Then, all the peaks were detected with a clear crest-to-trough distance above a certain quantity. In this case 0.003 m was used as the limit; such a small value was thought to be necessary to avoid missing genuine runups. Figure 6.2 shows the same extract after the filter has been applied, alongside the detected runups. In this case all unwanted runups have been removed although, for example at $t = 35$ s, there are some runups that should be included but have not been detected; this is more likely to happen with "sub-crests". However, in the absence of a better algorithm, this analysis will still be valid, especially with respect to the highest runups. In addition, the comparison between different SWAB runs is certainly valid.

For each of the four model tests, the SWAB model was set up with two different breaking criteria ($H/h > 0.6$ and $\partial\eta/\partial t > 0.25\sqrt{gh}$); these will be referred to as H60 and E25. For the H/h criterion, two friction factors were tested: 0.01 and 0.005; for the $\partial\eta/\partial t$ criterion, a friction factor of 0.01 was used. Tests with friction factors of 0.005 and 0.01 will be called F05 and F10 respectively. For each wave condition, three sets of randomly phased waves were generated, each consisting of 200 waves (based on T_{m02}). These will have the suffix S1, S2 and S3 respectively. Where the three sets of randomly phased runs have been combined, this will have the suffix SAll. For example, the SWAB run for the MA1 wave conditions, using the $H/h > 0.6$ breaking criterion, having a friction factor of 0.01, with the second set of random phases, will be known as MA1-H60-F10-S2. All these SWAB model runs used a time-step of $dt/T_{m02} = 1/2000$.

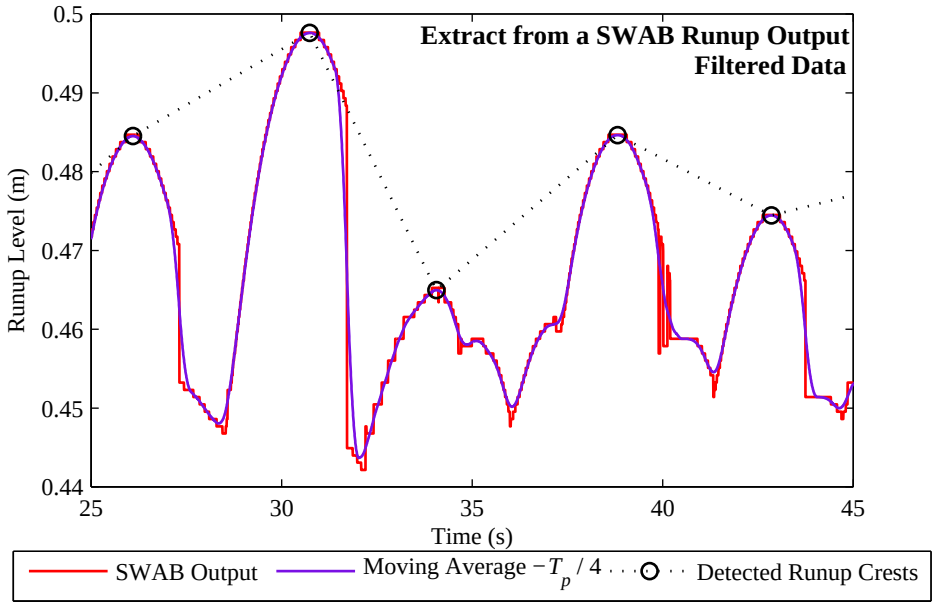

Figure 6.2: Extract from the same runup time-series, showing filtered data and individual runups

6.1.2 Effect of friction factor

Figure 6.3 shows significant wave heights across the domain, for Test MA1, as predicted by the SWAB model. It is clear that the friction factor makes a negligible difference, even close to the shoreline. Looking at an extract from a time-series of free-surface level in a still water depth of 0.01 m, 0.20 m from the shore (Figure 6.4), the difference is still very small. This shows that the friction factor (and bed friction in general) has little effect on nearshore waves. However, any differences are highlighted with the wave runup output. Figure 6.5 shows the runup levels for the same test MA1-H60-S1 at a similar time to the extract of Figure 6.4. Some runup crests are over 10% higher with the lower friction factor. Therefore, the friction factor does have an important influence on runup levels. As Figure 6.6 shows, the higher crests are affected to a greater extent than the smaller ones; in fact, the friction coefficient does not appear to have any significant effect on the lowest 40 % of runup crests. The effect of the friction coefficient may not have such a large effect on overtopping rates. This would be especially true when a large proportion of waves overtop a structure; in this case, the friction factor's influence will be closer to that shown in Figure 6.4. Equating friction factors with different types of beach or seawall surface roughness is beyond the scope of this thesis; however, the friction coefficients that have been used will be mentioned when dealing with wave runup.

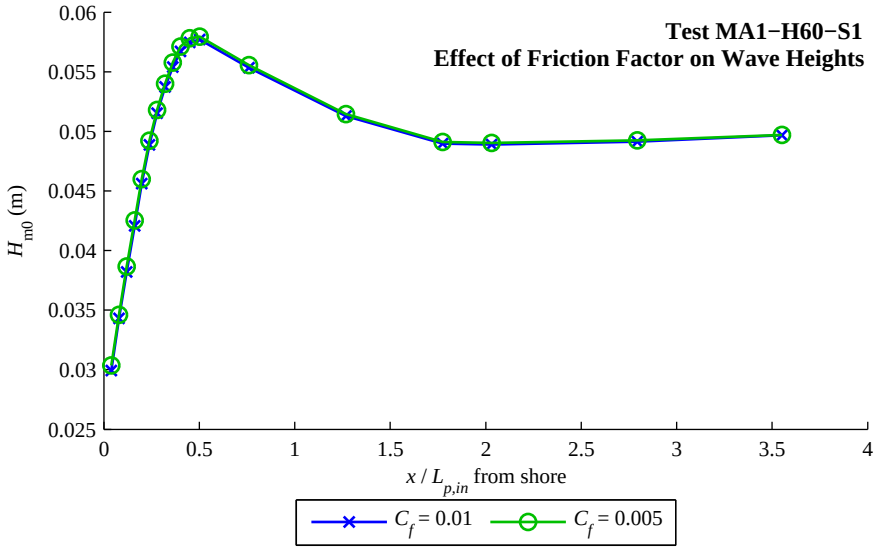

Figure 6.3: Effect of friction factor on significant wave heights: test MA1-H60-S1

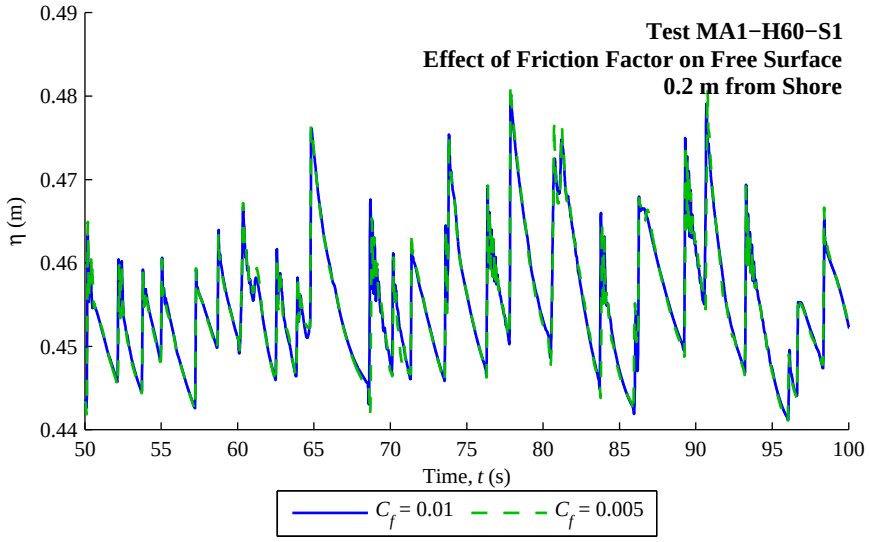

Figure 6.4: Effect of friction factor on free surface level close to the shore: test MA1-H60-S1

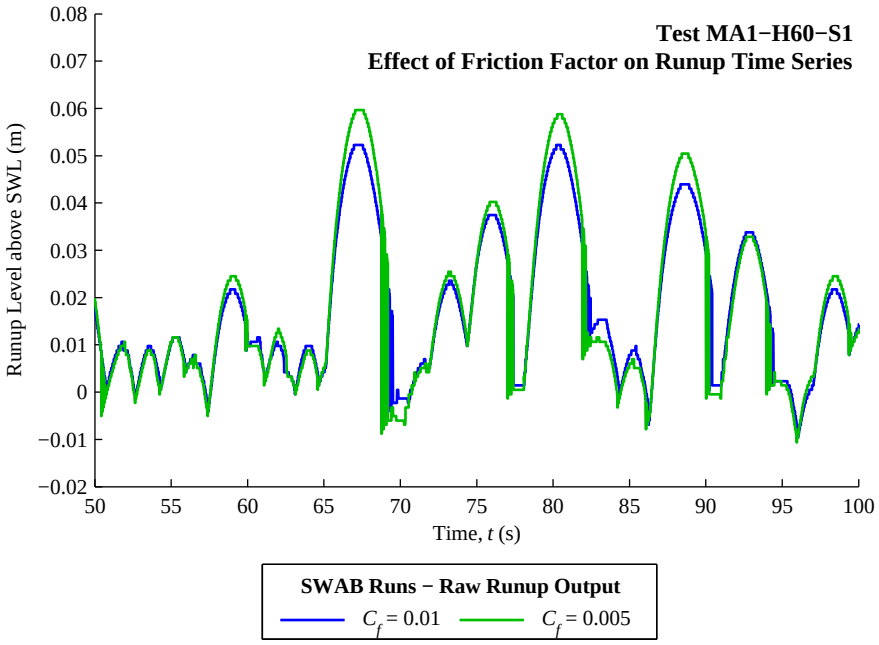

Figure 6.5: Effect of friction factor on runup level: test MA1-H60-S1

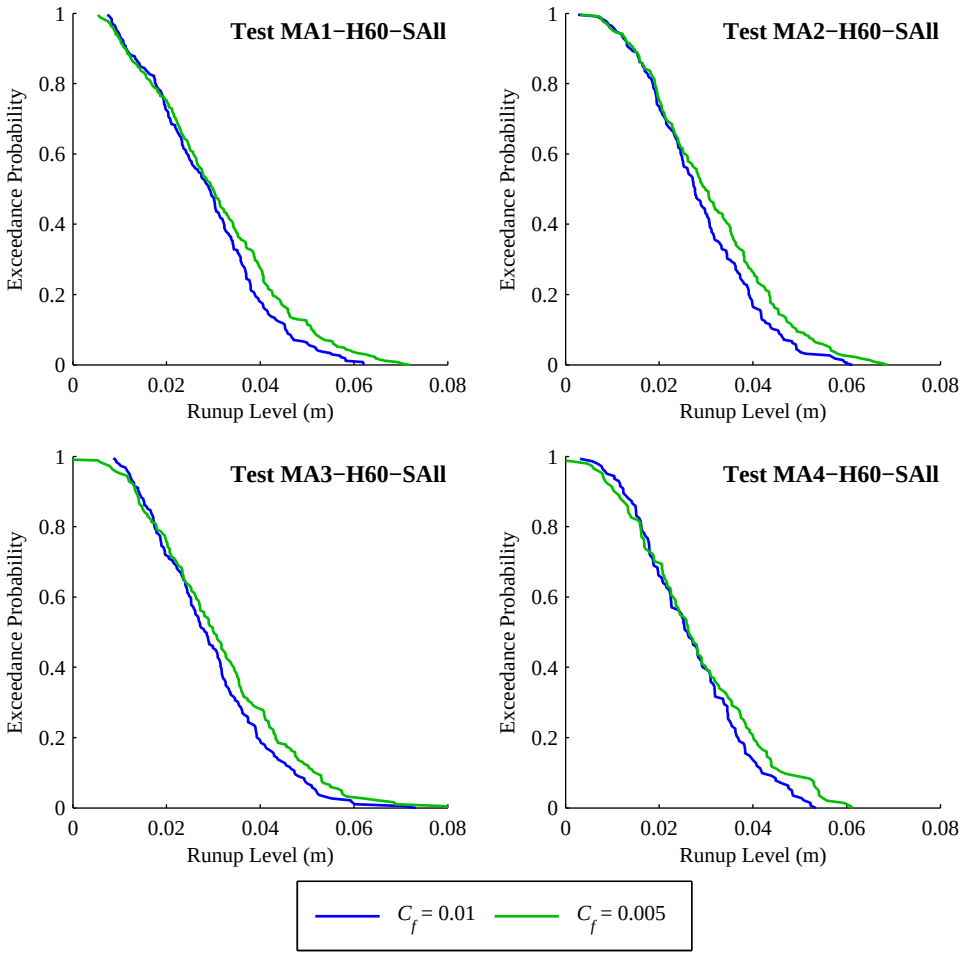

Figure 6.6: Effect of friction factor on runup distributions: all tests

6.1.3 Difference between random phases

There is some difference between the randomly phased runs throughout the domain. Figure 6.7 shows that significant wave heights differ most between runs near the onset of breaking, though due to waves becoming depth limited the difference appears to decrease as the waves move closer to the shore. However, looking more closely at the distribution of the highest waves 0.2 m from the shore (Figure 6.8), the random phases can cause considerable variation between the highest waves in a wave train. For example, the highest wave for test MA1-H60-F10-S1 is about 0.04 m in height, whereas for test MA1-H60-F10-S3 it is over 0.05 m, a difference of more than 20 %. It is not clear from Figure 6.9 whether the variation in the highest runups is greater than the general variation between the different phases. The differences in the values of the runup parameters $R_{1/3}$, $R_{1/10}$ and $R_{2\%}$, though significant, are not as high as 20 %. It is also apparent, by comparing Figure 6.8 with Figures 6.9 and 6.10, that those wave trains giving the highest waves at the shore do not necessarily cause the highest runups. For example, for test MA2-H60-F10, the S3 run gives highest nearshore waves about 0.02 m lower than the S1 run (Figure 6.8); however, from Figure 6.10, the S3 run gives an $R_{2\%}$ value 0.01 m higher than the S1 run. This shows that there is not a direct link between a highest individual wave at this location and a highest individual runup, which has implications on the use of NewWave for predicting extreme runup levels (although it does not discount a link between high waves slightly further offshore and high runup levels). However, it should also be noted that such time domain analysis can be unreliable, especially close to the shore where the surf beat is relatively large, due to the zero-crossing method of separating the waves; this was discussed at the end of Section 5.2.3.

6.1.4 Effect of breaking criterion

Differences in results between the $\partial\eta/\partial t$-type breaking criterion and the H/h-type breaking have already been discussed with respect to regular and random waves in Chapter 5. The analysis will be extended in this chapter to look at how these different models affect runup levels and overtopping rates.

Figure 6.11 shows significant wave heights in the nearshore. Due to a lack of published wave height data, they have been shown in comparison with results from the SWAN model. Note, SWAN was run with triad calculations disabled. In a similar way to the tests of the previous chapter, it is apparent that the H/h breaking criterion leads to underpredicted wave heights near the start of the surf zone, with accurate wave heights close to the shore. The $\partial\eta/\partial t$ criterion, on the other hand, gives less accurate wave heights close to the shore. However, the

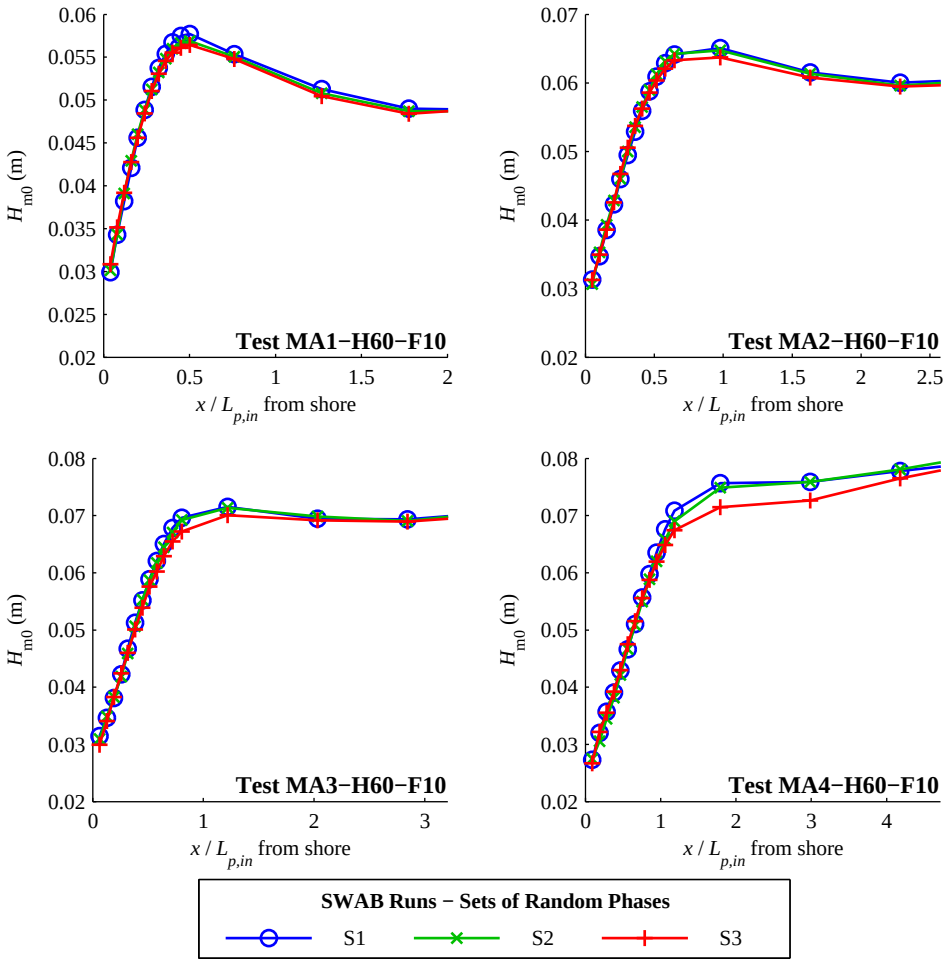

Figure 6.7: Effect of random phase on significant wave heights: tests H60-F10

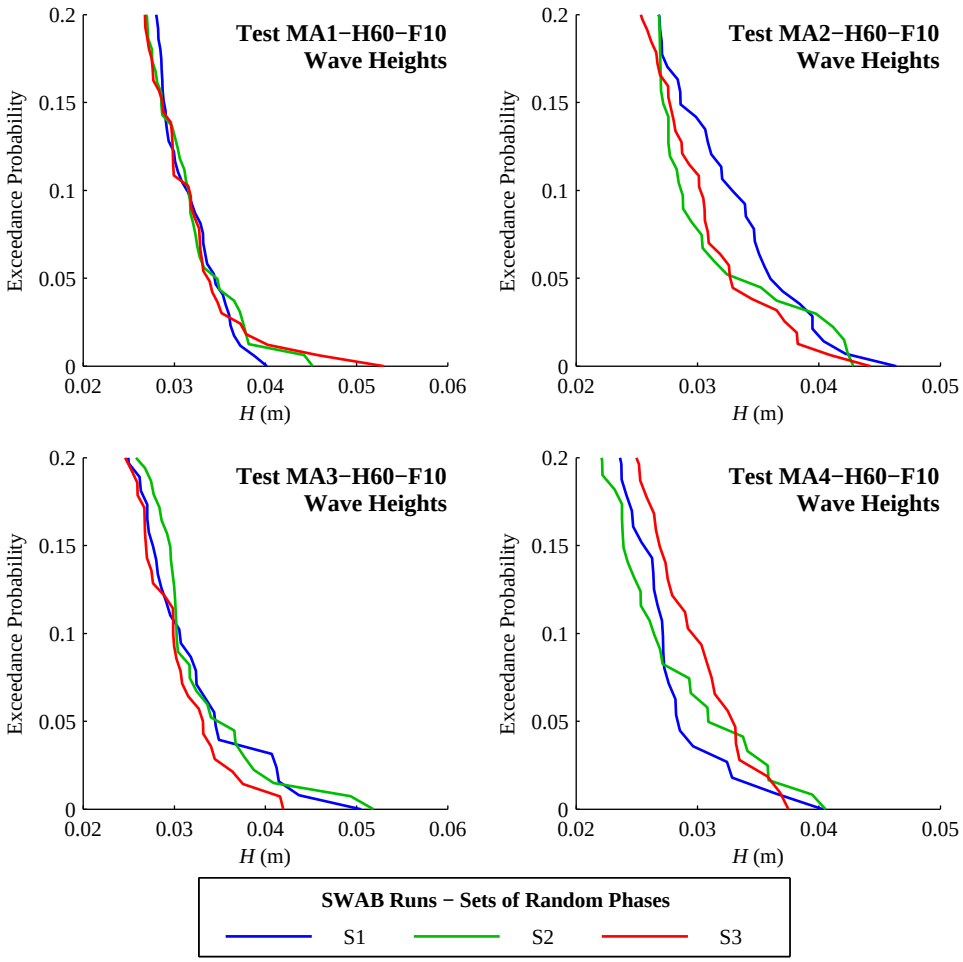

Figure 6.8: Effect of random phase on largest waves 0.2 m from the shore: tests H60-F10

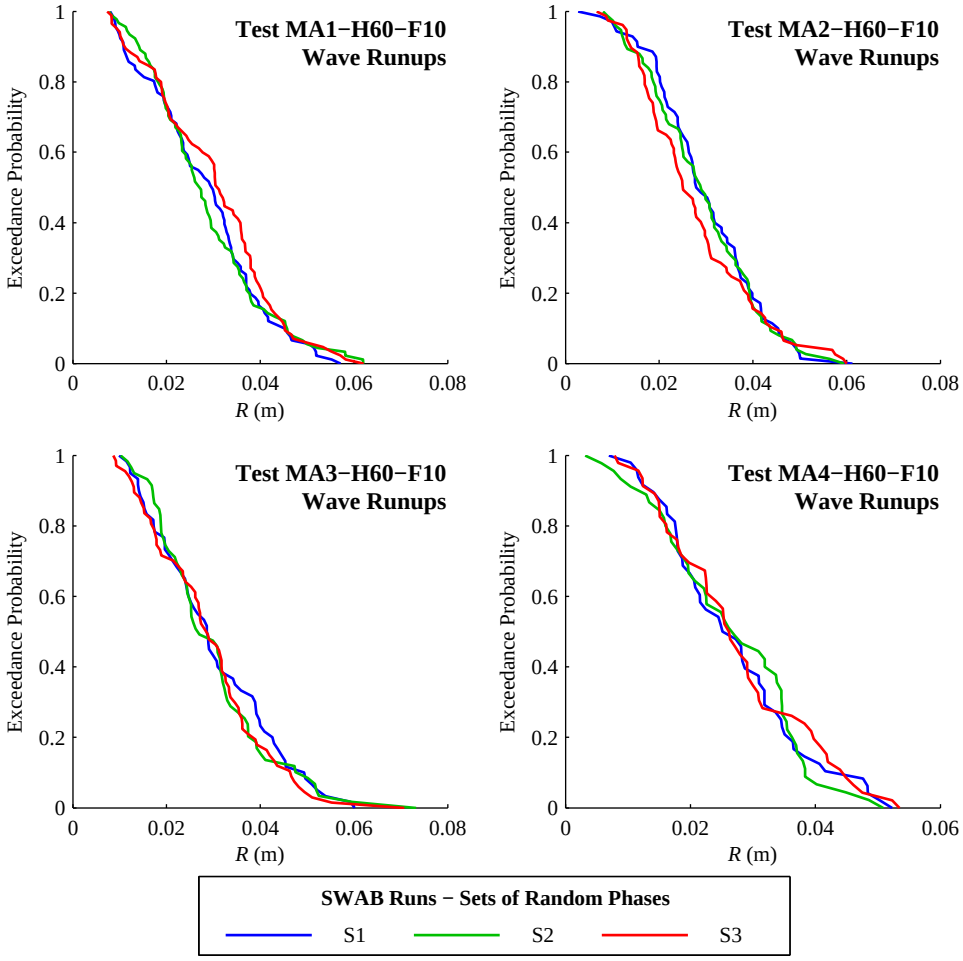

Figure 6.9: Effect of random phase on runup distributions: tests H60-F10

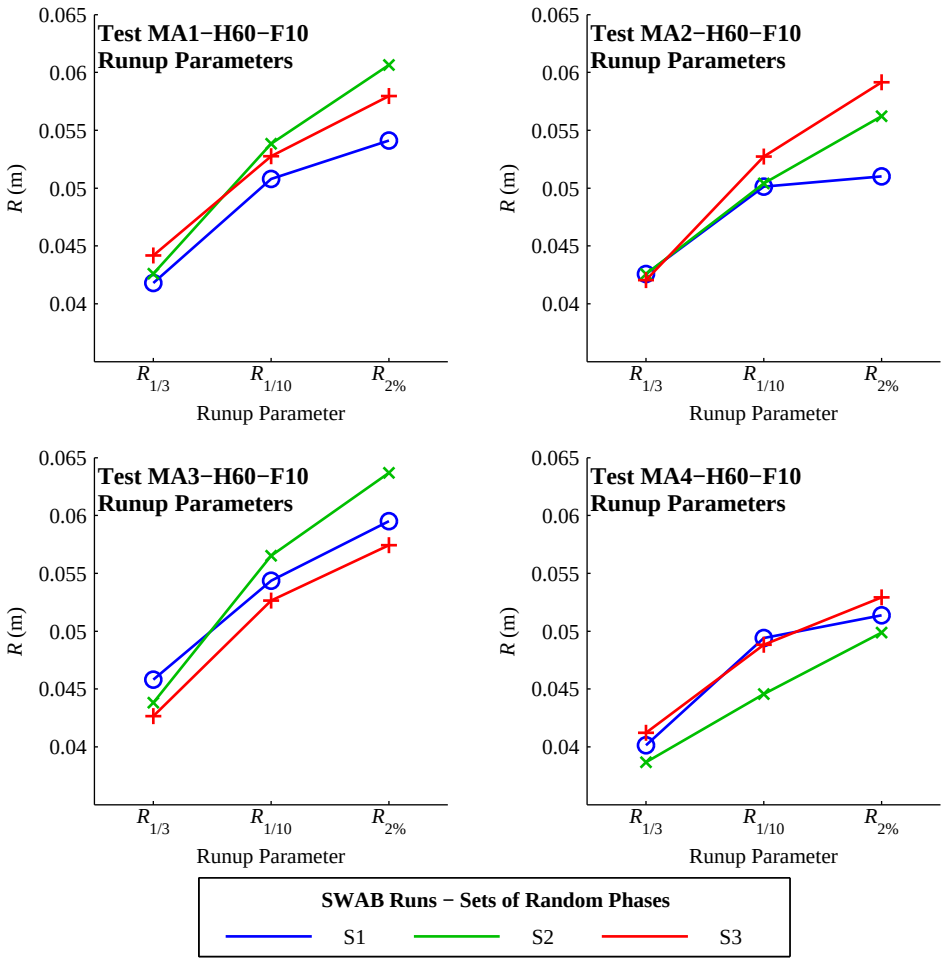

Figure 6.10: Effect of random phase on runup parameters: tests H60-F10

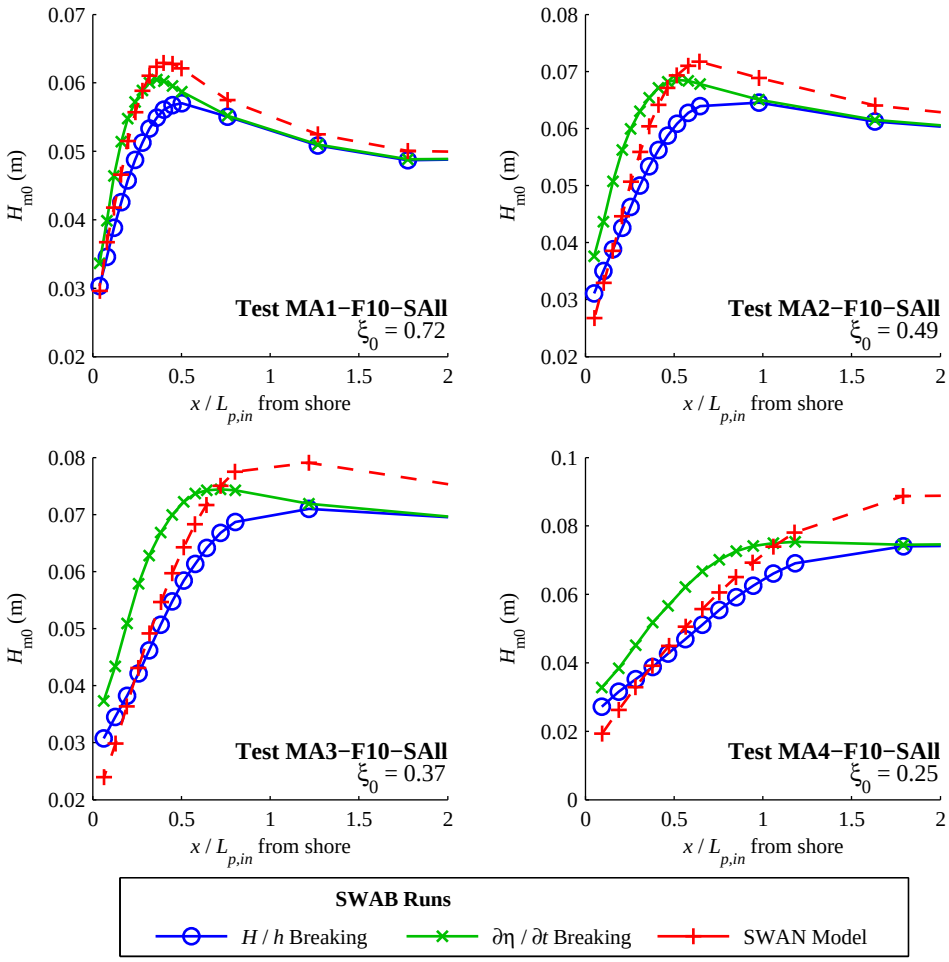

Figure 6.11: Effect of breaking criterion on significant wave heights: tests F10-SAll

accuracy of the SWAN model's results for waves close to the shore should be questioned. Figure 6.12a shows wave spectra for test MA3-F10-S1 approximately 1.2 $L_{p,in}$ from the shoreline; here although the SWAB model spectra are slightly lower than the SWAN model, the general shape is similar. However, close to the shore, the SWAN model gives a very different spectral shape (Figure 6.12b); therefore, it is probably unrealistic to use SWAN wave heights for comparison with SWAB at this location. It is interesting to note that the two breaking criteria give quite similar results in terms of spectral shape close to the shore.

The higher nearshore waves given by the $\partial\eta/\partial t$ criterion result in consistently higher wave runups (Figure 6.13). In comparison with Figures 6.6 and 6.9, the runups are consistently higher from the lowest to the highest. However, the $\partial\eta/\partial t$ criterion actually gives a lower number of individual runups, relative to the number of waves. As Figure 6.14 shows, both breaking criteria lead to underestimates in the number of individual runups (noting however that some may be missed due to the imperfect algorithm - see Section 6.1.1), but the H/h criterion does seem to give results closer to the experimental data. Note also that the friction

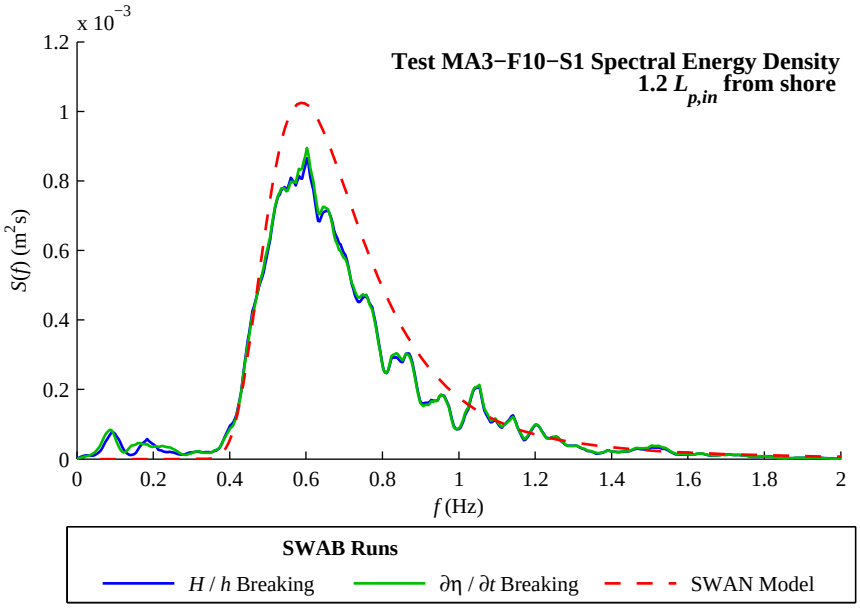

(a) 1.2 wavelengths from the shore, just prior to breaking

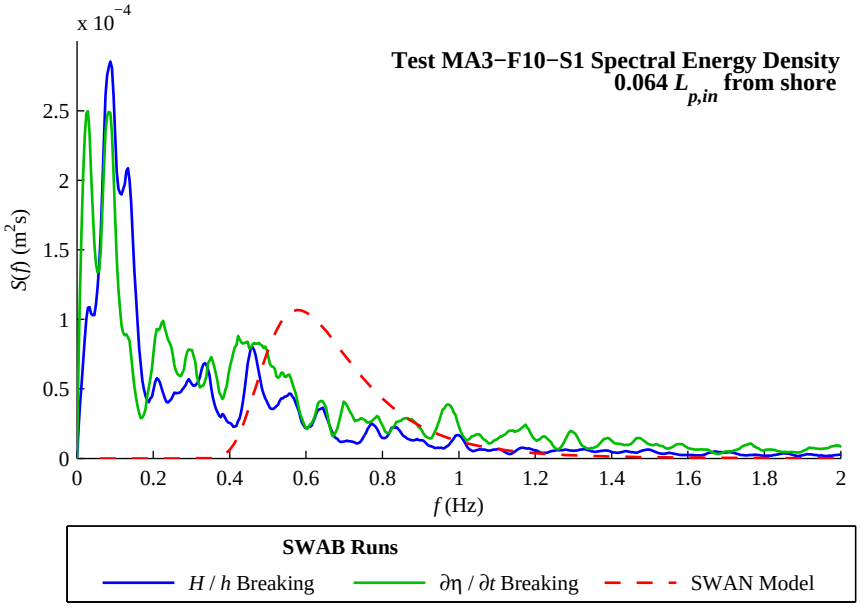

(b) 0.064 wavelengths from the shore

Figure 6.12: Nearshore spectal energy density: tests MA3-F10-S1

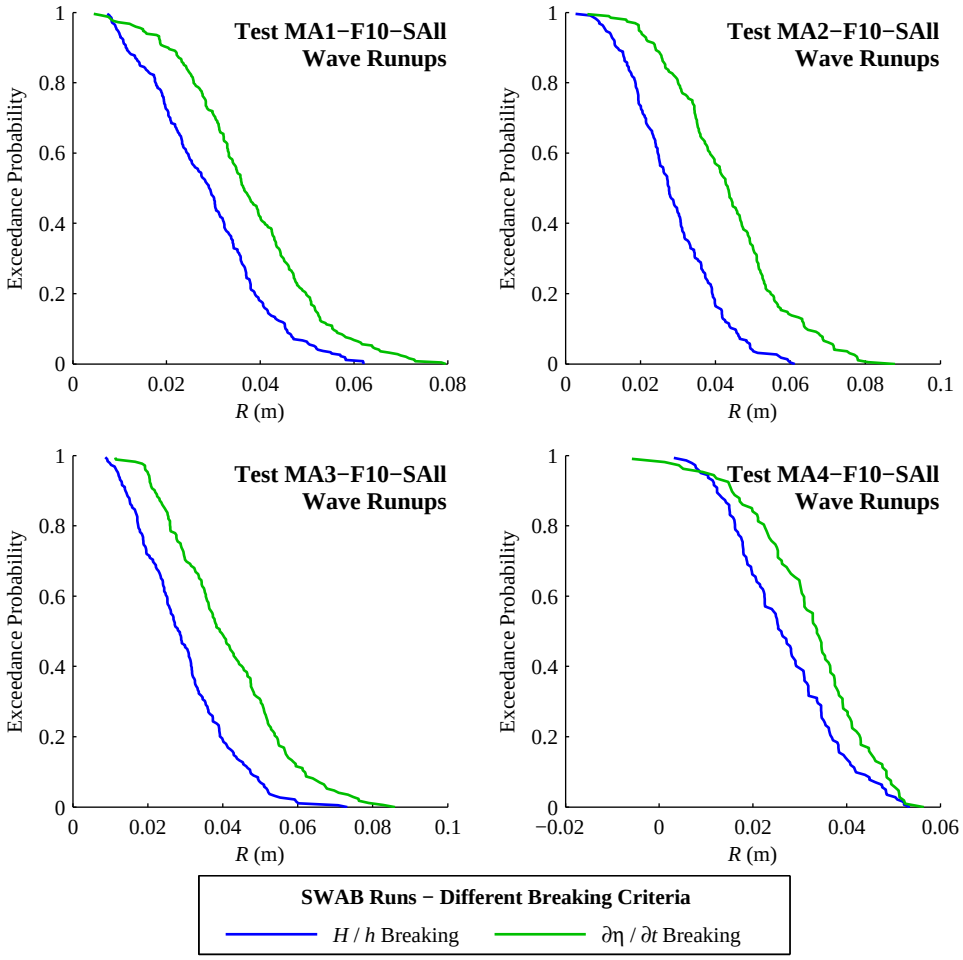

Figure 6.13: Effect of breaking criterion on wave runup distributions

coefficient makes very little difference to this ratio.

Mase [1989], like other authors, plot normalised wave runup levels as functions of the surf similarity parameter, ξ_0, based on the offshore wave steepness. From a much larger range of model tests on slopes from 1 in 5 to 1 in 30, relations were derived of form:

$$\frac{R}{H_0} = a\xi_0^b \tag{6.1}$$

where a and b are dimensionless parameters, dependent on which runup parameter R is being calculated. Figure 6.15 shows the calculated runup parameters from all tests, alongside the results from Mase [1989], including the associated power curves (equation (6.1)). Curves of the same form have been fitted to the SWAB model data. It appears that the $\partial\eta/\partial t$ criterion gives runups that are too large and the H/h criterion gives runups that are too small - this is to be expected from previous graphs. However, the curves associated with the H/h runs appear to be parallel to the curves of Mase [1989], whereas those associated with the $\partial\eta/\partial t$ criterion are not; it would seem that this association between ξ_0 and R/H_0 does not apply so well when

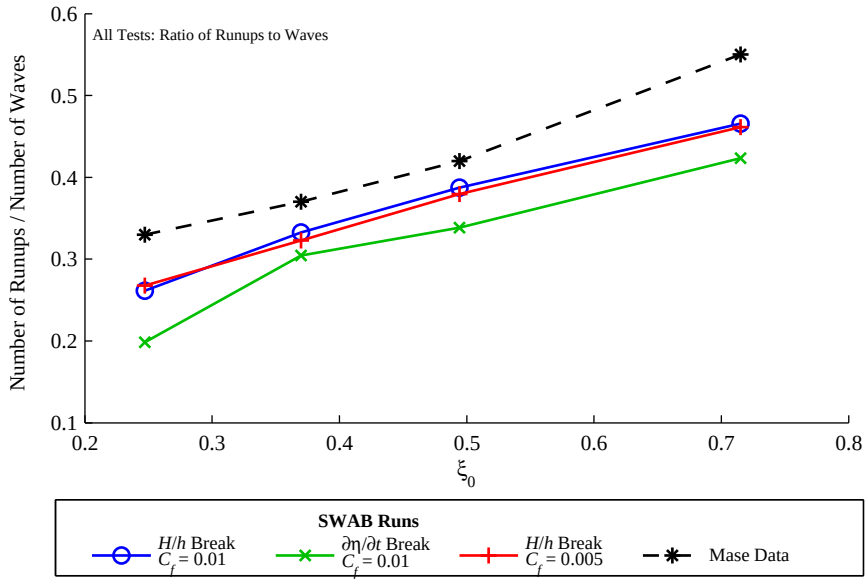

Figure 6.14: Effect of breaking criterion on proportion of runups to incident waves

$\partial\eta/\partial t$ breaking is used. With the H/h criterion and the lower friction coefficient, runup levels for these four tests are very similar to the data points of Mase [1989], though the curves are between 10 % and 20 % lower than those from the experiments.

6.2 Random Wave Runup with a Submerged Reef

6.2.1 Methodology

The results of Mase et al. [2004], with time-series from Mase [2008], were used to investigate random wave runup. The setting up of the SWAB model and the various SWAB runs are described in Section 5.3.1. The runup meter used in the experiments of Mase et al. [2004] was placed 3 mm from the face of the sloping seawall, and 10 cm (slope distance) from the base of the 1 in 3 slope; this gives a vertical distance of 0.0345 m from the base of the seawall to the start of the runup meter. Unfortunately, the runup data provided by Mase [2008] had an arbitrary zero level. To find the zero level, the runup data was sorted with the minimum runups (excepting a few anomalous data points with a lower level) being assumed to lie at this 0.0345 m level. Figure 6.16 shows some typical runup data, shown relative to the still water level.

To be consistent with the runup meter of the experiments, the SWAB 2.0 model was also set up using a limiting swash depth of 3 mm. However, the initial SWAB 3.0 model runs did not use this limit; instead, a smaller limit of 1.0×10^{-4} m was used. A comparison was made between the two different limits. As Figure 6.1 demonstrates, the lower limit would be expected

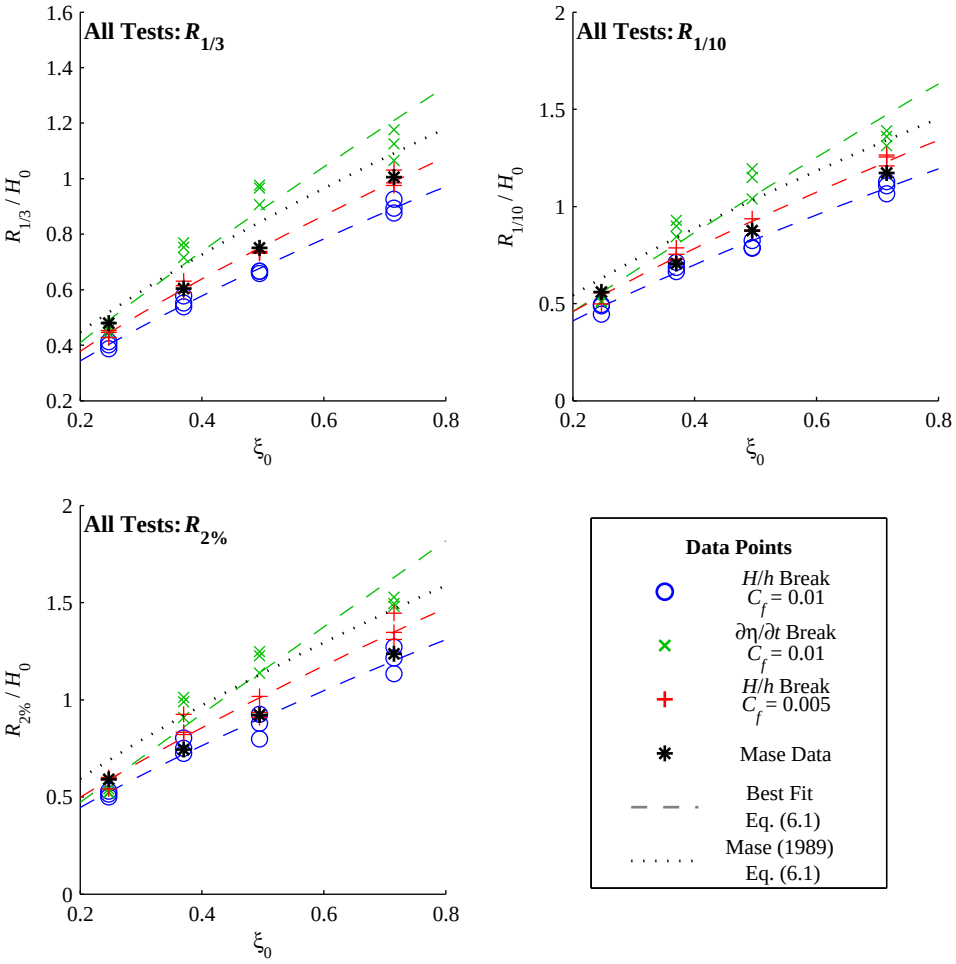

Figure 6.15: Runup parameters as a function of surf similarity parameter

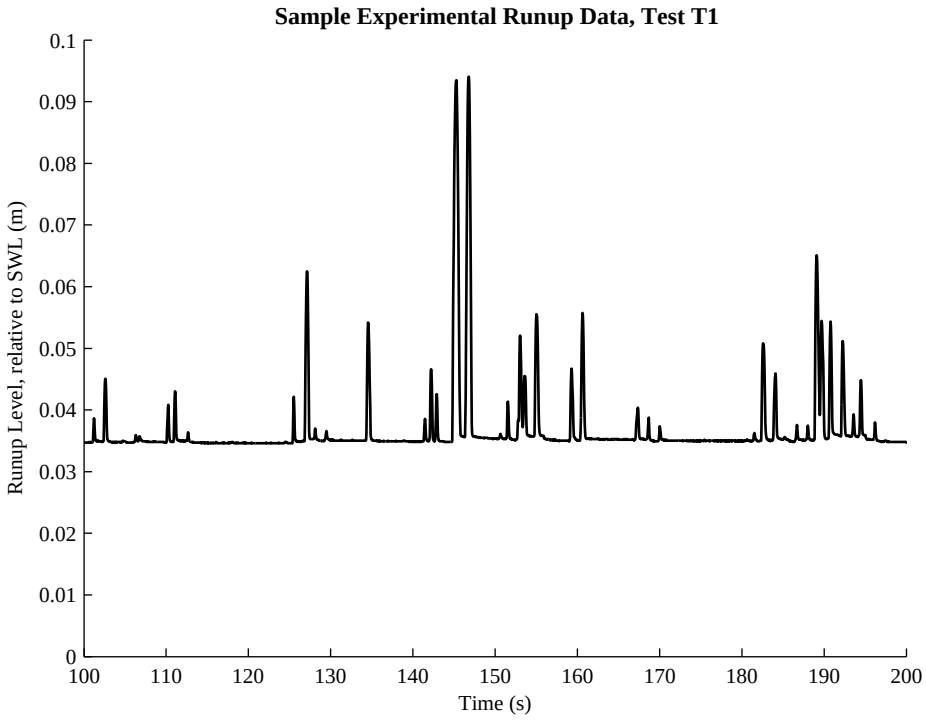

Figure 6.16: Extract from Mase et al. [2004] runup data

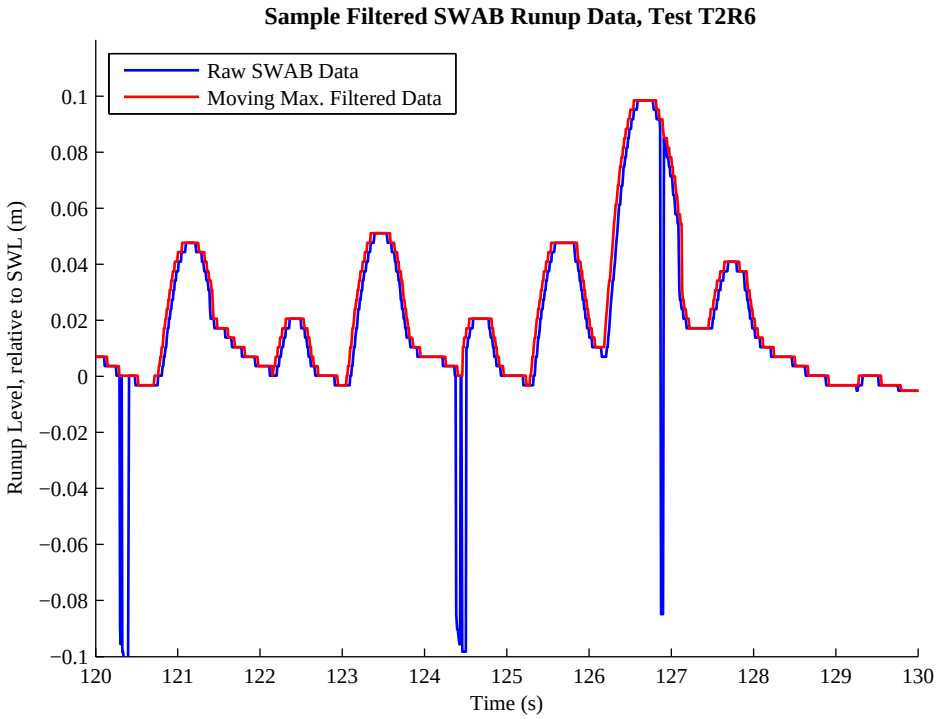

Figure 6.17: Extract from SWAB runup data: raw and filtered data

to slightly increase the runup crest levels but it will also increase unwanted oscillations in the SWAB data. To remove these oscillations, in this case it was found that a moving maximum filter worked better than a moving average filter; by applying this filter over windows of 10 time-steps, most unwanted oscillations were removed, without losing the run-down levels that are important for separating the runups. Figure 6.17 shows a typical expample of some filtered data. A zero-crossing method is used here to separate runups; one would expect it to be more reliable than the method used in Section 6.1.1. Therefore, a runup is said to begin when it exceeds a certain level; 0.036 m was selected as this level to avoid including noise in the minimum runup level as runups. The runup level is said to be the peak level before the next runup begins. Some runup crests will be neglected where the run-down does not go below 0.036 m; however, this is not important as long as the SWAB data and the experimental data are analysed in the same way.

6.2.2 Effect of friction factor on runup levels

Runs R1 and R2, using the SWAB 2.0 model, were used to show how the friction factor affects runup levels. Figure 6.18 shows runup distributions for these two runs, in comparison with the experimental data. Run R1 used a friction factor, C_f, of 0.005 and R2 used a factor of 0.015. For test conditions T1, there was very little difference between the two runs; in fact, the increased friction factor appears to give greater runups. However for test T2, with the longer

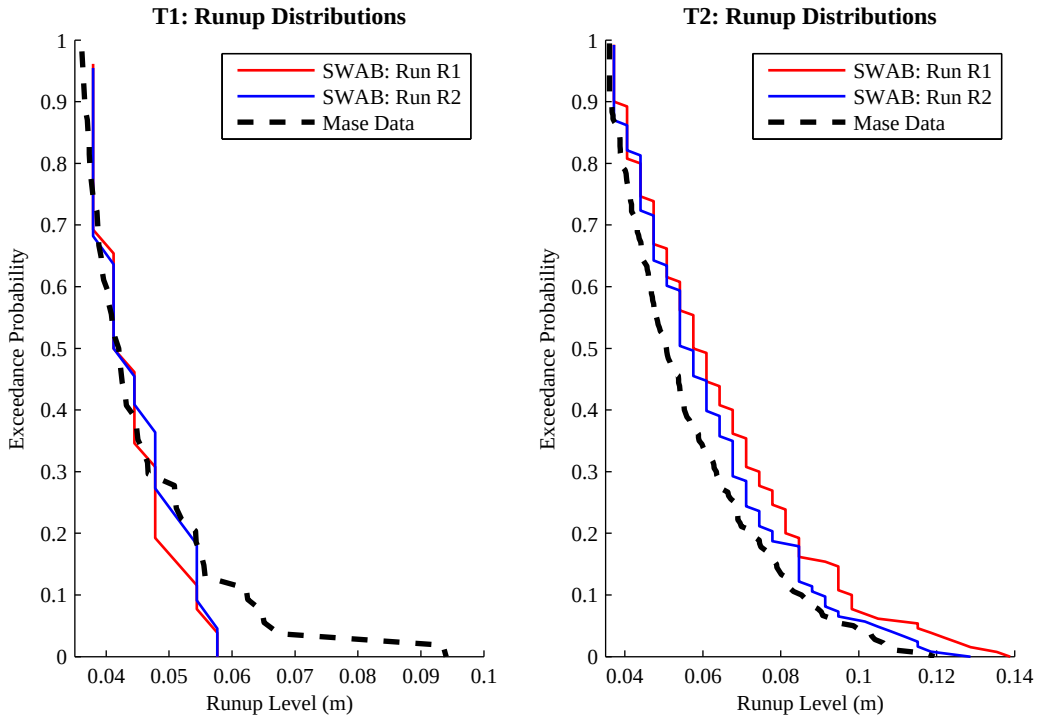

Figure 6.18: Runup distributions: Runs R1 and R2

waves, the increased friction factor reduces runup levels by approximately 10 %. As Figure 6.19 shows, the friction factor has an effect at all frequencies for test T2; for test T1, it only appears to have a significant effect between 0.4 Hz and 1.0 Hz.

6.2.3 Effect of swash limit on runup levels

Figure 6.20 show extracts from the time-series for filtered runup level from runs R5 and R6 for test conditions T1 and T2; it shows how the limiting depth affects the recorded runup level. It is interesting to note that, in the extracts shown, the R5 runups seem to be more greatly affected by this limit than the R6 runups; it is not clear why this should be the case. For consistency with the experimental data and the SWAB 2.0 model runs, it was decided to use the 3 mm limiting depth in the subsequent analysis.

6.2.4 Effect of breaking model on runup levels

Figure 6.21 shows wave runup distributions for Runs R1, R4, R5 and R6. Firstly, run R6, which uses the H/h breaking algorithm, gives very good results for both test conditions. This is not unexpected as the nearshore wave energy was very well predicted (see Figures 5.33 and 5.35). The SWAB 2.0 runs (R1 and R4) tended to underpredict runup for test T1 and overpredict it for test T2. Once again, this is consistent with the previous results for nearshore wave energy (Figures 5.32 and 5.34). It is apparent that the R1 run, where breaking continues between

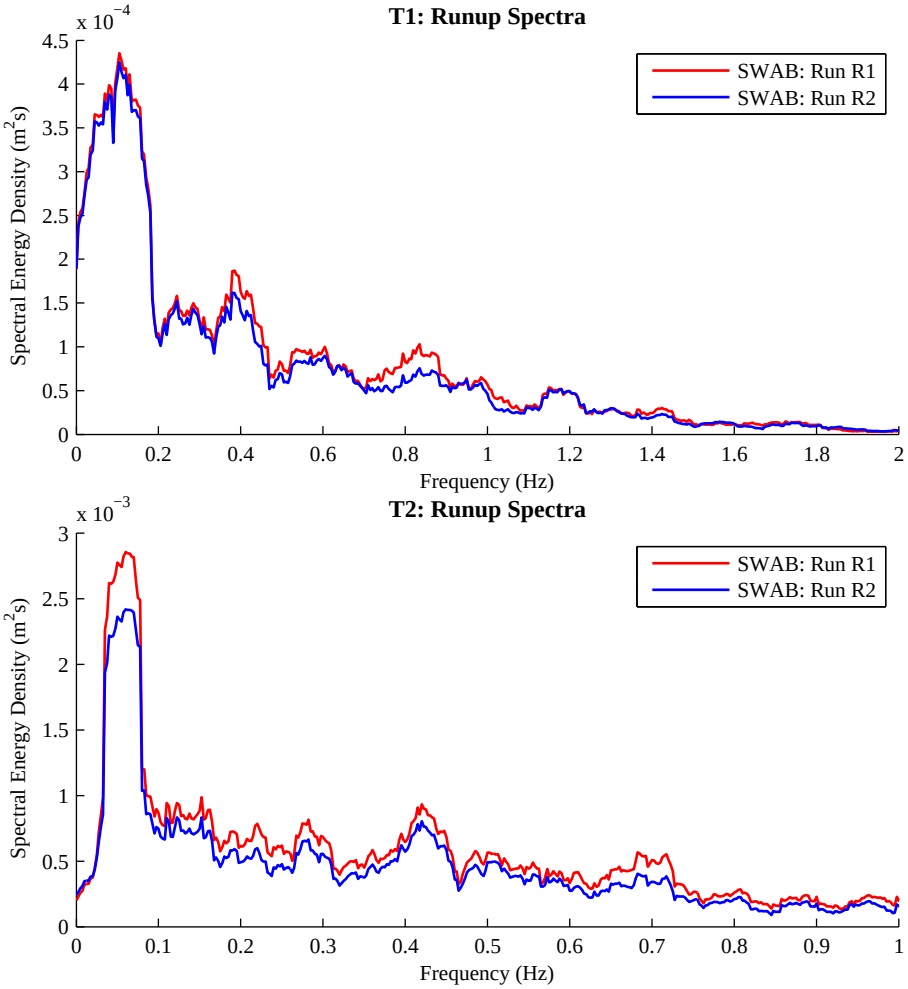

Figure 6.19: Runup energy spectra: Runs R1 and R2

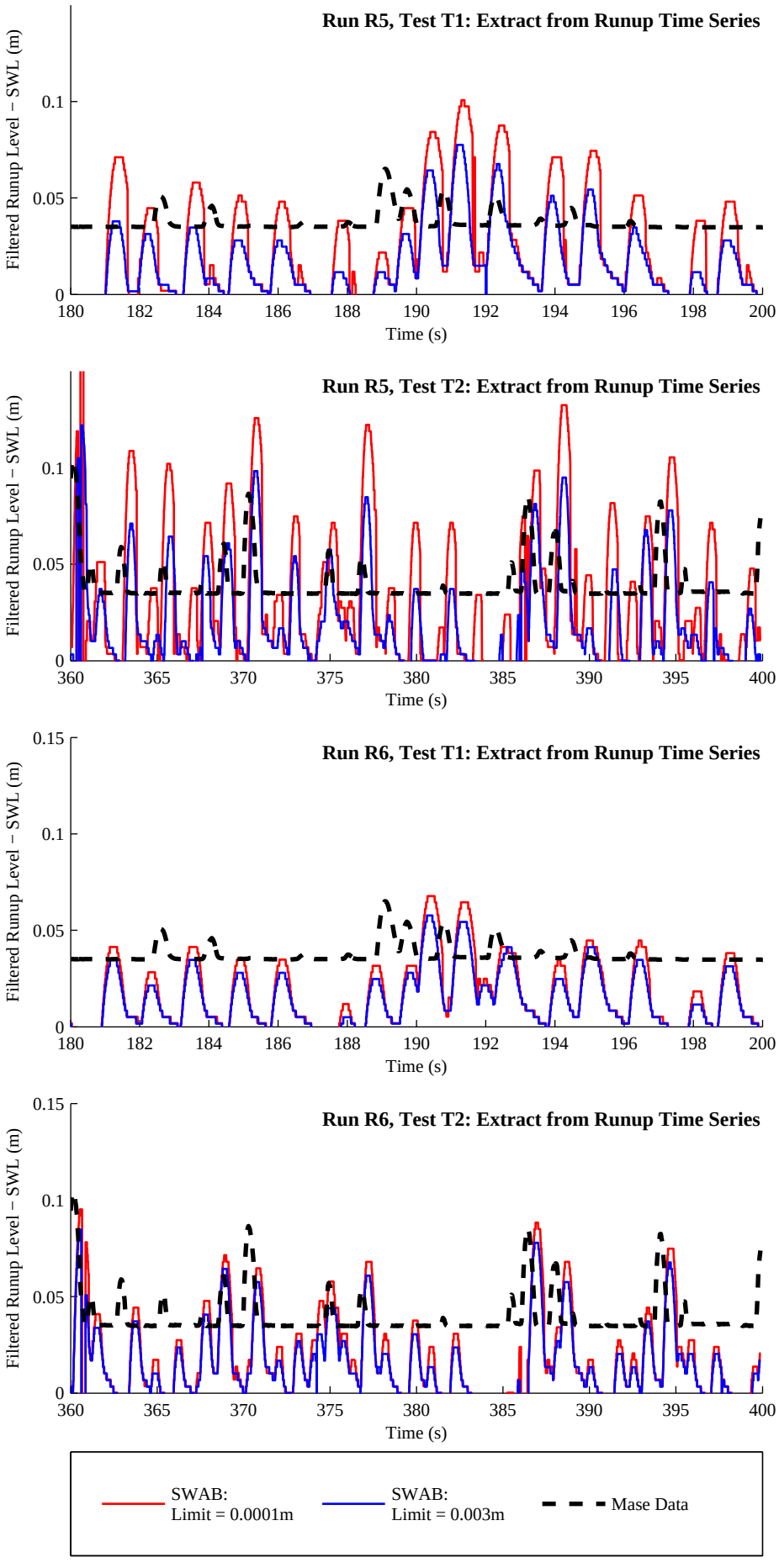

Figure 6.20: Extracts from runup time-series, showing the influence of the limiting swash depth

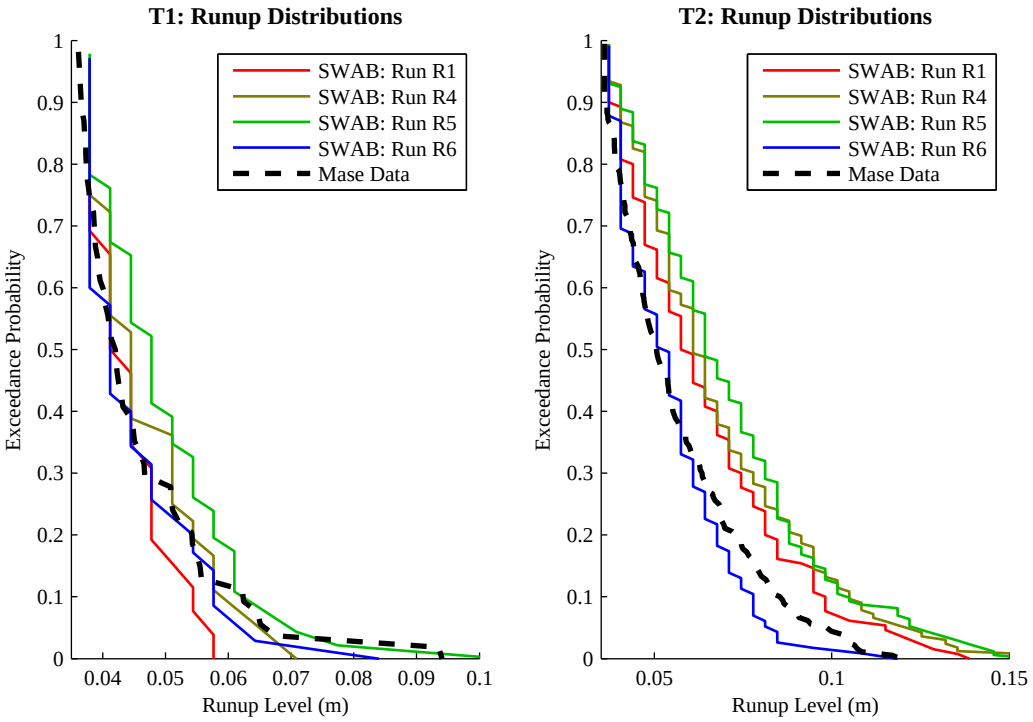

Figure 6.21: Runup distributions for tests T1 and T2: Runs R1, R4, R5 and R6

the reef and the shore, gives slightly lower runup levels than the R4 run, where breaking ceases. The R5 runs overpredicted runups for both test conditions. Although it used a very similar breaking algorithm to run R4, there were some minor differences. For run R4, absolute values for $\partial\eta/\partial t$ were used for the nearshore criterion; therefore breaking could initiate on the front or rear face of the wave; this was corrected for later versions of SWAB. As Figure 6.22 shows, the R5 runups have a greater proportion of energy around the peak frequency (approximately 1 Hz for test T1 and 0.5 Hz for test T2); this would suggest that less energy has been lost through wave breaking. Unfortunately it has not been possible to compare these runup energy spectra with the experimental data because of the 0.0345 m base level of the swash measurements (see Figure 6.16).

It is worth expressing a note of caution with the R6 runup distribution; the distributions shown in Figure 6.21 show runup exceedance probabilities relative to the number of runups. Tables 6.1 and 6.2 show the number of recorded runups. It is apparent that all SWAB runs underestimate the number of runups, but the R6 run does so quite severely. It may be possible to improve these results by reducing the friction coefficient; the R5 and R6 runs do use a higher coefficient ($C_f = 0.01$) than the R1 and R4 runs ($C_f = 0.005$). The number of recorded runups is also affected by the 0.036 m level that was used to separate individual runups. This level is quite high and it is apparent from examination of Figure 6.20 that a small underestimation of runup levels leads to many runup crests falling below the 0.036 m limit.

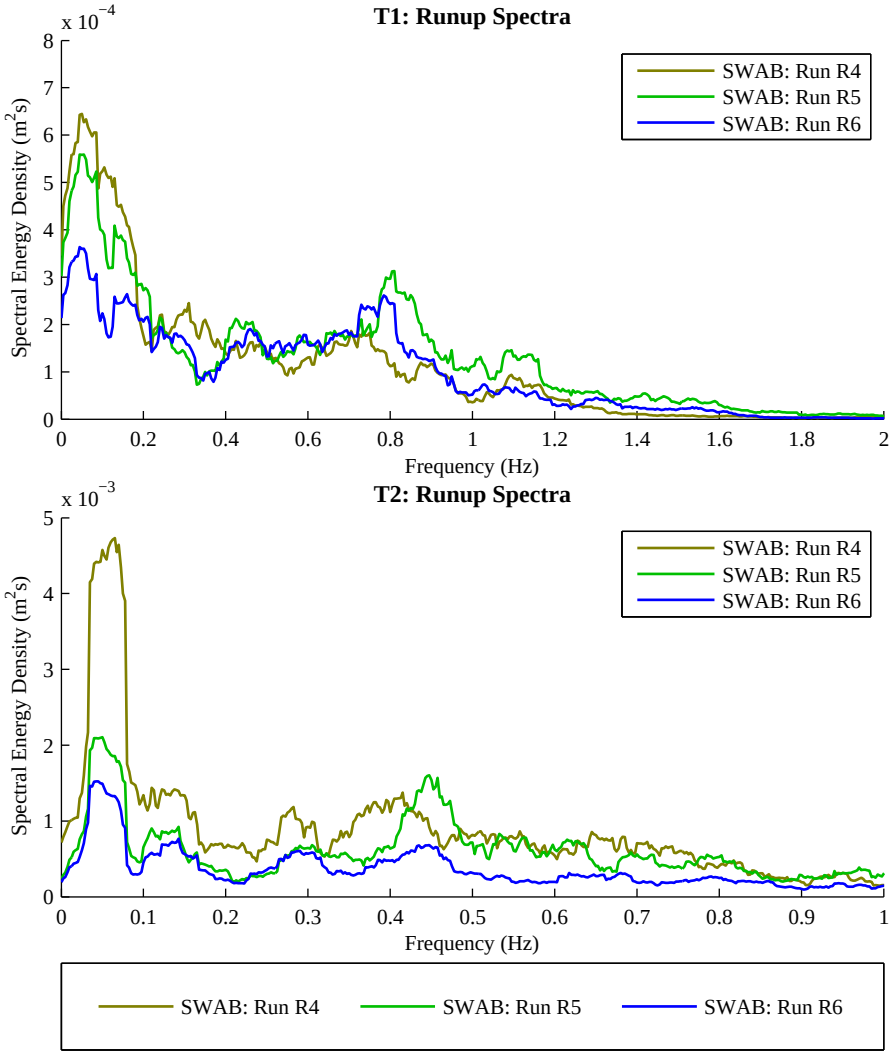

Figure 6.22: Runup spectra for tests T1 and T2: Runs R1, R4, R5 and R6

Table 6.1: Numbers of runups and incident waves: Test T1

Run Number	Number of Runups (N_R)	Number of Incident Waves (N_W)	Ratio of Runups to Waves (N_R/N_W)
R1	26	198	0.131
R4	36	198	0.182
R5	46	214	0.215
R6	35	214	0.164
Experimental Data	54	214	0.252

Table 6.2: Numbers of runups and incident waves: Test T2

Run Number	Number of Runups (N_R)	Number of Incident Waves (N_W)	Ratio of Runups to Waves (N_R/N_W)
R1	130	221	0.588
R4	166	221	0.751
R5	172	220	0.782
R6	115	220	0.523
Experimental Data	180	220	0.818

6.3 Conclusions

This chapter looked at the ability of the SWAB model to predict random wave runup. Random waves tests on a plane slope, and propagating over a submerged reef were used for this investigation. The following are the main findings from this chapter:

- As waves approach the shore, the effect of random phase becomes important; by testing three different runs of 200 waves, there was a 20 % difference between the highest waves over the three runs. This affects wave runups; values for $R_{2\%}$ varied by over 10 %.
- The friction factor makes very little difference to wave heights. However variations in C_f between 0.005, 0.01 and 0.015 can affect runup levels; maximum runups were affected by up to 10 % in some of the tests carried out. Lower runups are less affected by the friction factor than larger runups.
- Similarly to their effect on nearshore wave heights, the type of breaking algorithm has a significant influence on runup levels. The $\partial\eta/\partial t$ criterion generally resulted in the underestimation of runups for conditions with low surf similarity parameters, and overestimation for high surf similarity parameters. On the other hand, the H/h breaking model tended to underestimate runups for all values of ξ_0; however, the magnitude of this error was less affected by the value of ξ_0.
- For runups associated with waves propagating over a reef, the same general observations are true. Although the H/h breaking model slightly underestimates runup, the error is not dependent on the test conditions. For the $\partial\eta/\partial t$ breaking model, stopping the breaking process landward of the reef increased runup levels; a desirable consequence for the shorter waves, but not so for the longer period waves, where runup levels were already overestimated. The H/h breaking model also has the advantage of not requiring any manual input to stop the breaking process in deeper water.

Chapter 7

Wave Overtopping: Anchorsholme Seawall

7.1 Methodology

The results from the scale model tests of the seawall at Anchorsholme, Blackpool were used for this investigation; these tests are described in Section 4.3. Additionally, the field data included some recordings of overtopping volumes. Unfortunately, these do not fully correspond with the physical model tests, but some analysis can be performed.

For most tests, the SWAB model was set up with the same bathymetry as the flume. Two bathymetries were available: the bathymetry supplied before the wave flume experiments, and the re-surveyed bathymetry taken just prior to the start of testing (see Figure 4.11). (Note, the bed was formed of concrete so no change in bathymetry took place due to sediment transport). Initial testing with the SWAB model showed that the re-surveyed bathymetry gave a more accurate match in terms of the time taken for waves to travel between different probes; therefore, this bathymetry was used for all tests. The SWAB tests of these experiments were run at model scale. The wave input was located at Wave Probe 1, with 10 m of domain added offshore of this location to contain the sponge layer. The seawall profile could not be included to its full level of accuracy (see Figure 4.10); therefore, an approximation was made (Figure 7.1 (Inshore Section)), with wall forces applied at the locations shown. The influence of this force on waves near the seawall and on overtopping will be discussed in Sections 7.2.2 and 7.3. Landward of the seawall, a collection tank was included, with a reflective boundary condition (no sponge layer was needed).

The SWAB model was also set up to simulate the wave calibration tests in the flume. The

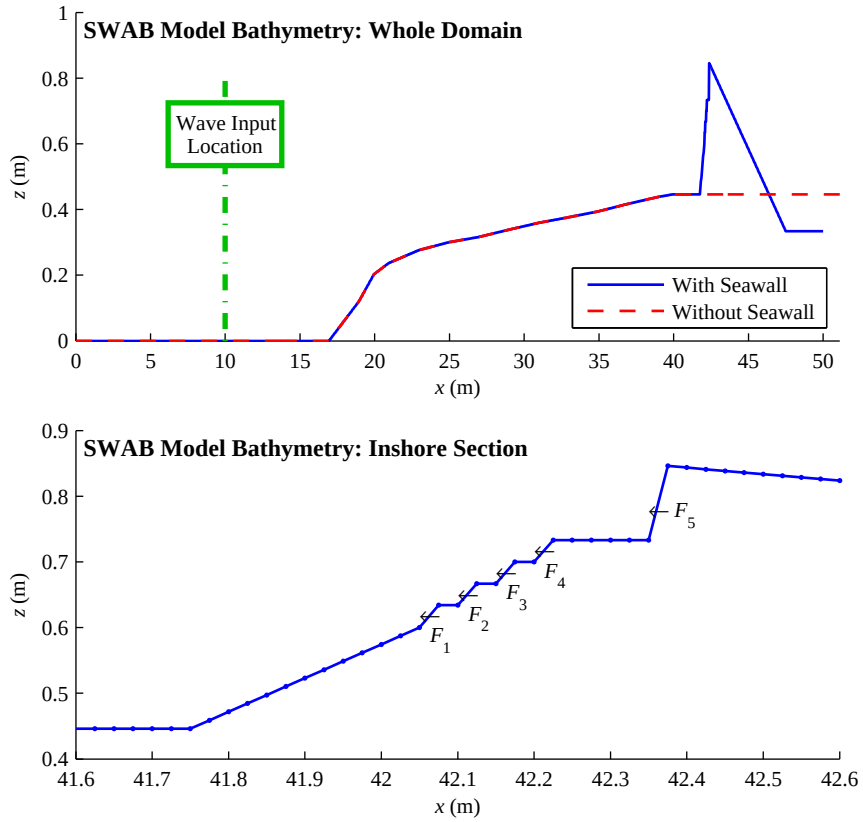

Figure 7.1: SWAB model bathymetries, including seawall bathymetry, with locations where wall forces were applied

SWAB bathymetry is shown in red in Figure 7.1. In this case a sponge layer was included at the inshore boundary; therefore the model domain was made a little longer to incorporate enough space for the sponge layer between the inshore boundary and Wave Probe 8.

Analysis of the time-series data from the wave flume showed some erratic data, possibly caused by damaged wave probes. For many of these time-series the erratic data come in the form of sporadic bursts of noise, which could be filtered out. However, in other cases the data are possibly useless. For most calibration runs (including post-calibration), the datasets from Wave Probe 6 are so erroneous that most of them are useless (Figure 7.2 gives a typical sample); also for the test runs with the seawall, parts of the time-series from Wave Probe 6 have erratic data. Therefore no data from Wave Probe 6 were used. For the post-calibration runs, the time-series from Wave Probe 1 also contained some bursts of erratic data. These were used to create inputs for the SWAB model. However, in the SWAB input files one can specify a maximum input frequency; by setting this to $5.0 f_p$ one is effectively imposing a low-pass filter on the input data, which should eliminate the problems. Figure 7.3 shows a sample of this data including the filtered time-series. For the test runs with the seawall, the Wave Probe 7 time-series contained very erratic data; this was not used. Probes 1, 3 and (rarely) 5 also contained some erratic data, for which a low-pass filter was used to eliminate the noise

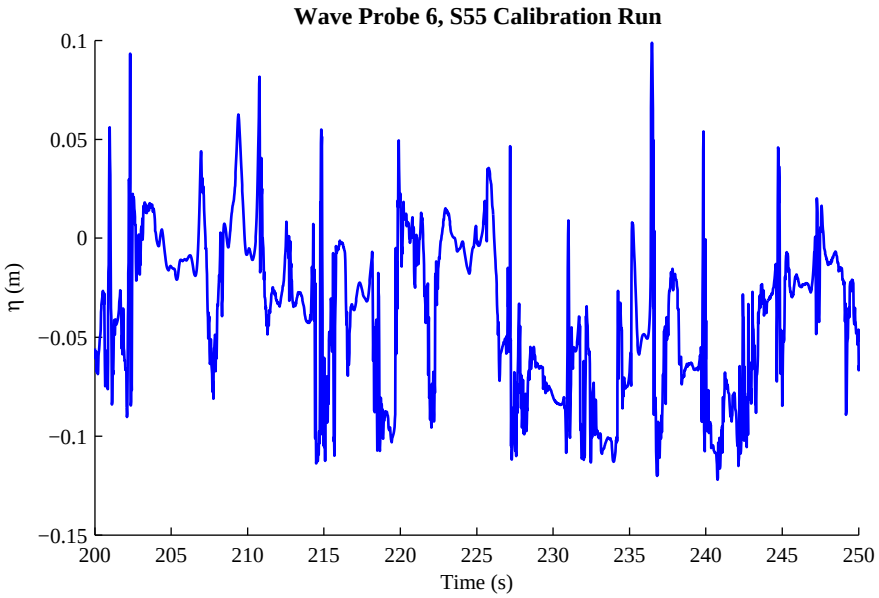

Figure 7.2: Wave Probe 6: useless data

(Figure 7.4). Because it is possible that some of these sporadic high frequency bursts may not have been detected in some datasets, and for consistency, the high frequency ($> 5.0 f_p$) motion was filtered from all the time-series, using MATLAB code.

For the input waves, wave flume time-series for Wave Probe 1 were available for both the calibration runs (i.e. without the seawall), and for the storm runs (i.e. with the seawall). Obviously, the storm run time-series consist of both incident and reflected waves. For the calibration time-series the incident waves should be the same as those for the storm run, whereas the reflected waves are expected to be negligible. Therefore, the calibration time-series were used for the wave input. By comparing the SWAB outputs at the other wave probe locations with the storm run time-series, it will be possible to examine how well SWAB models wave reflection from the seawall. Unfortunately, it is not possible to separate the incident and reflected waves of the wave flume data using the method of Frigaard and Brorsen [1995] (see Section 5.3.1) as the wave probes were spaced too far apart. The input wave conditions taken from the calibration runs at model scale are shown in Table 7.1. Surf similarity parameters were calculated using the slope between $x = 25\,\text{m}$ and $x = 40\,\text{m}$ in Figure 7.1 (this being where most breaking occurred), with deepwater wave conditions, estimated by using linear wave theory to transform the values of H_{m0} and T_p offshore from the wave input location; all surf similarity parameters are low, corresponding to spilling breakers. Note that the values in Table 7.1 refer to conditions at Wave Probe 1, and therefore do not correspond exactly to those in Table 4.7, which used Wave Probe 2.

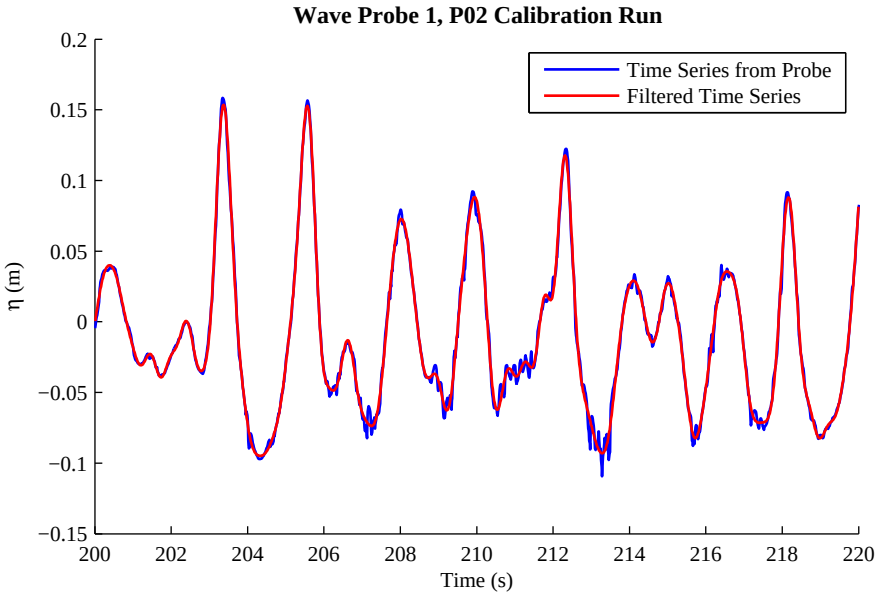

Figure 7.3: Wave Probe 1: for use as input data

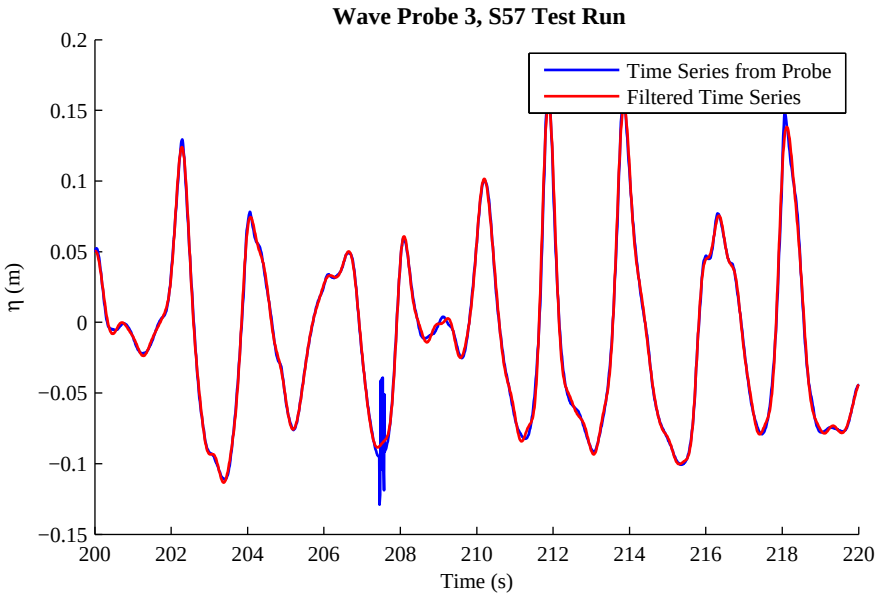

Figure 7.4: Wave Probe 3: showing short burst of erratic data

Table 7.1: SWAB model input wave conditions

Wave Condition	Wave Condition Code	d_{in} (m)	$H_{m0,in}$ (m)	$T_{p,in}$ (s)	ξ_0
Storm 23	S23	0.593	0.117	1.495	0.052
Storm 55	S55	0.644	0.223	1.945	0.050
Storm 57	S57	0.655	0.233	2.041	0.051
Storm 59	S59	0.635	0.219	2.040	0.053
Storm 131	S131	0.666	0.196	1.815	0.049
Storm 135	S135	0.593	0.172	1.992	0.058
Parametric 01	P01	0.655	0.290	2.235	0.051
Parametric 02	P02	0.654	0.238	2.220	0.055
Parametric 03	P03	0.644	0.228	1.963	0.049
Parametric 04	P04	0.593	0.261	2.123	0.051
Parametric 06	P06	0.644	0.268	2.235	0.053
Parametric 07 G75	P0775	0.666	0.204	2.220	0.060
Parametric 07 G85	P0785	0.666	0.229	2.220	0.056

7.2 Nearshore Waves: SWAB Results

7.2.1 Results without seawall

The SWAB model was run without the seawall (see Figure 7.1 for bathymetry), with results compared to the data from the calibration tests. Four different breaking types were examined; these are described in Table 7.2.

Figure 7.5 gives nearshore wave heights, for the first half of the storm waves, with the SWAB runs shown alongside wave heights from the experiments. The phased-out Boussinesq breaking model (EP25) performs very badly in the shallow water, although because the surf similarity parameters are very low a higher breaking coefficient may give better results. The double breaking model (E15H65) results in offshore wave heights being too low and nearshore wave heights too large. However, the other two breaking models (especially EW30) show better agreement with the experimental data. Neglecting the EP25 breaking model, Figures 7.6, 7.7 and 7.8 show moving average rms values of the free surface level time series at selected wave probes in comparison with the experimental data. In Figures 7.6 to 7.8, the moving average is calculated over a period $20T_p$. Note that the double break point (E15H65) model

Table 7.2: Breaking types for SWAB tests

Breaking Type Code	Description
EP25	$\partial\eta/\partial t$ criterion with phased-out Boussinesq terms Breaking where $\partial\eta/\partial t > 0.25\sqrt{gh}$
EW30	$\partial\eta/\partial t$ criterion calculated wave-by-wave Breaking applied to each whole wave where $\partial\eta/\partial t$ exceeds $0.3\sqrt{gh}$
E15H65	Double breaking criterion (see Section 3.2.2) Horizontal diffusion terms applied where $\partial\eta/\partial t > 0.15\sqrt{gh}$ Horizontal diffusion switched on and Boussinesq terms phased out when $H/h > 0.65$
HH60	H/h criterion calculated wave-by-wave Breaking applied to each whole wave where $H/h > 0.6$

was run over a shorter length of time than the other two models, and therefore the results in the figures do not extend over the full period shown.

The figures show that the E15H65 breaking model causes waves to decay too much in the deeper sections of the flume, and not enough in the shallower part of the flume. It would appear that introducing the horizontal diffusion too early causes the waves to be insufficiently depth-limited as they move into shallower water. The EW30 and HH60 breaking types (where the wave breaking is applied to the whole wave) are more effective at depth-limiting the breaking waves. As would be expected, the H/h type criterion causes the time-series of wave energy to become quite steady in the shallowest water (Wave Probe 7), though at a slightly higher level than the breaking coefficient C_{bh} would specify. The EW30 breaking does result in a more fluctuating energy level, which is qualitatively more similar to the experimental data, although these fluctuations do not tend to be in phase with those from the experiments. In Figures 7.6 to 7.8 four main peaks in incident wave energy can be identified in each of the three wave conditions, with the energy around 130 waves (i.e. $(t-x_{probe}/c_g)/T_p = 130$) being the greatest. For the S57 wave condition (Figure 7.7), the EW30 breaking model (wave breaking applied to the whole wave, $\partial\eta/\partial t$ criterion) causes too much energy loss to occur; by the time these waves reach the shore they are actually smaller than other waves in the time-series. It is unclear why too much wave breaking should happen for these waves in particular.

For the same three tests, spectral energy curves are shown in Figures 7.9, 7.10 and 7.11; note that in these figures the spectral energy density has been divided by the total spectral energy m_0, to make comparisons easier. Also, the spectral energy curves were taken from fast Fourier transforms of the time-series, using a window of $T_p/20$. Only results from wave probes 2, 5 and 7 are shown for clarity. At Wave Probe 2, before breaking occurs, the SWAB model agrees very well with the experimental data. At Wave Probe 5, the drop in energy around

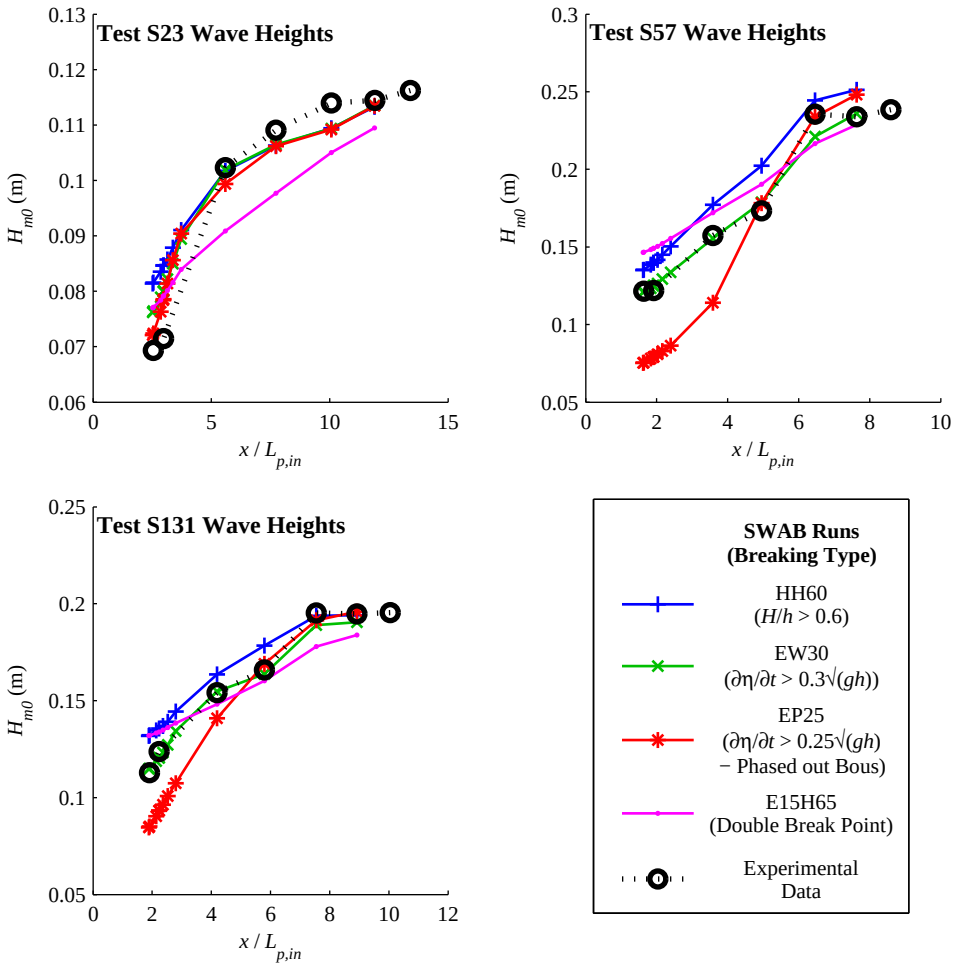

Figure 7.5: Significant wave heights for model without seawall - for first 410 s of waves (x is distance from inshore boundary of SWAB model)

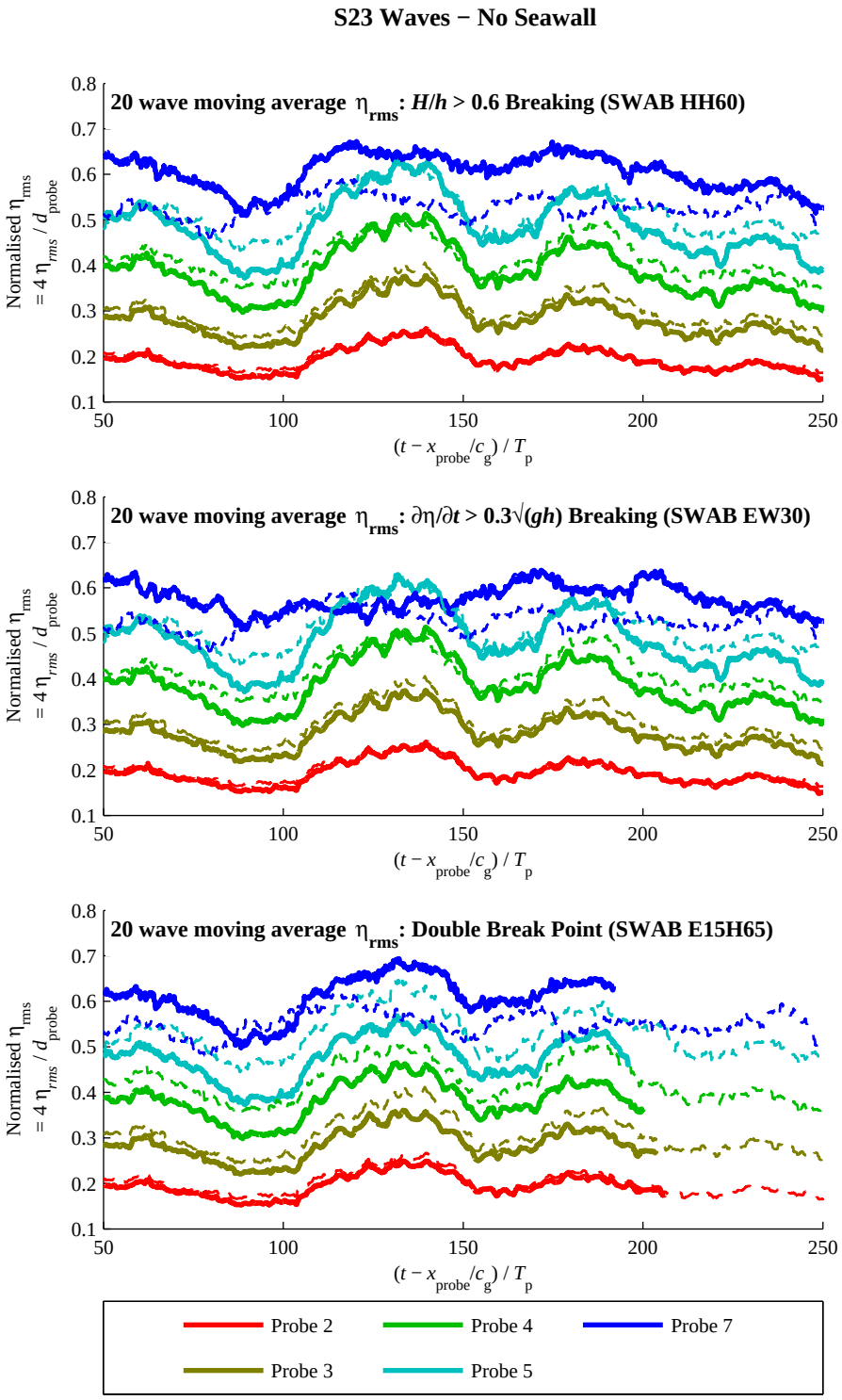

Figure 7.6: Time-series of 20 wave moving average normalised η_{rms}, at various wave probe locations, for S23 wave conditions. Experimental data shown as dotted lines and SWAB runs shown as solid lines

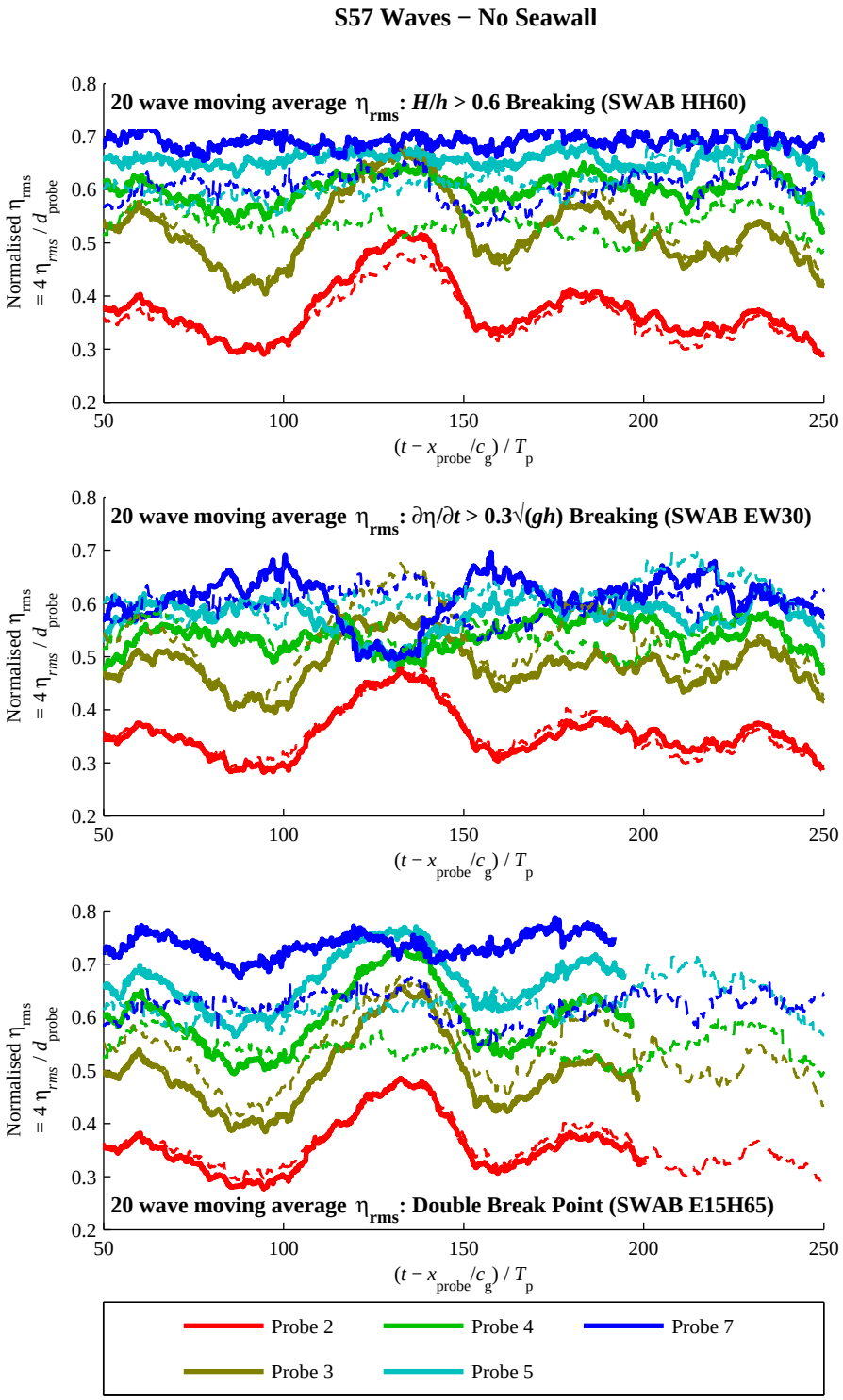

Figure 7.7: Time-series of 20 wave moving average normalised η_{rms}, at various wave probe locations, for S57 wave conditions. Experimental data shown as dotted lines and SWAB runs shown as solid lines

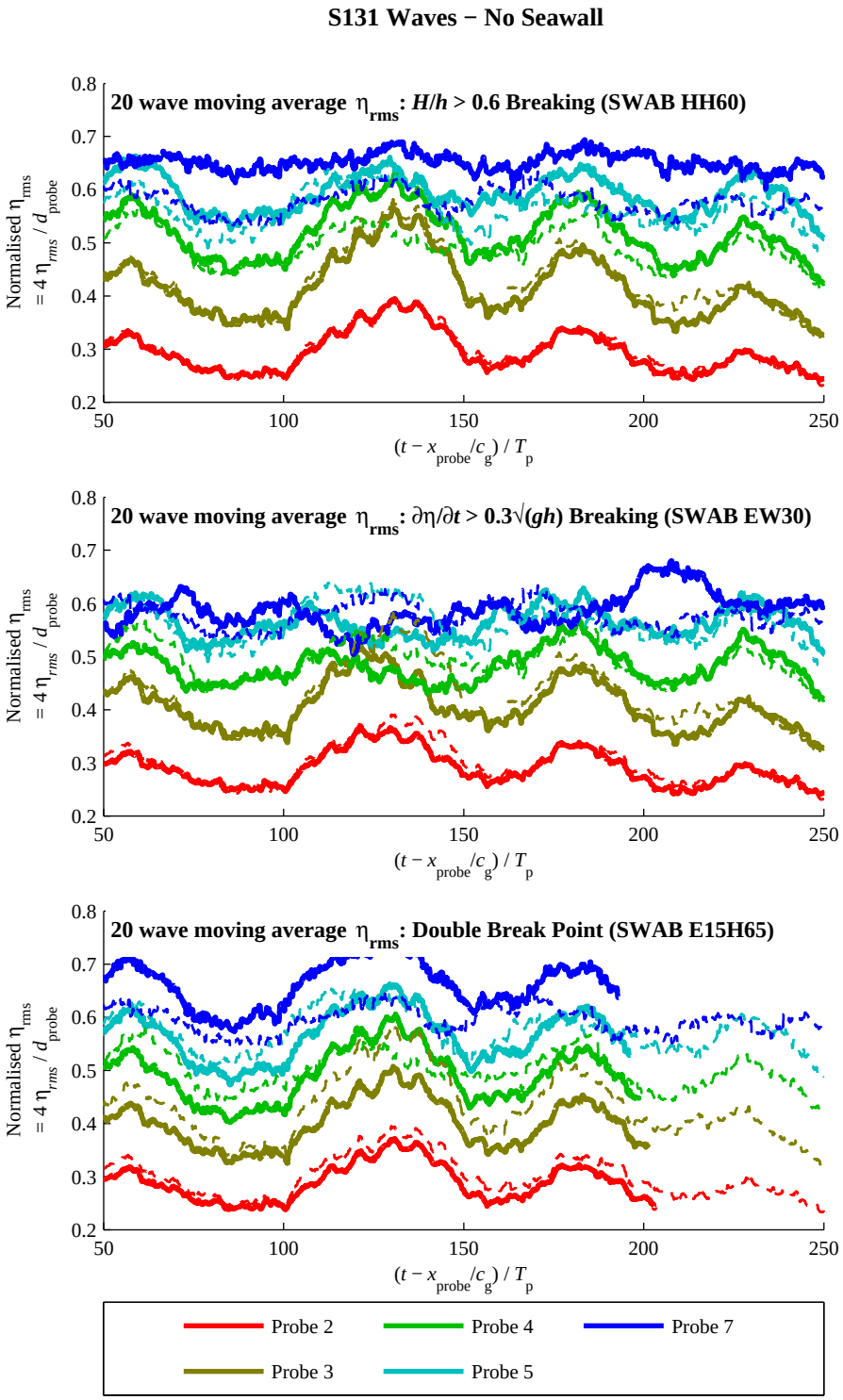

Figure 7.8: Time-series of 20 wave moving average normalised η_{rms}, at various wave probe locations, for S131 wave conditions. Experimental data shown as dotted lines and SWAB runs shown as solid lines

the peak frequency is smaller for the SWAB model than the experiment; all three breaking models give similar results at this location, except for test S131, where the E15H65 model (with the double break point) does not perform as well as the other two types. It may be that because too much energy loss occurred offshore, not enough waves are breaking by the time they reach Probe 5. One notable feature of the experimental data from Wave Probe 7 is the spectral peaks occurring at approximately $0.28f_p$, $0.44f_p$ and $0.38f_p$ respectively for the three test conditions. This corresponds to a wavelength of about 7 m. Wave Probe 7 was located 5.85 m from the back wall of the flume, which had a gravel beach placed in front to absorb reflections (see Figure 4.13). It is probable that these spectral peaks are caused by the reflection off this beach; a distance of 3.5 m would correspond to an antinode half a wavelength from the beach. There are also smaller spectral peaks of higher frequency, giving wavelengths of about 3.5 m, corresponding with the next antinode caused by the reflection. These reflections may also contribute to some of the differences in Figures 7.6, 7.7 and 7.8 between SWAB and the experimental data at Wave Probe 7.

7.2.2 Results with seawall

This seawall is rather a complex structure, with the four vertical steps and a recurve wall set back from the steps. It is not intended to do a detailed qualitative or quantitative study on the fluid mechanics at the wall; however, it will be useful (and interesting) to briefly examine some of the processes for the purpose of developing the SWAB model to more reliably predict overtopping.

Wave energy can reflect off the steps but it is also possible for eddies to form between the steps with the uprushing water flowing over these eddies. It is also possible for the steps and the recurve wall to force water vertically into the air; some of the water may overtop the structure, but there will be a loss of energy. Unless the discharge across the recurve wall is large, in which case it will be flooded, a significant proportion of the overtopping water is spray that has been forced upwards in this way. Figures 7.12 and 7.13 show the uprushing water on the steps; in Figure 7.12 it appears that the lowest step forces the water upwards leading to a low pressure region between the lowest step and the second step; this region exists between the second and third step, and to a lesser extent between the third and final step. The main body of uprushing water seems to form a jet that does not travel along the horizontal part of the crest, but impacts into the recurve wall; some of this water can be seen being reflected (by splashing) and some splashes over the top of the wall.

Figure 7.13 shows a breaking wave just reaching the steps; at this point the water being forced upward is visible at the lowest step. In Figure 7.14 the same wave has hit the recurve

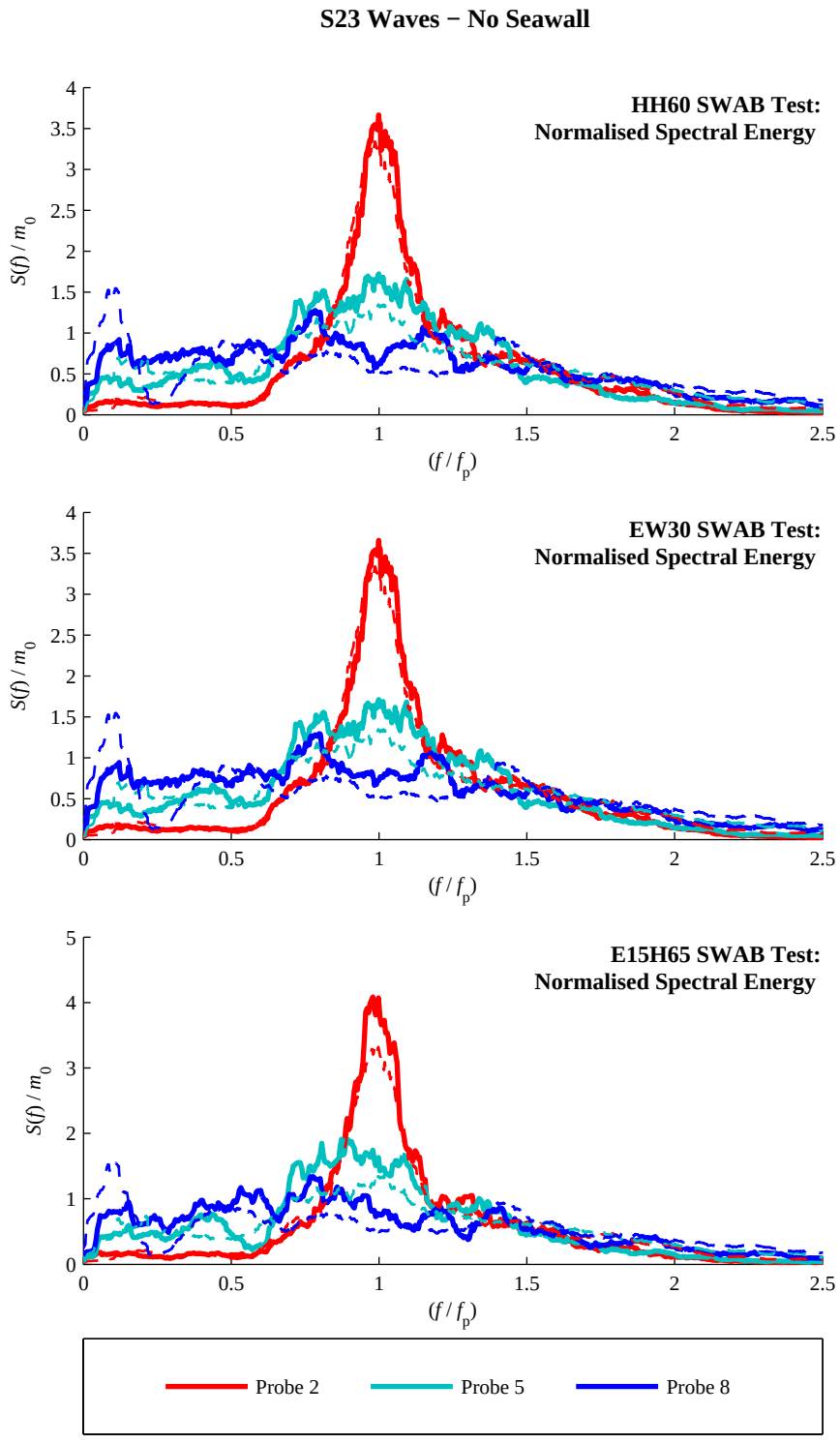

Figure 7.9: Normalised spectral energy density, at various wave probe locations, for S23 wave conditions. Experimental data shown as dotted lines and SWAB runs shown as solid lines

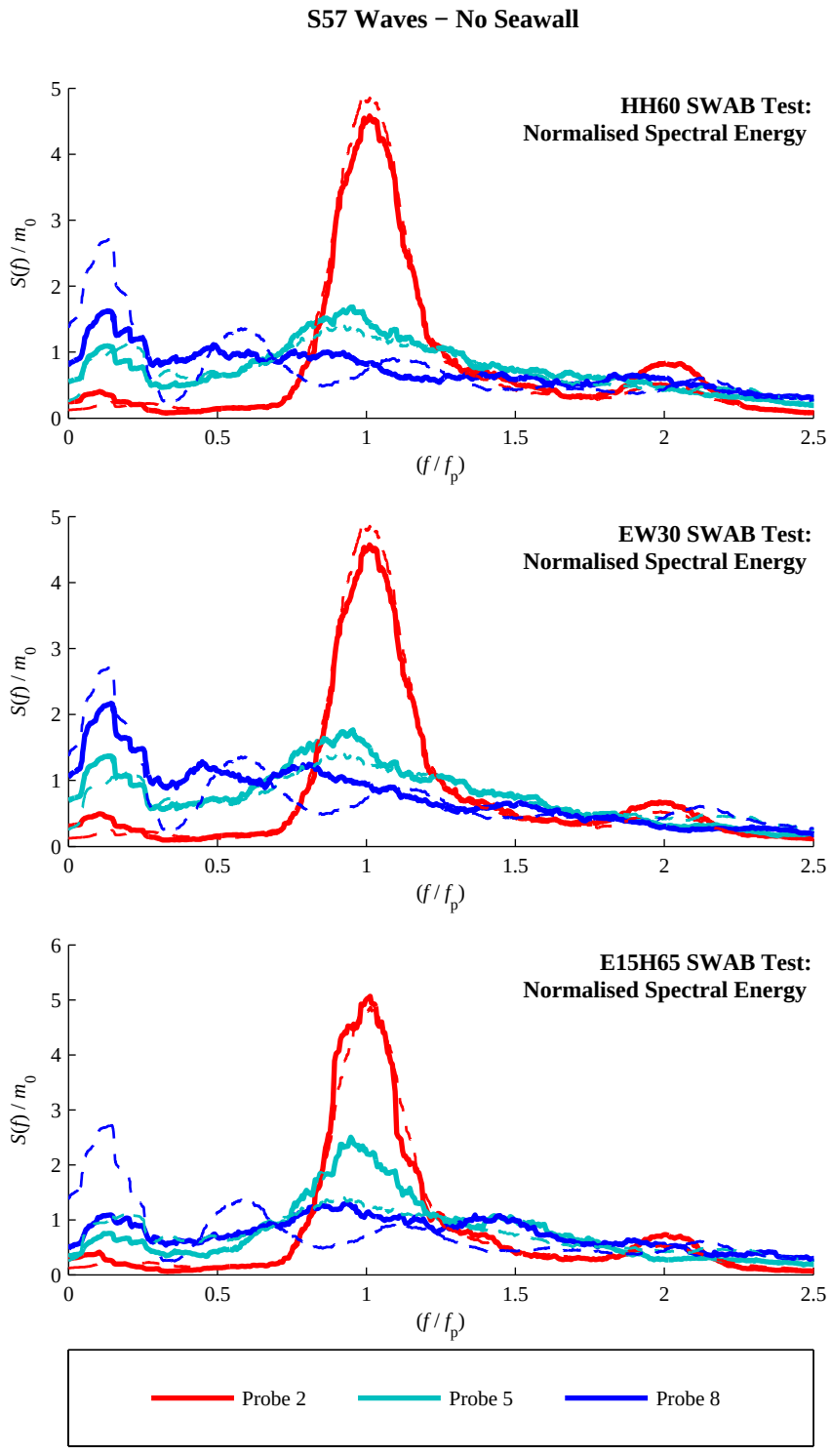

Figure 7.10: Normalised spectral energy density, at various wave probe locations, for S57 wave conditions. Experimental data shown as dotted lines and SWAB runs shown as solid lines

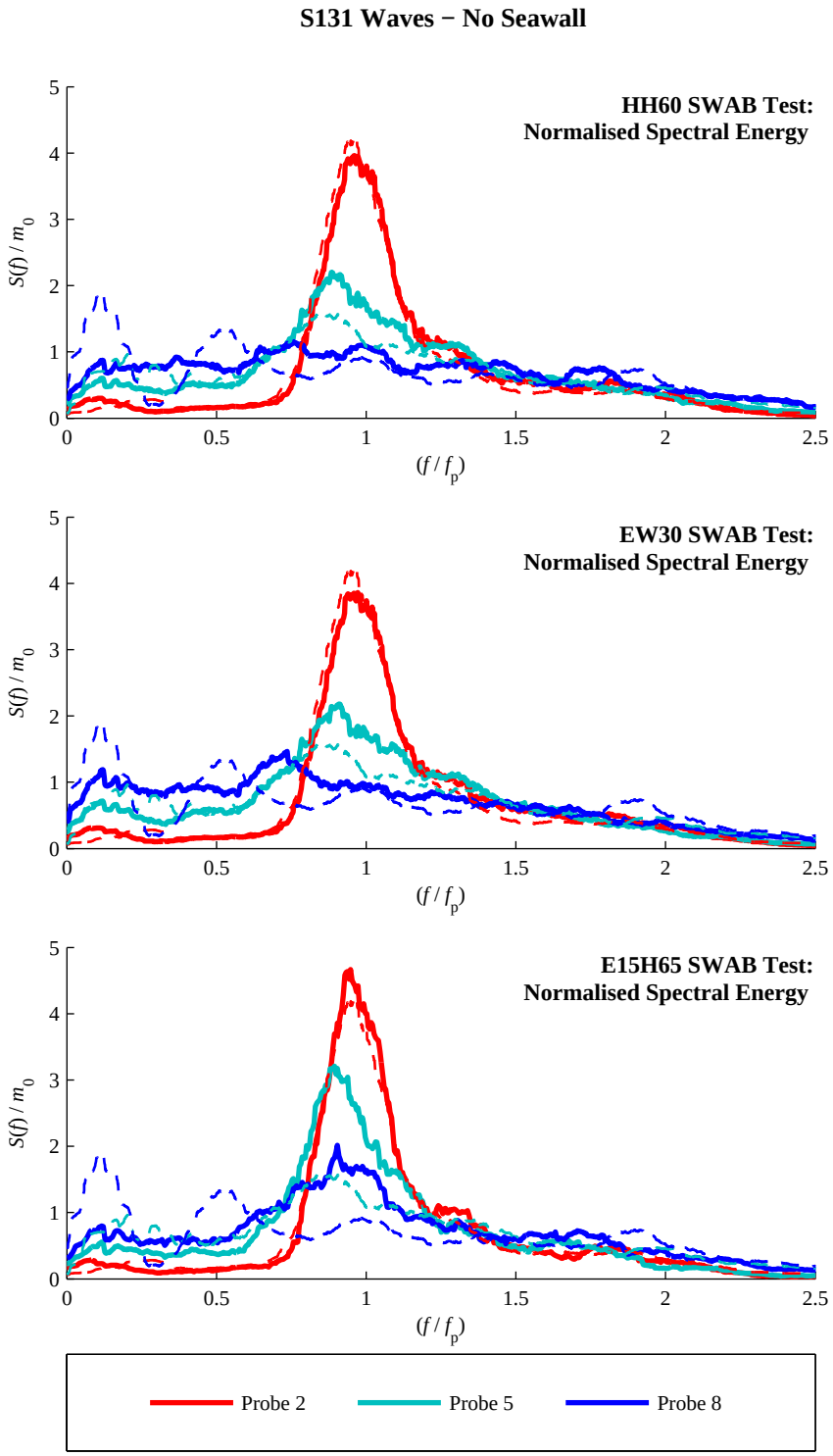

Figure 7.11: Normalised spectral energy density, at various wave probe locations, for S131 wave conditions. Experimental data shown as dotted lines and SWAB runs shown as solid lines

Figure 7.12: Uprushing water on the seawall, showing eddies at steps and splashing from recurve wall

Table 7.3: SWAB model tests with seawall

Test Name	k_{wall} for Steps	k_{wall} for Recurve Wall
KW0	0	0
KW1	0.5	1.0
KW2	0	1.0

wall; at this time it appears the water on the steps is changing direction, and the bubbles formed in the low pressure regions between the steps are making their way to the surface.

For the SWAB model of the seawall, it is to be expected that the factor k_{wall} (see equation (3.19)) should be greater for the recurve wall than for the four steps. However, the recurve wall does not efficiently reflect all the flow back in the opposite direction; k_{wall} will therefore be considerably less than 2. It is arguable whether this force should be imposed at the steps at all. To optimise the wall force, the three tests in Table 7.3 were carried out, and compared with the experimental data. All three tests used the HH60 breaking model (using the wave height to water depth ratio, wave-by-wave); the EWH30 model (using $\partial\eta/\partial t$, calculated wave-by-wave) would be expected to give similar results.

Figure 7.15 shows the free surface output for the S57 conditions from all three reflection tests, alongside that from the test run without the seawall. Even with the KW0 run the wave train has changed significantly; therefore, the reflection caused by the runup and run-down

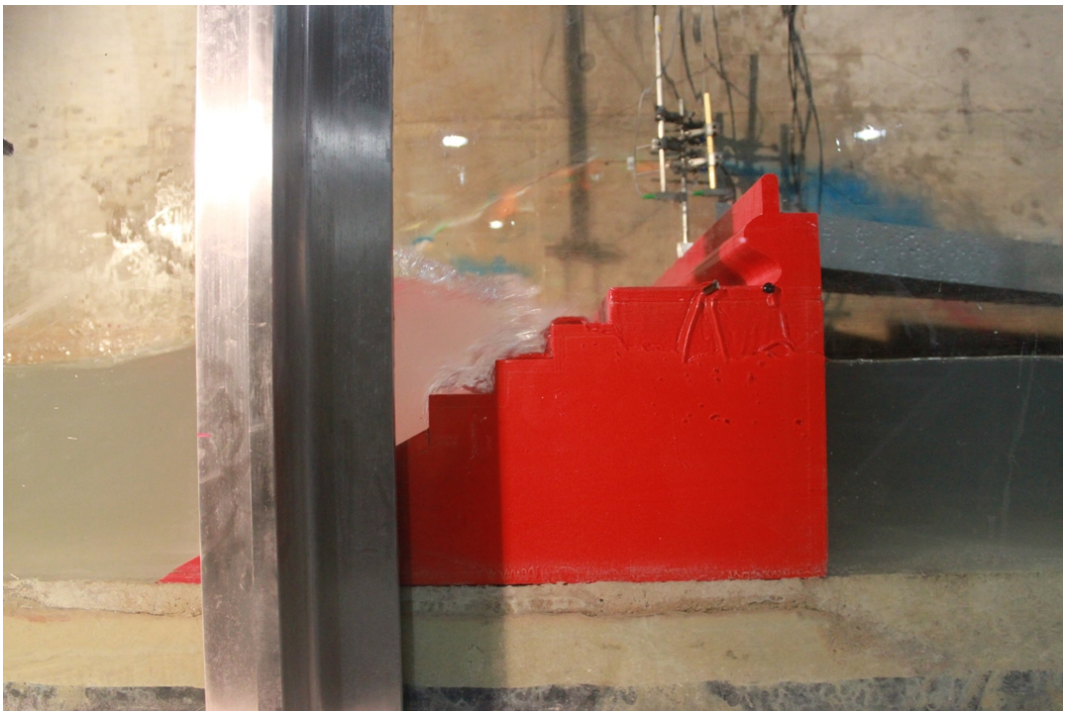

Figure 7.13: Uprushing water on steps from a breaking wave

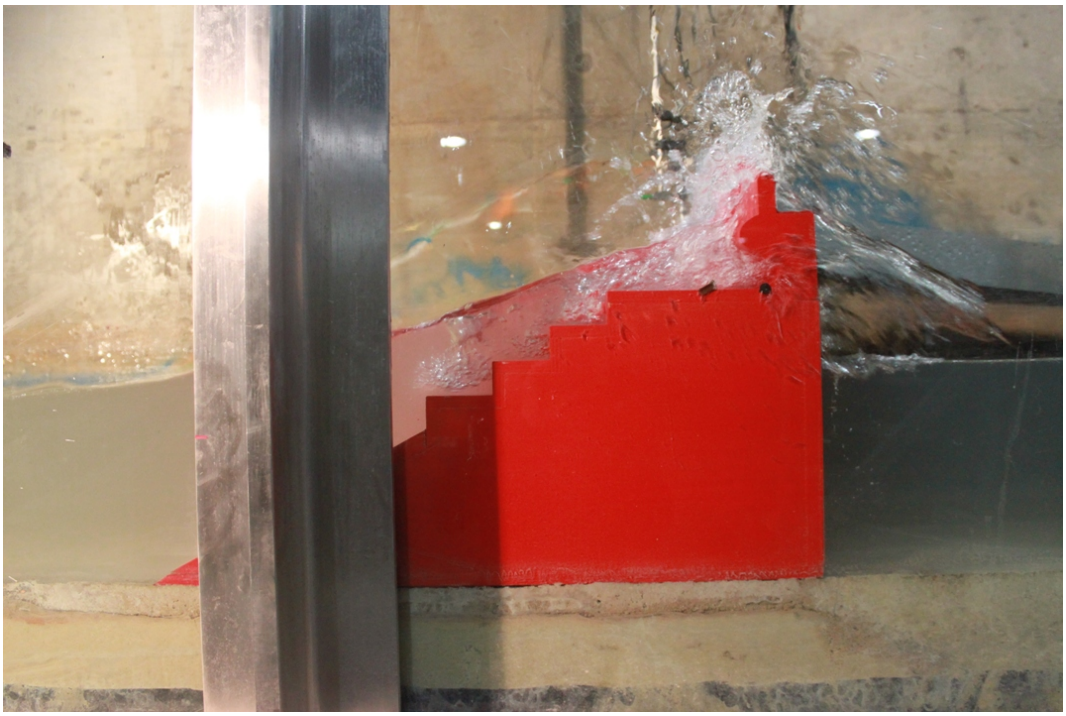

Figure 7.14: The wave of Figure 7.13 impacting on recurve wall

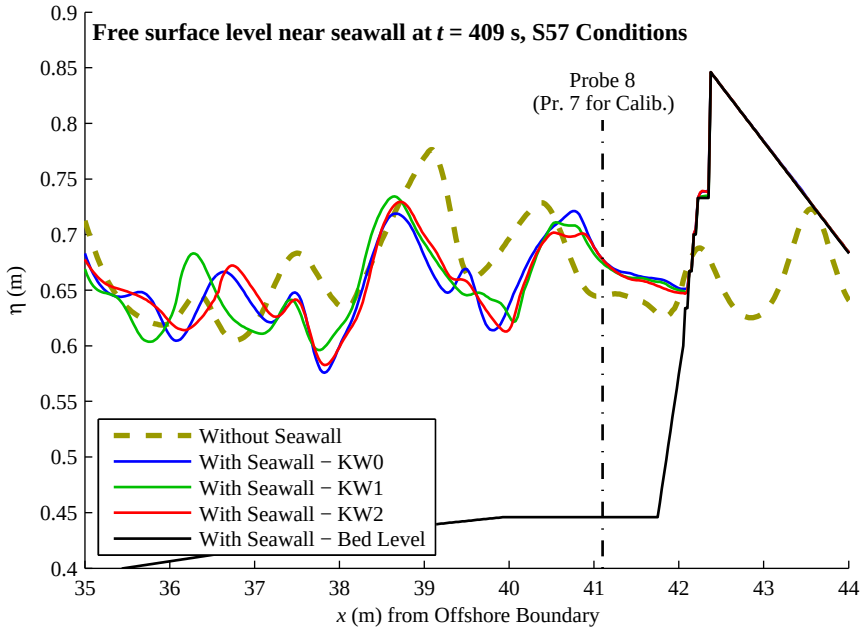

Figure 7.15: SWAB free surface levels, S57 conditions at $t = 409$ s

of the incident waves clearly has a much greater effect than the wall force. For this particular moment in time, the KW0 and KW2 runs are very similar; obviously if an incident wave does not reach the recurve wall, then its effect will be zero (apart from the possible effect of interaction from the run-down of a previous wave).

Figure 7.16 shows spectral energy curves for wave probes 2, 5 and 8, which are 7.5 m from the paddle, 8.4 m from the seawall toe and 0.67 m from the seawall toe respectively. Note that Wave Probe 8 for these tests with the seawall is at the same location as Wave Probe 7 in the tests without the seawall described in Section 7.2.1, for the S57 conditions. The effect of the different values of k_{wall} is very small, even at Wave Probe 8, near the seawall. At Wave Probe 2, and also at Wave Probe 5 where some waves are breaking, the SWAB model runs match very well with the experimental data. However, at Wave Probe 8 the low frequency peak is somewhat overestimated by SWAB, and there is another peak, around $1.35f_p$, that is not present in the experimental data. Wave Probe 8 was located 0.67 m from the seawall toe and 1.30 m from the seawall crest. Using linear wave theory, $1.35f_p$ corresponds to a wavelength of about 2 m, which would suggest this peak could be caused by reflections from the seawall (i.e. an antinode at $0.5L$ from the wall). There is also a distinct trough in the spectral energy curve at $0.7f_p$, corresponding to a wavelength of 4 m, resulting in a node. In the experimental data, a smaller peak exists at $2.01f_p$, corresponding to a wavelength of 1.24 m; again, this could be caused by reflections. However, the experimental data also features increased spectral energy at lower frequencies; between 0 and $1f_p$, the spectral energy is high throughout, with a trough

at about $1.3f_p$ (corresponding to $L = 2.08\,\text{m}$). It is unclear why this should be so: possibly reflection in the flume occurred mostly at the toe of the seawall (unlikely); the measurement of the location of Wave Probe 8 was inaccurate (more likely); or a combination of the two (i.e. an inaccurate wave probe location and the reflection in the flume occurring at slightly differently from the SWAB model). Also, in the flume a very small volume of water was able to travel around the side of the seawall; thus it would be possible that some wave energy could be transmitted beyond the seawall and off the back wall of the flume. This may also contribute to the difference between SWAB and the experiments in the low frequency region. Finally, some of the difference may be due to the active wave absorption at the wave paddle; it is not known how effective the system used at HR Wallingford is.

Figures 7.17, 7.18 and 7.19 show the effect of the seawall on the spectral energy at Wave Probe 8 (Wave Probe 7 for calibration run), for three test conditions: S55, S57 and S131. Note that these figures show actual spectral energy density; they have not been normalised in any way. The presence of the wall causes a very large increase in the low frequency region: the surf beat. The magnitude of this increase is approximately four-fold, both in the SWAB model and in the wave flume. If one considers the perfect reflection of a wave off a vertical wall, the wave height is doubled at the antinodes. Spectral energy density is proportional to the square of the amplitude; perfect reflection would therefore quadruple the energy at an antinode. These low frequency waves can therefore be assumed to be almost perfectly reflected by the seawall.

Figures 7.20, 7.21 and 7.22 show moving averaged rms water levels for tests S55, S57 and S131. Even at Wave Probe 8, located 0.67 m from the toe of the seawall, there is almost no difference between the different reflection parameters. There are some differences in timing between SWAB predictions and the experimental data; variations in η_{rms} over time at Wave Probe 5 and Wave Probe 8 occur with both, but the two datasets are rarely in phase. This is probably due to the spectral differences described above. However, despite the differences between SWAB and the experiments in terms of spectral energy density, these figures show that the overall wave energy in all parts of the flume are well predicted.

7.3 Wave Overtopping

7.3.1 Filtering of overtopping data

Due to the nature of the method of measuring overtopping in the flume, it may be difficult to produce SWAB time-series that are simultaneous with the experimental data. Firstly, the overtopping water ran down a chute into the collection tank; the time taken for this to occur is dependent on the discharge down the chute. Secondly, the water fell into the overtopping

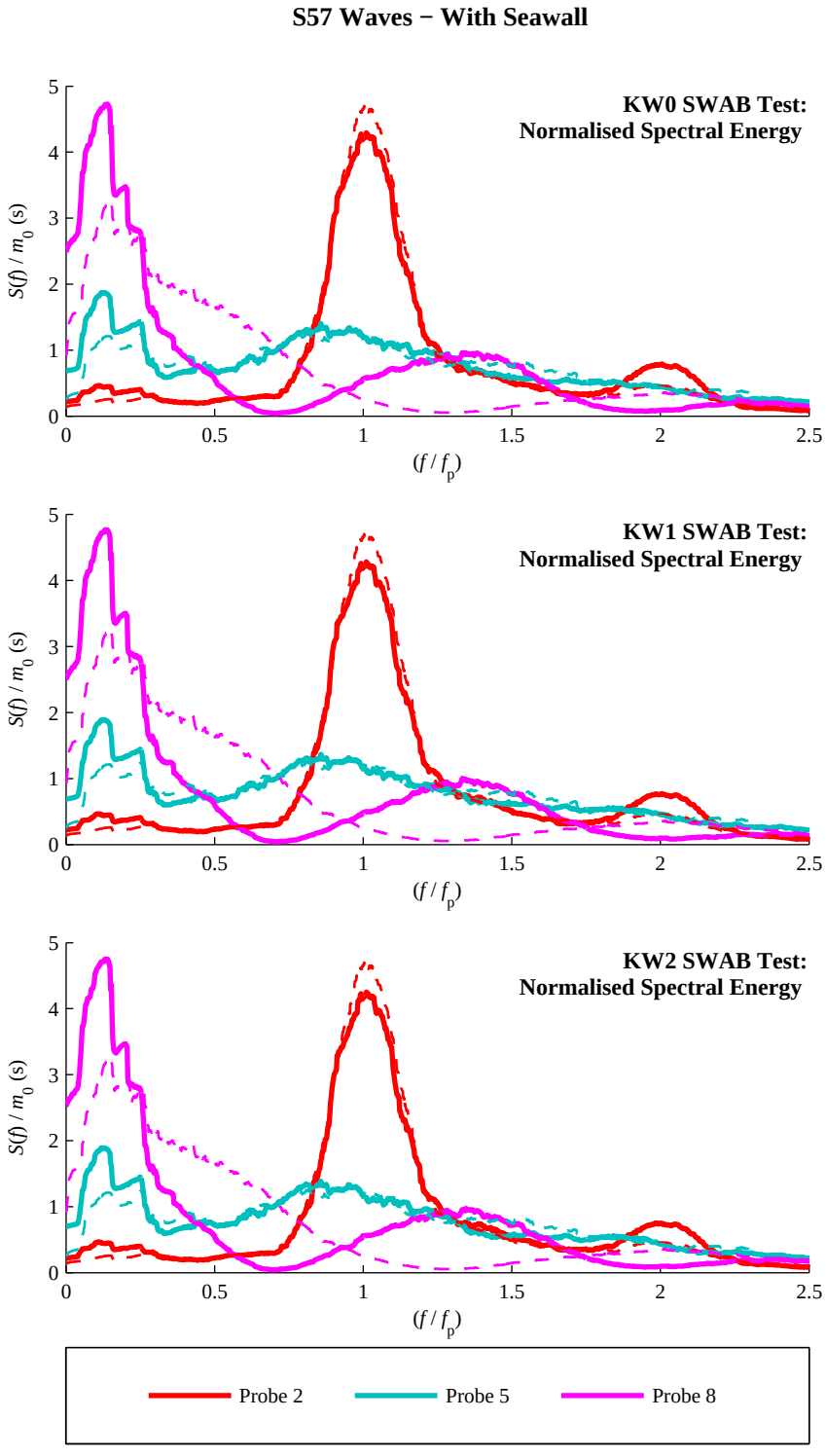

Figure 7.16: Normalised spectral energy density, at various wave probe locations, for S57 wave conditions. Experimental data shown as dotted lines and SWAB runs shown as solid lines

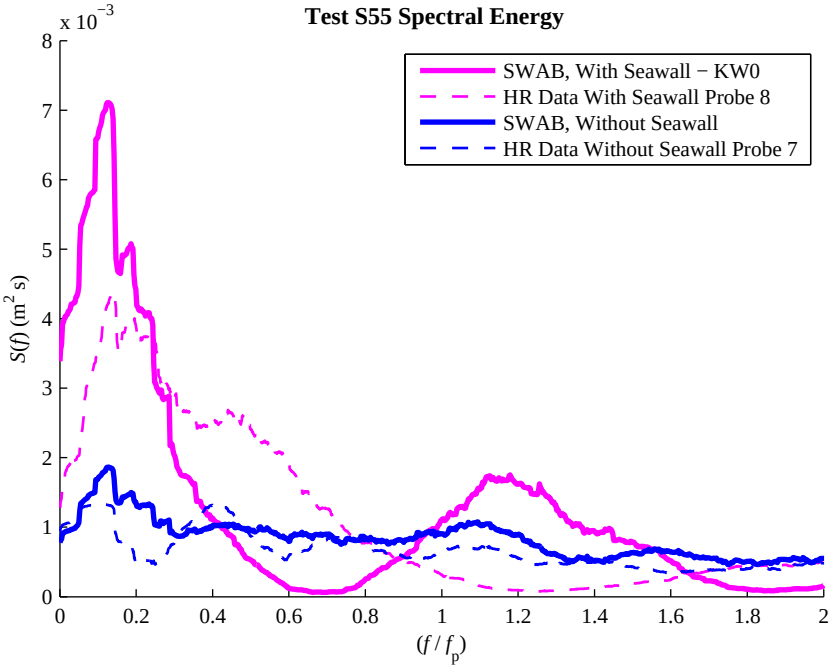

Figure 7.17: Spectral energy density at closest probe to seawall: comparison between KW0 run with seawall and test without seawall, S55 condition

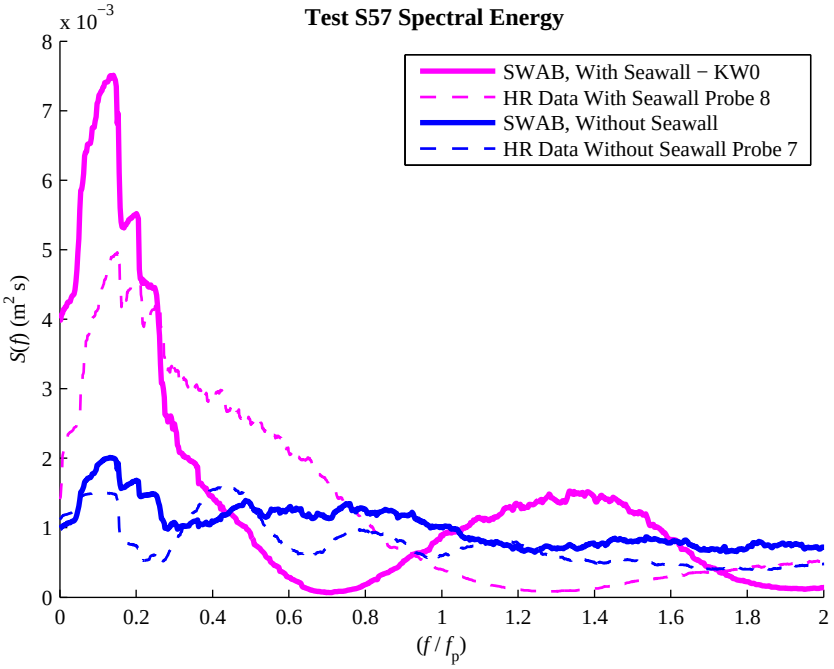

Figure 7.18: Spectral energy density at closest probe to seawall: comparison between KW0 run with seawall and test without seawall, S57 condition

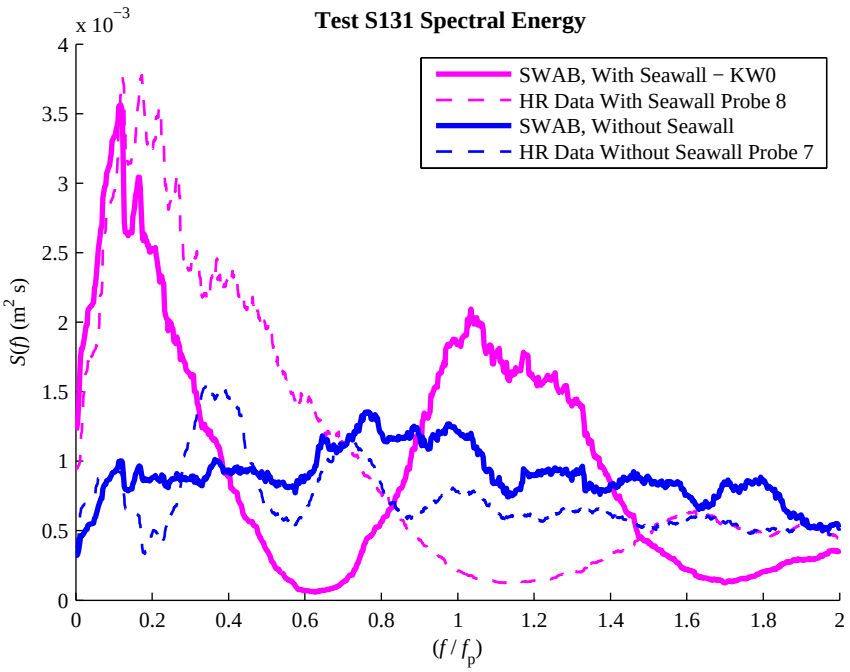

Figure 7.19: Spectral energy density at closest probe to seawall: comparison between KW0 run with seawall and test without seawall, S131 condition

tank, which had a gauge at the far end; the falling water caused seiching to occur, eventually settling to a higher water level. A typical extract from a time-series is shown in Figure 7.23. Small overtopping events caused a slow trickle of water to run down the chute; test S23, as shown in Figure 7.24, is a good example of this. Although many waves caused a small volume of water to enter the tank, only one event can be detected from the time-series; the other overtopping waves caused a slow but steady rise in the water level. Obviously, small waves had the same effect for other tests; in Figure 7.23, three main overtopping waves can be detected from the extract: at approximately 525 s, 560 s and 580 s. However, the level at 620 s does appear to be higher than it was at 580 s; this is probably due to the small overtopping events.

Figures 7.23 and 7.24 highlight the need to develop an algorithm to filter this raw overtopping data, before using it for comparison with the SWAB model. One cannot hope to assign a volume to every overtopping wave, but it is possible to do so for the main events. If one were to use a simple moving average filter, this could make detection of the largest events possible; one would need to select an appropriate averaging period to dampen the seiching in the overtopping collection tank, but it could also have the effect of smoothing out smaller events as well as merging closely spaced events. Therefore, a different type of filter was chosen.

Two particular features were noticed from the raw overtopping data. Firstly, an overtopping event caused an increase in oscillations in the tank, which slowly dampen as the water

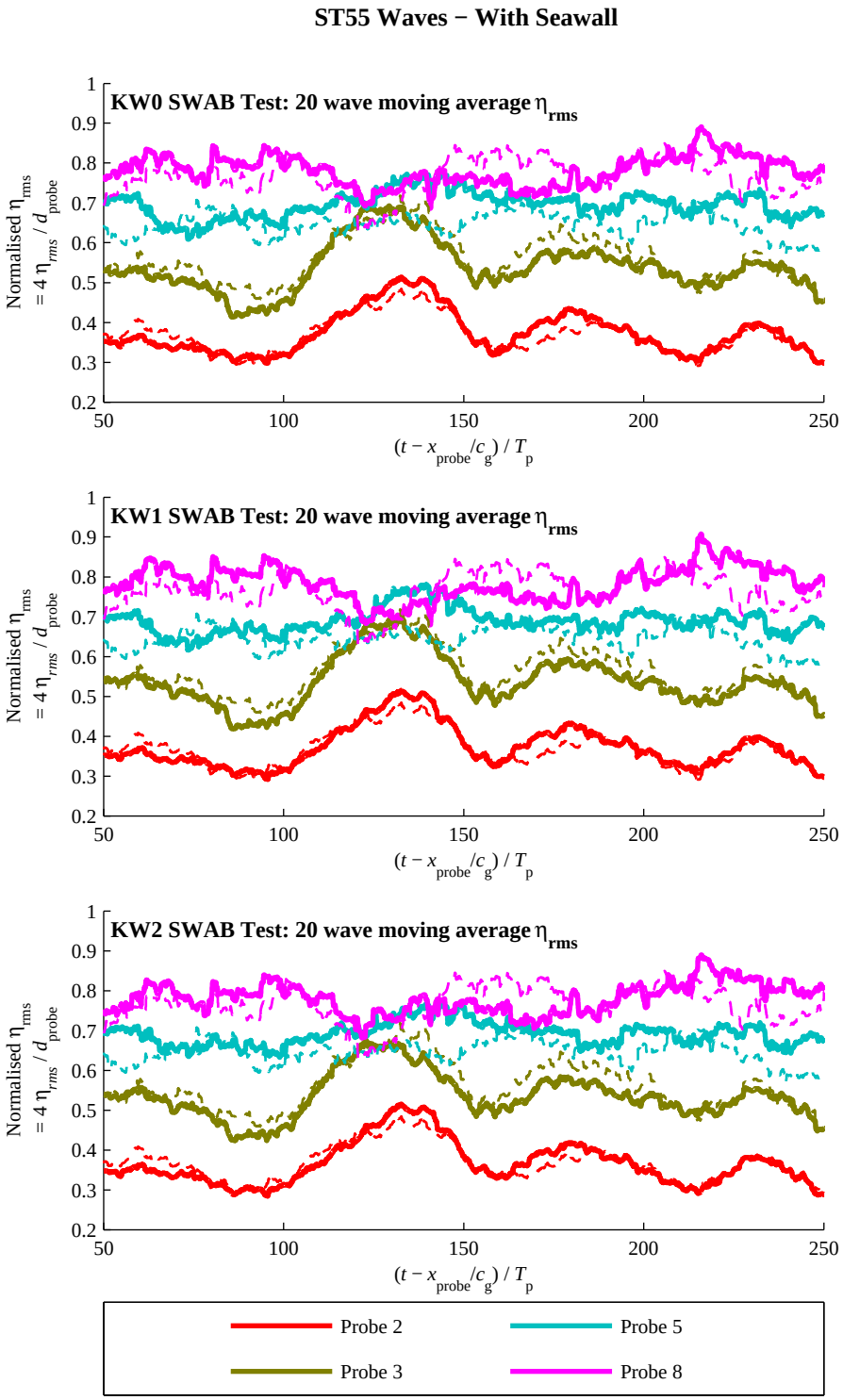

Figure 7.20: Time-series of 20 wave moving average normalised η_{rms}, at various wave probe locations, for S55 wave conditions. Experimental data shown as dotted lines and SWAB runs shown as solid lines

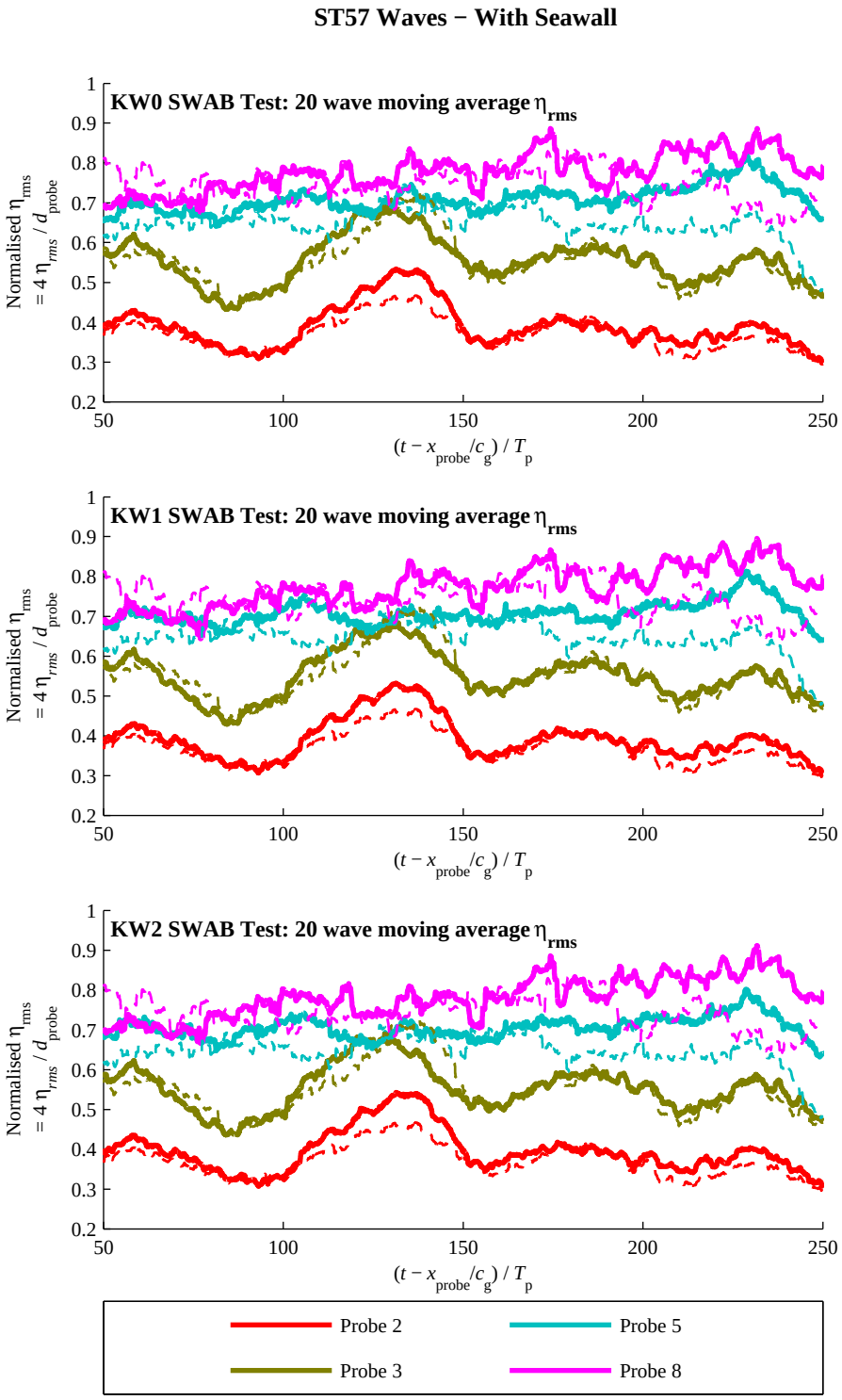

Figure 7.21: Time-series of 20 wave moving average normalised η_{rms}, at various wave probe locations, for S57 wave conditions. Experimental data shown as dotted lines and SWAB runs shown as solid lines

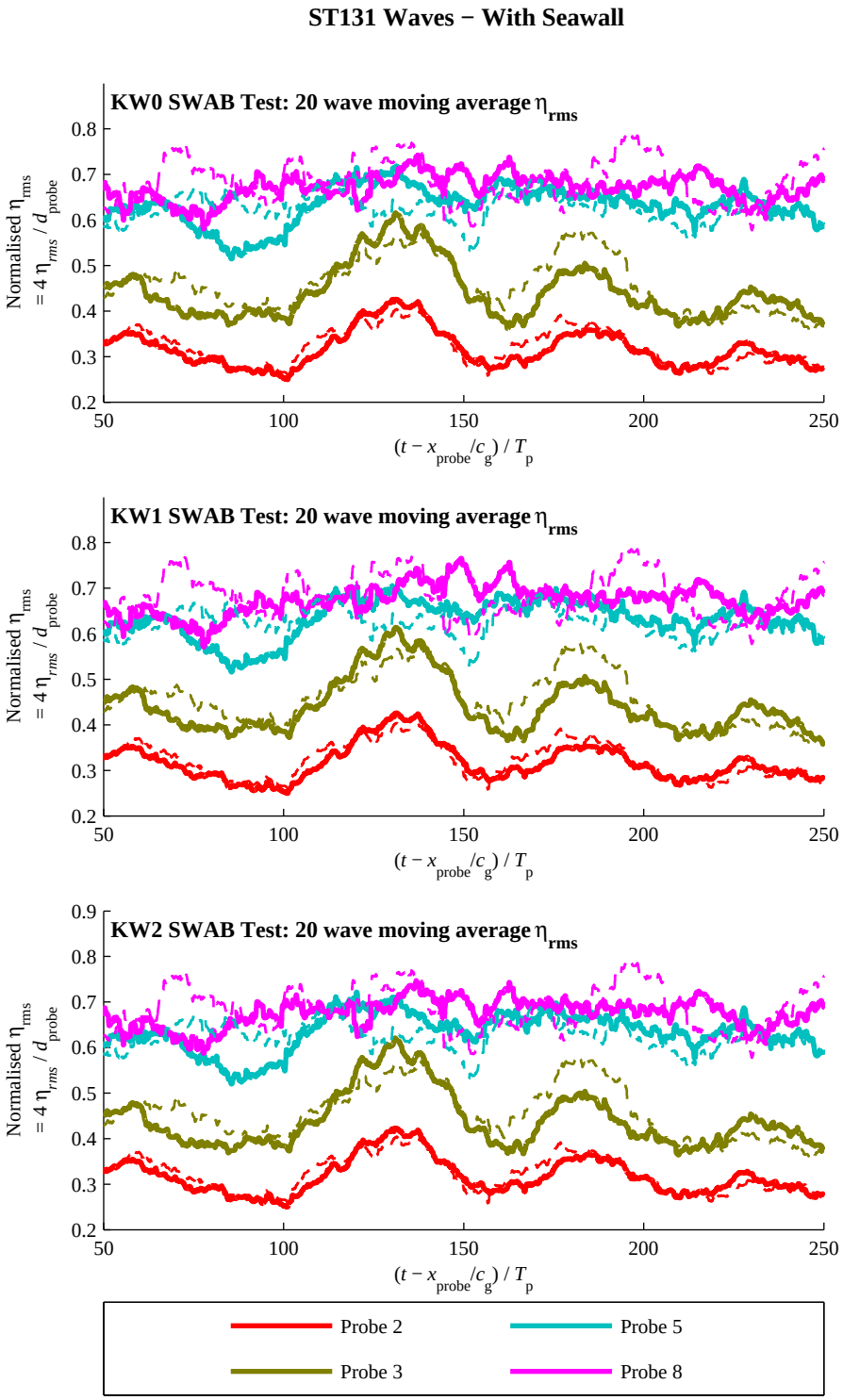

Figure 7.22: Time-series of 20 wave moving average normalised η_{rms}, at various wave probe locations, for S131 wave conditions. Experimental data shown as dotted lines and SWAB runs shown as solid lines

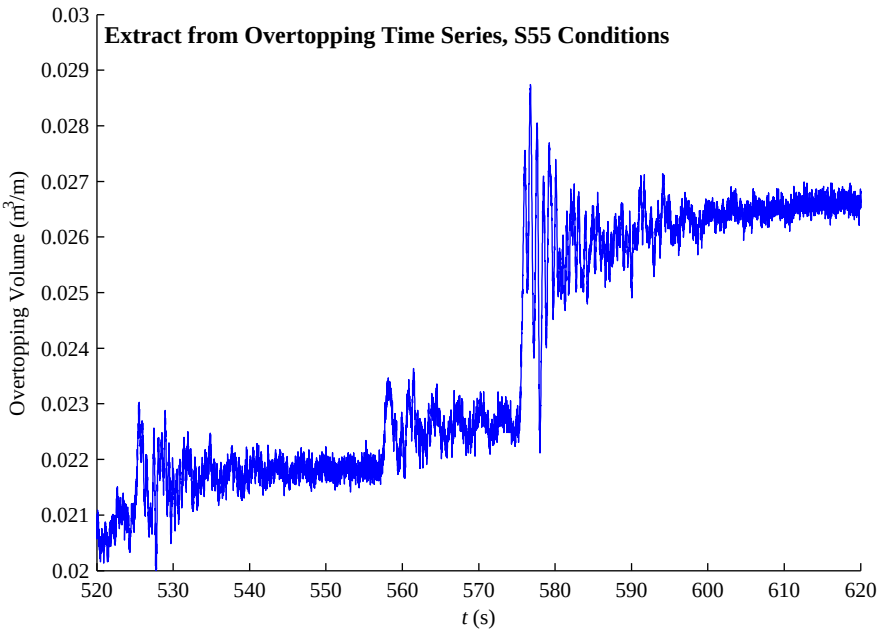

Figure 7.23: Extract from experimental overtopping time-series: S55 conditions

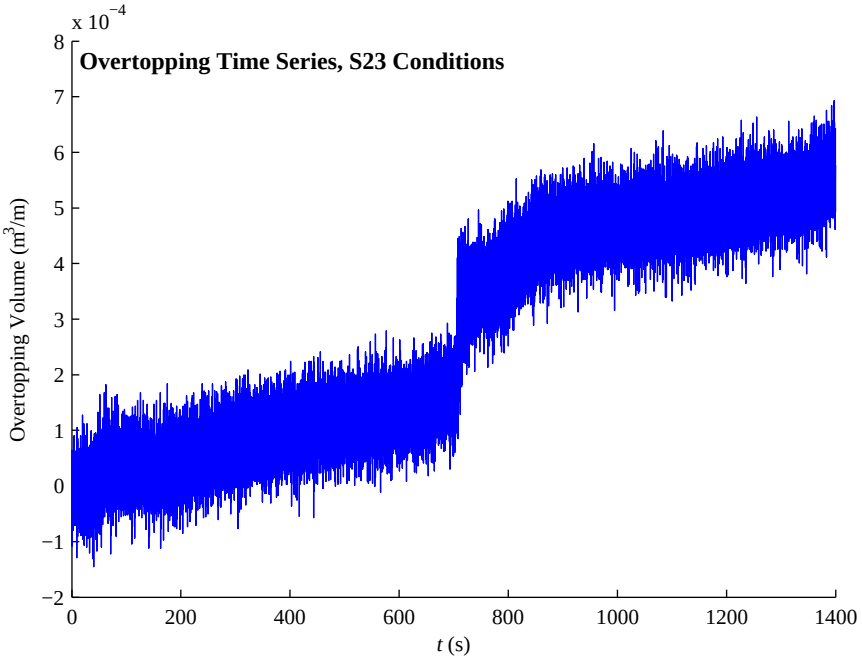

Figure 7.24: Experimental overtopping time-series: S23 conditions

level settles; each new overtopping event is characterised by this sudden increase in oscillations. Secondly, an overtopping event is also characterised by a jump in the water level; these new oscillations occur at a higher level than the previous oscillations. So, each overtopping event causes a jump in the variance of the water level, as well as a jump in the skewness (Skewness $= E(X-\bar{X})^3/\left(E(X-\bar{X})^2\right)^{3/2}$). Therefore, a moving variance or moving skew filter is likely to be more effective than a moving average filter. Figures 7.25 and 7.26 show moving variances and skewness, using a window of $2T_p$ (note that with these algorithms, high frequency noise ($f > 10f_p$) is filtered out at the start); individual overtopping events can then be obtained by detecting all peaks above a certain threshold. Once these events have been detected, the volume of each event could be calculated as the difference between the mean volume over $3T_p$ after the event (or until the next event, if that is sooner) and the mean volume over $3T_p$ before the event (or from the previous event, if they are less than $3T_p$ apart). Where an increase in volume occurred between events, it was assumed that overtopping occurred at a steady rate. With such a short window, a moving average filter would not have been able to smooth out the oscillations in the time-series; however, it also means that if waves close together overtop (though probably not two successive waves), it should be possible to separate their individual overtopping volumes. The moving skewness filter does not appear to be as effective at detecting small overtopping waves as the moving variance filter (e.g. at $t = 590$ s in Figure 7.25 and $t = 800$ s in Figure 7.26). However, the moving skewness filter does have the advantage that the individual spikes are very short in duration, which aids the detection of closely spaced events. Also, there is less variation in the magnitude of spikes from test to test (notice that the moving variance spikes in Figure 7.25 are in the order of 10^{-6}, whereas for the S23 test they are in the order of 10^{-9}). For these reasons, the moving skewness algorithm was preferred. It is important to remember that a perfect detection algorithm for overtopping events is not possible, with some real events remaining undetected and some false events being obtained. Figure 7.27 shows the filtered overtopping volume for the S55 condition, using the moving skewness algorithm.

7.3.2 SWAB results

Figure 7.28 shows time-series of overtopping volumes for the S55, S57 and S131 conditions, for the SWAB tests described in Table 7.3 in comparison with the experimental data. Clearly the wall force has a significant effect on the overtopping volumes. The KW0 test, without the wall force, consistently leads to overestimates of overtopping volumes, whereas the KW1 force consistently leads to underestimates. For the three cases shown below, the KW2 test (with the force only applied at the recurve wall) gives remarkably good results. As a note of

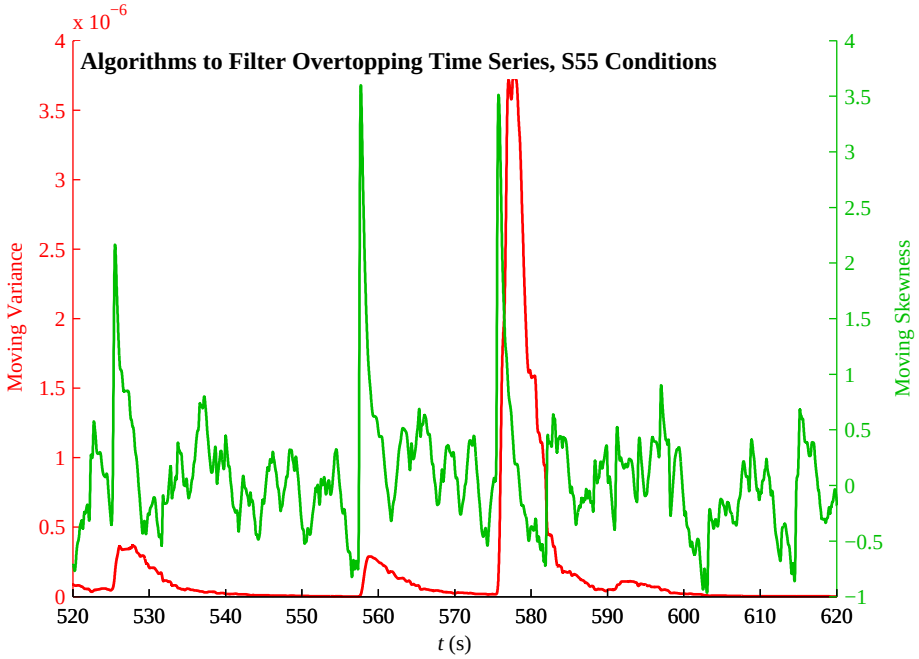

Figure 7.25: Moving variance (red line, left-hand y-axis) and skewness (green line, right-hand y-axis) filters applied to overtopping time-series of Figure 7.23

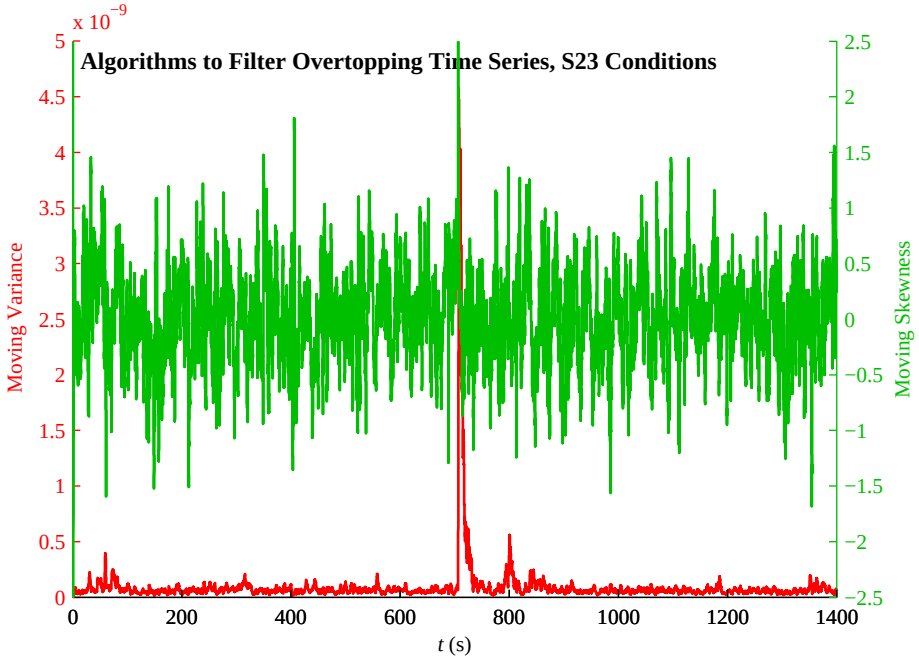

Figure 7.26: Moving variance (red line, left-hand y-axis) and skewness (green line, right-hand y-axis) filters applied to overtopping time-series of Figure 7.24

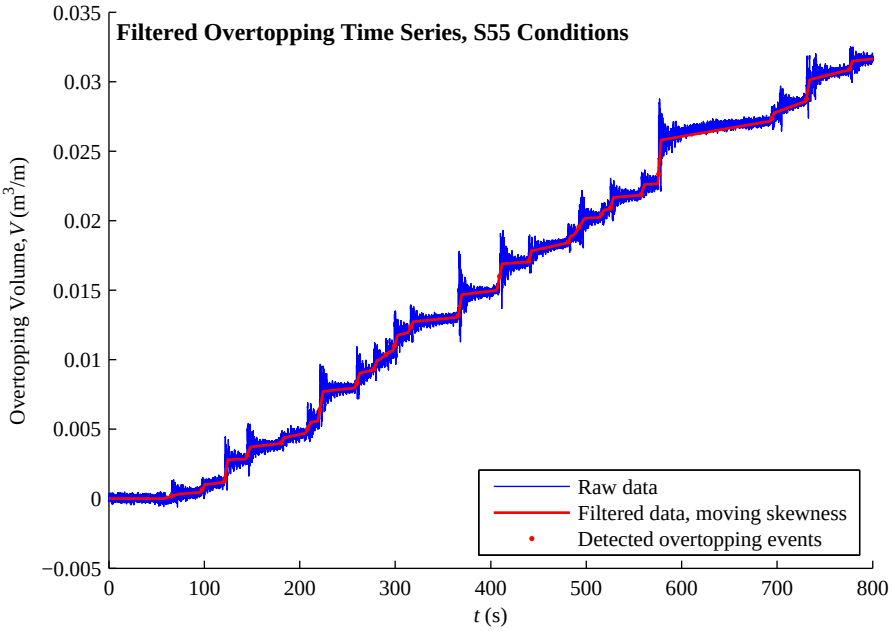

Figure 7.27: Extract from S55 overtopping time-series, showing original data and data filtered using a moving skewness algorithm

caution, it can be seen that the KW2 time-series does not match the experimental data event by event; this is to be expected as the nearshore waves, described in the previous section, did not necessarily match over time.

Figure 7.29 shows distributions of the individual overtopping events for the SWAB runs compared with the experimental data. The SWAB models were not run for the entire duration of the experimental runs; therefore the figure only refers to the distribution of overtopping events for the duration of the SWAB runs. It should be noted that the number of overtopping events is affected by the thresholds used to detect spikes in the moving skewness or variance time-series. To detect overtopping events in the SWAB time-series, the moving skewness filter was not suitable; at many points where the variance reduced to zero, the skewness approached infinity. Therefore the moving variance filter was employed. The same filter with the same thresholds were used for all the SWAB tests, and likewise for the experimental data. Using these detection methods, the KW2 tests appear to match rather closely with the experimental data, both in terms of the number of overtopping events and the shape of the distribution curves. The KW0 tests result in about double the proportion of overtopping waves (although mean overtopping rates are trebled - see Figure 7.28), and the largest overtopping waves have a considerably higher overtopping volume. The KW1 tests have the opposite effect, with too few overtopping waves of too small volume.

All the other tests of Table 7.1 were run using the KW2 wall force, still with the HH60

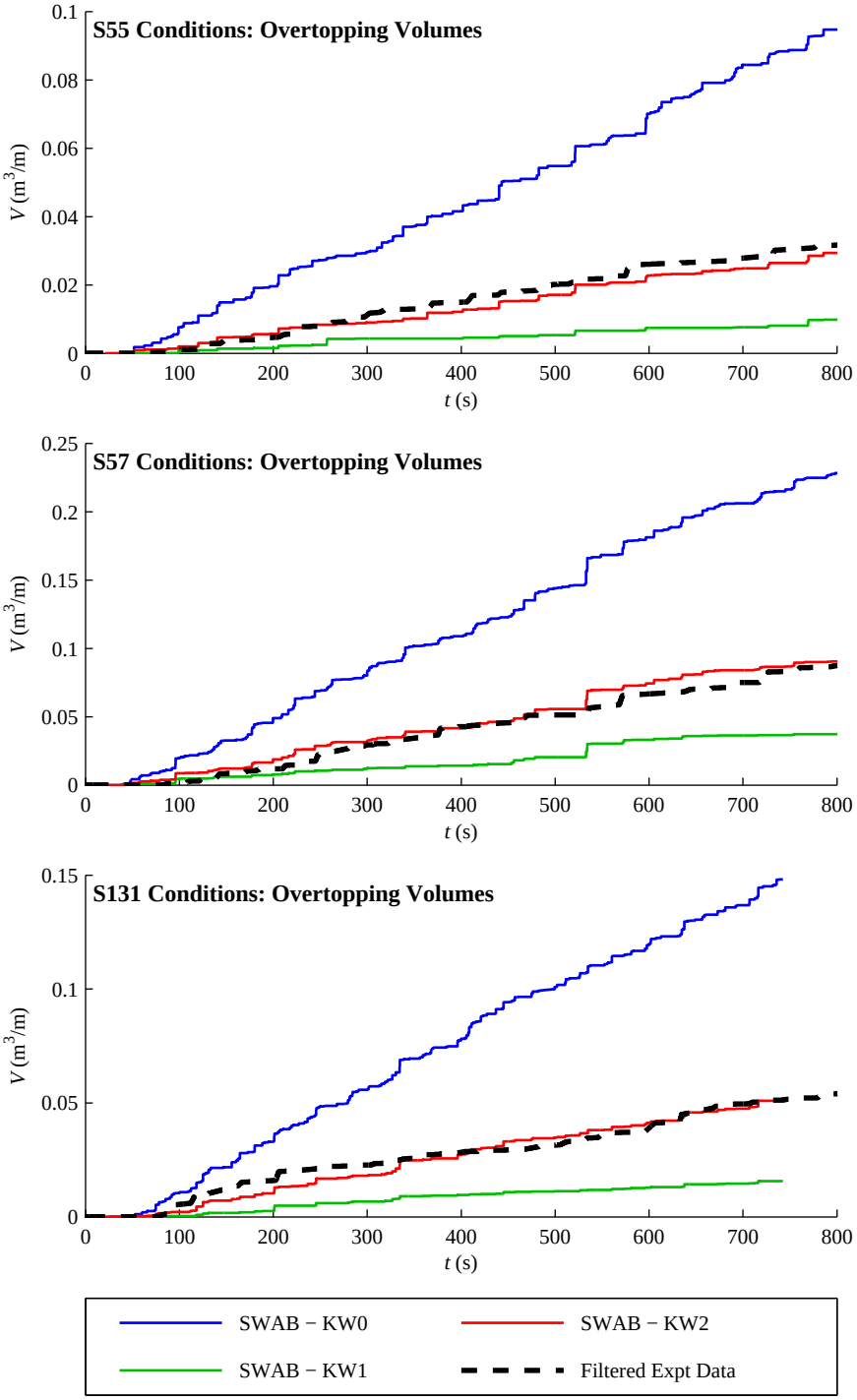

Figure 7.28: Time-series of overtopping volumes: SWAB tests compared with experimental data

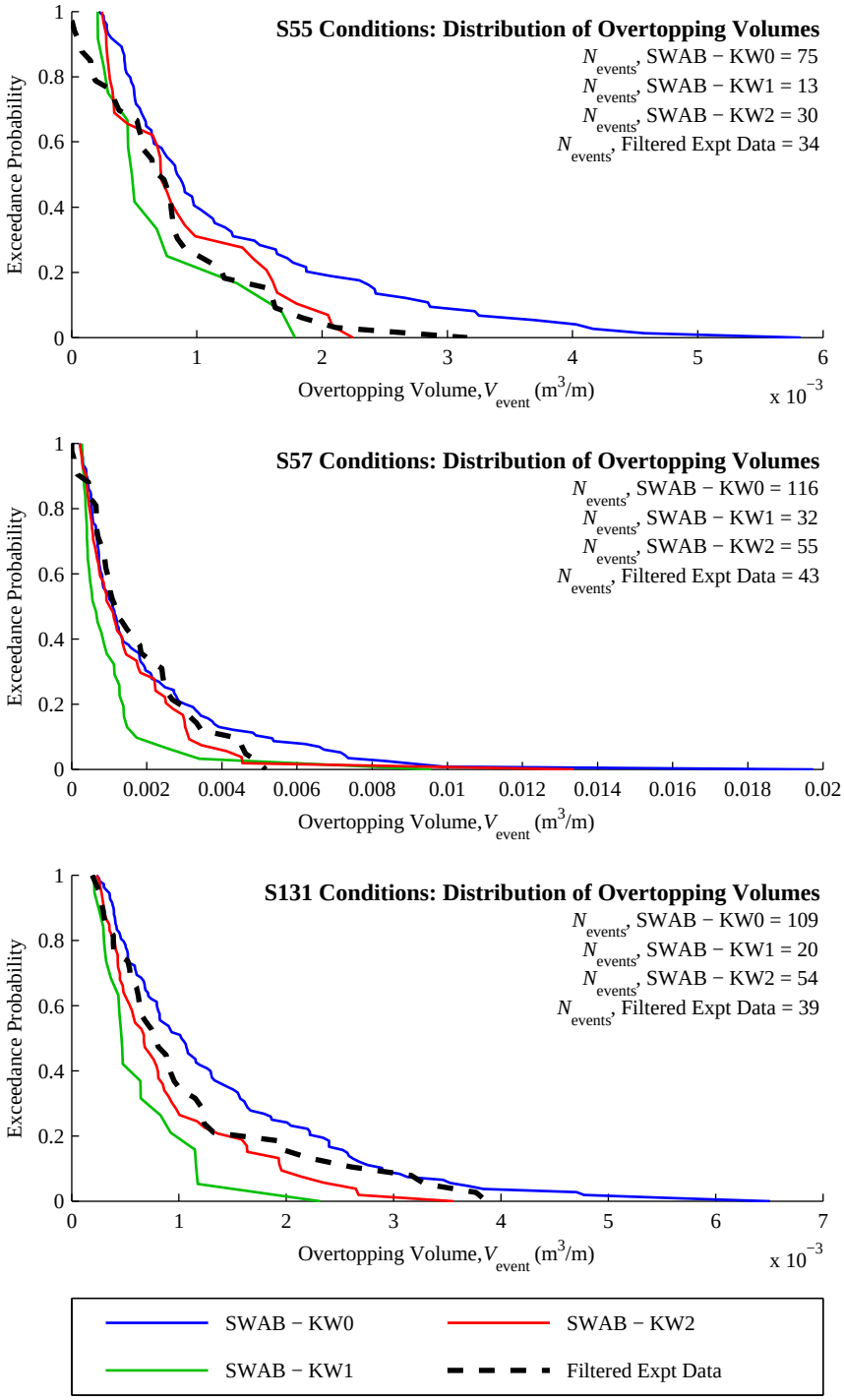

Figure 7.29: Distributions of overtopping volumes: SWAB tests compared with experimental data

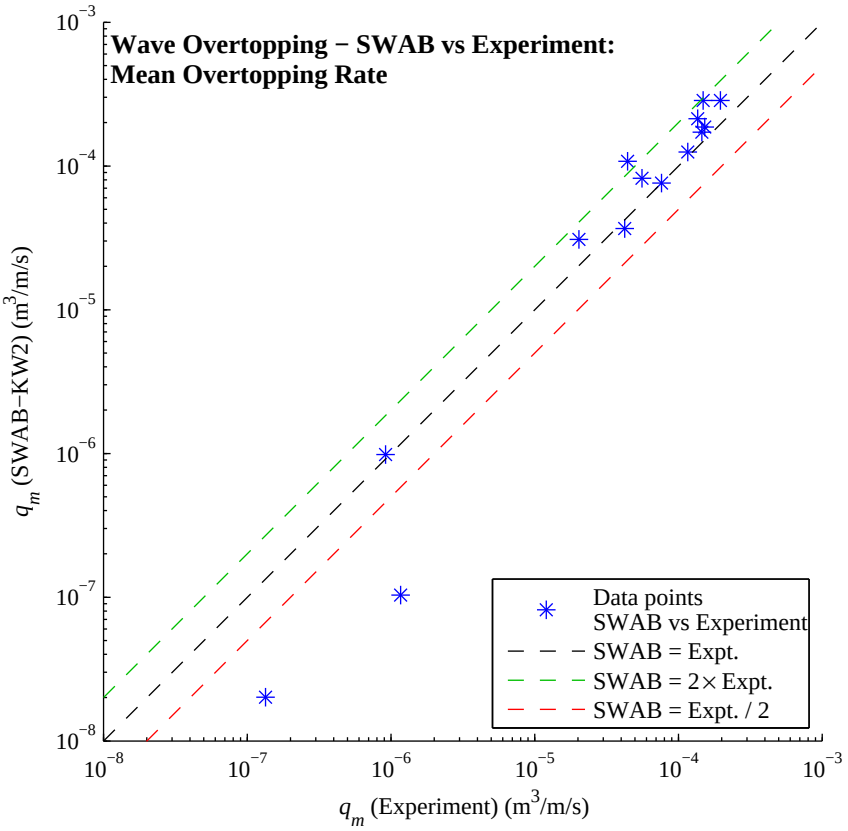

Figure 7.30: Mean overtopping rates for all tests: SWAB-KW2 versus experimental data

breaking model. Figures 7.30 and 7.31 show mean overtopping rates and maximum overtopping volumes for all the SWAB tests compared with those from the experimental data. Note that these figures do not refer to means and maxima over the whole of each experimental run. The time intervals were set from the time when the overtopping chute was placed behind the seawall, to either the time it was removed (due to the tank filling up) or the end of the SWAB run, whichever was sooner. The mean rates appear to be well predicted, except at the lower end of the scale. There is more uncertainty with maximum overtopping volumes; there may be a trend towards SWAB underpredicting this parameter at the lower end of the scale and overpredicting at the upper end, although with the size of the dataset it is not possible to make a definite conclusion on this.

The P07 test (see Table 7.1) was repeated twice in the wave flume: firstly as exact repeat of the P0785 test, and secondly as the P0775 test with a reduced gain to the paddle signal (H_{m0} is reduced by about 10 %). These repeats used exactly the same wave train (P0775 is simply slightly reduced in height). Figure 7.32 shows time-series of the two KW2 SWAB runs (force applied at recurve wall only) alongside the three experimental runs. It is apparent that the

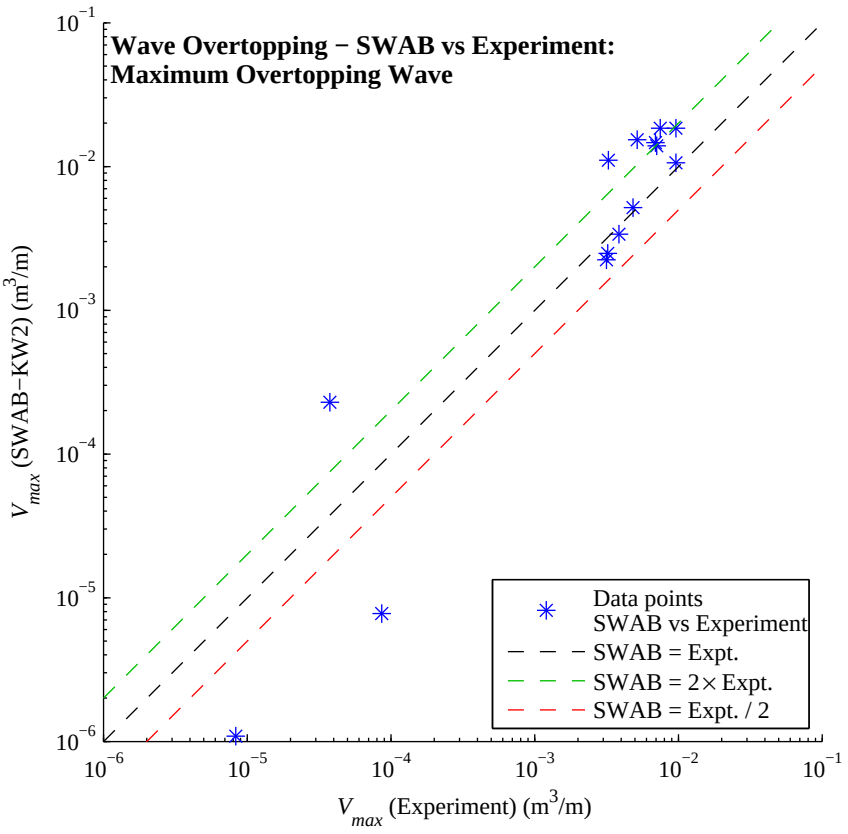

Figure 7.31: Volume of maximum overtopping wave for all tests: SWAB-KW2 versus experimental data

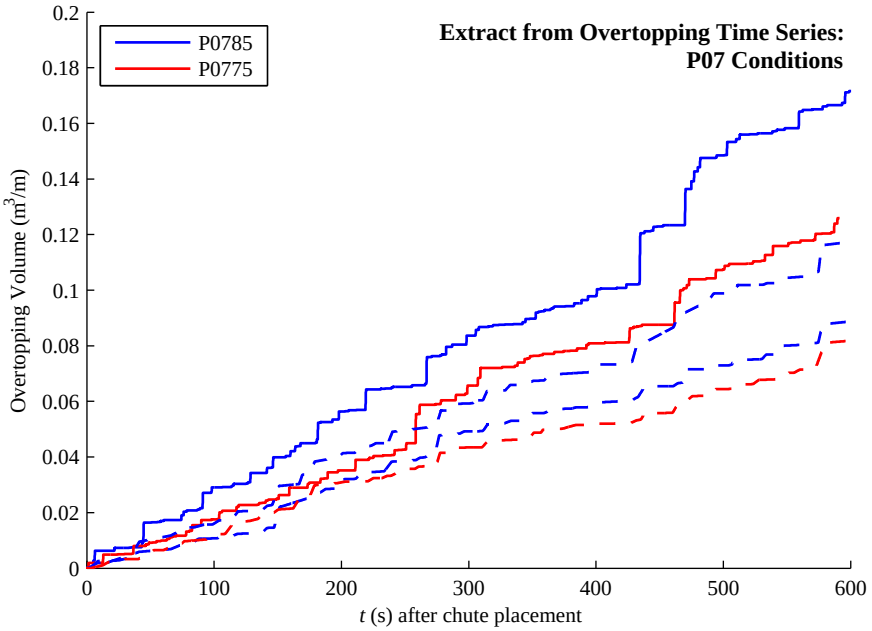

Figure 7.32: P07 overtopping time-series: SWAB-KW2 versus experimental data, showing repeated runs. Experimental data shown as dotted lines and SWAB runs shown as solid lines

SWAB model does overestimate overtopping rates for both gain values. However, there is also considerable variation in the results from the experiments; repeating exactly the same test caused a 25 % reduction in the overtopping rate. The reduced gain repeat caused a slight further loss in overtopping. Therefore, whenever overtopping calculations are carried out, one must be aware that the uncertainties are huge. If one were to repeat the same wave conditions with a different wave train (i.e. the same spectrum with different random phases and same water level), a rather different result would be likely; this will be analysed in more detail in Section 8.2.2. From the basis of the test conditions described previously, it cannot be said that the SWAB model would always overpredict. Further analysis of the performance of SWAB, against the field data and existing formulae as described in the EurOtop Manual [Pullen et al., 2007], will be described in the next section.

7.3.3 Comparison with field data and EurOtop calculations

The EurOtop Manual [Pullen et al., 2007] was described in Section 2.5.2. Three types of tool were recommended by the manual for this type of structure: the neural network (which will be used in the next chapter), the empirical equations, and the PC-Overtopping web-based tool, which is used here. Model geometry and wave conditions are entered into online forms, with results obtained instantaneously. It was designed for the assessment of dykes, and does not model vertical walls. Instead, the EurOtop Manual recommends a wall of slope $\tan\beta = 1$

should be used with application of a reduction factor of 0.65 to the overtopping rates. It should be mentioned that EurOtop specifies that wave conditions are those at the toe of the structure. The SWAB results for Wave Probe 8 were therefore used for input wave heights. However, the manual also recommends the use of a parameter $T_{m-1,0}$, which gives more weight to longer period waves. At Wave Probe 8, where peak frequency wave energy has been lost, and most of the energy is at very low frequency, this will give unreasonably long values for this wave period parameter. Therefore values of T_p, based on the wave spectra at Wave Probe 2, were used as input to the PC-Overtopping program (the use of T_p is given as an option in PC-Overtopping, where the assumption $T_p = 1.1T_{m-1,0}$ is made).

The basic equation form used by the EurOtop Manual [Pullen et al., 2007] for mean overtopping rates is (EurOtop equation 4.1):

$$\frac{q_m}{\sqrt{gH_{m0}^3}} = a \exp\left(-b\frac{R_c}{H_{m0}}\right) \tag{7.1}$$

where a and b are empirically derived constants and R_c is the freeboard, which is the vertical distance between the crest level and the still water level. The equation derived for simple sloped structures is of a similar form (EurOtop equation (5.8)); however, being derived from empirical equations for runup, it also includes the influence of the surf similarity parameter, ξ_0. The equation also includes factors for other influencing effects, including bed slope, roughness and obliquely incident waves. Assuming these factors should remain unchanged for these tests, they have been combined into two constants, k_1 and k_2. The equation becomes:

$$\frac{q_m}{\sqrt{gH_{m0}^3}\xi_0} = k_1 \exp\left(-k_2\frac{R_c}{\xi_0 H_{m0}}\right) \tag{7.2}$$

It is therefore desirable, for the purpose of comparison between SWAB, the wave flume experiments, the PC-Overtopping results and the available field data, to express all the data in terms of the two dimensionless parameters, $q_m/(\sqrt{gH_{m0}^3}\xi_0)$ and $R_c/(\xi_0 H_{m0})$. It should be noted that the value of ξ_0 used by the manual is based on the slope of the structure itself. For composite slopes the EurOtop Manual instructs the user to calculate the slope from the wave breaking point to the maximum runup level (which will be higher than the structure itself, if overtopping occurs). For the case of the seawall at Anchorsholme, all waves are breaking before they reach the structure; it was therefore thought more appropriate (and easier) to base ξ_0 on the foreshore slope ($\tan\beta \approx 0.01$).

The overtopping field dataset was collected between 11:04 am and 12:08 pm on 24th January 2008. These times correspond with Burst Numbers 54, 55 and 56 for the offshore AWAC

data (see Section 4.3.1). Unfortunately, the overtopping field data had not yet been made available when the physical model tests were set up; therefore only one model test (Storm 55) corresponds entirely with this data. Nevertheless, it is still possible to include this data for comparison with results from EurOtop and the SWAB model runs.

To express the field data in terms of dimensionless parameters requires a significant wave height. Because of the inaccuracy of the inshore AWAC data, the wave height at the toe of the structure cannot be assessed without some modelling, using SWAN for example. Therefore it was thought more appropriate to base the dimensionless parameters on H_{m0} at the offshore AWAC location. Wave heights at this location are very closely equivalent to the input wave heights in the wave flume as well as the input heights into the SWAB model; this check was explained briefly in Section 4.3.4. By using the offshore AWAC H_{m0} (calculated using the pressure sensor) for the field data, and the values of H_{m0} calculated from the Probe 1 calibration runs (Table 7.1) for the physical model tests and for the SWAB tests, something close to a like-for-like comparison is possible. Note however that the offshore AWAC data include reflected waves, whereas the Probe 1 calibration runs do not. One could have used the H_{m0} from the experimental data as an equivalent (which does include reflected waves). However, because Probe 1 and the offshore AWAC are not in equivalent locations, they would not contain the same nodes and anti-nodes in the frequency spectrum; therefore, it was thought that using the calibration H_{m0} from Wave Probe 1 would be a closer equivalent to the offshore AWAC H_{m0}.

Figure 7.33 shows the results of this exercise. There is considerable scatter in the results, which is to be expected with wave overtopping. Not enough testing has been done to determine whether the SWAB model gives results that follow the log-linear relation between $q_m/(\sqrt{gH_{m0}^3}\xi_0)$ and $R_c/(\xi_0 H_{m0})$, which according to EurOtop is corroborated by large quantities of physical model test and field data. The PC-Overtopping program gives a considerable overestimation of overtopping rates, generally by a factor of ten. However, the results are dependent on the interpretation of parameters such as the use of values at the structure toe, the choice between T_p and $T_{m-1,0}$ and various slope roughnesses. The field data correspond quite closely to the experimental data and the SWAB results; although the log-linear trend for the field data is quite different, this is due to the fact there are only three data points. The log-linear trend from the SWAB data also diverges from the experimental data for higher freeboards; however these correspond to lower overtopping rates, where errors in the overtopping volumes of only a few waves can have a considerable effect on the results.

The Storm 55 model test corresponds with the equivalent time-series of field data. It has already been shown in Section 7.3.2 (Figure 7.28) that the SWAB model, with the wall force applied only at the recurve wall, gives very accurate results for this test in comparison with

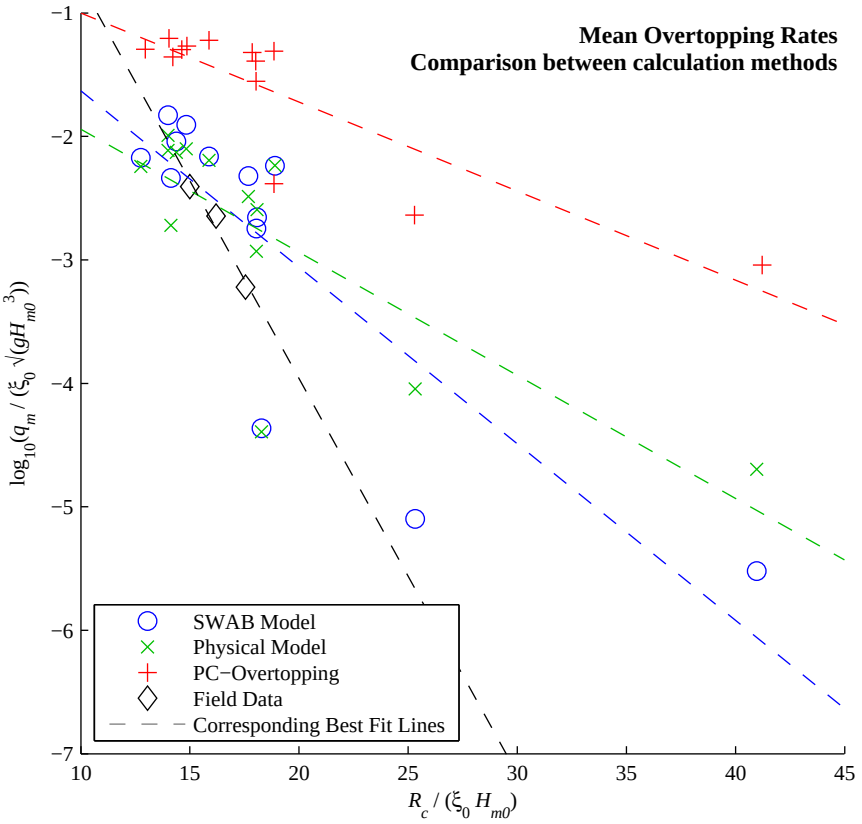

Figure 7.33: Dimensionless mean overtopping rate parameters: comparison between methods

the experimental data. Figure 7.34 shows overtopping volume time-series for the Storm 55 conditions, including the field data, with the experimental data and SWAB runs given at full scale (i.e. time multiplied by $\sqrt{15}$ and volume multiplied by 15^2). Also included in Figure 7.34 are results from three extra SWAB runs, two with the same input energy spectra but different random phases, and one with the initial water level increased by 5 mm (75 mm at full scale), with an additional increase of 15 mm over 470 s (model scale) due to the tide. This third extra run was included because it was noted in Section 4.3.1 that the actual level of the offshore AWAC is not known, and therefore there was some uncertainty in the actual levels. Water levels included with the field data (from an unknown source - not from the AWACs) gave a level of 4.744 maOD (instead of 4.670 maOD used in the flume) at the time of Storm 55 (11:30 am, 24th January 2008). For the experimental data and the SWAB model runs using the waves of the experiments (including the run with tide), only the first 300 s or so (i.e. 1200 s at full scale) is shown in Figure 7.34. The two SWAB runs with different random phases consisted of 250 waves each; therefore, near-complete runs are shown in the figure.

There is a considerable difference in overtopping rates between the three randomly phased SWAB runs; for the time period shown in the figure, mean overtopping rates between these three runs range from 1.69 l/s/m to 3.02 l/s/m. The effect of random phase is important and will be investigated further in Section 8.2.2. Also the small change in water level has a significant effect; this highlights the importance of using accurate data for the calculation of wave conditions and water levels. Obviously, any comparison with field data is very difficult; for example one small collection tank was used to provide representative overtopping rates over a frontage where longshore variations in waves, bathymetry and structure (as well as the wind, direction and speed unknown) can all have a considerable effect. Therefore, what can be considered to be a near agreement (within a factor of 2) between the field data and the SWAB results is very encouraging.

It can be concluded that for this particular seawall, the SWAB model runs and the physical model tests both give reasonably good predictions of mean overtopping rates, in comparison with the limited data available from the field. The use of more field and physical model data, from a wider variety of structures would be important to further validate the SWAB model as an overtopping prediction tool.

7.4 Conclusions

The data collected from the physical model tests of the Anchorsholme seawall have, alongside the (albeit slightly limited) field dataset, provided a useful test of the SWAB model. A more

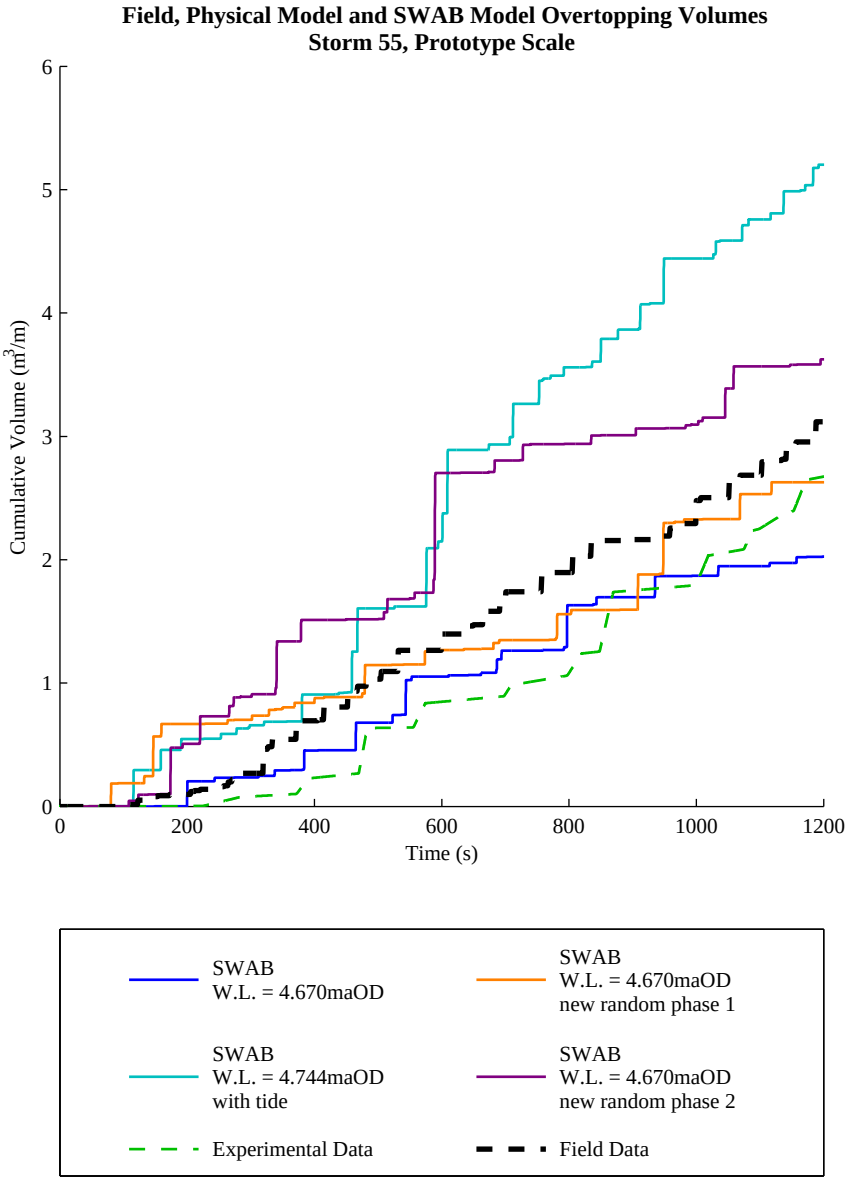

Figure 7.34: Overtopping volume time-series: comparison between various SWAB runs, experimental data and field data

detailed examination of the different types of breaking criteria has been possible, allowing the examination of how time-series of waves start to break in the deeper water, with the waves starting to become increasingly depth limited closer to the seawall. Additionally, the calibration runs have allowed this analysis to take place without the influence of reflection from the seawall.

With the seawall in place, the tests have enabled the SWAB wall force parameters to be optimised, and the influence of these forces on overtopping rates to be observed. It was stated in Chapter 2 that to this author's knowledge, no successful Boussinnesq-type model for random wave overtopping has been developed; therefore this investigation of seawall overtopping is quite important.

The main conclusions of this chapter can be summarised as follows:

- The SWAB model gives accurate results for nearshore wave heights; the accuracy is affected by the breaking algorithm. The H/h breaking criterion and the $\partial\eta/\partial t$ criterion where breaking is applied to the whole wave give the best results.

- The double breaking algorithm is not as effective as the single H/h and $\partial\eta/\partial t$ (whole wave) criteria at depth limiting the waves in the nearshore.

- Without the seawall, the SWAB model gives very good simulations of the wave energy spectra throughout the flume; some differences may occur due to some reflection off the inshore wall in the wave flume.

- The seawall makes a considerable difference to the nearshore waves. Moving average time-series of η_{rms} are accurately reproduced by the SWAB model (with and without the seawall). However, the wall force parameters make little difference to the nearshore waves in the SWAB model

- Near the seawall, wave energy spectra produced from the SWAB results differ from those of the physical model tests. It is not clear why this should be so, but differences in the position from which wave reflections occur probably have some effect.

- The SWAB wall force parameters do have a considerable effect on overtopping rates. The best results are achieved when the wall force is applied only at the recurve wall (with $k_{wall} = 1.0$). The SWAB model does not give particularly good representations of overtopping time-series, although the distributions of overtopping waves are quite accurate.

- By running all the tests, the SWAB model is within a factor of 2 of the experimental data for all but three of the tests. Two of these three tests have very low mean over-

topping rates. For these tests, the wall force was applied only at the recurve wall (with $k_{wall} = 1.0$). In general, the SWAB model overestimates the overtopping rates. The results for the maximum overtopping volume were not so accurate. However, it is important to remember that overtopping rates are very difficult to predict: repeating one of the experiments in the flume gave a reduction of 25 % in the mean overtopping rate.

- The SWAB results and the wave flume experiments correspond well with the overtopping rates recorded in the field; however the dataset is limited. The PC-Overtopping program recommended by the EurOtop manual gave rather large overestimates in mean overtopping rates; however, this program is not well suited to structures with vertical sections.

Despite the promising results, one should note the following:

- The surf similarity parameter is very low for all these tests. All breaking waves were spilling breakers and almost all waves were breaking when they reached the seawall. Plunging breakers and surging waves may not give such accurate results without modification of the breaking criteria.

- The overtopping rates were sensitive to the wall force parameters. It is possible that other seawalls or different wave conditions may require changes to these parameters.

Chapter 8

Overtopping Case Study: Walcott

8.1 Introduction

8.1.1 Background

In Chapter 1, we discussed the aims of the Flood Risk Management Research Consortium (FRMRC), and specifically Super Work Package (SWP) 2. The research aims to develop techniques and models to predict coastal flooding. Therefore, it is of great benefit to test the application of these linked models together using a case study. On 6th November 2007 the Met Office predicted a risk of a significant storm surge in the North Sea. With strengthening winds on 7th November, the surge moved southwards into the North Sea, reaching the East Anglian coast on the night of the 8th and morning of the 9th November 2007 [Met Office, 2011]. Although major flooding was feared, with water levels comparable to those of the surge of 1953, the actual peak sea level was slightly lower than predicted and widespread coastal flooding never occurred. However, at the village of Walcott on the north Norfolk coast there was significant wave overtopping and several homes were flooded. Walcott makes an interesting case study: it is unusual in that conditions in this single location were possibly more extreme than other nearby locations (such as the towns of Cromer and Lowestoft, where the nearest tide gauges are located).

Figure 8.1 shows the location of Walcott on the Norfolk Coast. It is situated about 25 km NNE of Norwich. A site visit to Walcott took place in November 2009, where some of the residents of Walcott and the coastal engineers of North Norfolk District Council were interviewed about the events of November 2007, as well as answering more general questions on flooding in the area. Walcott is unquestionably situated on a vulnerable stretch of coastline, exposed to the North Sea, surrounded by low-lying land, and fronted by easily erodible low

cliffs. Erosion at the village of Happisburgh, a few miles to the southeast, is a rather powerful example of what happens when coastal defences in this region are no longer maintained (Figure 8.2). From interviews with those who have been resident at Walcott for many years (especially Nigel Adams, the owner of Walcott Mace supermarket, Figure 8.3), it is apparent that flooding events occur rather frequently, approximately every 10 to 20 years. According to Mr Adams, the last major events of a similar magnitude to that of 2007 occurred in 1976 and 1978. Interviews of other residents gave information on the flood levels that were experienced. For example, the Walcott Caravan Park office, located next door to the supermarket, and less than 50 m from the seawall, had flood water entering through the letterbox (Figure 8.4). The owners of the Park office, who live at the property, claimed that almost every wave was coming over the seawall, though this is not something that can be verified.

To complicate the situation of flooding in Walcott, the surrounding area (like many low-lying rural areas) has a land drainage system, which usually takes fresh water back out to sea. During a storm surge, it is possible that sea water can actually travel landward via these drains. Figure 8.5 shows the Hundred Drain, from a location just across the road from the seawall. It is possible that flooding reported by residents further away from the seawall, behind the Caravan Park, may have travelled along this drain (Figure 8.6) Farmers have reported saltwater in their land drains (labelled on Figure 8.1); these include reports from Stalham, about 8 km south of Walcott.

8.1.2 The seawall, bathymetry and waves

In the previous work in this thesis, test cases have made use of the results of physical model tests, with a limited application of field data. Model bathymetries, wave conditions and water levels for these tests were either specified (in the case of the physical models), or measured on site (in the case of field tests) with the required data being relatively easy to access and extract. For a case study such as that of Walcott, obtaining the data is part of the challenge (including the interviews and photographs discussed in this chapter), and the input for the overtopping model is either the direct result of this data search, or has been calculated indirectly from the raw data through the modelling process outlined in the "Road Map" (Figure 1.1). Therefore, the quality of the results from this investigation is dependent on the previous stages of the process, and the accuracy of the overtopping modelling described here directly affects the flood inundation modelling that has been done by other researchers (Kuo Yan from the University of Oxford and Nicolas Chini from the University of Manchester). The photographs were taken by Maurice McCabe; the interviews were carried out by Maurice McCabe, Peter Stansby and Nicolas Chini (University of Manchester); the bathymetric data was obtained by

Figure 8.1: Walcott Location Maps

Figure 8.2: Coastal erosion at Happisburgh, Norfolk

Figure 8.3: Mace supermarket, Walcott, taken from outside Walcott Caravan Park office (crest of seawall is on right hand side of photo)

Figure 8.4: Walcott Caravan Park office, showing maximum flood levels on 9th November 2007

Figure 8.5: Hundred Drain, near Walcott seawall

Figure 8.6: Reported maximum flood level, from a location near the Hundred Drain

Nicolas Chini, who also did the TOMAWAC inshore wave modelling. Offshore wave, tide and surge modelling was done by the National Oceanography Centre, Liverpool.

Photographs of Walcott seawall are shown in Figures 8.7, 8.8 and 8.9. These photos were taken from the northwest end of Walcott village (the yellow circle in Figure 8.1). The first photograph (Figure 8.7) shows the sand/flint beach that fronts the seawall, with wooden groynes to restrict longshore sediment movement. The profile of the seawall can be seen as it changes direction in the middle distance. The second photograph (Figure 8.8) looks towards Walcott village from the seawall; it shows the low level of the village and the distance of the nearest houses from the seawall. Like the Hundred Drain, the coastal road drainage also outfalls through the seawall (Figure 8.9); these drains are apparently quite effective in allowing flood water to escape, but could also allow sea water to flow landward. The recurve at the crest of the seawall can be clearly seen in this photograph. No design drawings of the seawall were used for this study, but surveys have been carried out at regular intervals along the Norfolk coastline, including at Walcott (these were made available by the Environment Agency); the detail of these surveys is quite sufficient for the SWAB model. Additionally, Light Detection and Ranging (LIDAR) data was obtained from the Environment Agency. This data covers the entire stretch of coastline (rather than just discrete profiles), although its seaward extent is dependent on the tide level at the time of survey (the LIDAR surveys do not record under-

Figure 8.7: Looking northwest along seawall, showing sand/flint beach and groynes

water bathymetry) and the crest of the seawall is not always picked up (due to the LIDAR resolution).

Offshore wave data was calculated using a coupled POLCOMS-WAM model. POLCOMS [Holt and James, 2001] is a continental shelf tide and surge model, with an approximate 12 km grid resolution. This was coupled with the WAM wave model [WAMDI Group, 1988] by Osuna and Wolf [2005]. POLCOMS-WAM calculates tides and surges; however, another dataset of water levels was taken from the CS3 model. The CS3 model [Smith, 1994] was developed by the National Oceanography Centre, Liverpool, and calculates tides and storm surges on a 12 km grid resolution, but unlike the POLCOMS-WAM model does not include waves. Maximum water levels from CS3 were found to be approximately 0.3 m below POLCOMS maximum levels; a comparison with the tide gauge records at Cromer and Lowestoft showed that the water levels from CS3 are probably more accurate [Chini, 2010] and are therefore used for this investigation. Inshore waves, on a finer grid resolution, were calculated using TOMAWAC (Benoit et al. [1996]). Hourly wave output from POLCOMS-WAM, with the water levels from CS3, were used as an offshore boundary condition to the TOMAWAC model; in addition, nearshore winds taken from Met Office were also included in the model.

Hourly wave spectra from the TOMAWAC model were output at the location shown in

Figure 8.8: Looking southeast along seawall, showing low-lying coastal road and Walcott village

Figure 8.9: Looking at seawall from beach, showing road drain outfall

Table 8.1: Waves and water levels for storm of 8th/9th November 2007 at Walcott, taken from TOMAWAC output. Note, the energy spectrum was only calculated at 25 discrete frequencies; therefore possible values for the peak period are similarly limited

Time (hours)	Water Level (mOD)	Wave Height, H_{m0} (m)	Peak Wave Period, T_p (s)
0	0.392	2.058	9.23
1	0.856	2.112	10.15
2	1.652	2.227	10.15
3	2.419	2.359	10.15
4	2.905	2.461	10.15
5	3.075	2.521	10.15
6	2.917	2.534	11.17
7	2.427	2.486	11.17
8	1.658	2.390	11.17
9	0.857	2.284	11.17
10	0.246	2.195	11.17
11	-0.166	2.123	12.29

Figure 8.10; because the SWAB model is one-dimensional, these were integrated:

$$S(f) = \int_0^{2\pi} S(f, \theta) d\theta \tag{8.1}$$

This may produce a small overestimation in wave heights at the seawall, though refraction will tend to bend all incident waves towards the shore. Figure 8.10 shows the directional wave spectrum after 6 hours (the maximum), superimposed on the map of the area; the wave direction remained steady throughout the storm. According to equation (5.24) of the EurOtop Manual [Pullen et al., 2007], with short-crested waves angled approximately 30° from the shoreline, the overtopping rate will be about 90 % of the rate from waves angled directly towards the shore. Ideally, a model in two horizontal dimensions would resolve any issues about wave direction. The TOMAWAC output was located at the position shown in Figure 8.10; this is at OS Grid Reference TG 36870 33861, with a bed level of -13.90 mOD. The surveyed profile for 2007 extended from TG 36525 33481, with a bed level of -12.66 mOD, landward to TG 36014 32873, and is shown superimposed on Figure 8.10. The other available surveyed profiles lay along the same line, but extended further offshore. Although TOMAWAC output and the profile are located 500 m apart, due to the water depth it could be assumed that the wave conditions were approximately the same at both points. Integrated directional wave spectra (using equation (8.1)) from the TOMAWAC output are shown in Figure 8.11. Table 8.1 summarises the wave and water level parameters during the storm.

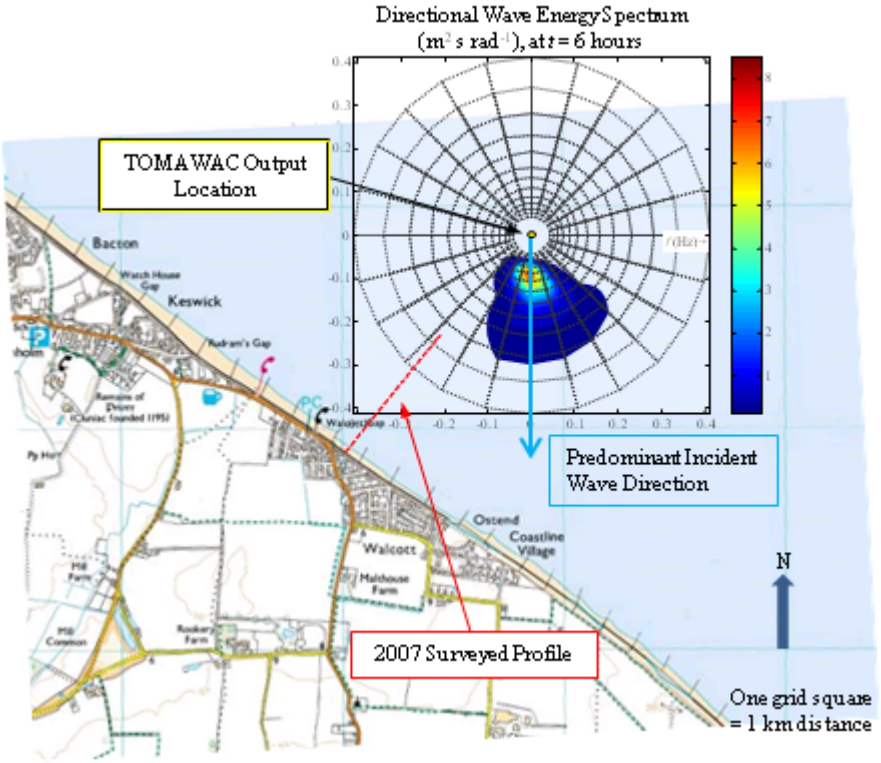

Figure 8.10: Directional wave energy spectrum, during peak of storm

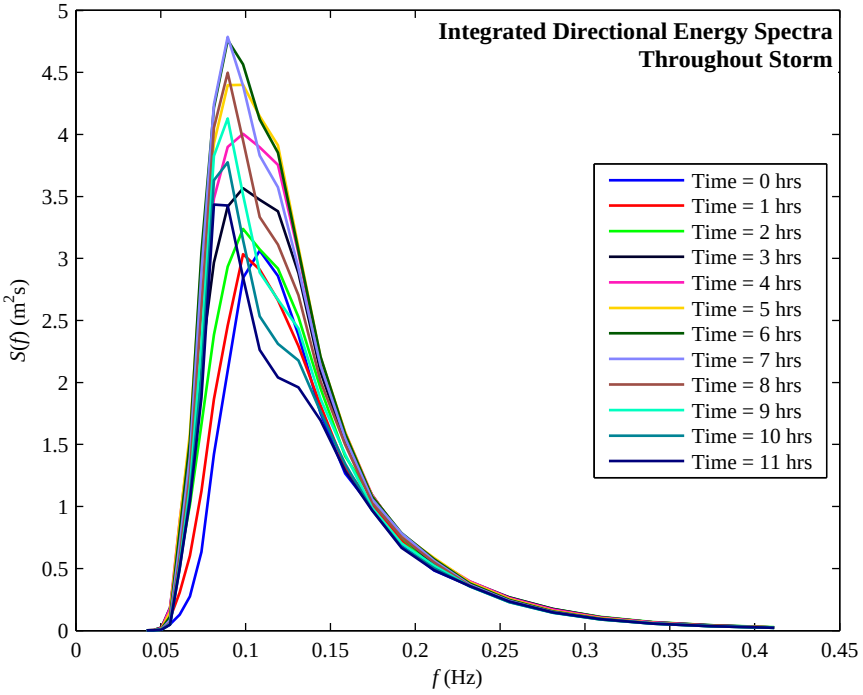

Figure 8.11: Integrated directional wave spectra

8.1.3 Investigation of wave overtopping

The overtopping investigation at Walcott was divided into three parts:

- To study the effect of beach profile and beach level on overtopping discharge;
- To calculate wave overtopping for the event of 8th/9th November 2007, providing information for the flood inundation modellers, and;
- To calculate overtopping rates for wave heights and water levels of various joint return periods, for a joint probability analysis.

The SWAB model was used for all three parts of the investigation. The methodology, including setting up the SWAB model, and results from each of these three investigations will be described in the following sections. The effect of different breaking criteria on the results will not be studied in this chapter; for all tests, the SWAB model used the double breaking algorithm (see Sections 3.2.2 and 7.2), with $C_{bt} = 0.2$ and $C_{bh} = 0.7$. In Chapter 7, it was not found to be the best breaking algorithm, although significant wave heights near the structure should be reasonably accurate.

8.2 Effect of Beach Levels on Wave Overtopping

8.2.1 Methodology

The four beach profiles that were used for this investigation are shown in Figure 8.12; they date from 1991, 1996, 2001 and 2007, located along the line shown in Figure 8.10. The 1996 profile seems to be slightly anomalous further offshore; when the profiles are lined up at the seawall, the offshore level is noticeably higher than the others. Whether or not this profile is accurate will not affect the outcome of this investigation, which is concerned with how the profile affects overtopping and not with beach profile change itself.

The SWAB model was set up with each of the four profiles. It can be assumed that the seawall location has not changed over the sixteen years; therefore, each profile was lined up at the seawall crest. Because some profiles extended further offshore than others, the profiles were cut off seaward of the shortest profile (the 2007 profile). Each profile was then extended horizontally seaward by (approximately) one wavelength to give a distance over which the waves can form, with an extra 200 m of horizontal bed seaward of the wave input location to accomodate the offshore sponge layer. Behind the seawall, an overtopping collection tank was set up, with a reflective boundary to prevent the overtopping water from being lost. At the seawall itself, the wall force, described in Section 3.3, was applied to the three near-vertical

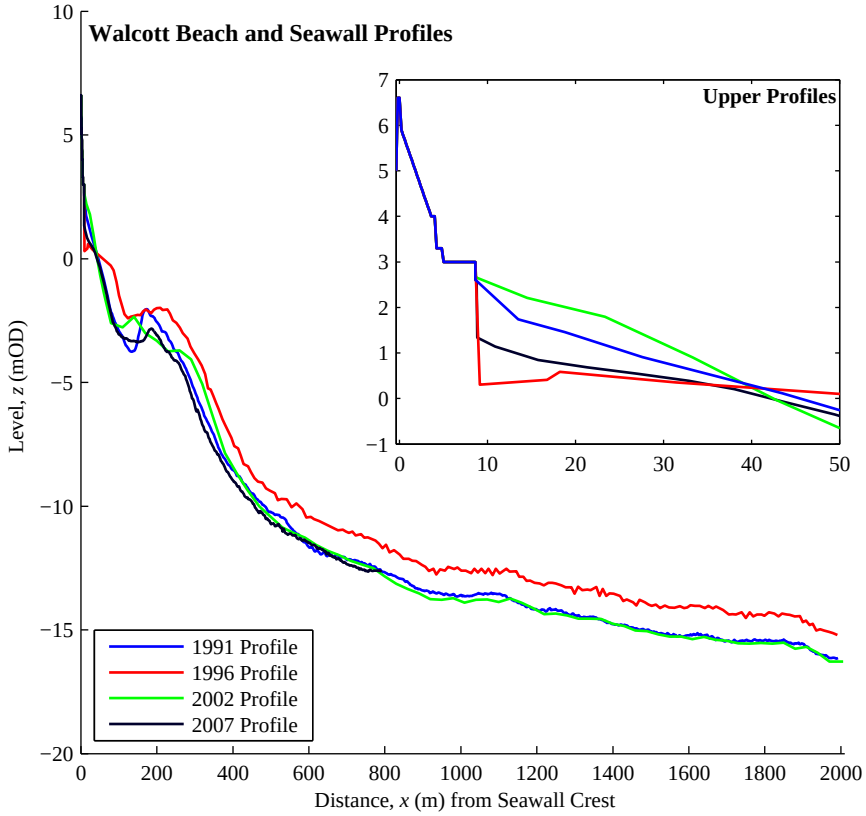

Figure 8.12: Surveyed beach profiles (seawall crest is at $x = 0$ m)

sections of seawall with a reflection factor, k_{wall}, of 1.0. These modified profiles are shown in Figure 8.13.

A further nine profiles were extracted along the seawall from the LIDAR data; because these profiles do not extend far offshore, they were merged with the 2007 profile approximately 40 m seaward of the seawall. At the crest of the seawall, the resolution of the LIDAR meant that the highest point was not always captured; therefore, the upper part of the crest from the SWAB-modified surveyed profiles (Figure 8.13) was used instead of the LIDAR surveyed crests. These LIDAR cross-sections were extracted at approximately equal distances along the seawall, in a direction perpendicular to the crest-line of the seawall. The sections were positioned such that they did not cross groynes, and also such that more than one profile was situated in each groyne bay. Contours from the LIDAR data and the profile locations, superimposed on the OS map of the area, are shown in Figure 8.14. The upper part of these profiles, as used for the SWAB model, are shown in Figure 8.15.

The wave conditions selected for this investigation were similar to, but not the same as those discussed in Section 8.1.2. Significant wave heights, H_{m0}, were 2.43 m and water levels were a constant 3.20 mOD. The input wave energy spectrum is shown in Figure 8.16. Since it

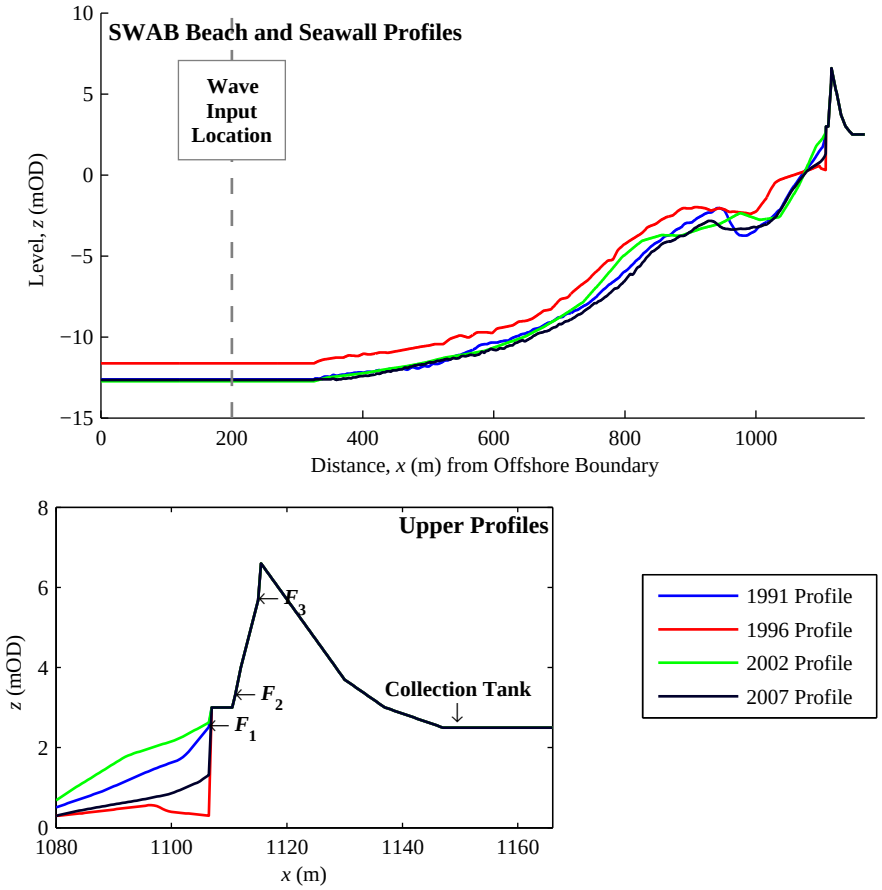

Figure 8.13: Beach profiles, modified for the SWAB model

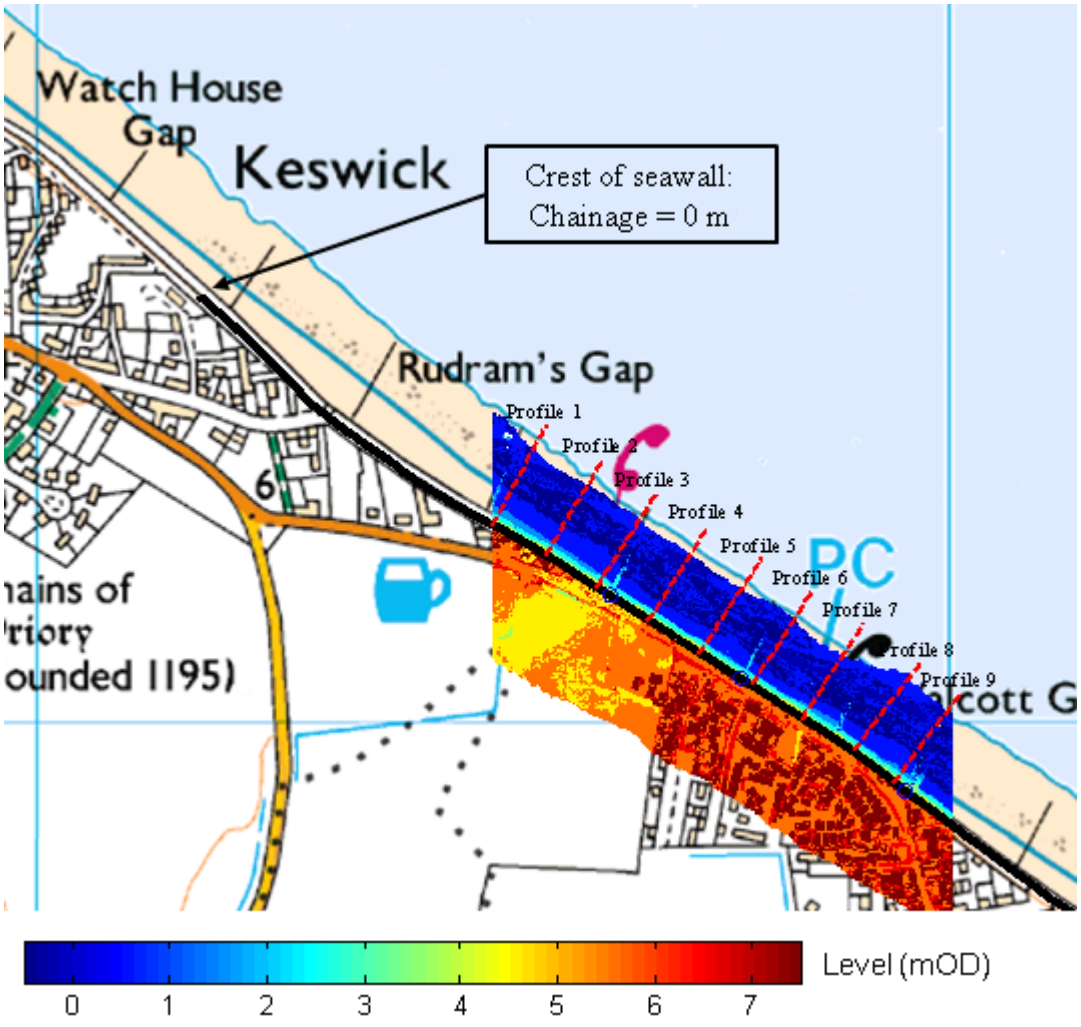

Figure 8.14: LIDAR contours with extracted profiles

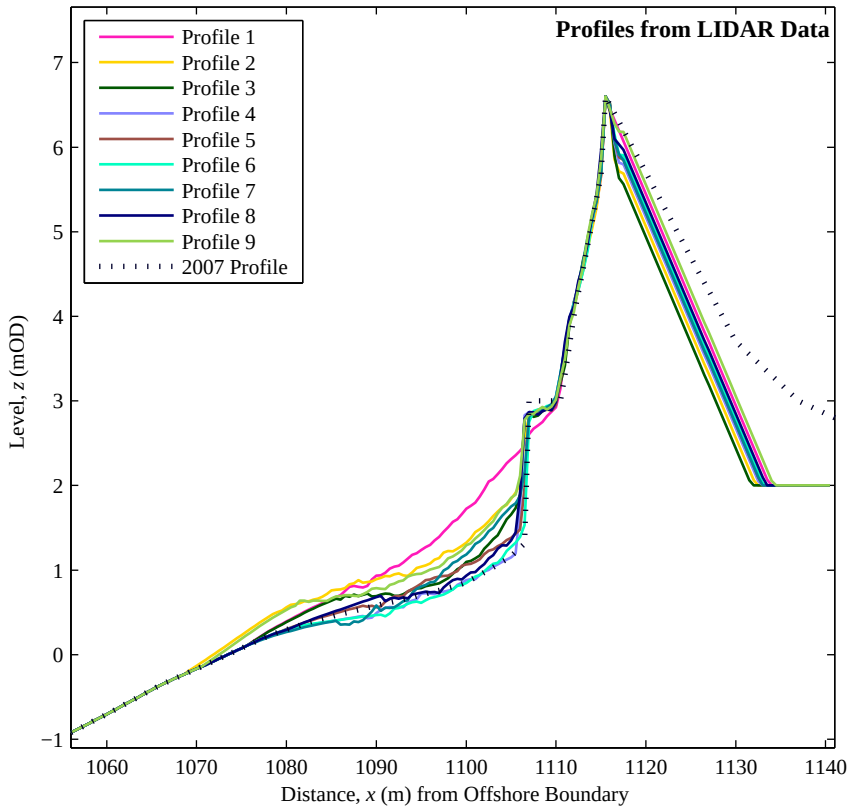

Figure 8.15: Profiles extracted from LIDAR data

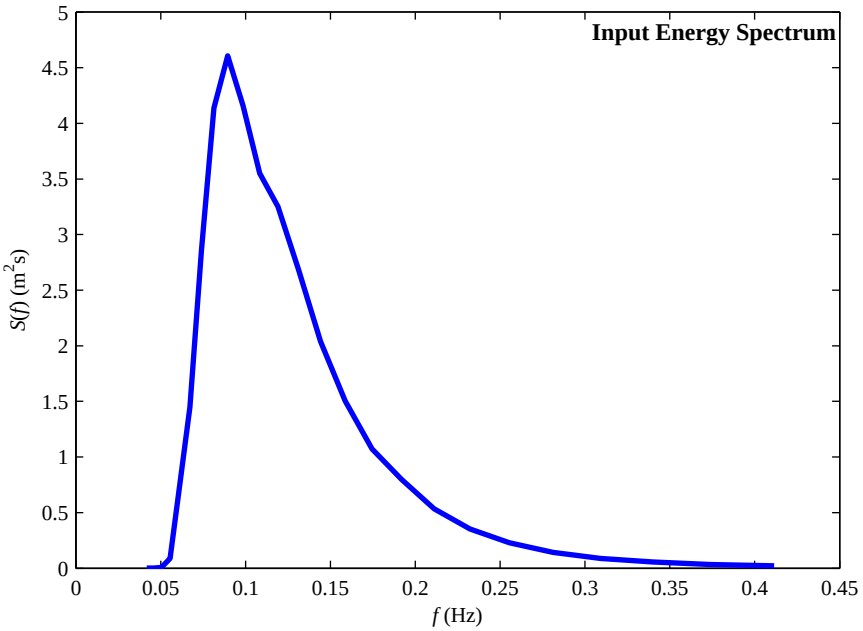

Figure 8.16: Input wave energy spectrum

had not yet been estabished as to what variation in overtopping rates would occur from one wave train to another, a set of eleven different randomly phased runs were set up of 200 waves each. Wave height distributions for the incident waves of all eleven runs are shown in Figure 8.17.

8.2.2 Overtopping of surveyed profiles

Spectral significant wave heights in the nearshore for all SWAB runs are shown in Figure 8.18a. The beach level starts to have a noticeable effect on wave heights 66 m from the seawall crest (note, measurements were only taken at the locations shown in the figure). With a water level of +3.2 mOD, the still water depth at this location varies between 3.3 m (1996 profile) and 4.9 m (2002 profile). With a significant wave height of about 2.4 m, some waves will be breaking at this location and depth-limitation is starting to occur. However, the variation in wave heights between profiles is more apparent 16 m from the seawall. Here, most waves will be breaking, and the higher beach level of the 2002 profile means that wave heights are much lower. Figure 8.18b shows a measure of the variation of the highest waves between runs. There is a noticeable increase in the difference between the highest and lowest $H_{1/10}$ close to the shore, though little correlation between the variation and the beach level. This difference between runs will become more noticeable in the analysis of overtopping rates.

Figure 8.19 shows time-series of overtopping volumes for all the SWAB model runs. It is apparent that there is considerable variation between runs, though on average the lowest

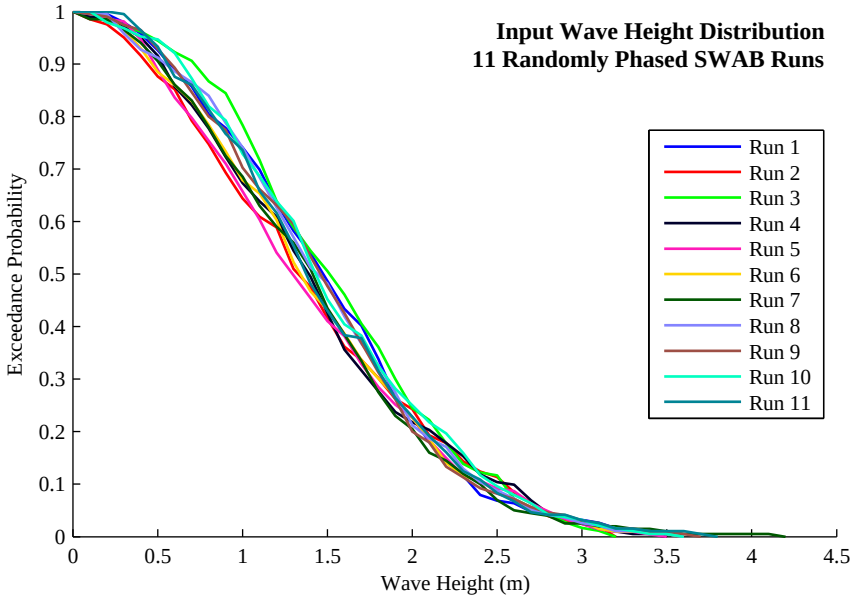

Figure 8.17: Input wave height distributions

beach level results in the greatest overtopping. By looking at overtopping results as a function of the beach level at the seawall (Figure 8.20), some trends emerge. There appears to be some negative correlation between the beach level at the seawall and the mean overtopping rate. The volume of the maximum overtopping wave does not seem to be affected by the beach level. It is interesting to note that the ratio V_{max}/q_{mean} is approximately 1000 s; Figure 4.4 of the EurOtop Manual [Pullen et al., 2007] gives very similar values of this ratio for waves of a similar height, albeit for smooth slopes. The proportion of overtopping waves is affected by increasing the beach level, although for low levels this proportion does not seem to go above about 60 %. It is also apparent that for the higher beach levels, the variation between runs becomes rather small, with between 27 % and 32 % of waves overtopping the seawall for the 2002 profile.

Three of the eleven sets of random phases were chosen to be run on the profiles extracted from the LIDAR data. Run 6 was chosen as its mean overtopping rates correspond very closely to the means over all eleven runs. Runs 1 and 2 both have overtopping rates that differ somewhat from the mean. Overtopping parameters for these three runs, as a function of beach level for the surveyed profiles, are shown in Figure 8.20. There are some differences between the LIDAR profiles and the surveyed profiles. In particular, Profile 1 has a high beach level but does not appear to have a prominent step at the base of the structure (about 8 m from the seawall crest). Mean overtopping rates for Run 1 are shown in Figure 8.21; there appears to be little correlation between the overtopping rate and the beach level. Note that the mean overtopping rates for these runs are considerably higher than those represented in Figure 8.20;

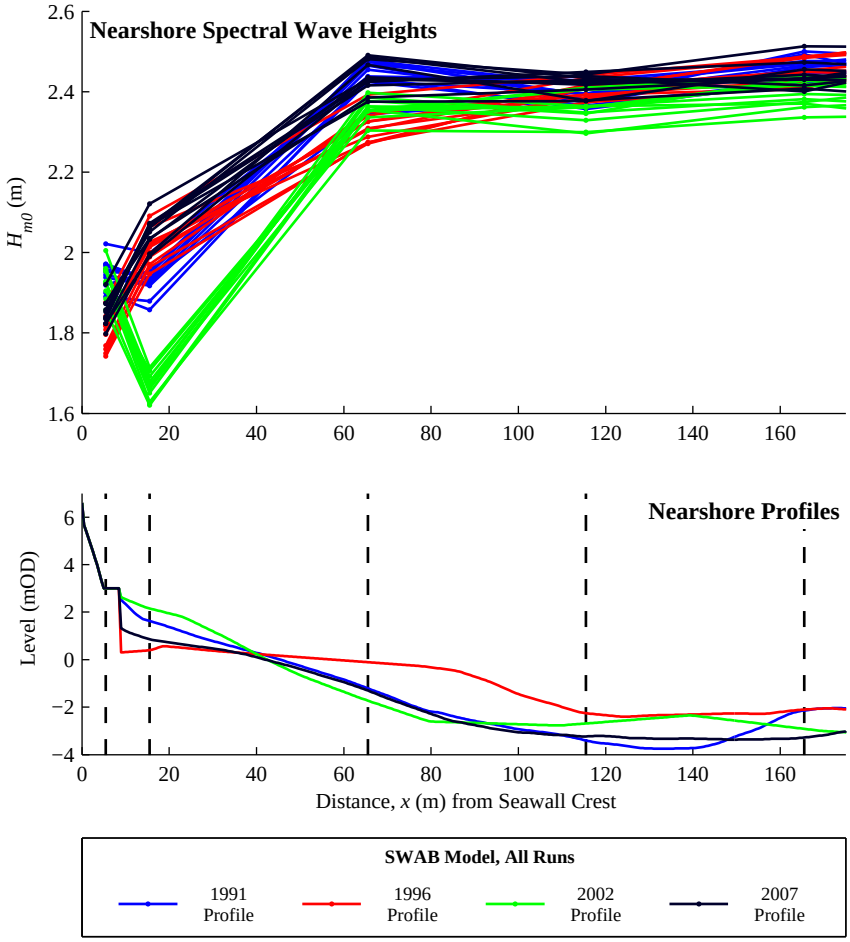

(a) Spectral significant wave heights

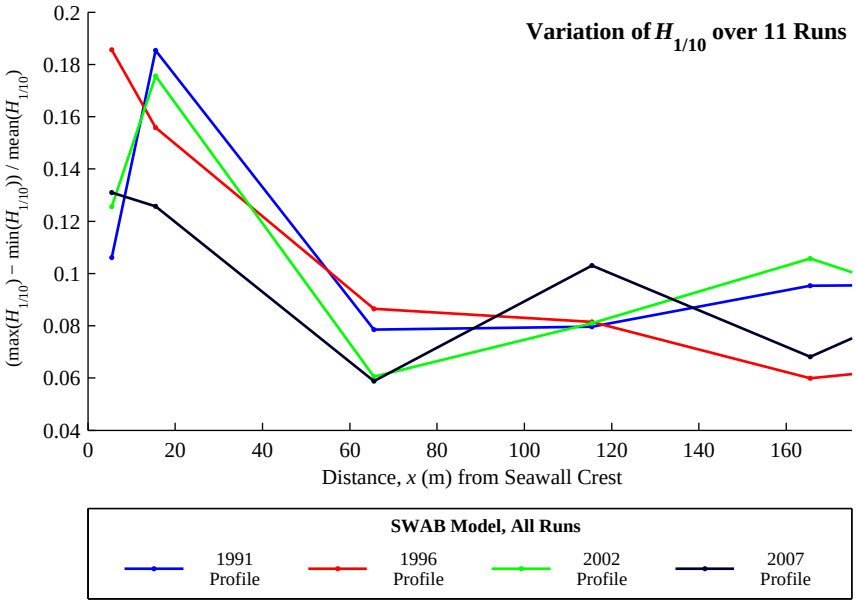

(b) Variation in the height of the highest tenth of waves ($H_{1/10}$) between maximum and minimum of the 11 runs

Figure 8.18: Wave heights in the nearshore, for 11 different SWAB runs

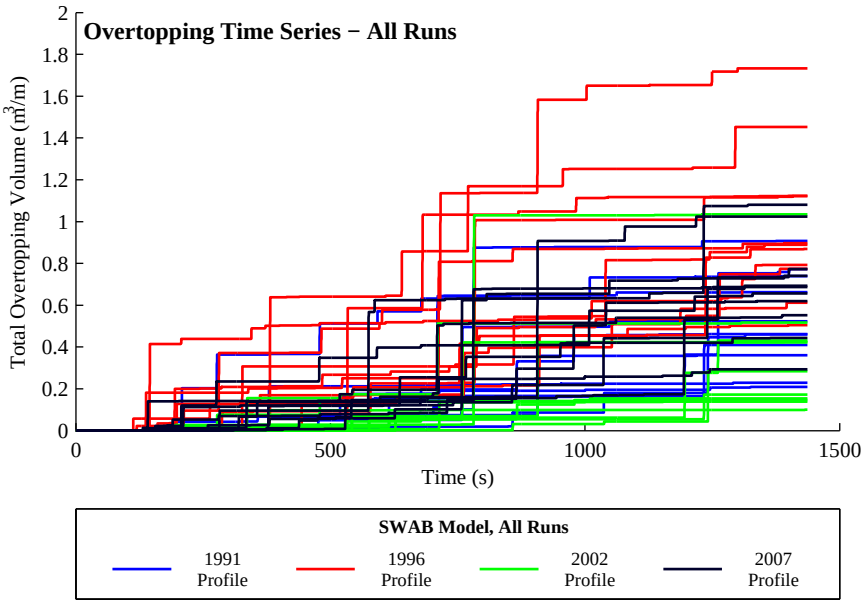

Figure 8.19: Time-series of cumulative overtopping volumes, for 11 different SWAB runs

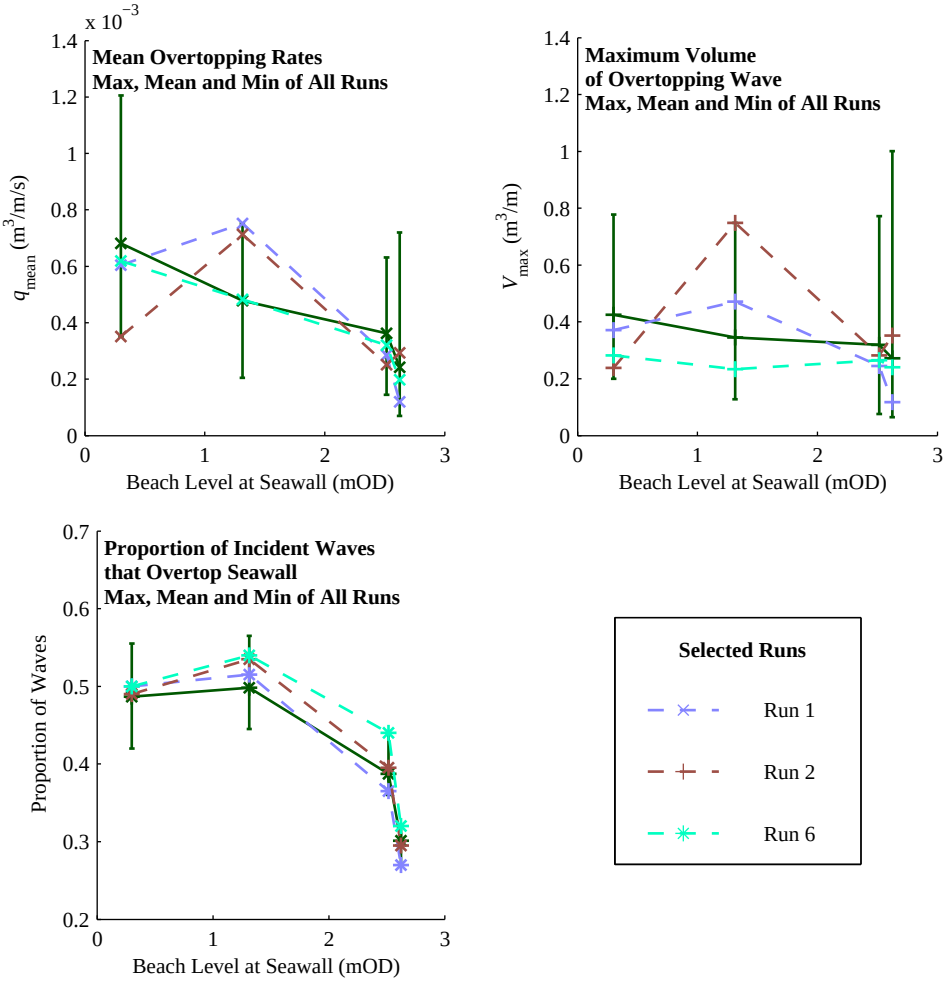

Figure 8.20: Overtopping as a function of beach level at seawall, showing maxima, minima and mean values over 11 SWAB runs, as well as values from three selected runs

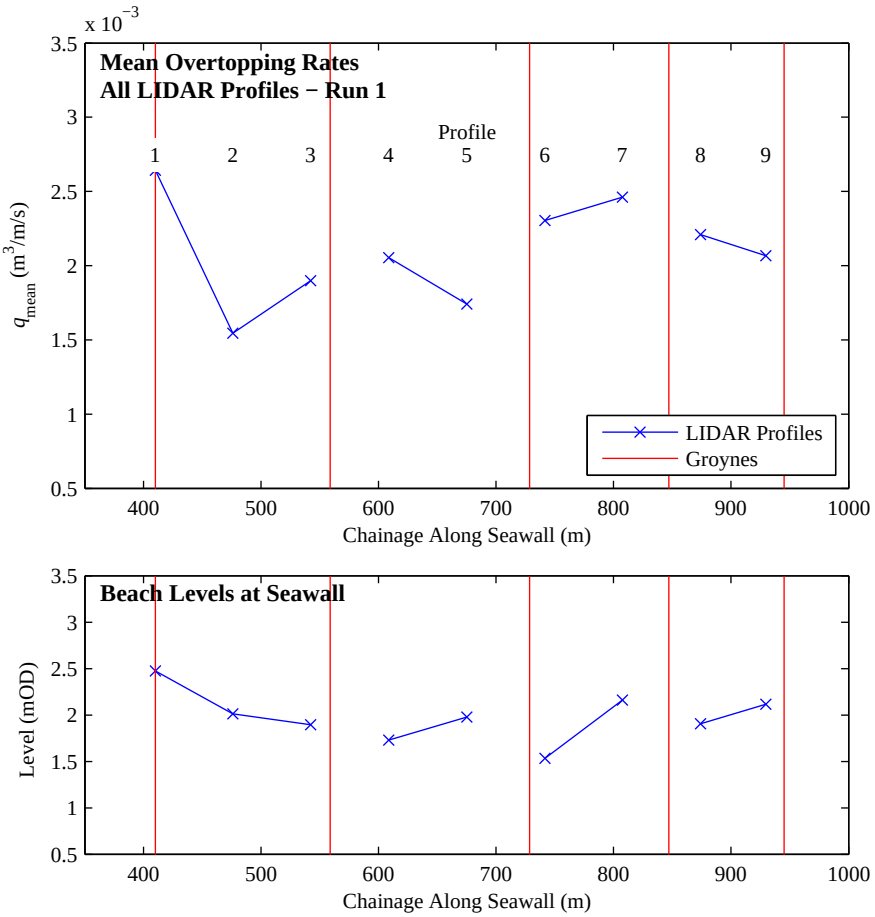

Figure 8.21: Mean overtopping rates for all LIDAR profiles for Run 1, with corresponding beach levels

that is because the wall force F_2, above the seawall berm (see Figure 8.13) was not included. In addition for Profile 1, where the lower part of the seawall is almost indetectable, the wall force F_1 was also not applied. These overtopping rates are therefore considerably too high, but demonstrate the lack of any general trend in overtopping from one part of Walcott to another.

Runs 2 and 6 were applied to profiles 1, 2, 4 and 7, this time including all the wall forces: F_1, F_2 and F_3. These four profiles correspond to a range of beach levels. Figure 8.22 shows there is some variation between the four profiles. The lowest beach level (Profile 4) gives the greatest overtopping. The exception appears to be Profile 7, which has a high beach level. However closer inspection (see Figure 8.15) shows that although Profile 7 has a higher beach level at the seawall than Profile 2, immediately offshore of the seawall it has a slightly lower level. Although there is a considerable difference in maximum overtopping volumes between Run 2 and Run 6 (for Run 2, between 77 % and 90 % of the total volume comes from one wave), Figure 8.23 shows that the mean overtopping rates correspond quite well with those of Figure 8.20.

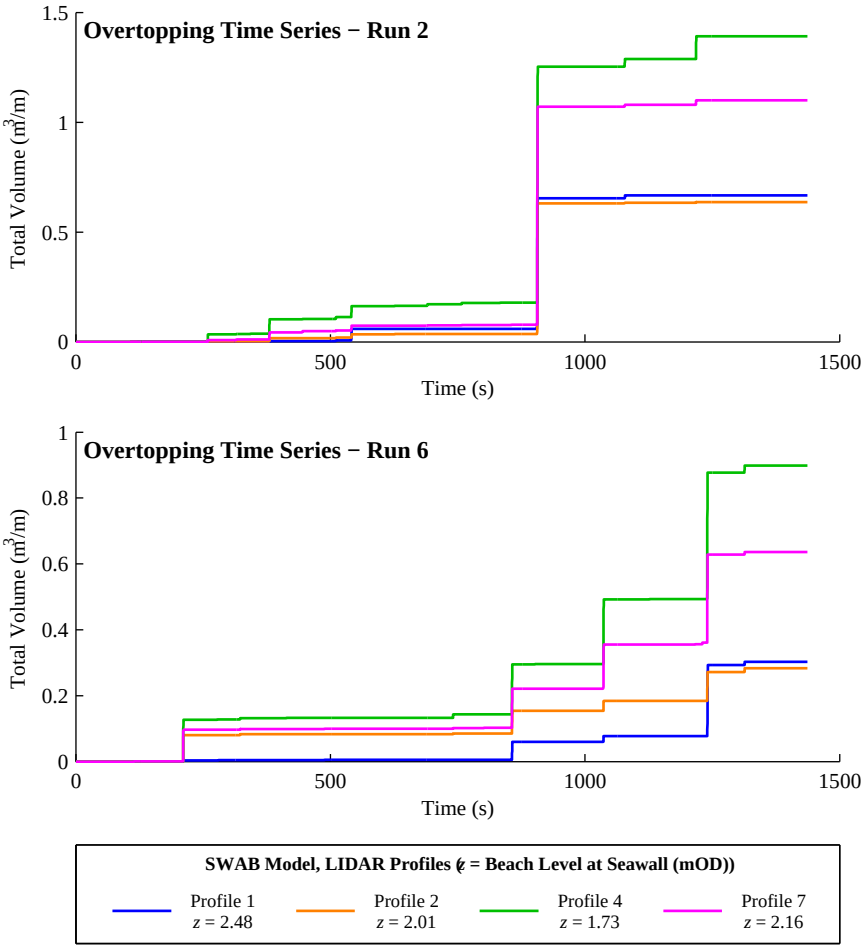

Figure 8.22: Overtopping time-series for LIDAR profiles 1, 2, 4 and 7

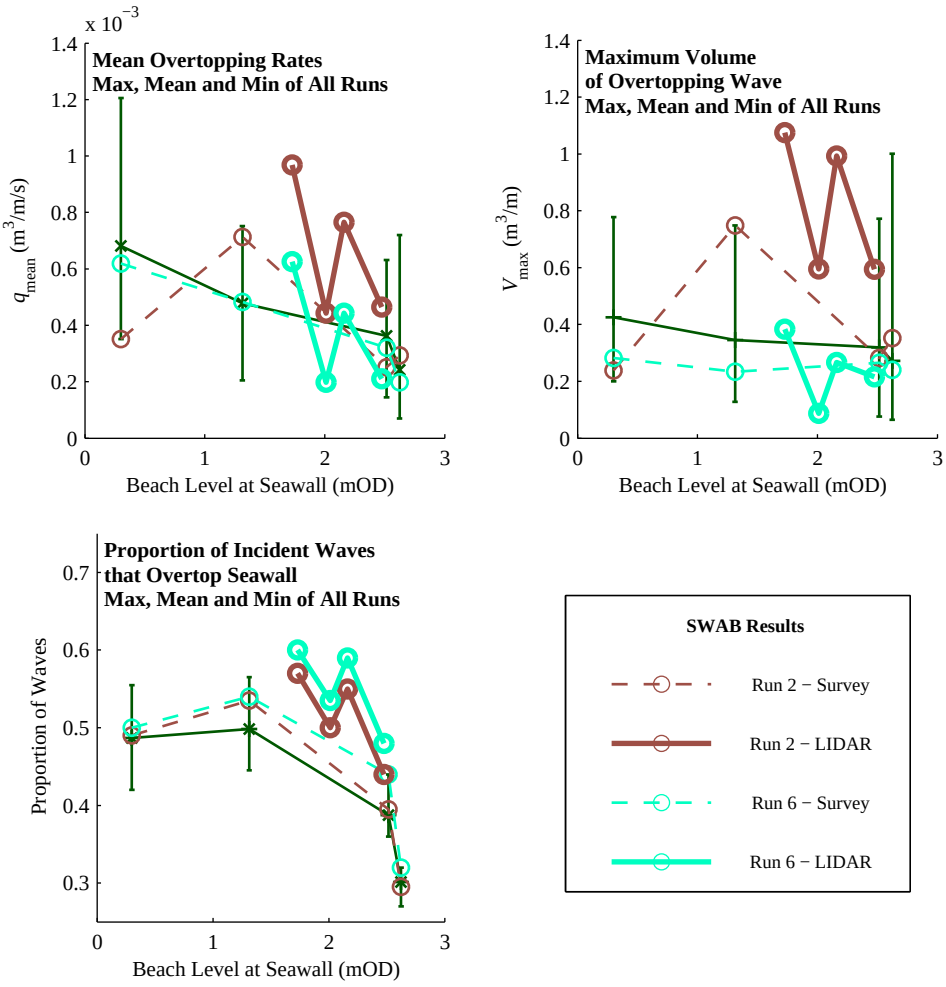

Figure 8.23: Overtopping as a function of beach level at seawall: Figure 8.20 with superimposed results from LIDAR profiles

8.2.3 Effect of beach level on overtopping

From the above investigation, the following general observations have been made:

- As expected, the beach profile has a noticeable effect on significant wave heights in the surf zone.
- In the inner surf zone, the mean height of the largest waves becomes more variable between different randomly phased runs.
- A lower beach level at the seawall generally leads to greater mean overtopping rates. This is largely due to a greater proportion of overtopping waves.
- There is a large variation in mean overtopping rates and maximum overtopping volumes between different randomly phased runs. This variation is generally greater than the effect of the beach level (e.g the minimum overtopping rate for the lowest beach level is only slightly greater than the mean rate for the highest beach level).
- The beach levels vary along the Walcott seafront. This will lead to variable overtopping rates, though there is no general trend from one end of the seafront to the other.

However, there are some qualifications to these observations:

- The randomly phased runs consisted of 200 waves each (about 25 minutes of storm). The variation between different wave trains will be reduced over longer events.
- Two dimensional effects have not been considered and may have an effect on overtopping rates, especially with respect to the variation in rates along the seafront. In particular, refraction due to the variation in beach levels across each groyne bay, as well as reflection from the groynes, may have an important effect.

8.3 Full Storm Overtopping

8.3.1 Methodology

A SWAB model run of the storm of the 8th/9th November 2007 was carried out. Section 8.1.2 describes the methodology for obtaining the hourly directional wave spectra and water levels that were used as the SWAB model input; these conditions are shown in Table 8.1 and the hourly spectra are shown in Figure 8.11. Obviously, variation in waves and water levels continues all the time. The SWAB model currently has no facility for varying wave conditions during a model run; however changes in water level are possible (see Section 3.4.1). The water

levels and wave spectra were given hourly, both at the same time. Therefore these hourly water levels were used as the start and end levels for each model run, and a representative wave spectrum was calculated for the duration of each run by taking the mean of the start and end wave spectra. The water levels and spectra were calculated in this way because it was thought to be important to capture the maximum water level during the storm.

Figure 8.24 shows the hourly water levels and wave heights. It was not expected that any overtopping would occur before three hours had passed or after eight hours had passed; therefore, to save calculation time and disk space these hours were not modelled. The 2007 surveyed beach profile was used, with the knowledge from the previous investigation that there would be some variation in rates along the frontage, but with no general trend from one end to the other. It should be noted that each hour was only run once; a different result would be obtained by running the storm with different random phases, but because the total length of run has been increased from 25 minutes to 300 minutes, the variance in the expected result is greatly reduced.

For structures of the shape of the seawall at Walcott, with multiple vertical sections as well as a berm and a recurve wall, the EurOtop Manual [Pullen et al., 2007] recommends the use of the neural network tool. However, the neural network only gives outputs of mean overtopping rates and some of the input parameters may be open to interpretation. For example, it is not clear from the neural network's manual [Coeveld et al., 2005] whether or not wave setup should be included in the water level parameters. Two neural network runs for the storm at Walcott were performed by Chini [2011], with and without the inclusion of wave setup. The hourly outputs from the TOMAWAC model were used to calculate the required wave parameters. The wave heights and water levels are those shown as blue lines in Figure 8.24. However, the neural network requires wave conditions at the toe of the structure; Chini [2010] used TOMAWAC again to transform these offshore conditions to the seawall. Note that TOMAWAC does not calculate wave setup; therefore it was assumed that the setup would be 19 % of the breaking wave height; using linear wave theory, this is the setup at the shoreline when the breaking height to depth ratio is 0.8 [Dean and Dalrymple, 1991].

8.3.2 Results and comparison with EurOtop method

Figure 8.25 shows the cumulative volume overtopping the structure, alongside a time-series of the overtopping rate. For this storm simulation, the SWAB model showed that a total of $8.02\,\mathrm{m}^3/\mathrm{m}$ overtopped the structure during these 5 hours; this gives a mean rate of $0.445\times10^{-3}\,\mathrm{m}^3/\mathrm{m/s}$. However, more than half of this overtopping occurred between 5 hours and 6 hours, when the mean rate was $1.35\times10^{-3}\,\mathrm{m}^3/\mathrm{m/s}$. According to the EurOtop Man-

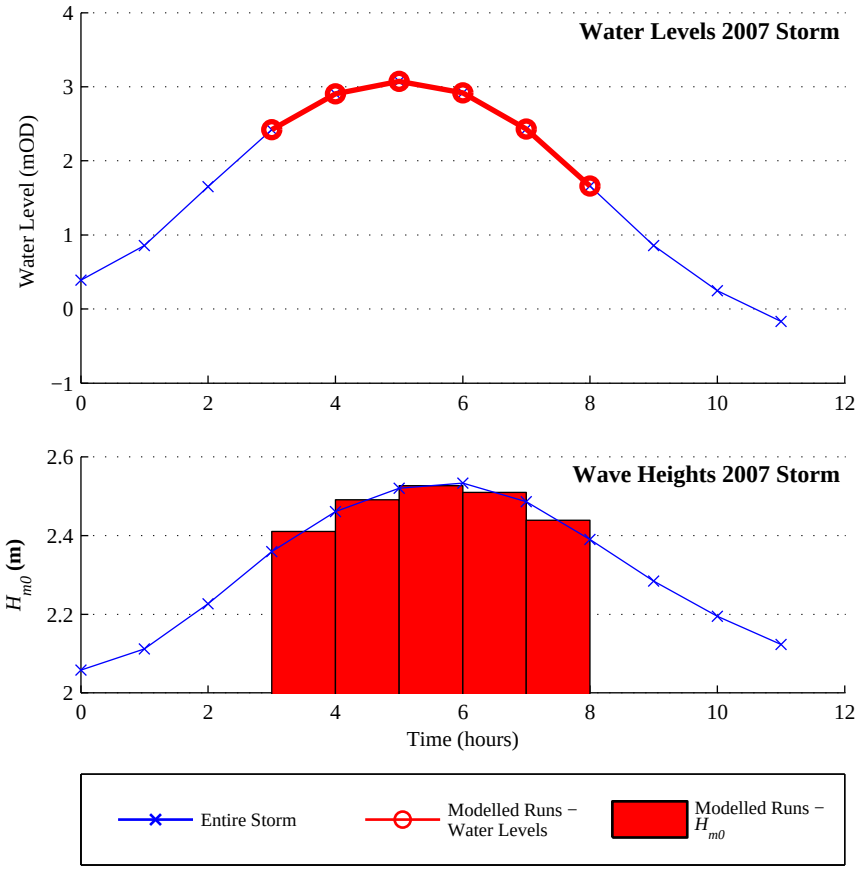

Figure 8.24: Hourly water levels and significant wave heights for Walcott storm

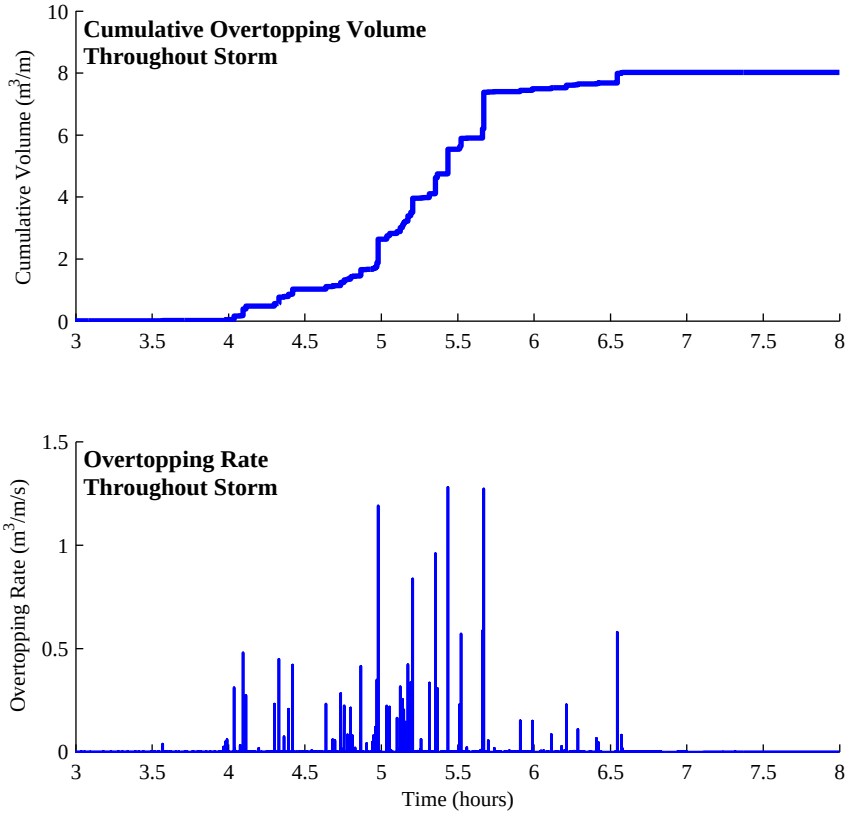

Figure 8.25: SWAB results for overtopping volumes and rates

ual, this rate is not enough to cause structural damage to the seawall, or the roadway behind (>200×10^{-3} m^3/m/s would be required, Pullen et al. [2007, Table 3.5]), but could be dangerous to trained staff walking behind the seawall (1×10^{-3} to 10×10^{-3} m^3/m/s limit, Pullen et al. [2007, Table 3.2]).

From this knowledge it is difficult to assess how accurate these results are; however, reports from residents may be more useful. It was said that during the peak of the storm most waves were overtopping the structure. Between 5 hours and 5½ hours 23 waves overtopped the structure in the SWAB simulation; this equates to one wave every 80 s, which is approximately one wave in eight. This is less than the residents reported.

The time-series of overtopping rates were used as input to flood inundation models. Chini and Stansby [2011] set up an inundation model with the TELEMAC software [Hervouet, 2007], which solves the nonlinear shallow water equations using a finite-element method. Their analysis included a comparison between the maximum flood levels predicted by their inundation model with the maximum levels reported by the local residents. At the Caravan Park office, where water was reported entering the letterbox (Figure 8.4), the simulation of Chini and Stansby [2011] gave a maximum depth of 0.65 m. This is quite similar to the reported

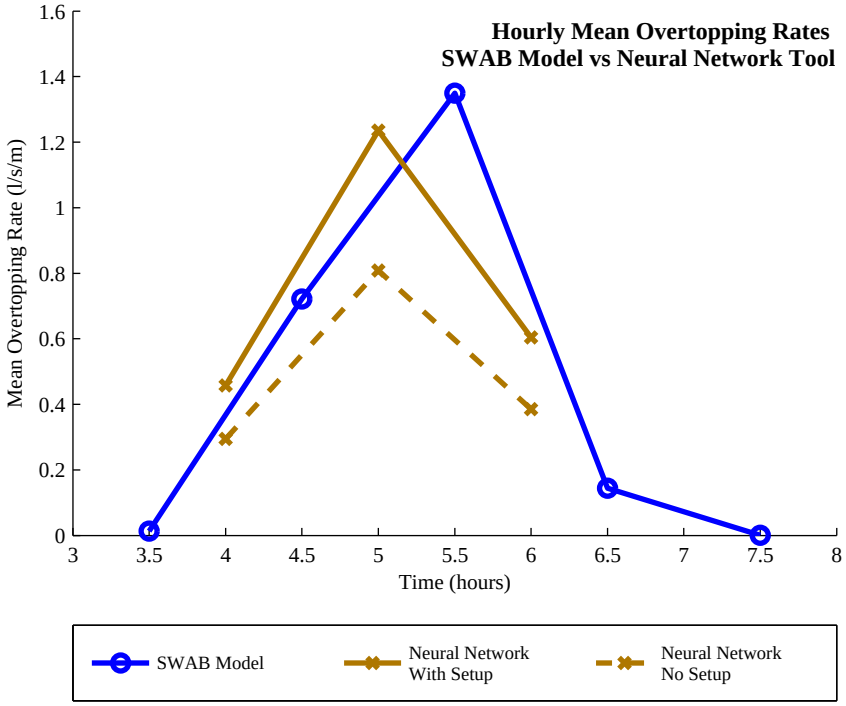

Figure 8.26: SWAB results and neural network results for hourly mean overtopping rates

level. However, at the location behind the Caravan Park, near the Hundred Drain (Figure 8.6) a maximum depth of 0.36 m resulted, which is significantly lower than the level described in the photograph.

In comparison with the neural network tool, recommended by the EurOtop Manual, the agreement is very good. Figure 8.26 shows the hourly mean overtopping rates. The neural network gave error messages for all but hours 4, 5 and 6, explaining that the freeboard was out of the range of validity for the other hours; it can be assumed that a zero value for overtopping is reasonable at these times. The inclusion of wave setup does make a significant contribution to the overtopping results. It will be shown in the next section that the neural network is rather more sensitive to changes in water level than the SWAB model, and the close agreement between the models may be quite fortuitous.

To conclude, it appears that the overtopping rates predicted by the SWAB model and the neural network are reasonable, though possibly a slight underestimation. There are many possible sources for difference between the simulation and the reported event. These include:

- Actual waves and water levels being slightly higher than those resulting from the CS3, POLCOMS-WAM and TOMAWAC models;
- Errors introduced by the SWAB model, possibly in the breaking parameters;
- Errors in the flood inundation modelling, which includes the assumption that overtop-

ping rates were uniform along the entire frontage, and assumptions in the modelling of pathways along which flood water could travel;

- The assumption that no water could enter (or leave) through the seawall into (or out from) the highway drains and the land drains;
- Exaggeration by local residents of the effects of the storm of 8th and 9th November 2007.

Despite this variety of possible error sources, the simulation of a storm event has proved to be an interesting exercise, with quite promising results. It shows the value of using this range of models on different scales to be able to predict and recreate real events.

8.4 Joint Probability Analysis

8.4.1 Methodology

The objective of this part of the investigation is to determine the return period of the event of November 2007, to use SWAB to calculate mean overtopping rates for a range of return periods, and to compare the SWAB overtopping rates with those calculated using the neural network. The joint probability analysis was carried out by Chini [2010], who performed multiple TOMAWAC simulations to calculate sets of wave height and water level combinations corresponding to a range of return periods. Wave periods were considered for inclusion in the joint probability analysis, but they were found to be dependent on wave height; therefore for each wave height, a corresponding wave period was given. Figure 8.27 shows the wave heights and water levels for various return periods, and the relationship between wave height and wave period. The conditions shown in the figure correspond to the location shown in Figure 8.10. Because, the neural network requires wave conditions at the toe of the structure, Chini [2010] used TOMAWAC to transform these offshore conditions to the seawall.

The SWAB model was run using a range of wave heights and water levels for which overtopping would occur (for example, there would be no point wasting computer time and disk space for the condition where $H_{m0} = 3.3$ m with a water level of -1.0 maOD). It was not necessary to use the exact wave heights and water levels of Figure 8.27, so long as the relationship between height and period remains. For each condition, three different randomly phased SWAB runs were set up; because wave periods and hence wave spectra varied between runs, the same sets of random phases were not used for different conditions (i.e. every single run had a different random set of phases). Each run consisted of 150 waves, using a JONSWAP spectrum with a peak enhancement factor of 3.3.

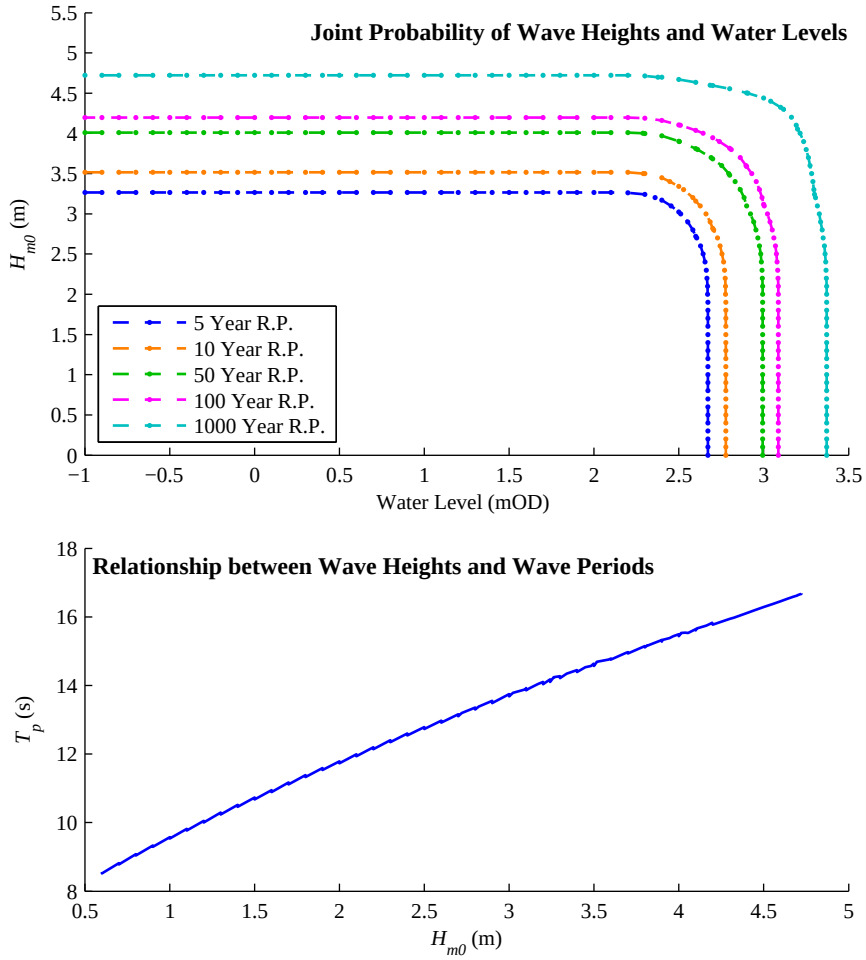

Figure 8.27: Joint probability analysis: wave heights, periods and water levels

8.4.2 Results of analysis

Figure 8.28 shows a colour plot for the mean overtopping rates from the three SWAB runs and Figure 8.29 shows the results from the neural network runs. It is apparent that at the peak of the 2007 storm, the water levels and wave conditions represented a 100 year return period, and the severity of the storm was due to the high water levels - the wave heights were unremarkable. By comparing Figure 8.28 with 8.29, some differences occur. The SWAB model gives greater overtopping rates for higher significant wave heights, whereas at low water levels the neural network gives very low overtopping rates even for larger waves. One can conclude that the SWAB model is more sensitive to wave height and the neural network is more sensitive to water level. Part of this difference may possibly be explained by the breaking criterion that was used here; in Section 7.2.1 it was shown that the double breaking algorithm may not be effective enough at depth-limiting the incident waves.

For the storm of 2007, it is coincidental that both methods gave quite similar results. The SWAB model would suggest that other 1 in 100 year events may give greater overtopping rates; because it is the *combination* of wave heights and water levels that cause overtopping, the model predicts that a 1 in 100 year event with higher waves and a lower maximum water level would give greater mean overtopping rates. In fact, the SWAB model predicts that a 1 in 10 year event, with a maximum water level of 2.6 mOD and wave height of 3.2 m, would give similar overtopping rates to the storm of 2007. It is noteworthy that the report from one resident that similar flooding occurs every 10 to 20 years at Walcott is corroborated by this analysis using the SWAB model. However, the neural network shows instead that the 2007 storm was in the most severe region for a 1 in 100 year event, and that similar overtopping rates would only occur approximately every 100 years.

Figure 8.28 does contain some apparently illogical results. For example, when the water level is 2.24 m and the wave height is increased from 3.25 m to 3.5 m, the mean overtopping rate is shown to decrease. This type of discrepancy can be explained by the fact that only 450 waves were run for each condition; the analysis of Section 8.2.2 (see Figure 8.19, for example) highlighted the random nature of the wave overtopping. This effect may be exaggerated when only a small proportion of waves would be expected to overtop the structure. To eliminate these illogical results, more waves would need to be run using the SWAB model.

There is also a difference between the overtopping rates corresponding to the 2007 storm shown in Figures 8.28 and 8.29, and the rates shown in Figure 8.26. At 5 hours, the neural network run of the previous analysis gave an overtopping rate of 1.2 l/s/m, whereas here a similar significant wave height and water level gives a rate of 2.0 l/s/m. Firstly, a JONSWAP

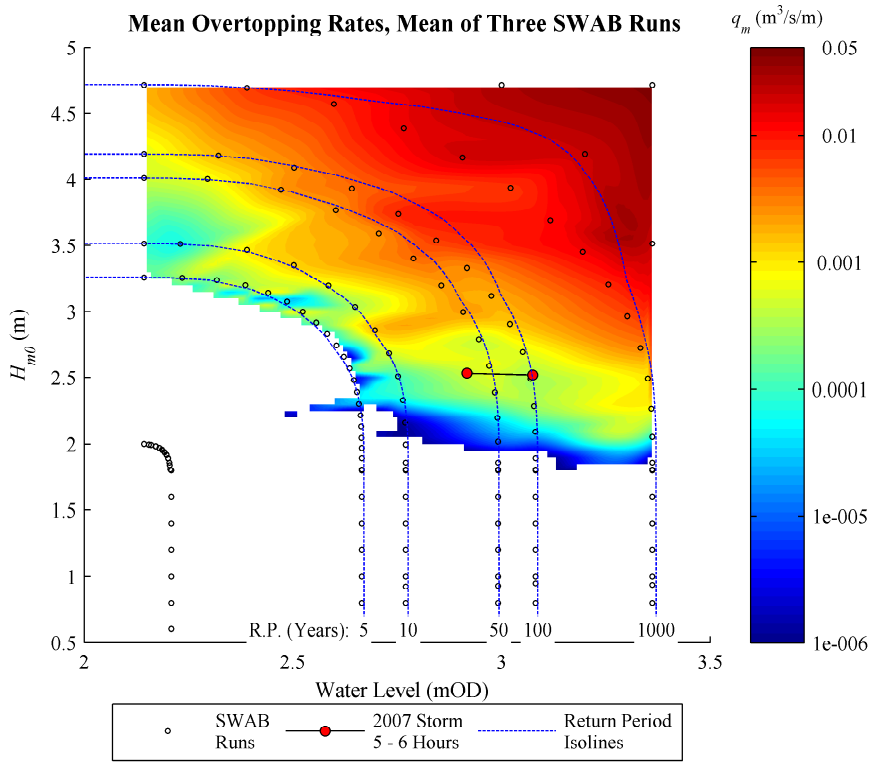

Figure 8.28: Mean overtopping rates as a function of H_{m0} and water level: SWAB runs

spectral shape was assumed in this analysis, with the relationship between H_{m0} and T_p being that shown in Figure 8.27; the previous analysis used the spectra of Figure 8.11. It has already been said that SWAB results vary significantly depending on the random phases used to calculate the incident waves. For the neural network runs, TOMAWAC was used to transform the offshore waves to the toe of the structure; in the previous section the full directional spectra were used in this transformation, but in this analysis the JONSWAP spectra were assumed to be normally incident. These small differences result in quite a large difference in overtopping rate. This also highlights how important the interpretation of the required parameters for the neural network becomes: a small variation in one of these parameters can significantly affect the overtopping rates. With the SWAB model, the sensitivity to changes in the incident parameters is also present, but they are not open to the same level of interpretation.

With sea-level rise, the return periods of events such as the one of 2007 will become more frequent, even without changes in the wave climate. Analysis of these effects are out of the scope of this thesis. Chini et al. [2010] and Chini and Stansby [2011] have examined the effect of climate change on Walcott and the Norfolk coast in more detail.

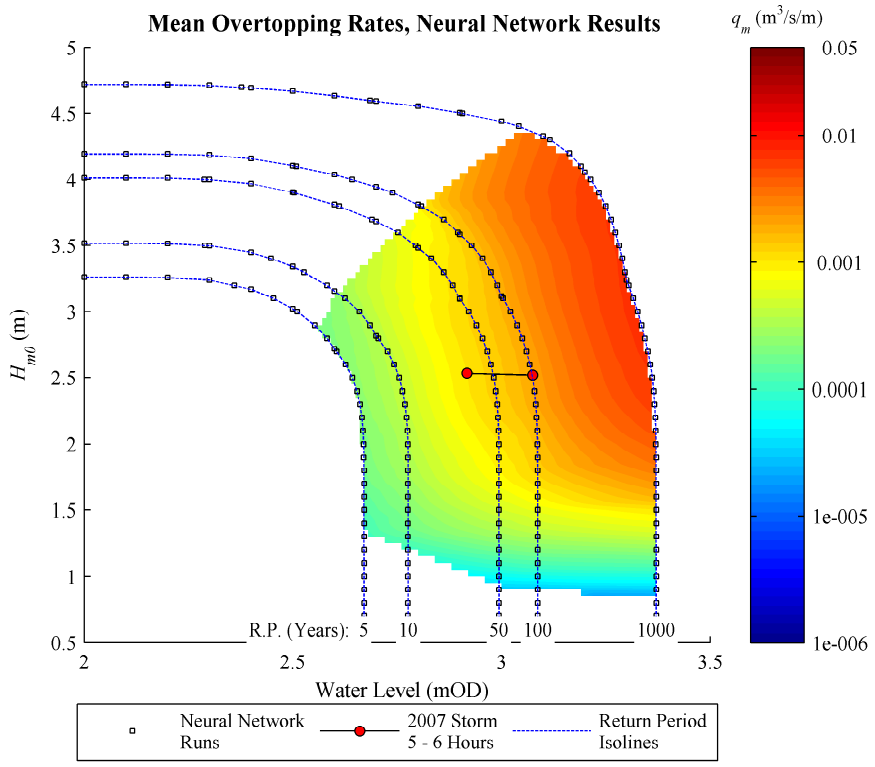

Figure 8.29: Mean overtopping rates as a function of H_{m0} and water level: Neural network runs

8.5 Conclusions

This study has proved to be a rather useful exercise in the prediction of wave overtopping, and shows how the SWAB model can be used as a tool for practical investigations. The main points from this case study are as follows:

- The SWAB model showed how beach levels can affect overtopping rates. For the seawall at Walcott, a lower beach level will probably lead to increased overtopping.
- The model runs using different randomly phased wave trains highlighted how variable overtopping rates can be. For this case, the variation between wave trains had a greater effect on overtopping rates than the beach level. These results are something that cannot be demonstrated so effectively with the empirical tools of the EurOtop Manual (although they do give probabilistic results). Repeats of the same conditions with different wave trains can be done using physical model tests, but at a much greater expense.
- Overtopping rates will vary along the Walcott seafront, but without any definite trend from one end to the other. Modelling in two horizontal dimensions would be of great use to investigate longshore effects.

- The SWAB model produced a simulation of the storm of the 8th and 9th November 2007. Overtopping rates from the SWAB model possibly gave a slight underestimate; the proportion of overtopping waves and the maximum flood levels appear to be less than those reported by the local residents. Results from the neural network tool, as recommended by the EurOtop Manual, are in close agreement with the SWAB results.

- The storm of the 8th and 9th of November was probably a 1 in 100 year event. However, a joint probability analysis using the SWAB model suggests that more frequently occurring conditions with lower water levels and higher waves may also give significant overtopping. The neural network is less sensitive to wave height and more sensitive to water level, and would not predict such large overtopping with a more frequent event. One of the residents suggested that similar overtopping rates occur every 10 to 20 years, which is supported by the SWAB model joint probability analysis.

Chapter 9

Nearshore Model Coupling

9.1 Introduction

In the previous chapters, the performance of a shallow water and Boussinesq-type model has been examined. However, some of the results highlighted the difficulites involved with the transitions between non-breaking and breaking waves. Also, the numerical solution of the Boussinesq terms in the equations is not straightforward, and with the wrong time-step can cause damping effects such as those presented in Section 3.8.1. Furthermore, an additional problem that has not yet been discussed is the extension of the modelling to two horizontal dimensions. The equations become more difficult, including $\frac{\partial^2}{\partial x \partial y}$ terms for which implicit finite volume solutions may not be possible.

Phase-averaged models such as Simulating WAves Nearshore (SWAN) [Booij et al., 1999] or TELEMAC-based Operational Model Addressing Wave Action Computation (TOMAWAC) [Benoit et al., 1996], which were discussed in Chapter 2, solve the energy-balance equation, calculating a range of effects on the directional wave energy spectrum. Good predictions of wave spectra result over wide areas of deep and shallow water with a relatively short computation time. However, these models do not give information on individual waves, they cannot consider shoreline effects such as runup and overtopping and can only represent reflection in a phase-decoupled sense. Phase-resolving models, such as shallow water or Boussinesq-type models are therefore needed to address these problems on a wave-by-wave basis. In this chapter, the wave spectrum from SWAN is taken at a position inshore of where waves have broken to input to a Non-Linear Shallow-Water (NLSW) equation solver, thereby bypassing the Boussinesq solver and its associated approximations for wave breaking. NLSW solvers are depth-averaged and assume hydrostatic pressure; they are non-dispersive and consequently generate steep wave fronts and are thus only suited to bore-like breaking waves.

Note, progress in including non-hydrostatic pressure has been made by Stelling and Zijlema [2003] but this is not considered here. Mass and momentum are conserved, while grossly simplifying the complex turbulent and mixing processes associated with wave breaking, e.g. Stansby and Feng [2005]. The same solver (the SWAB 3.0 model) is used here as was used in the preceeding chapters, without the Boussinesq solving routines. Although such coupling might seem a natural and convenient step, this approach appears not to have been tested previously. Here, one-dimensional (1D) modelling of waves propagating up a plane beach of moderate slope is compared with available experimental data for runup. Note, these results have also been published by McCabe et al. [2011].

9.2 Methodology

9.2.1 The SWAN and NLSW models

SWAN was discussed briefly in Section 2.2.3. It is a third-generation open source wave model which was developed for domains including shallow water. It is a phase-averaged model, implicitly solving the spectral action balance equation. The effects of generation, dissipation and nonlinear wave-wave interactions are all represented, and the phenomena of shoaling, refraction, setup, diffration, as well as simple wave reflections are all modelled. The shallow-water model used here is the same as the SWAB 3.0 model described in Chapter 3, incorporating equations (3.1) and (3.2), without the pre-breaking Boussinesq terms. A friction coefficient of $C_f = {}^{2\tau}/_{(\rho u|u|)} = 0.01$ was applied throughout. Waves are generated by the same method of Larsen and Dancy [1983], where the time variation of surface elevation is input at a point inside the domain, although for all cases the value of c_g used to calculate wave input will always be equal to $\sqrt{gh}$. As before, outward propagating waves are absorbed by a sponge layer and the landward propagating waves of interest interact with the beach. Because the waves should ideally be input at a location with a horizontal bed and the input location corresponds to a position on a slope, the horizontal bed for the incident wave was extended for five discrete spatial steps inshore of the input position in the model domain. A one-way coupling of the SWAN to the NLSW model was employed. The surface elevation time-series was created from the SWAN spectrum by simply adding sinusoids with amplitudes and frequencies defined by the spectra, each with a phase from a uniform random distribution. This is the principle of linear superposition and is clearly an approximation for nonlinear waves in the surf zone. In many cases there will be wave setup at the coupling location. SWAN includes wave setup in its output for mean water level; these values are used for the still water level in the NLSW model.

9.2.2 Comparisons with physical model tests

To validate the coupled models they were applied to experimental data from three laboratory test campaigns performed in wave flumes by Stive [1985], Ting [2001] and Mase [1989]. The first two were used to study wave transformation on plane slopes, whereas the third focuses on wave runup. Table 4.2 in Section 4.2 details the physical model test parameters, with d_1 denoting still water depth at the paddle and the deepwater wave length L_{0p}, associated with the peak wave period T_p, is used as a representative horizontal length scale. These model tests are described briefly in Section 4.2.

SWAN runs were set up, using the wave paddle positions from the physical model tests as wave input positions for the numerical tests. SWAN is able to calculate Pierson-Moscowicz and JONSWAP spectra, but the TMA spectrum used by Ting [2001] was calculated manually then read into SWAN. Each SWAN spectral output contained 200 frequency divisions. For each test a number of locations were selected in the nearshore for coupling SWAN to the NLSW model. Each NLSW run consisted of 200 waves. There may be some variation between NLSW runs with the same input conditions due to the random input phases. Therefore, three random seedings were used to calculate input phases for the comparisons with Stive [1985] and Ting [2001]. Because the investigation of wave runup is concerned with extreme values, results may be more sensitive to the random input phases; therefore ten random seedings were used for the comparisons with Mase [1989].

9.3 Results

9.3.1 Wave heights and setup

Figure 9.1 shows rms wave heights for each of the Stive [1985] tests. The SWAN model gives good predictions for all tests. It is apparent that the use of triad interactions makes little difference to wave heights in the surf zone. Because the wave energy associated with the triads is not randomly phased, triads were not employed for subsequent SWAN calculations.

With random waves there is no fixed 'break point'; therefore, four coupling points were selected starting from where the reduction in wave heights starts to become apparent. For the NLSW runs, three random seedings were tested from each coupling point. Figure 9.2 shows rms wave heights and Figure 9.3 shows wave setup for these coupled NLSW runs, for test ST3, in comparison to the experimental data and SWAN results. It is apparent that if the coupling location is too far offshore, wave energy is lost prematurely, although closer to the shore wave heights become similar to those predicted by SWAN. The coupling location appears to have

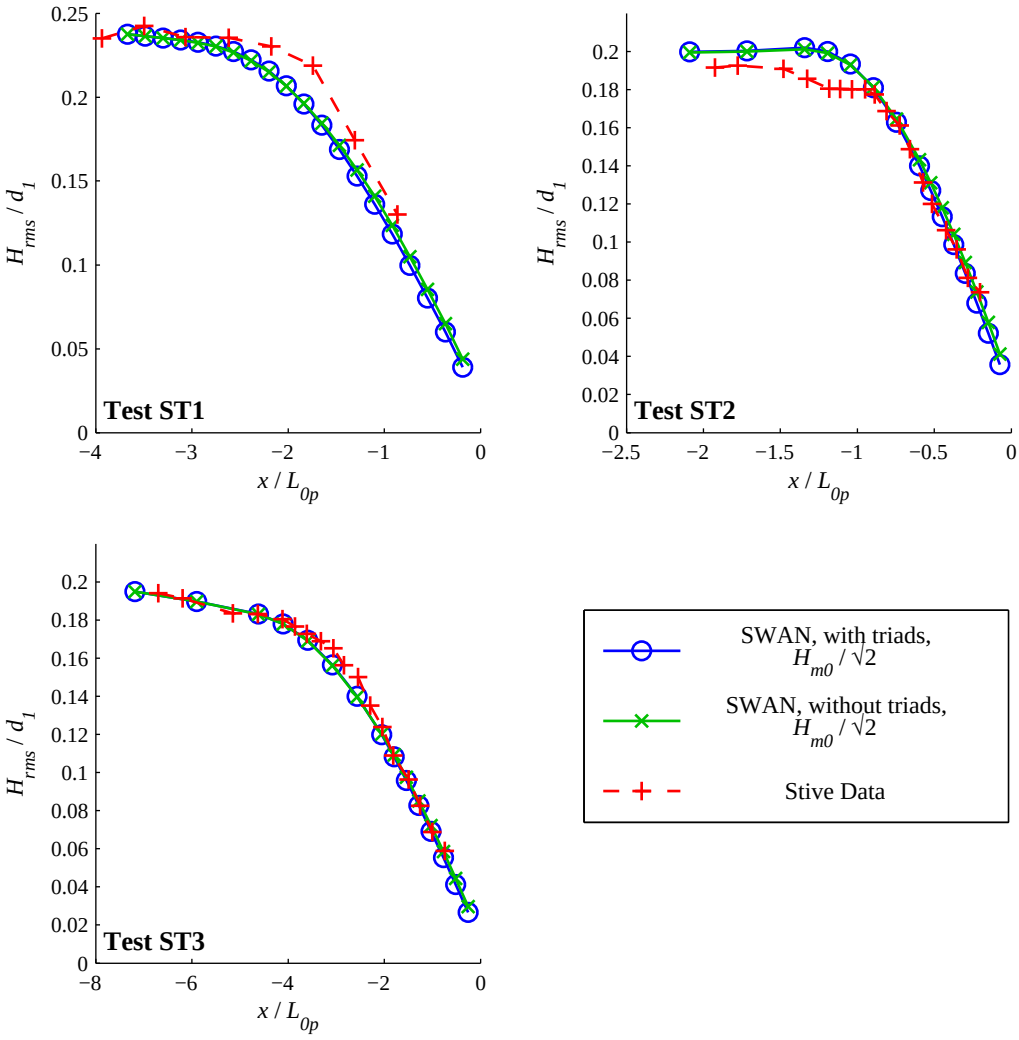

Figure 9.1: Rms wave heights for runs of Stive [1985], and SWAN simulations calculated using triads and without triads, for tests (a) ST1, (b) ST2 and (c) ST3. For SWAN and NLSW it was assumed that $H_{rms} = \sqrt{2} H_{m0}$.

little effect on rms wave heights and wave setup near the shore, with values closely matching those predicted by SWAN. Figure 9.3 shows that an instant set-down occurs at the coupling location as waves are input to the NLSW model. It is unclear why this happens; it may be that there are nonlinear effects that have not been considered when inputting waves into the NLSW model.

There appears to be little difference in wave heights or wave setup between random seedings. In Figure 9.3 (a), however, there are small differences in wave setup close to the shore; therefore, the effect of random seeding on wave runup statistics may be significant and will be investigated below. Ting [2001] provided results for proportions of breaking waves in the nearshore. Figure 9.4 compares the physical data with the SWAN output for proportions of breaking waves, which is based on the model of Battjes and Janssen [1978]. The SWAN model underestimates the proportion of breaking waves, with the inclusion of triad interactions increasing this underestimation. The Ting [2001] data show that most waves are breaking once H_s/d exceeds approximately 0.7, where d is the local water depth, showing the occurrence of wave height saturation to be about one wave length L_{0p} from the shoreline. For SWAN modelling with $H_s/d = 0.7$, however, the proportion of breaking waves is only 10 %, marking the onset of wave breaking.

Figure 9.5 shows similar results to Figure 9.2, with the NLSW coupled runs indicating good nearshore predictions for significant wave heights. Five starting points for the NLSW model runs were selected from about 1.3 deepwater wavelengths L_{0p} from the shore, to well inside the surf zone about $0.6L_{0p}$ offshore. For each coupling location, the NLSW model was run three times each with different randomly seeded phases; once again there was little difference in wave heights between random seedings. SWAN results without triads were used for the coupling. Again, the improvement is best using starting points closer to the shoreline. The predicted individual wave height distributions are shown in Figure 9.6 at three distances from the shore. Note that the use of triad interactions would have given erroneous results here because random phases were used to create the NLSW input waves; therefore, the spectral energy at twice the peak frequency would no longer be bound, giving inaccurate wave height distributions. Agreement is variable; the NLSW model gives too many smaller waves, especially $0.5L_{0p}$ from the shore. This is less apparent close to the shore, where the largest waves are quite well predicted. The disagreement may be due to the random phases imposed at input, following the practice for offshore waves, which may not be a good representation for waves which become more regular in shallow water. However improvement would ideally require experimental investigation.

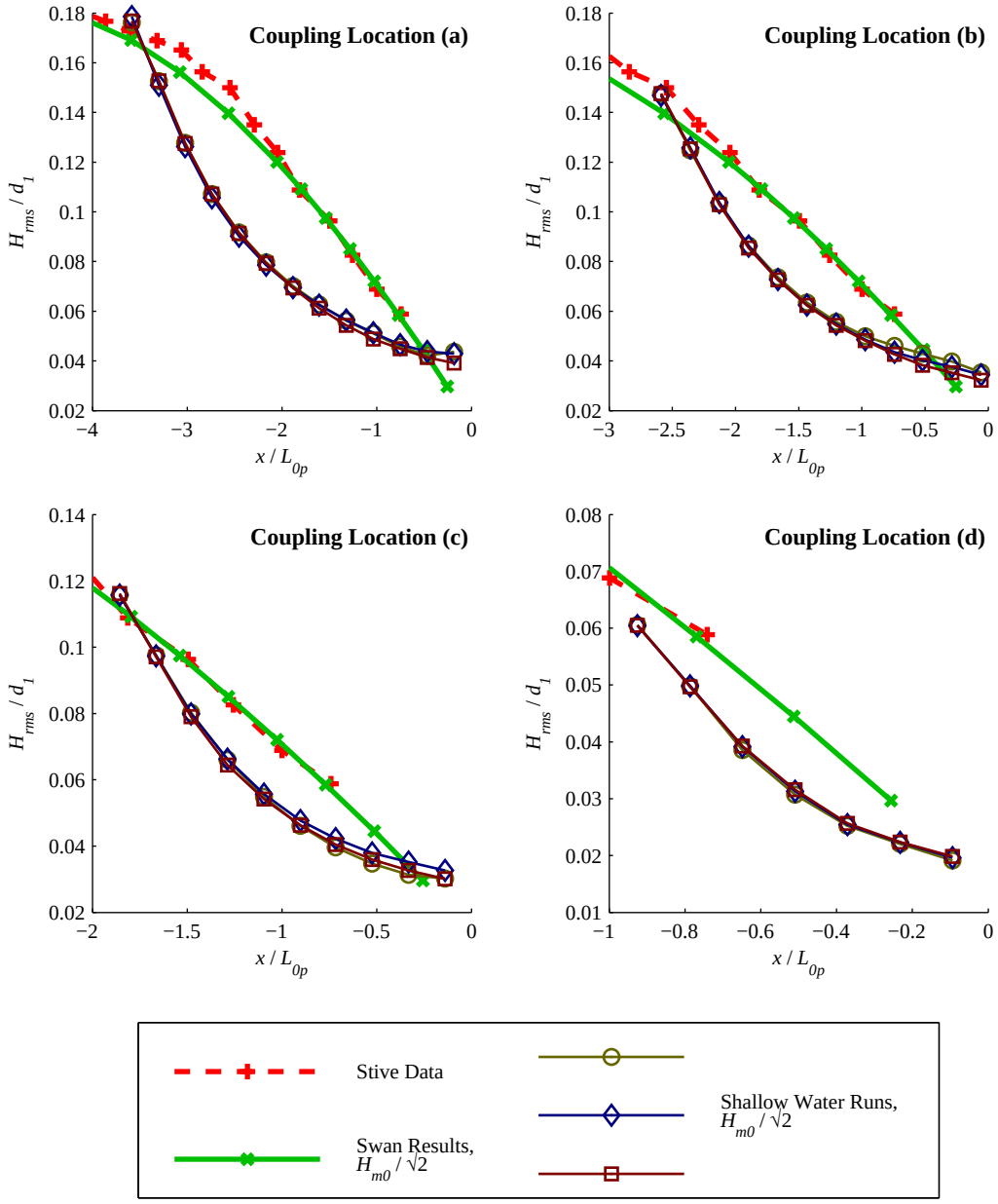

Figure 9.2: Wave heights in nearshore for ST3 tests, showing data of Stive [1985], SWAN results and three random phased coupled NLSW model runs, based on SWAN output at coupling locations where $(H_{m0}/d_{in};\, k_p d_{in})$ = (a) (0.479; 0.929), (b) (0.551; 0.682), (c) (0.607; 0.562), (d) (0.702; 0.373). For SWAN and NLSW it was assumed that $H_{rms} = \sqrt{2} H_{m0}$.

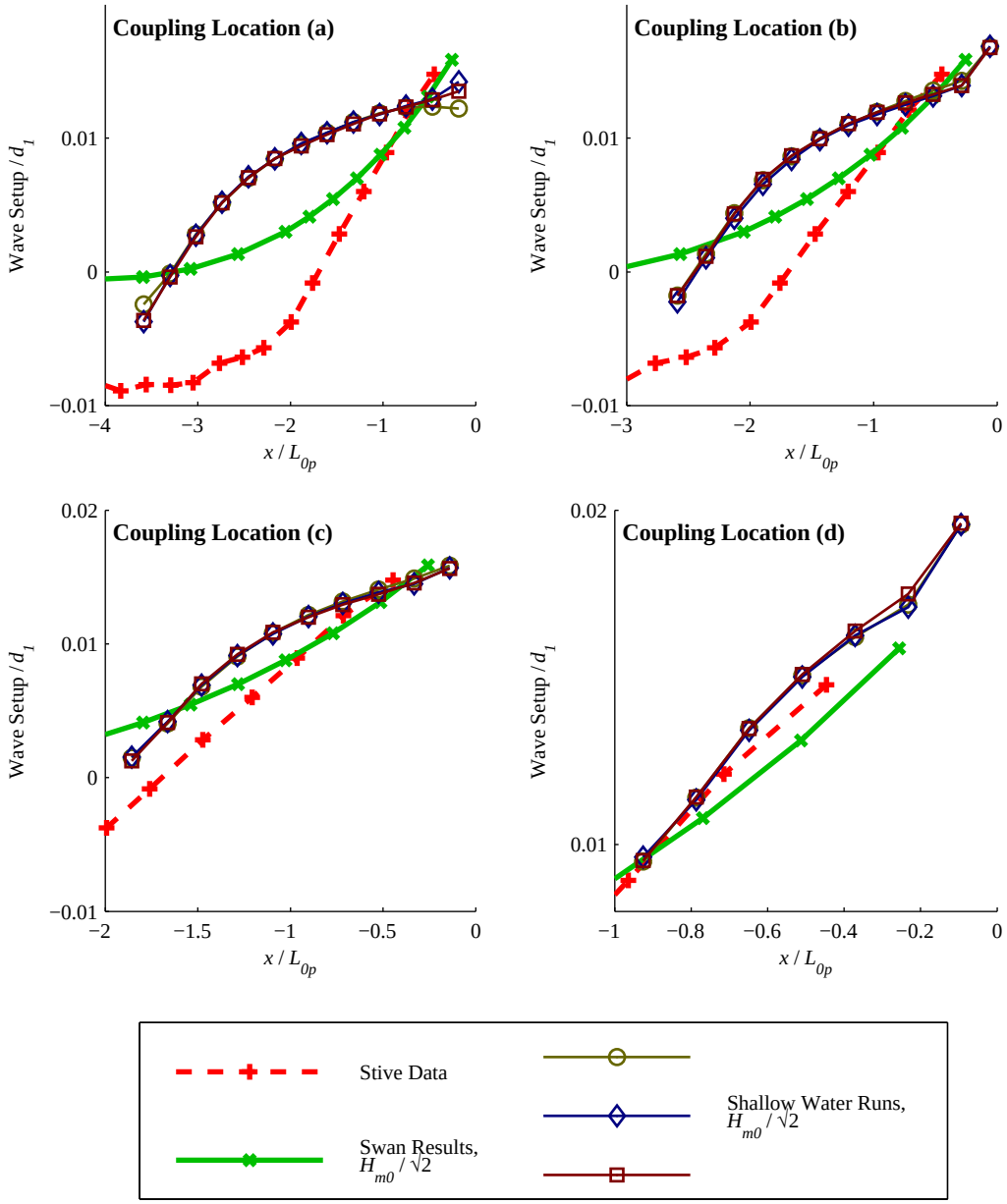

Figure 9.3: Nearshore wave setup for ST3 tests, showing data of Stive [1985], SWAN results and three random phased coupled NLSW model runs, based on SWAN output at same coupling locations shown in Figure 9.2.

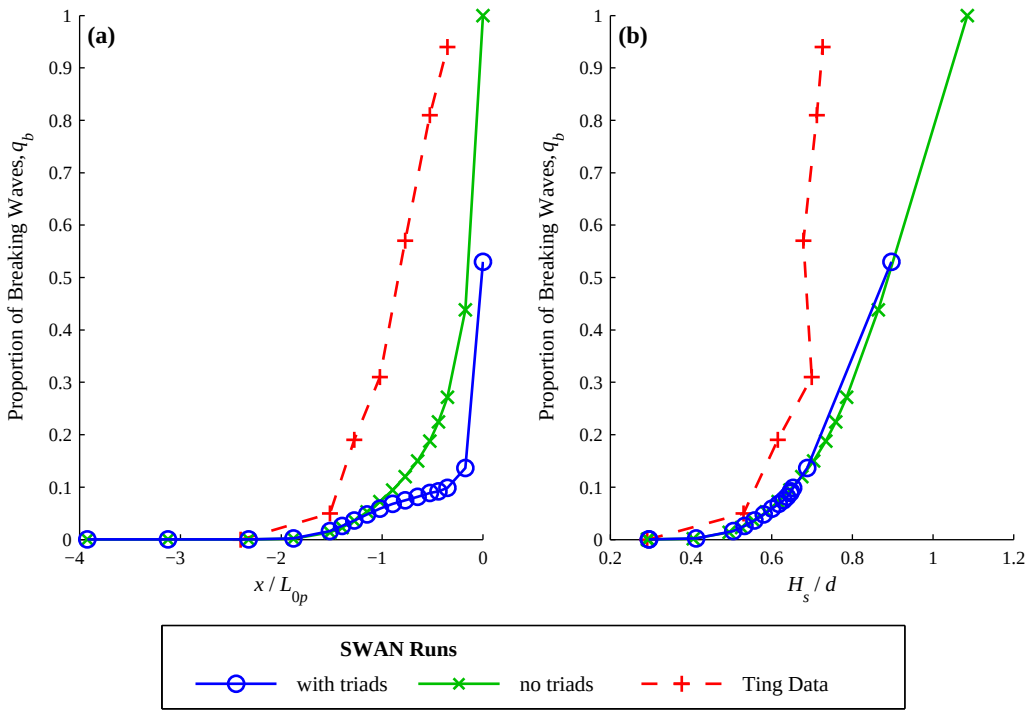

Figure 9.4: Proportions of breaking waves, q_b, for Test TI as a function of: (a) dimensionless distance from shore and, (b) wave height to depth ratio

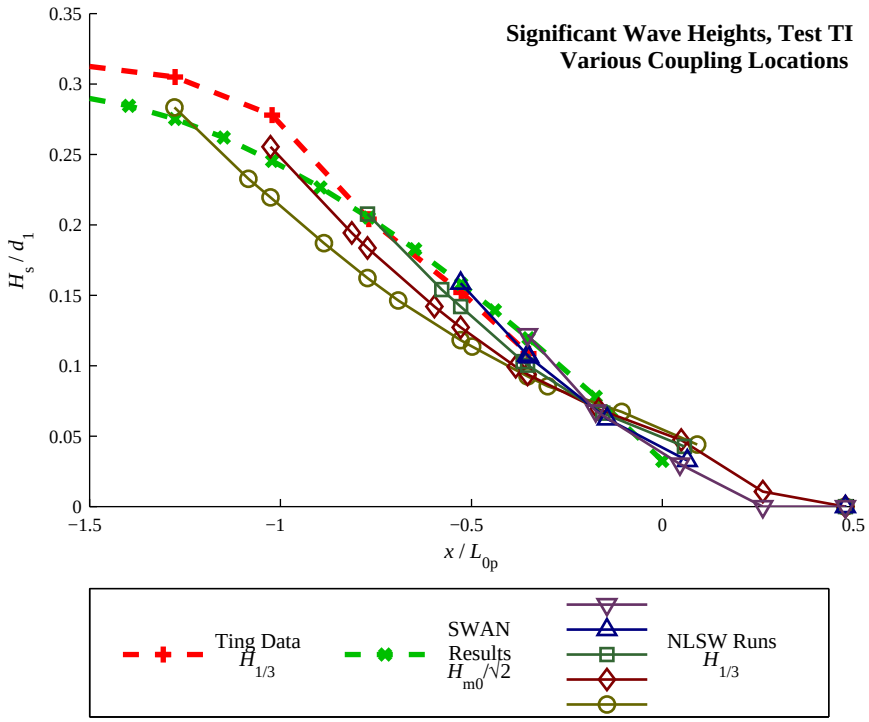

Figure 9.5: Significant wave heights nearshore for Test TI, with mean values for $H_{1/3}$ from three randomly phased NLSW runs, at coupling locations where $(H_{m0}/d_{in};\ k_p d_{in})$ = (–o–) (0.556; 0.498), (–◇–) (0.616; 0.443), (–□–) (0.675; 0.384), (–Δ–) (0.735; 0.321), (–∇–) (0.786; 0.268), compared with data of Ting [2001] and SWAN results for H_{m0}

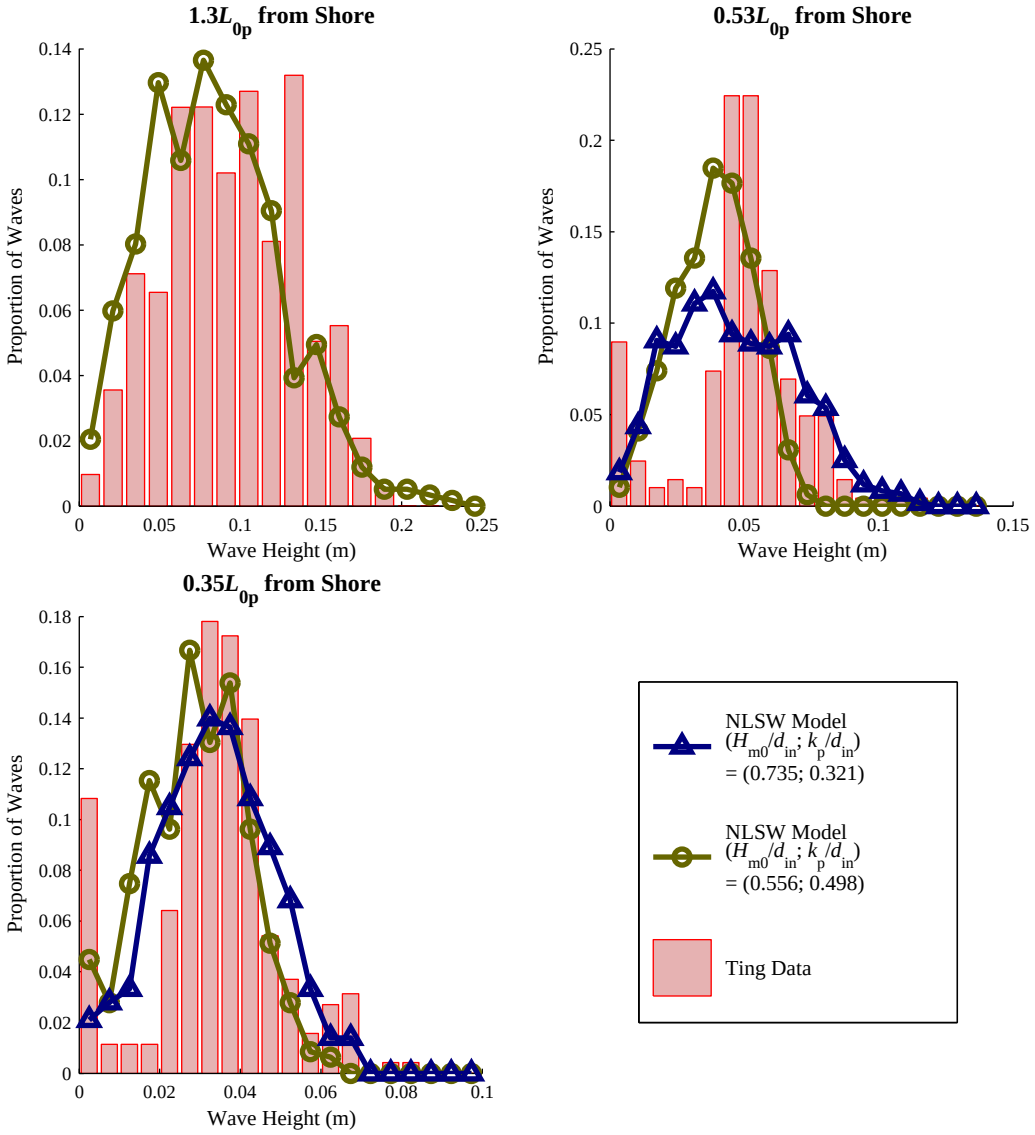

Figure 9.6: Wave height distributions for Test TI, showing data of Ting [2001] as grey bars, and mean of three randomly phased NLSW runs, at two coupling locations

9.3.2 Wave runup

Mase [1989] calculated runup data by separating time-series into runup crests and measuring their levels relative to the still-water-level. A similar methodology was used to calculate runup from the NLSW runs. Runup is a combination of low and high frequency shoreline movement and sometimes the NLSW model results had small high frequency 'wiggles'. Therefore the model time-series for swash levels were sampled at a time interval of $0.1T_p$, with all maxima greater than 0.003 m above adjacent minima being counted; reducing this to 0.001 m made little difference to the important 98th percentile runup parameter ($R_{2\%}$). For each of the tests of Mase [1989] - MA1, MA2, MA3 and MA4 - five or six coupling locations were tested with values of $k_p d_{in}$ in the range of 0.2 to 0.6 and H_{m0}/d_{in} in the range of 0.2 to 1.2, crossing the boundaries between intermediate and shallow water and breaking and non-breaking waves. Figure 9.7 shows the errors in the 98th percentile runup $R_{2\%}$ calculated for the coupled SWAN-NLSW runs, relative to the experimental data, as a function of the conditions at the coupling location. It is apparent that the dispersion parameter $k_p d_{in}$ is not as effective as the nonlinearity or breaking parameter H_{m0}/d_{in} in determining the optimal coupling location. Results from all four Mase [1989] test conditions are shown, and a value of $H_{m0}/d_{in} \approx 0.65$ appears to be best. According to the data of Ting [2001] in Figure 9.4, this corresponds to about 20 % of waves breaking.

Figure 9.8 shows values for runup statistics for tests MA1 to MA4. Runup statistics were presented for random waves, normalised with respect to deepwater wave height H_0 as a function of surf similarity parameter ξ_0. $R_{1/3}$ is the average of the highest third of runups, $R_{1/10}$ is the average of the highest tenth of runups and $R_{2\%}$ is the 98th percentile runup. For comparison with the physical model statistics the optimal coupling location of $H_{m0}/d_{in} \approx 0.65$ was used for the coupled NLSW results shown in Figure 9.8 (for MA1 $H_{m0}/d_{in} = 0.63$, for MA2 $H_{m0}/d_{in} = 0.64$, for MA3 $H_{m0}/d_{in} = 0.67$, for MA4 $H_{m0}/d_{in} = 0.66$). NLSW results in Figure 9.8 show maximum, minimum and mean values from the ten randomly phased runs for each test. As expected, there is some variation between random phases, with maximum $R_{2\%}$ values being 108 % to 112 % of the mean values, and minima being 84 % to 91 % of mean values. For the $R_{1/3}$ and $R_{1/10}$ statistics the variations are smaller. The mean values for $R_{2\%}$ are between 2 % and 8 % lower than the experimental data. Errors for $R_{1/3}$ and $R_{1/10}$ are larger, with the NLSW underestimating runup by up to 20 %. A different coupling location, possibly with higher values of H_{m0}/d_{in}, may give better results. These results also depend on the accuracy of the SWAN spectral modelling.

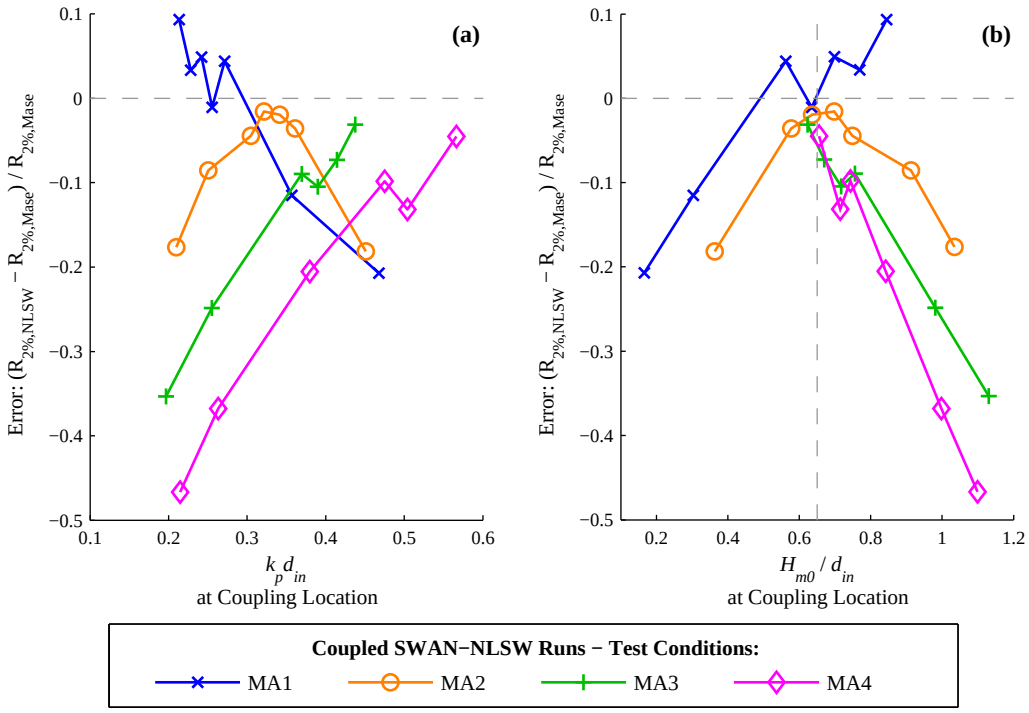

Figure 9.7: Error in runup for coupled NLSW runs, compared with Mase's [1989] experimental results, as a function of (a) $k_p d_{in}$ at coupling location, (b) H_{m0}/d_{in} at coupling location. Results are given for four wave conditions: MA1, MA2, MA3 and MA4. Errors shown are mean values of ten randomly phased runs

9.4 Conclusions

This investigation shows the potential of coupling a phased-averaged wave propagation model, in this case SWAN, directly to a NLSW model to predict the runup statistics due to random waves on a uniform slope. The surface elevation time-series for input to the NLSW model was approximated by the linear superposition of frequency components in the spectrum with random phase. Different random seedings have little effect on wave heights in the nearshore, but do cause variation in the 98th percentile runup statistics; this is consistent with the results from previous chapters. SWAN predicted significant wave height variation well but not the proportion of breaking waves. The runup $R_{1/10}$ and the 98th percentile were however predicted within 10 % for an input location with $H_{m0}/d_{in} = 0.65$, which corresponds to approximately 20 % of breaking waves in experiments and the onset of breaking according to SWAN modelling. The tests cover a range of relatively mild slopes, although real beaches generally have shallower slopes. For steeper slopes, reflection will be more significant and the approach limited since SWAN only approximates reflection. However this efficient approach is certainly effective for the test cases studied, which are representative of many real situations.

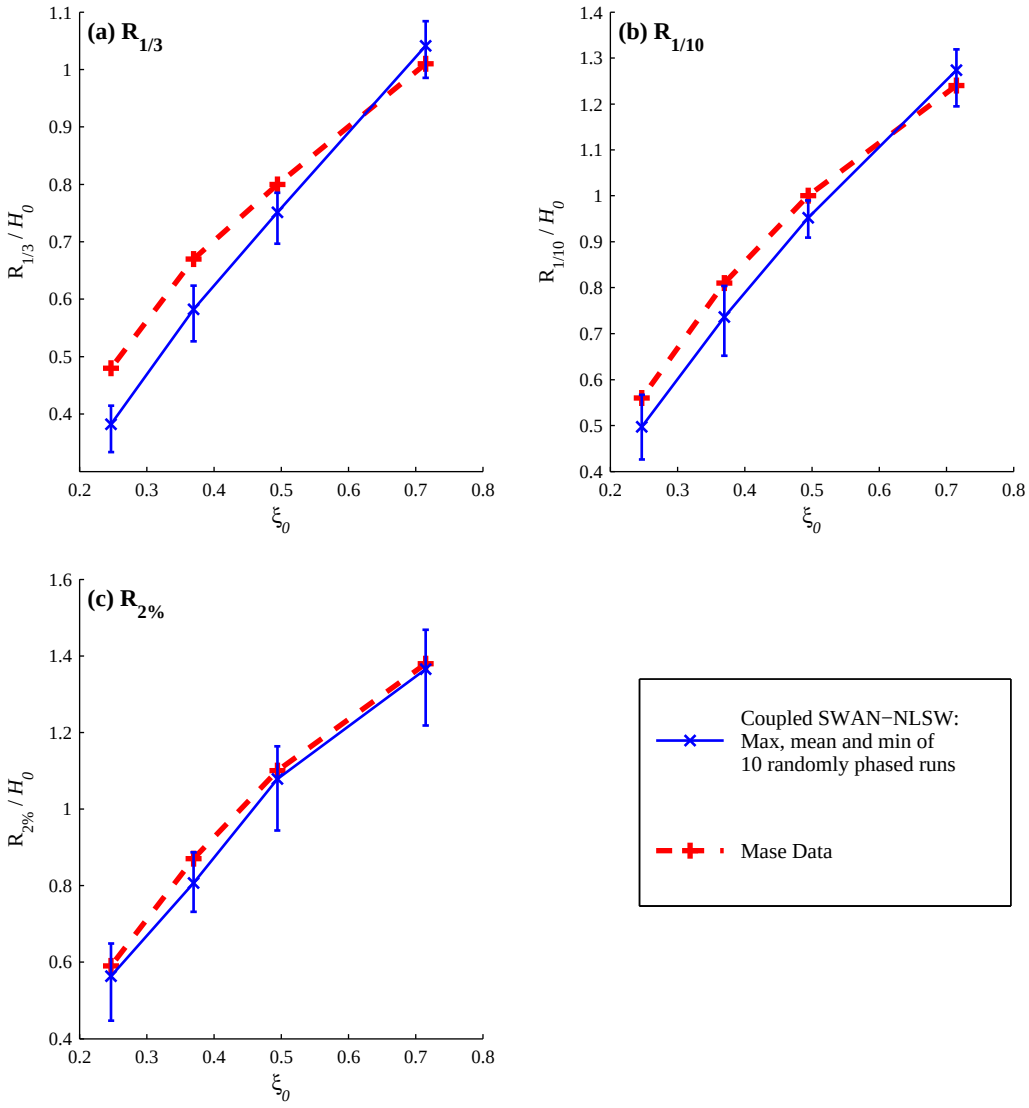

Figure 9.8: Wave runup statistics (a) $R_{1/3}$, (b) $R_{1/10}$ and (c) $R_{2\%}$ versus surf similarity parameter $\xi_0 = \tan\beta \left(H_0/L_{0p}\right)^{-1/2}$, where H_0 is deepwater significant wave height, and L_{0p} deepwater wavelength based on peak period

Chapter 10

Conclusions

10.1 Summary of this Research

The main aim of this research was to develop a tool to more reliably simulate wave overtopping on a wave-by-wave basis. Present options for calculating overtopping rates are either the use of physical model tests, or empirical tools such as those described in the EurOtop Manual [Pullen et al., 2007]. Physical model tests are expensive and time consuming; empirical tools may not be suited to all types of structure, may require input parameters that are ambiguous or difficult to calculate, and will give results that are limited in detail (never on a wave-by-wave basis). Some research on the use of nonlinear shallow water equations to model wave overtopping has been done (e.g. Dodd [1998], Shiach et al. [2004]) but such models are only suited to the propagation of breaking waves in shallow water. To be of practical use they require input from a spectral energy model, which can calculate the transformation of waves from deep water to the surf zone.

Various Boussinesq-type equations have been developed since the work of Peregrine [1967]. Originally derived for solitary waves, they have since been modified to become applicable to periodic waves in intermediate and, more recently, deep water. They are related to the nonlinear shallow water equations but contain extra terms to take account of the non-hydrostatic pressure and vertical accelerations that exist in such conditions. However, since Boussinesq-type equations contain third and higher order derivatives, it can be difficult to build a reliable numerical solver. Moreover, there is no intrinsic mechanism for the modelling of breaking waves; Boussinesq models therefore require some sort of extra algorithm to model breaking waves and a criterion to detect when breaking should start and stop.

The Shallow Water And Boussinesq (SWAB) model uses the equations of Madsen and Sorensen [1992], in one horizontal dimension, solving them using a semi-implicit finite vol-

ume method. These equations have been widely tested and give good linear dispersion characteristics for relative depth values, d/L, of up to 0.5, corresponding to the limit between transitional and deep water. For breaking waves, the Boussinesq terms are switched off (or phased out over a short distance) and the model becomes a nonlinear shallow water model, with the addition of horizontal diffusion terms (similar to those of Kennedy et al. [2000]) to simulate the energy losses that occur during the breaking process. Two main criteria to determine the onset of breaking were tested: breaking occurring when the rate of change of free surface level, $\partial\eta/\partial t$, exceeds a limiting value $C_{bt}\sqrt{gh}$; and a criterion calculated on a wave-by-wave basis, with breaking occurring when a wave height to water depth ratio, H/h, exceeds a value, C_{bh}. Throughout the investigation, comparisons have been made between these two breaking models. These breaking criteria are demonstrated in Figure 10.1a and 10.1b.

To incorporate waves overtopping a seawall, one must be able to model wet and dry areas of the domain. Many existing Boussinesq-type models either represent a sloping bed as a nearly impermeable structure, which is simple to implement but would be unsuitable for collecting water overtopping a seawall; or use the method of Lynett et al. [2002], where the depth and velocity variables are linearly extrapolated into the "dry" part of the domain, and would also be unsuitable for the modelling of waves overtopping a seawall. However, by using the nonlinear shallow water equations in the surf zone such an algorithm is unnecessary. The SWAB model represents the "dry" part of the domain by a very small depth of water, $h_{\min}$; this enables any number of shorelines to exist. In this "dry" part of the domain the pressure head and velocity is set to zero. However a "dry" cell will fill if it is adjacent to a "wet" cell and there is inward flux across the boundary. Many tests on runup and overtopping have been analysed throughout this investigation and the shoreline boundary works very well.

The transformation of offshore waves into runup and overtopping is a rather complex process even for waves propagating directly towards the shore. During these processes, transfers of energy take place to higher frequency harmonics as linear waves become more nonlinear, and also to lower frequency components as wave groups and the onset of breaking generate surf beat. The SWAB model must therefore give reasonably accurate predictions of these energy transfers over a wide range of conditions to be of any use for the simulation of wave runup and overtopping.

Initial testing of the SWAB model was carried out on a horizontal bed, investigating wave propagation over a range of wave conditions, different types of wave input, damping effects and nonlinear effects. For regular waves, the type of wave input is important: Airy waves worked well for Ursell numbers of less than 20; when $Ur > 20$ a stream function based wave input (based on the derivation of Rienecker and Fenton [1981]) was more suitable, except in

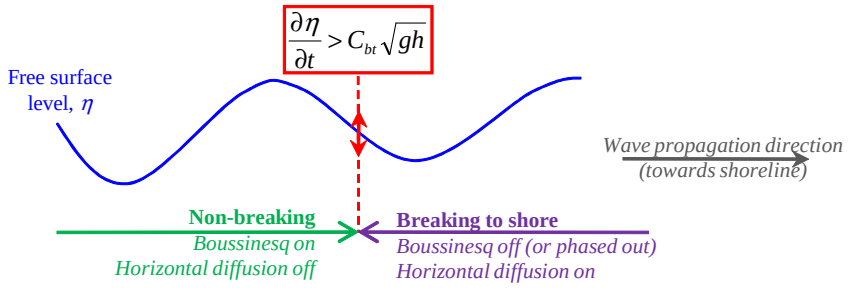

(a) $\partial\eta/\partial t$ breaking criterion

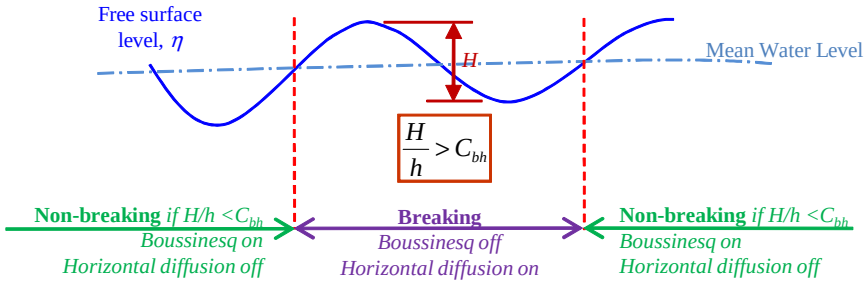

(b) H/h breaking criterion

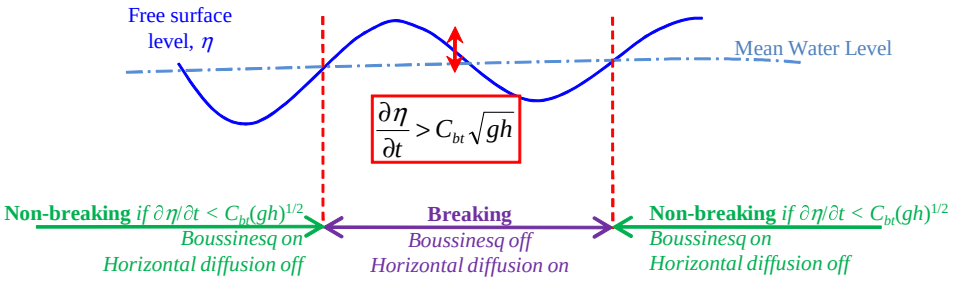

(c) Wave-by-wave $\partial\eta/\partial t$ breaking criterion

Figure 10.1: Main breaking criteria used by SWAB

deeper water (when $kd > 0.5$). Damping effects occur due to the calculation of the Boussinesq terms; this effect increases as kd increases, but also as the time-step dt/T is increased. When $dt/T = 1/500$ there is a 5 % loss of wave height over five wavelengths when kd exceeds 1; when $dt/T = 1/2500$ a similar damping occurs over five wavelengths when kd exceeds 2.5. Tests on random waves showed similar levels of damping; this will have a greater effect on higher frequency components. Also, nonlinear interactions were observed, with energy being transferred to higher harmonics when the wave height to depth ratio became large.

In comparison with the data from regular waves, the SWAB model was able to accurately calculate nearshore wave heights and wave setup, but this was found to be dependent on the breaking algorithm used. For the $\partial\eta/\partial t$ criterion, the value of the coefficient, C_{bt}, required to give accurate nearshore wave heights decreased as the surf similarity parameter, ξ_0 (where $\xi_0 = \tan\beta/\sqrt{H_0/L_0}$), was increased. For $\xi_0 \geq 0.38$ none of the tested values of C_{bt} were sufficient to give reasonable nearshore wave heights. This criterion was therefore unsuitable for plunging breakers. On the other hand, the wave height to depth ratio, calculated for each incoming wave, proved to be a more reliable breaking parameter and the optimal breaking coefficient, C_{bh}, did not vary with ξ_0; a value of $C_{bh} = 0.6$ appeared to work well for all SWAB tests on regular and random waves. For the random waves overtopping a seawall, an additional $\partial\eta/\partial t$ criterion was tested, but with the breaking process applied to the whole wave (in a similar way to the H/h criterion). This criterion is shown in Figure 10.1c and it gave much better results for nearshore wave heights and wave energy than the original $\partial\eta/\partial t$ criterion. For the larger values of surf similarity parameter, although the H/h method gave good wave heights for breaking waves, the breaking process is initiated too soon; therefore, the heights of waves near the break point were consistently too low. However, in general the H/h criterion is preferred, with $C_{bh} = 0.6$.

Because there is no fixed break point with the random wave tests, the errors with the H/h criterion and pre-breaking waves were no longer so apparent. As before, the $\partial\eta/\partial t$ criterion gave erroneous significant wave heights in the surf zone for higher surf similarity parameters. It should be noted that the commencement of breaking when $H/h > 0.6$ does not actually restrict wave heights to $0.6h$, although depth limitation does occur to a certain extent. SWAB model simulations of the experiments of Ting [2001] showed that the highest waves were actually overpredicted close to the shore for both breaking algorithms, with values of $H_{1/10}/h \approx 1.2$ being recorded, as opposed to the experimental value of $H_{1/10}/h \approx 1.0$; reducing the breaking coefficients, C_{bt} and C_{bh} improved the results somewhat.

The analysis of waves propagating over a submerged reef gave another interesting comparison between the breaking algorithms. The availability of time series data [Mase et al.,

2004, Mase, 2008] added to the usefulness of this exercise. With the original $\partial\eta/\partial t$ criterion (Figure 10.1a), the breaking process continues between the break point and the shore. Therefore additional SWAB model runs were set up, whereby breaking was forced to occur on the reef, forced to stop just landward of the reef, then the normal $\partial\eta/\partial t$ criterion applied as the waves moved towards the shore. An analysis of moving average values of η_{rms} was carried out; this is a measure of the changing level of wave energy at a particular location. From this, it was found that stopping breaking landward of the reef made little difference to waves as they approached the shore, although there was some improvement in the prediction of spectral energy around the peak frequency, f_p, of the nearshore waves.

For the H/h model, the breaking can automatically stop if h increases sufficiently; therefore such manual forcing of breaking conditions was not required. For both short ($\xi_0 = 0.25$) and long period waves ($\xi_0 = 0.52$), this breaking model gave near perfect values for η_{rms} close to the shore, and the spectral energy density was accurately modelled throughout the frequency spectrum. This included the low frequency part of the spectrum, where the "surf beat" makes an important contribution to runup levels. However, attempts to measure the shape of nonlinear waves and breaking waves through the use of skewness and "atiltness" parameters [Goda, 2000], showed much poorer comparisons with the experimental data.

Mase et al. [2004] recorded wave runup time series for the experiments with the submerged reef. Other runup parameters for waves propagating over a plain slope were available from Mase [1989]. Runup levels were affected by the SWAB breaking criteria in a similar way to the nearshore wave heights. When the surf similarity parameter was low (< 0.3), the $\partial\eta/\partial t$ criterion gave good results but as ξ_0 increased, the overestimation of runup levels increased. For the experiments with the submerged reef, the model runs where breaking was stopped landward of the reef, with the normal $\partial\eta/\partial t$ criterion applied near the shore, showed some increase in runup levels compared with those where breaking was not stopped; however this was an undesirable consequence when runup levels were already too high. The accuracy of runup levels using the H/h breaking model showed little dependence on ξ_0, though in general runup parameters were very slightly underestimated. It was found that there was some dependence on the friction factor; although changing C_f had negligible effect on nearshore waves, decreasing its value from 0.01 to 0.005 could increase the 98th percentile runup level, $R_{2\%}$ by 10 %. Lower runup levels were less affected by the friction coefficient.

One very important feature of the runup tests was the effect of the random wave train on runup levels. Changing the random phases associated with the wave input spectral components made very little difference to significant wave heights as they travelled towards the shore; however, differences can occur in the wave height distributions. The most commonly

used runup parameter, $R_{2\%}$, is concerned with the very highest runups; therefore quite large differences can occur from one randomly phased wave train to another. From three randomly phased SWAB runs of 200 waves each, $R_{2\%}$ levels varied by over 10 %. When overtopping is caused by only a small proportion of overtopping waves the difference between random wave trains will be even greater. In fact, in one case when exactly the same wave train was repeated in the wave flume, a reduction of 25 % in the mean overtopping rate occurred! It is true that with longer tests, these differences will be reduced (although too many waves would cease to correspond to a real storm event), but they are nevertheless important. This difference between wave trains is something that cannot be analysed using empirical models, which can at most give probabilistic analyses of events. Also, although physical model tests can be repeated with different wave trains, it requires a much greater time expense; certainly one could never repeat the number of model runs that have been done for this research.

The SWAB model's results for wave overtopping at Anchorsholme seawall were very encouraging, although the effect of the force imposed by the seawall was important. It is worth remembering that the equations used by SWAB were not derived for steep slopes. However, they do take account of the hydrostatic pressure gradient; therefore reflection will occur due to the pressure gradient associated with water running up a slope, but no reflection will be associated with a flow impacting against a steep wall. This is why an artificial wall force has been introduced. An empirical constant k_{wall} (see equation (3.19)) controls the force imposed on a flow directed into a wall; if $k_{wall} = 1$, that is equivalent to the horizontal flow being reduced to zero, if $k_{wall} = 2$, the horizontal flow is reversed.

Although this force made little difference to nearshore wave heights, its influence on controlling the flow of water over the crest of the seawall was large. Imposing this force at the steps situated on the seawall slope, as well as the recurve wall, led to underestimates in overtopping rates. Using a value for k_{wall} of 1.0 at the recurve wall and zero at the steps led to consistently accurate overtopping rates. It is true that observations of the overtopping flow in the wave flume showed that the recurve wall sent the incident flow in many directions: seaward, landward and vertically upward. From this it would seem that $k_{wall} = 1.0$ is a realistic value. Maybe in situations where a recurve wall cleanly directs the incident flow seaward a higher value of k_{wall} would be more appropriate. There do not appear to have been other attempts to model waves against a seawall in this way, and more calibration would be useful.

As it has already been stated, the overtopping rates calculated by the SWAB model were very encouraging; for the three tests examined in detail, mean overtopping rates were nearly identical to those recorded in the laboratory. For the fourteen tests that were carried out in the wave flume, all but three SWAB runs gave mean overtopping rates that were within a

factor of two of the experimental results; two of these three runs were for tests with very low mean rates. It is interesting to note that SWAB tended to overestimate overtopping rates for these tests, whereas for the runup experiments it tended to underestimate levels (when the H/h breaking was used); however it should again be stressed that these results were dependent on the force applied at the seawall. The comparison with the limited available field data was very promising; both the SWAB model and the physical model tests gave mean rates very close to those recorded in the field for the same wave conditions. It should again be mentioned that large differences occurred between random wave trains.

The SWAB model analysis of overtopping from the November 2007 storm at Walcott appeared to confirm the remarks made above: time series of overtopping rates were calculated using SWAB, and through the flood inundation analysis by other researchers were shown to be realistic in comparison to the reports of residents. As well as directly modelling overtopping rates, SWAB was used as a tool for analysis of other aspects of flooding at Walcott. Beach levels were found to have some effect on overtopping rates, though not as much as the effect of different randomly phased wave trains. Also, SWAB was used to estimate overtopping rates for various events as part of a joint probability analysis. Results from the analysis were in agreement with reports that flooding events occur at Walcott every ten to twenty years.

Some comparison was made with the empirical modelling tools associated with the EurOtop manual [Pullen et al., 2007]. The PC-Overtopping tool was used to estimate overtopping rates at Anchorsholme seawall, but consistently gave overestimates. The neural network tool was used for the Walcott analysis. For the modelling of the 2007 storm at Walcott, its results agreed very well with SWAB, but it was found to be much more sensitive to changes in water level (and less sensitive to changes in wave height) than the SWAB model. These empirical tools are generally much more difficult to use than the SWAB model, and there is much more of a "black box" aspect to their operation.

An alternative approach to Boussinesq modelling is by coupling a spectral energy model to a nonlinear shallow water solver. It has already been stated that nonlinear shallow water models have been used previously to calculate wave overtopping. Because they can only be used in shallow water it tends to remain unmentioned that some coupling must be required to be able to use them as a practical tool; however there appears to be no previous published research on where this coupling should take place. The results shown here (also published by McCabe et al. [2011]) suggest that the optimal coupling location is determined by the wave height to depth ratio, with best results for wave runup parameters when the coupling location is at $H_{m0}/d = 0.65$, where d is the still water depth at the coupling location. Notice the similarity beween this and the $H/h > 0.60$ breaking criterion that has been used throughout the SWAB

testing. This coupled spectral energy / nonlinear shallow water method gives good results close to the shore, and because there are no Boussinesq terms it is more easily upgraded to two horizontal dimensions. However, it would be difficult to apply to submerged reefs for example, and has not yet been tested for wave overtopping.

To conclude, this substantial range of tests has shown that the SWAB model is a potentially valuable tool for the analysis of wave overtopping, and more flexible, powerful and easier to use than existing empirical tools. It seems that no other Boussinesq-type solver has yet been used to model wave overtopping, with such a wide range of testing to support its reliability.

10.2 Future Work

Despite (or because of) the promising results from the SWAB model, there are a number of areas that require further research. These are summarised below:

- All the modelling that has been described here is in one horizontal dimension. Depending on the situation, two dimensional effects can be very important. The main problem with extending the SWAB model to two dimensions is with the fully implicit solution of the Boussinesq terms. For the two dimensional case there are some $\partial^2/\partial x \partial y$ terms that, according to Stansby [2011, personal communication], make this type of solution very difficult. On the other hand, the nonlinear shallow water solver used in Chapter 9 already exists in a two dimensional form; possibly the coupled spectral energy to shallow water method is a more practical way to extend to two dimensions.

- It was clear that the H/h breaking model (Figure 10.1b) performed better than the original $\partial\eta/\partial t$ criterion (Figure 10.1a). However, the SWAB model testing of Anchorsholme seawall also applied the $\partial\eta/\partial t$ criterion on a wave-by-wave basis (Figure 10.1c), and it appeared to perform reasonably well. Further testing of this breaking method, over a greater range of conditions (including plunging breakers) may be useful.

- There was a tendency for the SWAB model to underestimate runup levels (with the H/h breaking algorithm), but for the Anchorsholme tests overtopping rates were slightly overestimated. It could be that different friction factors were required. However, one major area that could contribute is the wall force algorithm. Further calibration is needed on this artificial method to reflect flow at a seawall. Overtopping time-series data with different shapes of seawall would be invaluable for this research.

- It is not yet clear exactly where the SWAB model is unsuitable, apart from depths of $kd > 3$ where it should not be used. Random wave tests have included surf similarity

parameters of up to 0.715, which does not include surging waves. Also, it has already been stated that testing on different shapes of seawall would be helpful; it is not clear whether there is a limit on how much vertical or near-vertical seawall can be accurately modelled using SWAB.

- It has been stressed that different randomly phased wave trains can greatly affect runup levels and especially overtopping rates. It would be of interest to carry out some statistical analysis of the variance in overtopping rates as a function of the number of incident waves, to give guidance on how many different model runs should be tested.

- At present, overtopping waves in the SWAB model fall into a collection tank. This tank takes up part of the model domain and hence adds to the calculation time. Overtopping volumes are calculated from the flux passing over the seawall crest, so this tank is not really needed. A reliable outflow boundary condition would therefore improve the performance of the model.

- A sediment transport routine has been written for the SWAB model, but it has not been tested here. Physical model tests that include sediment transport are problematic, due to incorrect Reynolds scaling. Including sediment transport could be useful when investigating the runup and overtopping of sand dunes or shingle barriers. One could also investigate how beach levels change during storm events, which is something that is rather difficult to measure in the field. Additionally, the model could be extended to research breach initiation and breach growth.

- The aim of this research is to develop the SWAB model as a practical tool. At present its operation requires the generation of several text files for the input parameters and some important parameters can only be set in the code itself. Current work on the SWAB model includes the development of a front end for the code; a possible solution is to build a spreadsheet-based input program for setting up multiple SWAB runs. This would make the SWAB model considerably easier to use.

- Alongside the development of the front end, a manual will be written to describe how to use the SWAB model. The SWAB model is not to be used alone. Therefore, advice will be included on how it should be used alongside offshore spectral energy and surge models, and how SWAB should be set up to provide input data for flood inundation models.

There are many possible routes for further research, either in developing the model or by using it as a research tool. It is hoped that the SWAB model and the knowledge gained from this research project will be of some benefit to coastal engineers and researchers.

List of References

M.B. Abbott, H.M. Petersen, and O. Skovgaard. On the numerical modelling of short waves in shallow water. *Journal of Hydraulic Research*, 16(3):173–204, 1978.

Y. Agnon, P.A. Madsen, and H.A. Schäffer. A new approach to high-order Boussinesq models. *Journal of Fluid Mechanics*, 399:319–333, 1999.

J.M. Alsina and T.E. Baldock. Improved representation of breaking wave energy dissipation in parametric wave transformation models. *Coastal Engineering*, 54:765–769, 2007.

T.E. Baldock, C. Swan, and P.H. Taylor. A laboratory study of nonlinear surface waves on water. *Philisophical Transactions of the Royal Society of London*, A354(1707):649–676, 1996.

T.E. Baldock, P. Holmes, S. Bunker, and P. Van Weert. Cross-shore hydrodynamics within an unsaturated surf zone. *Coastal Engineering*, 34:173–196, 1998.

T.E. Baldock, D.A. Huntley, P.A.D. Bird, T. O'Hare, and G.N. Bullock. Breakpoint generated surf beat induced by bichromatic wave groups. *Coastal Engineering*, 39:213–242, 2000.

J.A. Battjes. *Computation of set-up, longshore currents, run-up and overtopping due to wind-generated waves*. Phd thesis, Delft University of Technology, 1974.

J.A. Battjes. Surf zone dynamics. *Annual Review of Fluid Mechanics*, 20:257–293, 1988.

J.A. Battjes. Shallow water wave modelling. In *Proceedings of the International Symposium: Waves - Physical and Numerical Modelling*, volume 1, 1994.

J.A. Battjes and J.P.F.M. Janssen. Energy loss and set-up due to breaking of random waves. In *Proceedings of 16th International Conference on Coastal Engineering*, pages 569–587, 1978.

J.A. Battjes and M.J.F. Stive. Calibration and verification of a dissipation model for random breaking waves. *Journal of Geophysical Research*, 90, C5:9159–9167, 1985.

J.A. Battjes, H.J. Bakkenes, T.T. Janssen, and A.R. van Dongeren. Shoaling of subharmonic gravity waves. *Journal of Geophysical Research*, 109(C02009):1–15, 2004.

S. Beji and J.A. Battjes. Experimental investigation of wave propagation over a bar. *Coastal Engineering*, 19:151–162, 1993.

M. Benoit, F. Marcos, and F. Becq. Development of a third generation shallow-water wave model with unstructured spatial meshing. In *Proceedings of 25th International Conference on Coastal Engineering*, pages 465–478, 1996.

P. Besley. Wave overtopping of seawalls. Design and assessment manual. Technical report, HR Wallingford, Report W178, 1999.

F. Bocquet, J. Flowerdew, P. Hawkes, P. Pullen, and N. Tozer. Probabilistic coastal flood forecasting: Forecast demonstration and evaluation. Technical report, Environment Agency, Science Project SC050069/SR2, 2009.

N. Booij, R.C. Ris, and L.H. Holthuijsen. A third-generation wave model for coastal regions. 1. Model description and validation. *Journal of Geophysical Research*, 104(C4):7649–7666, 1999.

A.G.L. Borthwick, M. Ford, B.P. Weston, P.H. Taylor, and P.K. Stansby. Solitary wave transformation, breaking and run-up at a beach. *Proceedings of the Institution of Civil Engineers: Maritime Engineering*, MA3:97–105, 2006.

M.J. Boussinesq. Théorie des ondes et des remous qui se propagent le long d'un canal rectangulaire horizontal, en communiquant au liquide contenu dans ce canal des vitesses sensiblement pareilles de la surface au fond. *Journal de Mathématiques Pures et Appliquées, Deuxième Série*, 17:55–108, 1872.

E. Bouws, H. Günther, W. Rosenthal, and C.L. Vincent. Similarity of the wind wave spectrum in finite depth water: 1. Spectral form. *Journal of Geophysical Research*, 90(C1):975–986, 1985.

E. Bouws, H. Günther, W. Rosenthal, and C.L. Vincent. Similarity of the wind wave spectrum in finite depth water. Part 2: Statistical relations between shape and growth stage parameters. *Deutsche hydrographische Zeitschrift*, 40(1):1–24, 1987.

A.J. Bowen, D.L. Inman, and V.P. Simmons. Wave set-down and set-up. *Journal of Geophysical Research*, 73(8):2569–2577, 1968.

C.L. Bretschneider. Wave variability and wave spectra for wind-generated gravity waves. Technical report, Beach Erosion Board Corps of Engineers Technical Memorandum 118, 1959.

R.K. Bullough and P.J. Caudrey. Solitons and the Korteweg-de Vries equation: Integrable systems in 1834-1995. *Acta Applicandae Mathematicae*, 39:193–228, 1995.

G.F. Carrier and H.P. Greenspan. Water waves of finite amplitude on a sloping beach. *Journal of Fluid Mechanics*, 4(1):97–109, 1958.

D.E. Cartwright and M.S. Longuet-Higgins. The statistical distribution of the maxima of a random function. *Proceedings of the Royal Society of London. Series A, Mathematical and Physical Sciences*, 237(1209):212–232, 1956.

M.J. Cassidy, R.E. Taylor, and G.T. Houlsby. Analysis of jack-up units using a Constrained NewWave methodology. *Applied Ocean Research*, 23:221–234, 2001.

N. Chini. Personal Communication, 2010.

N. Chini. Personal Communication, 2011.

N. Chini and P.K. Stansby. Coastal inundation at Walcott using TELEMAC system, 2011. http://www.ciria.com/landform/pdf/Peter Stansby_Nicholas Chini.pdf.

N. Chini, P. Stansby, J. Leake, J. Wolf, J. Roberts-Jones, and J. Lowe. The impact of sea level rise and climate change on inshore wave climate: A case study for East Anglia (UK). *Coastal Engineering*, 57:973–984, 2010.

E.M. Coeveld, M.R.A. van Gent, and B. Pozueta. *Neural Network: Manual NN_OVERTOPPING 2*, 2005.

A.D.D. Craik. The origins of water wave theory. *Annual Review of Fluid Mechanics*, 36:1–28, 2004.

F. D'Alessandro and G.R. Tomasicchio. The BCI criterion for the initiation of breaking process in Boussinesq-type equations. *Coastal Engineering*, 55:1174–1184, 2008.

R.G. Dean. Evaluation and development of water wave theories for engineering application. Technical report, 1974.

R.G. Dean and R.A. Dalrymple. *Water Wave Mechanics for Scientists and Engineers*, volume 2 of *Advanced Series on Ocean Engineering*. World Scientific Publishing, 1991.

M.W. Dingemans. *Water Wave Propagation over Uneven Bottoms*, volume 13 of *Advanced Series on Ocean Engineering*. World Scientific Publishing, 1997.

N. Dodd. Numerical model of wave run-up, overtopping and regeneration. *ASCE Journal of Waterway, Port, Coastal and Ocean Engineering*, 124(2):73–81, 1998.

Y. Eldeberky and J.A. Battjes. Spectral modeling of wave breaking: Application to Boussinesq equations. *Journal of Geophysical Research*, 101(C1):1253–1264, 1995.

Flood Risk Management Research Consortium. FRMRC Website, 2008. http://www.floodrisk.org.uk.

P. Frigaard and M. Brorsen. A time-domain method for separation incident and reflected irregular waves. *Coastal Engineering*, 24:205–215, 1995.

H.M. Fritz, C. Blount, R. Sokoloski, J. Singleton, A. Fuggle, B.G. McAdoo, A. Moore, C. Grass, and B. Tate. Hurricane Katrina storm surge distribution and field observations on the Mississippi Barrier Islands. *Estuarine, Coastal and Shelf Science*, 74:12–20, 2007.

C.J. Galvin. Breaker type classification on three laboratory beaches. *Journal of Geophysical Research*, 73(12):3651–3659, 1968.

M.F. Gobbi, J.T. Kirby, and G. Wei. A fully nonlinear Boussinesq model for surface waves. Part 2: Extension to O(kh)4. *Journal of Fluid Mechanics*, 405:181–210, 2000.

Y. Goda. *Random Seas and Design of Maritime Structures*, volume 15 of *Advanced Series on Ocean Engineering*. World Scientific Publishing, second edition, 2000.

The WAMDI Group. The WAM Model - A third generation ocean wave prediction model. *Journal of Physical Oceanography*, 18:1775–1810, 1988.

R.T. Guza and E.B. Thornton. Swash oscillations on a natural beach. *Journal of Geophysical Research*, 87(C1):483–491, 1982.

J.W. Hall, P.B. Sayers, M.J.A. Walkden, and M. Panzeri. Impacts of climate change on coastal flood risk in England and Wales: 2030 - 2100. *Philosophical Transactions of the Royal Society of London*, A364:1027–1049, 2006.

J.B. Hansen and I.A. Svendsen. Regular waves in shoaling water, experimental data. Technical report, Institute of Hydrodynamics and Hydraulic Engineering, Technical University of Denmark, ISVA Series Paper 21, 1979.

K. Hasselmann, T.P. Barnett, E. Bouws, H. Carlson, D.E. Cartwright, K. Enke, J.A. Ewing, H. Gienapp, D.E. Hasselmann, P. Kruseman, A. Meerburg, P. Mller, D.J. Olbers, K. Richter, W. Sell, and H. Walden. Measurements of wind-wave growth and swell decay during the joint north sea wave project (jonswap). *Ergnzungsheft zur Deutschen Hydrographischen Zeitschrift Reihe*, A(8):95, 1973.

P.J. Hawkes, C. Bagenholm, B.P. Gouldby, and J. Ewing. Swell and bi-modal wave climate around the coast of England and Wales. Technical report, HR Wallingford Report SR 409, 1997.

T.S. Hedges. Regions of validity of analytical wave theories. *Proceedings of the Institution of Civil Engineers: Water, Maritime and Energy*, 112:111–114, 1995.

T.S. Hedges and H. Mase. Modified Hunt's equation incorporating wave setup. *ASCE Journal of Waterway, Port, Coastal and Ocean Engineering*, 130(3):109–113, 2004.

J-M. Hervouet. *Hydrodynamics of Free Surface Flows: Modelling with the Finite Element Method*. Wiley, 2007.

C.W. Hirt and B.D. Nichols. Volume of fluid (VOF) method for the dynamics of free boundaries. *Journal of Computational Physics*, 39(1):201–225, 1981.

R.A. Holman and A.H. Sallenger. Setup and swash on a natural beach. *Journal of Geophysical Research*, 90(C1):945–953, 1985.

J.T. Holt and I.D. James. An s coordinate density evolving model of the northwest european continental shelf: 1, model description and density structure. *Journal of Geophysical Research*, 106(C7):14015–14034, 2001.

L.H. Holthuijsen. *Waves in Oceanic and Coastal Waters*. Cambridge University Press, 2007.

M. Hulme, X. Lu, J. Turnpenny, T. Mitchell, G. Jenkins, R. Jones, J. Lowe, J. Murphy, D. Hassell, P. Boorman, R. McDonald, and S. Hill. Climate change scenarios for the United Kingdom: The UKCIP02 scientific report. Technical report, Tyndall Centre for Climate Change Research, 2002.

A. Hunt. *Extreme waves, overtopping and flooding at sea defences*. Dphil thesis, Oxford University, 2003.

I.A. Hunt. Design of seawalls and breakwaters. *Proceedings of American Society of Civil Engineers*, 85:123–152, 1959.

K.-R. Jin and Z.-G. Ji. Calibration and verification of a spectral wind-wave model for Lake Okeechobee. *Ocean Engineering*, 28(5):571–584, 2001.

A.B. Kennedy, Q. Chen, J.T. Kirby, and R.A. Dalrymple. Boussinesq modeling of wave transformation, breaking and runup. I: 1D. *ASCE Journal of Waterway, Port, Coastal and Ocean Engineering*, 126(1):39–47, 2000.

G. Kim, C. Lee, and K.-D. Suh. Extended Boussinesq equations for rapidly varying topography. *Ocean Engineering*, 36:842–851, 2009.

J.T. Kirby. Boussinesq models and applications to nearshore wave propagation, surf zone processes and wave-induced currents. In *Advances in Coastal Modeling, Ed. V.C. Lakhan*, pages 1–41. 2003.

N. Kobayashi and A.W. Raichle. Irregular wave overtopping of revetments in surf zones. *ASCE Journal of Waterway, Port, Coastal and Ocean Engineering*, 120(1):56–73, 1994.

N. Kobayashi, A.K. Otta, and I. Roy. Wave reflection and run-up on rough slopes. *ASCE Journal of Waterway, Port, Coastal and Ocean Engineering*, 113(3):282–298, 1987.

N. Kobayashi, G.S. DeSilva, and K. Watson. Wave transformation and swash oscillation on gentle and steep slopes. *Journal of Geophysical Research*, 94(C1):951–966, 1989.

D.J. Korteweg and G. de Vries. On the change of form of long waves advancing in a rectangular canal, and on a new type of long stationary waves. *Philisophical Magazine Series 5*, 39(240): 422–443, 1895.

J. Larsen and H. Dancy. Open boundaries in short wave simulations - a new approach. *Coastal Engineering*, 7:285–297, 1983.

C. Lee, Y.-S. Cho, and K. Yum. Internal generation of waves for extended Boussinesq equations. *Coastal Engineering*, 42:155–162, 2001.

C. Lee, Y.-S. Cho, and S.B. Yoon. A note on linear dispersion and shoaling properties in extended Boussinesq equations. *Ocean Engineering*, 30:1849–1867, 2003.

P. Lin and P.L.F. Liu. A numerical study of breaking waves in the surf zone. *Journal of Fluid Mechanics*, 359:239–264, 1998.

P.L.F. Liu and I.J. Losada. Wave propagation modeling in coastal engineering. *Journal of Hydraulic Research*, 40(3):229–240, 2002.

M.S. Longuet-Higgins. On the statistical distribution of the heights of sea waves. *Journal of Marine Research*, 9:245–266, 1952.

M.S. Longuet-Higgins. On the distribution of the heights of sea waves: Some effects of nonlinearity and finite band width. *Journal of Geophysical Research*, 85(C3):1519–1523, 1980.

M.S. Longuet-Higgins and E.D. Cokelet. The deformation of steep surface waves on water. I. A numerical method of computation. *Proceedings of the Royal Society of London. Series A, Mathematical and Physical Sciences*, 350(1660):1–26, 1976.

M.S. Longuet-Higgins and R.W. Stewart. Changes in the form of short gravity waves on long waves and tidal currents. *Journal of Fluid Mechanics*, 8:565–583, 1960.

M.S. Longuet-Higgins and R.W. Stewart. Radiation stresses in water waves; a physical discussion, with applications. *Deep-Sea Research*, 11:529–562, 1964.

Halcrow Group Ltd, HR Wallingford, and John Chatterton Associates. National appraisal of assets at risk from flooding and coastal erosion, including the potential impact of climate change. Technical report, DEFRA, 2001.

P.J. Lynett, T.-R. Wu, and P.L.F. Liu. Modeling wave runup with depth-integrated equations. *Coastal Engineering*, 46:89–107, 2002.

P.J. Lynett, J.A. Melby, and D.-H. Kim. An application of Boussinesq modeling to hurricane wave overtopping and inundation. *Ocean Engineering*, 37:135–153, 2010.

P.A. Madsen and H.A. Schäffer. Higher-order Boussinesq-type equations for surface gravity waves: derivation and analysis. *Philisophical Transactions of the Royal Society of London*, A356: 3123–3184, 1998.

P.A. Madsen and H.A. Schäffer. A review of Boussinesq-type equations for surface gravity waves. In *Advances in Coastal and Ocean Engineering, Ed. P. L-F. Liu*, volume 5, pages 1–95. 1999.

P.A. Madsen and O.R. Sorensen. A new form of the Boussinesq equations with improved linear dispersion characteristics. Part 2. A slowly varying bathymetry. *Coastal Engineering*, 18:183–204, 1992.

P.A. Madsen and O.R. Sorensen. Bound waves and triad interactions in shallow water. *Ocean Engineering*, 20(4):359–388, 1993.

P.A. Madsen, R. Murray, and O.R. Sorensen. A new form of the Boussinesq equations with improved linear dispersion characteristics. *Coastal Engineering*, 15:371–388, 1991.

P.A. Madsen, O.R. Sorensen, and H.A. Schaffer. Surf zone dynamics simulated by a Boussinesq type model. Part I. Model description and cross-shore motion of regular waves. *Coastal Engineering*, 32:255–287, 1997a.

P.A. Madsen, O.R. Sorensen, and H.A. Schaffer. Surf zone dynamics simulated by a Boussinesq type model. Part II: surf beat and swash oscillations for wave groups and irregular waves. *Coastal Engineering*, 32:289–319, 1997b.

P.A. Madsen, H.B. Bingham, and H. Liu. A new Boussinesq method for fully nonlinear waves from shallow to deep water. *Journal of Fluid Mechanics*, 462:1–30, 2002.

P.A. Madsen, D.R. Fuhrman, and B. Wang. A Boussinesq-type method for fully nonlinear waves interacting with a rapidly varying bathymetry. *Coastal Engineering*, 53:487–504, 2006.

P.A. Madsen, D.R. Fuhrman, and H.A. Schäffer. On the solitary wave paradigm for tsunamis. *Journal of Geophysical Research*, 113, C12012:1–22, 2008.

H. Mase. Spectral characteristics of random wave run-up. *Coastal Engineering*, 12:175–189, 1988.

H. Mase. Random wave runup height on gentle slope. *ASCE Journal of Waterway, Port, Coastal and Ocean Engineering*, 115(5):649–661, 1989.

H. Mase. Frequency down-shift of swash oscillations compared to incident waves. *Journal of Hydraulic Research*, 33(3):397–411, 1995.

H. Mase. Personal Communication, 2008.

H. Mase, A. Miyahira, and T.S. Hedges. Random wave runup on seawalls near shorelines with and without artificial reefs. *Coastal Engineering Journal*, 46(3):247–268, 2004.

M.V. McCabe, P.K. Stansby, and D.D. Apsley. Coupled wave action and shallow-water modelling for random wave runup on a slope. *Journal of Hydraulic Research*, 49:515–522, 2011.

J. McCowan. On the highest wave of permanent type. *Philosophical Magazine Series 5*, 38(233): 351–358, 1894.

Met Office. Met Office Website, 2011. http://www.metoffice.gov.uk/about-us/who/how/case-studies/floods-2007.

W.H. Munk. The solitary wave theory and its application to surf problems. *Annals of the New York Academy of Sciences*, 51(3):376–424, 1949.

O. Nwogu. Alternative form of Boussinesq equations for nearshore wave propagation. *ASCE Journal of Waterway, Port, Coastal and Ocean Engineering*, 119(6):618–638, 1993.

Office of Naval Research and Rijkswaterstaat. Swan website, 2011. http://swanmodel.sourceforge.net.

T. Okamoto and D.R. Basco. The Relative Trough Froude Number for initiation of wave breaking: Theory, experiments and numerical model confirmation. *Coastal Engineering*, 53:675–690, 2006.

P. Osuna and J. Wolf. A numerical study of the effect of wave-current interaction processes in the hydrodynamics of the Irish Sea. In *Proceedings of the 5th International Conference on Ocean Wave Measurement and Analysis: WAVES2005, Madrid, Spain*, 2005.

Overtopping Neural Network. Overtopping neural network calculation tool, 2007. http://www.deltares.nl/en/software/630304/overtopping-neural-network.

M.W. Owen. Design of seawalls allowing for wave overtopping. Technical report, HR Wallingford, Report EX924, 1980.

PC-Overtopping. PC-Overtopping online calculation tool, 2007. http://www.overtopping-manual.com/calculation_PC.html.

D.H. Peregrine. Long waves on a beach. *Journal of Fluid Mechanics*, 27:815–827, 1967.

O.M. Phillips. The equilibrium range in the spectrum of wind-generated waves. *Journal of Fluid Mechanics*, 4(4):426–434, 1958.

O.M. Phillips. On the dynamics of unsteady gravity waves of finite amplitude. Part 1. The elementary interactions. *Journal of Fluid Mechanics*, 9(2):193–217, 1960.

W.J. Pierson and L. Moscowicz. A proposed spectral form for fully developed wind seas based on the similarity theory of S. A. Kitaigorodskii. *Journal of Geophysical Research*, 69(24):5181–5190, 1964.

T. Pullen, N.W.H. Allsop, T. Bruce, A. Kortenhaus, H. Schuttrumpf, and J.W. van der Meer. *EurOtop. Wave Overtopping of Sea Defences and Related Structures: Assessment Manual*, 2007.

D. Reeve, A. Chadwick, and C. Fleming. *Coastal Engineering: Processes, Theory and Design Practice*. Spon Press, 2004.

S.O. Rice. Mathematical analysis of random noise. Parts I and II. *Bell System Technical Journal*, 23(3):282–332, 1944.

S.O. Rice. Mathematical analysis of random noise. Part III. *Bell System Technical Journal*, 24(1):46–156, 1945.

M.M. Rienecker and J.D. Fenton. A Fourier approximation method for steady water waves. *Journal of Fluid Mechanics*, 104:119–137, 1981.

R.C. Ris, L.H. Holthuijsen, and N. Booij. A third-generation wave model for coastal regions 2. Verification. *Journal of Geophysical Research*, 104(C4):7667–7681, 1999.

V. Roeber, K.F. Cheung, and M.H. Kobayashi. Shock-capturing Boussinesq-type model for nearshore wave processes. *Coastal Engineering*, 57:407–423, 2010.

J.R. Rossiter. The North Sea storm surge of 31 January and 1 February 1953. *Philosophical Transactions of the Royal Society of London*, A246(915):371–400, 1954.

E. Rusu, P. Pilar, and C.G. Soares. Evaluation of the wave conditions in Madeira Archipelago with spectral models. *Ocean Engineering*, 35(13):1357–1371, 2008.

H.A. Schäffer and P.A. Madsen. Further enhancements of Boussinesq-type equations. *Coastal Engineering*, 26:1–14, 1995.

H.A. Schäffer, P.A. Madsen, and R. Deigaard. A Boussinesq model for waves breaking in shallow water. *Coastal Engineering*, 20:185–202, 1993.

M.C. Shen and R.E. Meyer. Climb of a bore on a beach. Part 3. Run-up. *Journal of Fluid Mechanics*, 16(1):113–125, 1963.

J.B. Shiach, C.G. Mingham, D.M. Ingram, and T. Bruce. The applicability of the shallow water equations for modelling violent wave overtopping. *Coastal Engineering*, 51:1–15, 2004.

C. Small and R.J. Nicholls. A global analysis of human settlement in coastal zones. *Journal of Coastal Research*, 19(3):584–599, 2003.

J.A. Smith. The operational storm surge data archive. Technical report, Proudman Oceanographic Laboratory, Report No. 34, 1994.

R.J. Sobey. Variations on Fourier wave theory. *International Journal for Numerical Methods in Fluids*, 9:1453–1467, 1989.

M.A. Srokosz. On the probability of wave breaking in deep water. *Journal of Physical Oceanography*, 16:382–385, 1986.

P. Stansby, R. Xu, B. Rogers, A. Hunt, A. Borthwick, and P. Taylor. Modelling tsunami overtopping of a sea defence by shallow-water Boussinesq, VOF and SPH methods. In *Floodrisk 2008, Oxford*, 2008.

P.K. Stansby. Solitary wave runup and overtopping by a semi-implicit finite-volume shallow-water Boussinesq model. *IAHR Journal of Hydraulics Research*, 41(6):639–648, 2003.

P.K. Stansby. Personal Communication, 2011.

P.K. Stansby and T. Feng. Kinematics and depth-integrated terms in surf zone waves from laboratory measurement. *Journal of Fluid Mechanics*, 529:279–310, 2005.

P.K. Stansby, A.C. Hunt, R. Xu, P.H. Taylor, A.G.L. Borthwick, T. Feng, and D.R. Laurence. Wave overtopping from focussed wave groups: experiments and modelling. In *2nd IMA Conference on Flood Risk Assessment*, 2007.

G.J. Steendam, J.W. Van der Meer, H. Verhaeghe, P. Besley, L. Franco, and M.R.A. Van Gent. The international database on wave overtopping. In *Proceedings of the International Conference on Coastal Engineering*, pages 4301–4313, 2004.

G. Stelling and M. Zijlema. An accurate and efficient finite-difference algorithm for non-hydrostatic free-surface flow with application to wave propagation. *International Journal for Numerical Methods in Fluids*, 43(1):1–23, 2003.

G.S. Stelling and M. Zijlema. Numerical modeling of wave propagation, breaking and run-up on a beach. In *Advanced Computational Methods in Science and Engineering, Lecture Notes in Computational Science and Engineering*, volume 71, pages 373–401. 2010.

M.J.F. Stive. A scale comparison of waves breaking on a beach. *Coastal Engineering*, 9:151–158, 1985.

G.G. Stokes. On the theory of oscillatory waves. *Mathematical and Physical Papers*, 1:197–229, 1880.

I.A. Svendsen. Wave heights and setup in a surf zone. *Coastal Engineering*, 8:303–329, 1984.

I.A. Svendsen and J. Veeramony. Wave breaking in wave groups. *ASCE Journal of Waterway, Port, Coastal and Ocean Engineering*, 127(4):200–212, 2001.

H.U. Sverdrup and W.H. Munk. Wind, sea and swell: Theory of relations for forecasting. Technical report, U.S. Navy Hydrographic Office Publ. No. 601, 1947.

G. Symonds, D.A. Huntley, and A.J. Bowen. Two-dimensional surf beat: Long wave generation by a time-varying breakpoint. *Journal of Geophysical Research*, 87(C1):492–498, 1982.

C.E. Synolakis. The runup of solitary waves. *Journal of Fluid Mechanics*, 185:523–545, 1987.

E.B. Thornton and R.T. Guza. Transformation of wave height distribution. *Journal of Geophysical Research*, 88, C10:5925–5938, 1983.

F.C.K. Ting. Laboratory study of wave and turbulence velocities in a broad-banded irregular wave surf zone. *Coastal Engineering*, 43:183–208, 2001.

F.C.K. Ting and J.T. Kirby. Observation of undertow and turbulence in a laboratory surf zone. *Coastal Engineering*, 24:51–80, 1994.

P. S. Tromans, A. Anaturk, , and P. Hagemeijer. A new model for the kinematics of large ocean waves-application as a design wave. *Proceedings of First Offshore and Polar Engineering Conference*, 3:64–71, 1991.

F. Ursell. The long wave paradox in the theory of gravity waves. *Mathematical Proceedings of the Cambridge Philosophical Society*, 49(4):685–694, 1953.

J.W. Van der Meer and J.P.F.M. Janssen. Wave run-up and wave overtopping at dikes. In *Wave forces on inclined and vertical structures*, pages 1–27. ASCE, 1995.

M.R.A. van Gent. The modelling of wave action on and in coastal structures. *Coastal Engineering*, 22:311–339, 1994.

M.R.A. van Gent. Wave runup on dikes with shallow foreshores. *ASCE Journal of Waterway, Port, Coastal and Ocean Engineering*, 127(5):254–262, 2001.

M.R.A. van Gent, H.F.P. van den Boogaard, B. Pozueta, and J.R. Medina. Neural network modelling of wave overtopping at coastal structures. *Coastal Engineering*, 54:586–593, 2007.

J. Veeramony and I.A. Svendsen. The flow in surf-zone waves. *Coastal Engineering*, 39:93–122, 2000.

J.R. Weggel. Maximum breaker height. *ASCE Journal of Waterway, Harbors and Coastal Engineering Division*, 98:529–548, 1972.

G. Wei, J.T. Kirby, S.T. Grilli, and R. Subramanya. A fully nonlinear Boussinesq model for surface waves. Part 1: Highly nonlinear unsteady waves. *Journal of Fluid Mechanics*, 294: 71–92, 1995.

R.L. Wiegel. A presentation of cnoidal wave theory for practical application. *Journal of Fluid Mechanics*, 7(2):273–286, 1960.

J.M. Witting. A unified model for the evolution of nonlinear water waves. *Journal of Computational Physics*, 56:203–236, 1984.

S.B. Yoon and J.W. Choi. A note on extension of fully dispersive weakly nonlinear wave equations for rapidly varying topography. *Coastal Engineering Journal*, 43(3):143–160, 2001.

J.A. Zelt. The runup of nonbreaking and breaking solitary waves. *Coastal Engineering*, 15: 205–246, 1991.